Development of half-Heusler type thermoelectrical materials in a range of temperature from 300 to 500 ° C

Alizée Visconti

To cite this version:

Alizée Visconti. Development of half-Heusler type thermoelectrical materials in a range of temperature from 300 to 500 ° C. Thermics [physics.class-ph]. Université Grenoble Alpes, 2017. English. NNT : 2017GREAI112 . tel-01796818

HAL Id: tel-01796818
https://theses.hal.science/tel-01796818v1

Submitted on 22 May 2018

Communauté
UNIVERSITÉ Grenoble Alpes

THÈSE

Pour obtenir le grade de

DOCTEUR DE LA COMMUNAUTE UNIVERSITE GRENOBLE ALPES

Spécialité : **Matériaux, Mécanique, Génie Civil et Electrochimie**

Arrêté ministériel : 25 mai 2016

Présentée par

Alizée VISCONTI

Thèse dirigée par **Guillaume Bernard-Granger,**

préparée au sein du **Laboratoire de Modélisation et Matériaux pour la Métallurgie du CEA-Grenoble**
dans **l'École Doctorale Ingénierie – Matériaux Mécanique Energétique Environnement Procédés Production (I-MEP2)**

Développement de matériaux thermoélectriques de types half-Heusler pour applications dans la gamme de température 300 à 500°C

Thèse soutenue publiquement le **19 octobre 2017,**
devant le jury composé de :

Madame Anne DAUSCHER
Chargée de Recherche CNRS, HDR, Institut Jean Lamour, Rapporteur
Monsieur Jérôme CHEVALIER
Professeur des Universités, Laboratoire MATEIS, Rapporteur
Monsieur Jean-Michel MISSIAEN
Professeur des Universités, Laboratoire SIMAP, Président du jury
Madame Sylvie FOUCAUD
Professeur des Universités, Laboratoire SPSCT, Examinateur
Monsieur Jacques NOUDEM
Professeur des Universités, Laboratoire CRISTMAT, Examinateur
Madame Christelle NAVONE
Ingénieur de Recherche, CEA-Grenoble, Encadrant de thèse
Monsieur Guillaume BERNARD-GRANGER
Directeur de Recherches, CEA-Marcoule, Directeur de thèse
Monsieur Natalio MINGO
Directeur de Recherches,CEA-Grenoble, Invité

Title:

Development of half-Heusler thermoelectric materials for applications in the 300 to 500°C temperature range.

Abstract:

In this work, the n-type $Hf_{0.25}Zr_{0.25}Ti_{0.5}NiSb_{0.006}Sn_{0.994}$ and p-type $Hf_{0.44}Zr_{0.44}Ti_{0.12}CoSb_{0.8}Sn_{0.2}$ half-Heusler formulations have been investigated to address the development of thermoelectric materials for applications in the 300 to 500 °C temperature range. Both composition have been elaborated using a cold crucible levitation melting furnace, ball milling and SPS. The sintered materials have been characterised in terms of their microstructure and thermoelectric properties. In both cases, Hf oxide-based precipitates, located at the grain boundaries of the sintered polycrystal, are detected. They are thought to decrease the thermal conductivity by scattering lattice vibrations. Based on this conclusion, two ways to reduce the price per kilogram of such materials have been explored. First, by suppressing the hafnium of the raw composition and incorporating ex-situ HfO_2 nanoparticles. Secondly, by doing some key steps of the material synthesis under ambient atmosphere (air), which greatly simplify the global manufacturing process.

Keywords:

Thermoelectricity, Half-Heusler, Spark Plasma Sintering, Microstructure

Titre:

Développement de matériaux thermoélectriques de types half-Heusler pour applications dans la gamme de température 300 à 500°C.

Résumé:

Ce travail porte sur l'étude des matériaux half-Heusler de formulation $Hf_{0.25}Zr_{0.25}Ti_{0.5}NiSb_{0.006}Sn_{0.994}$, pour le type n, et $Hf_{0.44}Zr_{0.44}Ti_{0.12}CoSb_{0.8}Sn_{0.2}$, pour le type p, pour répondre à la nécessité de développer des matériaux thermoélectriques pour des applications dans une gamme de température allant de 300 à 500 °C. C'est deux compositions ont été élaborées par fusion à induction en creuset froid, broyage planétaire et frittage SPS. Les matériaux ont été caractérisés du point de vue de leur microstructure et de leurs propriétés thermoélectriques. Dans les deux cas, la présence de précipités à base d'oxyde d'hafnium aux joints de grains du matériau pollycristallin a été détectée. Ces précipités permettent la diminution de la conductivité thermique du matériau par diffusion des phonons. En se basant sur cette observation, nous avons étudié deux options possibles afin de réduire le coût de revient de tels matériaux. Premièrement, en supprimant l'hafnium et en ajoutant des nanoparticules de HfO_2 à la composition de base. Et deuxièmement, en effectuant certaines étapes clefs de la synthèse de ces matériaux sous atmosphère ambiante (air), ce qui permet une simplification du procédé global de fabrication.

Mots clefs:

Thermoélectricité, Half-Heusler, Spark Plasma Sintering, Microstructure

Introduction

The search for alternative energy technologies has taken an accelerated pace in the last 50 years due to an increasing concern about climate change. Indeed, the use of nuclear energy being controversial in many countries, added to the need to decrease the use of fossil supplies, have led to a rising interest in new technologies to provide a sustainable supply of clean energy. In this quest to find new energy sources, it is interesting to point out that, today, a lot of energy is wasted as heat released into the environment. As a potential solution, thermoelectric power generators could be used to transform the waste heat into useful electrical energy.

Thermoelectric generators are directly converting heat into electricity and vice versa. They consist of an assembly of n and p-type semiconducting legs connected electrically in series and thermally in parallel. An applied temperature difference between n and p-sides drives charge carriers displacement in the material (electrons for an n-type material and holes for a p-type), leading to their diffusion from the hot side to the cold one. Therefore a current flow is generated through the circuit. However, thermoelectricity did not get much attention until 1950, when Ioffe reported that doped semiconductors can be used to generate refrigeration or electricity. From there, despite their relatively low efficiency and high cost, thermoelectric devices have attracted interest because of their advantages over conventional power generator or cooling devices: no moving part, no liquid involved, high reliability, noiseless, long life time without maintenance and also low environmental impact.

At the end of the 20th century, thermoelectric devices became a well-established technology for cooling electronic displays and radioisotope thermoelectric generators (RTG) in NASA or ESA space probes. Over the last several decades, the increased energy demand combined with the environmental concerns, led to another potential use of thermoelectricity as an alternative energy source by recovering the huge amount of heat lost in industrial or domestic applications. Nowadays, thermoelectricity is limited by its efficiency factor, around 10 % for power generation, mainly governed by the material's properties incorporated in a device. Even if a low performance may be acceptable for some applications, such as the one cited before, it has to be improved in order to be cost effective for others. For example, presently, thermoelectric devices are actively considered as clean energy sources for waste heat recovery in automotive applications or geothermal and solar energy segments. Therefore, the actual key challenge is to address the market devoted to the waste-heat recovery in the 300-500 °C temperature range. Waste-heat recovery in cars and trucks can make a large impact as transport account is responsible for 20 % of all carbon released in the atmosphere. Moreover, wasted-heat in industry (metallurgy/nuclear…) is also a major concern. Both recovery problematics may be addressed using thermoelectric devices efficient in the 300-500 °C temperature range.

The dimensionless figure of merit, $ZT=S^2\sigma T/\kappa$, with T the absolute temperature, of a material is used to evaluate its thermoelectric performance. A high ZT can be obtained by optimising the transport properties of the material. Both the Seebeck coefficient (S) and electrical conductivity (σ) must be as large as possible, while thermal conductivity (κ) must be minimised. A possible strategy to obtain good thermoelectric materials is then based on minimising the thermal conductivity of the selected semiconductors without affecting the electronic transport. This can be achieved by inducing additional phonon scattering sources in the materials, in order to decrease the phonon lifetime.

Numerous thermoelectric material pairs have been investigated and developed over the last 20 years. Most of the already known class of thermoelectric materials have been improved and new classes have been developed, leading to a significant improvement of ZT values being optimum in different temperature ranges. In order to be efficient and to be viable for large scale manufacturing of power generators, a thermoelectric material has to fulfil several requirements. First, the raw materials chosen have to be non-toxic, cheap and abundant. Secondly, the manufacturing process should be robust and suitable for large volume production. Last but not least, the selected materials have to exhibit acceptable thermoelectric properties in the temperature range of interest for the final application. They must also have a long-term thermal stability in different kinds of environments and good mechanical properties.

Half-Heusler materials have been shown to be good candidates in the 300 to 600 °C temperature range. Indeed, due to their semiconductor like band structure, they exhibit a large Seebeck coefficient and high electrical conductivity. Unfortunately, the thermal conductivity of half-Heusler materials is rather high when compared to other thermoelectric materials. Therefore, the main research efforts on half-Heusler formulations, devoted to be used for thermoelectric applications, have been focused on decreasing the thermal conductivity, while maintaining good electronic transport.

Accordingly, the main objective of the PhD thesis was to investigate the link between the microstructure and the thermoelectric properties of n and p-types half-Heusler alloys from the generic compositions MNiSn (n-type) and MCoSb (p-type), with M being Ti, Zr and Hf. All investigated compositions have been elaborated by a three step process: (i) ingots synthesis using cold crucible levitation melting, (ii) subsequent ball milling to obtain a calibrated powder and (iii) sintering by spark plasma sintering (SPS) to obtain dense polycrystalline pellets that are characterised regarding their microstructure and thermoelectric properties from room temperature to 500-600 °C.

The present PhD manuscript is divided into five chapters. The first one consists of an extensive literature review. The concepts related to thermoelectricity are summarised. Then, the different kinds of materials suitable for thermoelectric conversion are presented, with a focus on what options are available to improve their performance. Based on the actual requirements for thermoelectric applications in the 20-600 °C temperature range, the choice to investigate half-Heusler alloys is discussed. Finally, the global strategy that will guide our experimental work is described.

The second chapter is devoted to the presentation and understanding of elaboration and characterisation methods retained in the framework of our investigations. The procedure to obtain almost dense pellets of sintered polycrystalline n and p-types materials is detailed. Then it is explained how the materials have been characterised from the thermoelectric and microstructural point of views.

The third chapter focuses on results regarding the manufacturing and characterisation of n-type half-Heusler samples having the $Hf_{0.25}Zr_{0.25}Ti_{0.5}NiSb_{0.006}Sn_{0.994}$ target composition. Pellets have been synthetized at different temperatures and microstructure observations are used in order to evaluate how the sintered microstructure influences the thermoelectric properties.

Based on the conclusions made on the $Hf_{0.25}Zr_{0.25}Ti_{0.5}NiSb_{0.006}Sn_{0.994}$ n-type composition, chapter four explores the ways to reduce the price per kilogram of such a given material and how to simplify its manufacturing process, without introducing any detrimental effect on the thermoelectric properties. For this purpose, two approaches have been retained. The first one consists of investigating the thermoelectric and microstructural properties of sintered pellets made of a composite material, obtained by mixing a hafnium free n-type $Zr_{0.5}Ti_{0.5}NiSb_{0.006}Sn_{0.994}$ powder with hafnium oxide-based ex-situ nano-particles. The second approach consists of simplifying the global manufacturing process, by doing some key steps under ambient atmosphere (air) rather than in inert glove boxes. Accordingly, we will show that such a way promotes the formation of an in-situ nanometer-sized-precipitation that enables to keep the ZT value to a good level for all the temperature range of interest, while strongly simplifying the handling operations. In both cases, microstructure characterisation will highlight the presence of oxide precipitates in the sintered pellets and their effect on the thermoelectric properties will be discussed.

Chapter five is a quick overview of results obtained on a p-type $Hf_{0.44}Zr_{0.44}Ti_{0.12}CoSb_{0.8}Sn_{0.2}$ composition fabricated through the same strategy as the one adopted for the n-type $Hf_{0.25}Zr_{0.25}Ti_{0.5}NiSb_{0.006}Sn_{0.994}$ one and derived compositions.

Finally, a general conclusion gives also some prospects of possible future investigations.

Chapter I

Thermoectricity and half-Heusler materials

This chapter recalls firstly what is thermoelectricity and what are the physical principles involved. Then the different families of thermoelectric materials are shortly presented and compared to the half-Heusler group that will be investigated in the context of the thesis. Finally, the strategy adopted for our investigations is described.

I - Thermoelectricity

This part describes the physical principles of the thermoelectric phenomenon and the challenges to face to be able to develop materials that could be used to design thermoelectric devices with optimal properties.

I.1 - Thermoelectric effects

a. Seebeck effect

The first thermoelectric phenomenon was noticed in 1821 by Thomas Seebeck[1]. He highlighted that, by connecting two dissimilar conductors at different temperatures, an electric field was generated, deflecting the needle of a compass placed nearby. The same effect, illustrated in Figure I.1 is observed for a gradient of temperature established in a bulk material.

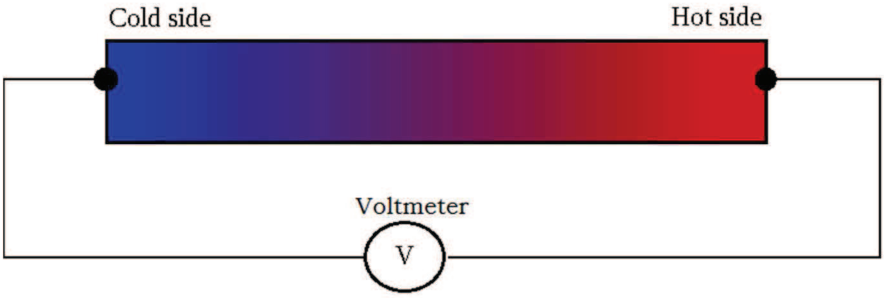

Figure I.1 : *Seebeck effect – Difference of potential induced by a temperature gradient in a given material.*

At the hot end, the energy of charge carriers is higher than the one at the cold end. This difference causes the diffusion of charge carriers from the hot side to the cold side. The charge separation in the material generates an electric field and consequently a difference of potential between the two sides.

The difference of potential produced, *dV,* is proportional to the temperature gradient applied, *dT*, and the ratio of *dV* to *dT* is called the Seebeck coefficient or the thermoelectric power, *S*, as shows in (I.1)

$$S = -\frac{dV}{dT} \qquad (I.1)$$

This coefficient can be positive or negative depending respectively on whether the charge carriers are holes or electrons.

b. Peltier effect

In 1834, Jean-Charles Peltier (later Lord Kelvin) discovered the complimentary effect of the Seebeck one[2]. In that case, a temperature change occurred around the junction of two dissimilar materials, such as metals or semiconductors, when an electric current flowed through them. As shown in Figure I.2 for two dissimilar materials, X and Y, the junction is either cooled or heated depending on the direction of the current flow. Indeed, the charge carriers, electrons or holes, carrying the current will transport charge and heat.

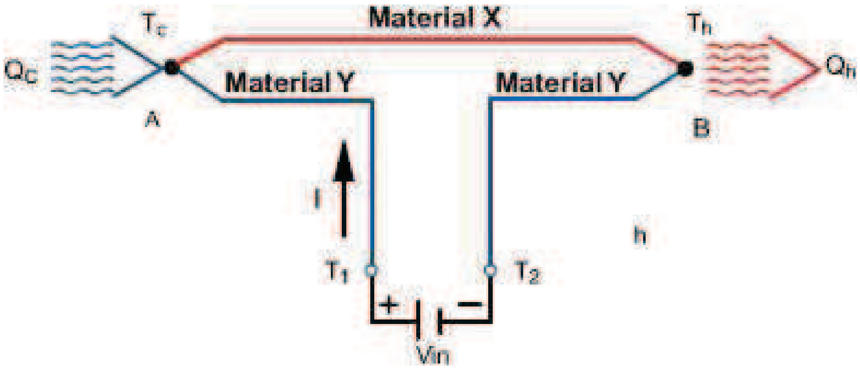

Figure I.2 : *Peltier effect in two dissimilar materials X and Y.*

The rate of heating, Q, at the junction between material X and Y is proportional to the current, *I*, by the equation (I.2):

$$Q = \pi_{XY}\, I\,, \qquad with\, \pi_{XY} = \pi_X - \pi_Y \qquad (I.2)$$

π_{XY} is called the Peltier coefficient of the junction X and Y of witch the respective Peltier coefficients are π_X and π_y. The Peltier effect represents the amount of heat current carried per unit charge in a given material. Thereby, even though across the junction between two distinct materials the current flow is continuous, as each material got its own Peltier coefficient, there will be a discontinuity of the associated heat flow at the junction. Thus, if an electric current flows from a given material 1 to a distinct material 2, if $\pi_1 < \pi_2$, there will be a cooling effect at the junction. On the contrary, if $\pi_1 > \pi_2$, there will be a heating effect at the junction. For instance, in the case of Figure I.2, $\pi_X < \pi_Y$.

c. Thomson effect.

A third thermoelectric effect was predicted and subsequently experimentally observed by William Thomson in 1851, by establishing the relationship between the Seebeck and the Peltier effects. Indeed, the Thomson effect predicts that, if an electric current passing through a material is accompanied by a temperature gradient, it will generate a heat exchange, cooling or heating depending on the material, with the environment. [3]

For a spatial coordinate *x* and a current *I*, the gradient of heat flux $\frac{dq}{dx}$ (q is heat) is linked to the temperature gradient $\frac{dT}{dx}$, by the equation (I.3):

$$\frac{dq}{dx} = \tau_{XY}\, I\, \frac{dT}{dx} \qquad \text{(I.3)}$$

where τ_{XY} represents the Thomson coefficient.

Afterward, Thomson suggested the relations (I.4) and (I.5), known as the Kelvin relations, connecting the three thermoelectric coefficients introduced previously:

$$\pi_{XY} = S_{XY}\,\mathrm{T} \qquad \text{(I.4)}$$

$$\tau_{XY} = T\,\frac{dS_{XY}}{dT} \qquad \text{(I.5)}$$

where *T* is the absolute temperature. These relations are useful to obtain both π_{XY} and τ_{XY} as the Seebeck coefficient can be easily measured experimentally.

d. Energy conversion: cooling and power generation

Whether it is for a refrigerator or for a generator, a thermoelectric device consists of an assembly of couples of semi-conductors electrically connected. A couple is formed by a p-type material, which has holes as charge carriers and a positive Seebeck coefficient, and by an n-type material, in which charge carriers are electrons and having a negative Seebeck coefficient. In an n-type semiconductor, the Fermi level is greater than that of an intrinsic semiconductor and it is close to the conduction band, as seen in Figure I.3 (a). On the contrary, the Fermi level of a p-type semiconductor is closer to the valence band, as shown in Figure I.3 (b).

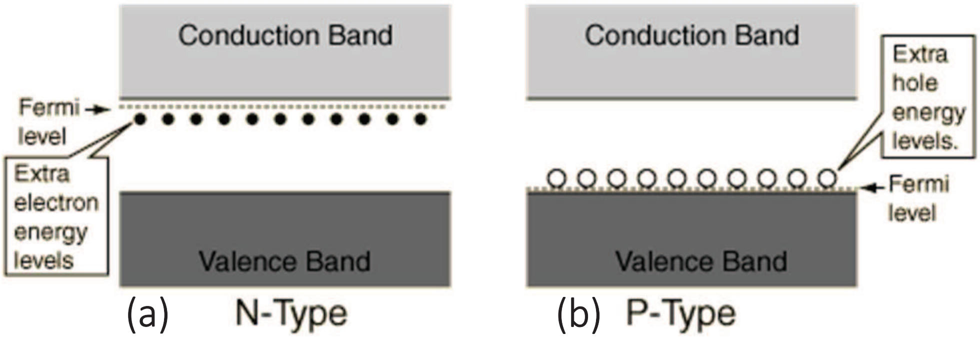

Figure I.3 : *Fermi levels in an n-type semiconductor (a) and in a p-type semiconductor (b).*

Both n and p-types are connected with a conductor material, so that the different couples are set electrically in series and thermally in parallel to form a thermoelectric couple as shown in Figure I.4 (a) and (b).

In Figure I.4 (a), a temperature difference is imposed across the thermoelectric couple, generating a current. Therefore, a part of the heat source will be converted into electrical power; it is the thermoelectric generator situation. Similarly, as shown in the Figure I.4 (b), a current passing through the thermoelectric couple will generate a temperature gradient and, accordingly, the module can be used as a refrigerator.

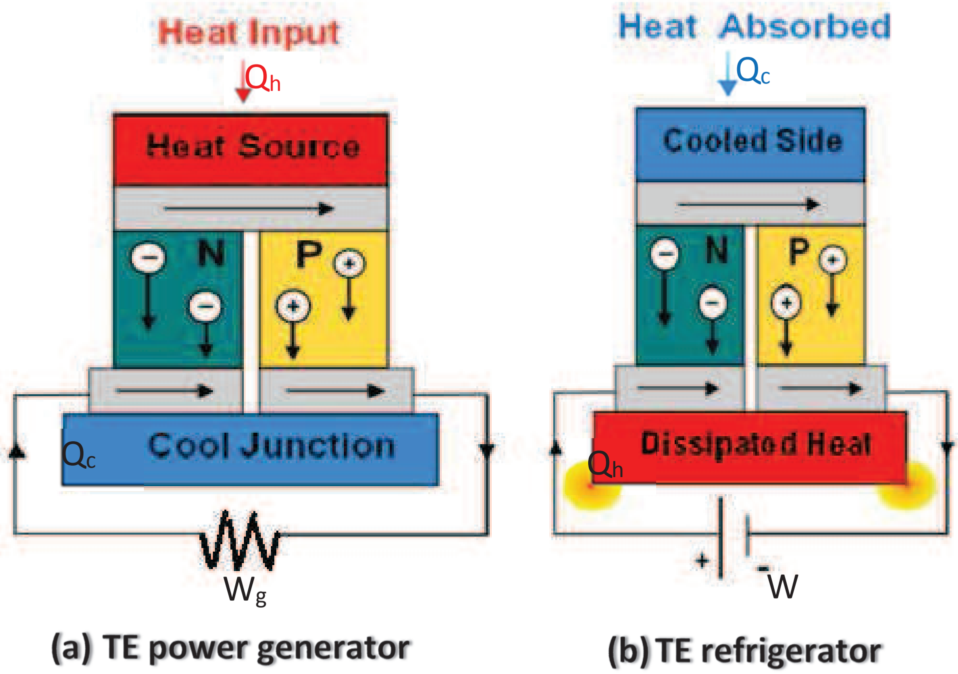

Figure I.4 : *Thermoelectric couple for (a) power generation or (b) cooling device.*

e. Thermoelectric device efficiency

Considering that: (i) the n and p branches have constant cross sections A_n and A_p, and equal length L_n and L_p, (ii) the heat flux is only in one direction, (iii) S (Seebeck coefficient), ρ (electrical resistivity) and κ (thermal conductivity) are independent of temperature, (iv) the contact resistances and the thermoelectric power at interfaces can be neglected and (v) finally considering that the stationary state is reached, [4] the efficiency of a thermoelectric device can be calculated. The efficiency of a thermoelectric generator, η, is defined as the ratio between the electrical power delivered, W_g, to the heat flow transmitted to the heat source, Q_h:

$$\eta = \frac{W_g}{Q_h} = \frac{I\left[\left(S_p - S_n\right)\Delta T - IR\right]}{K\Delta T + \left(S_p - S_n\right)IT_h - \frac{1}{2}I^2R} \tag{I.6}$$

$$with: \; K = \frac{\kappa_p A_p}{L_p} + \frac{\kappa_n A_n}{L_n} \quad and \quad R = \frac{\rho_p L_p}{A_p} + \frac{\rho_n L_n}{A_n} \tag{I.7}$$

where:

- ΔT is the difference of temperature between the cold, T_c, and the hot junction, $T_{h,}$

- the denominator term involves, in order: the thermal conductance heat flow generated by the temperature gradient $K\Delta T$, the heat generated by the Peltier effect $\left(S_p - S_n\right)IT_h$, and finally the Joule heating term $\frac{1}{2}I^2R$ due to the total resistance of the couple. K and R are respectively the total thermal conductance and the total thermal resistance.

The maximum efficiency of the power generator, η_{max}, is given by[1]:

$$\eta_{max} = \frac{(T_h - T_c)}{T_h} \frac{\left(1 - ZT_{np}\right)^{1/2} - 1}{\frac{T_c}{T_h} + \left(1 + ZT_{np}\right)^{1/2}} \tag{I.8}$$

$$with \qquad ZT_{np} = \frac{(S_p - S_n)^2 T}{[\,(\rho_p \kappa_p)^{1/2} + (\rho_n \kappa_n)^{1/2}\,]^2} \tag{I.9}$$

where ZT_{np} is the n/p couple figure of merit for a thermoelectric device and T is the average temperature between the cold and hot surfaces.

In equation (I.8) the term $\frac{(T_h - T_c)}{T_h}$ is the Carnot efficiency, η_{carnot}, which is the maximum efficiency of the device to turn heat into useful energy.

Similarly, the coefficient of performance, COP, of a thermoelectric cooling device can be calculated. It is defined as the cooling power produced, Q_c, divided by the rate of electric energy fed to the system, W:

$$COP = \frac{Q_c}{W} = \frac{-K\Delta T + (S_p - S_n)IT_c - \frac{1}{2}I^2R}{I\left[(S_p - S_n)\Delta T + IR\right]} \tag{I.10}$$

where all parameters have been already defined previously.

Here again, a maximum coefficient of performance, *COP_{max}*, value can be obtained:

$$COP_{max} = \frac{T_c}{(T_h - T_c)} \frac{(1 + ZT_{np})^{1/2} - \frac{T_h}{T_c}}{1 + (1 + ZT_{np})^{1/2}} \tag{ I.11}$$

where all parameters have been already described before.

Equations (I.8) and (I.11) clearly show that the efficiency of thermoelectric devices directly depends on the *ZT* of the materials incorporated. As shown in Figure I.5, the development of higher ZT materials leads to better performance of thermoelectric devices.

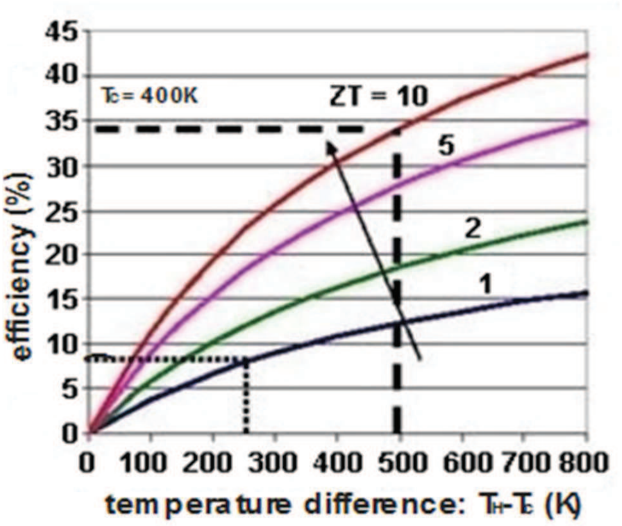

Figure I.5 : *Efficiency of a power generator depending on the temperature difference and on the* ZT_{np} *parameter of the thermoelectric couples.*

f. Thermoelectric figure of merit

As seen before, the performance of a thermoelectric material is described by a dimensionless figure of merit, *ZT*, defined as:

$$ZT = \frac{S^2\sigma T}{\kappa} = \frac{S^2 T}{\rho\kappa} \tag{I.12}$$

where: *S* is the Seebeck coefficient, σ is the electrical conductivity which is equivalent to the inverse of the electric resistivity, *1/ρ*, κ is the thermal conductivity, and finally, *T* is the absolute temperature. The expression $S^2\sigma$ is referred as the power factor.

The challenge is the optimisation of the material's transport properties. Indeed, looking at the expression (I.12) we can see that in order to have a high *ZT* value, the power factor must be as high as possible and the thermal conductivity as low as possible. However, there is an interrelation between the three parameters *S*, σ and κ. These three parameters are directly influenced by the carrier concentration, *n*, as show in Figure I.6.

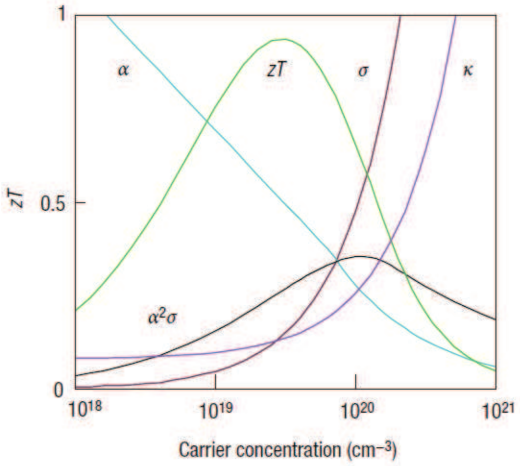

<u>Figure I.6 :</u> *Variation of S, σ, κ, ZT and power factor as a function of the carrier concentration*[5].

As the carrier concentration increases, the electrical conductivity increases. However, in the same time the Seebeck coefficient decreases and the thermal conductivity increases. According to Figure I.6, the *ZT* parameter is then maximal for a range of carrier concentration ranging from 10^{19} to 10^{21} cm^{-3}, which corresponds to the charge carrier concentration of heavily doped semiconductors.

I.2 - Transport properties

The relation (I.12) shows a strong dependence of the ZT parameter on, both, electrical and thermal conductivities. In order to find the better compromise and maximise the figure of merit, we have to perfectly understand the influence of both parameters.

a. Electrical conductivity

For semiconductors, a general expression of the electrical conductivity can be calculated from Boltzmann's transport equation by using the Fermi-Dirac distribution function and an isotropic parabolic band energy model[6]:

$$\sigma = \frac{2e^2\tau}{m^*} \left(\frac{m^* k_B T}{2\pi\hbar^2}\right)^{3/2} e^{-\frac{|E_F|}{k_B T}} \tag{I.13}$$

where: e is the electron charge, τ a relaxation time, which corresponds to the mean scattering time between carriers collisions, m^* is the effective mass of the carriers, k_B is the Boltzmann constant, $\hbar$ the reduced Planck constant and E_F the Fermi energy of the semiconductor.

Therefore, the electrical conductivity is strongly correlated to the dopant specie and concentration. Through the Fermi level, it is also linked to the material intrinsic properties, as the electronic and crystalline structure and the atomic mass, for example. Finally, the electrical conductivity is also influenced by the different scattering mechanisms activated in the material. This point will be addressed in section I.1.3.

b. Seebeck coefficient

From the Boltzmann's transport equation again, a general expression for the Seebeck coefficient can be derived in a simplified form as:

$$S = \frac{1}{eT} \frac{\int \sigma(E)(E - E_F) dE}{\int \sigma(E) \frac{\partial f_0}{\partial E} dE} \tag{I.14}$$

where: e is the electron charge, $\sigma(E)$ is the electrical conductivity for the electrons that fill the energy levels between E and E+dE[7], f_0 is the Fermi-Dirac distribution function, E_F is the Fermy energy equals to the chemical potential at 0 K and T is the absolute temperature[8].

Equation (I.14), shows that the Seebeck coefficient is proportional to E-E_F. Thus, in theory, higher Seebeck coefficients can be expected if the low energy carriers are cut off, which is called energy filtering[9].

c. Thermal conductivity

The thermal conductivity characterizes the transport of heat in solids. Thermal energy is transferred by thermalized electrons in the conduction band and lattice vibrations (phonons). Thus, the total thermal conductivity, κ, can be written as:

$$\kappa = \kappa_{carrier} + \kappa_{lattice} \tag{I.15}$$

- Electronic thermal conductivity.

When the carriers are passing through the material and transport electrical energy, they also transport heat. And the thermal conductivity due to the carriers can be an important feature, especially for heavily doped semiconductors (carrier concentration in the range 10^{19}-10^{20} cm^{-3}). According to the Wiedemann-Franz law[10], the carrier contribution to the thermal conductivity is written as:

$$\kappa_{carrier} = \frac{3}{2} (\frac{k_B}{e})^2 \sigma T \qquad \text{(I.16)}$$

Equation (I.16) can also be written as $\kappa_{carrier} = L \, \sigma \, T$, with L the Lorenz number. Lorenz number is not a completely constant value (it depends on temperature and material); Charles Kittel gives values ranging from 2.23×10^{-8} V².K^{-2} for copper at 0 °C to 3.2×10^{-8} V².K^{-2} for tungsten at 100 °C[11].

- Lattice thermal conductivity.

Another contribution to the thermal conductivity of a material is the heat carried by lattice vibrations, also known as phonons. A good approximation for it can be derived from the classical kinetic theory[12]:

$$\kappa_{lattice} = \frac{C_v \, \upsilon_S \, l}{3} \qquad \text{(I.17)}$$

where: C_v is the specific heat capacity at constant volume, υ_S is the average sound velocity and l is the mean free path of phonons.

At very low temperatures, because of the low amount of phonon excitation and because of their very long wavelength associated, phonon scattering in negligible and the lattice thermal conductivity is dominated by the Debye thermodynamic law, given by[13]:

$$\kappa_{lattice} = \frac{C_v \, \upsilon_S \, l}{3} \approx \frac{\upsilon_S \, l}{3} \, (\frac{T}{\theta_D})^3 \qquad \text{(I.18)}$$

with θ_D the Debye temperature.

However above the Debye temperature, C_v approaches the classic constant value *3NR* with *N* the number of mole of the considered material. Thus, the lattice thermal conductivity is dominated by the behavior of the mean free path of phonons, *l*, since the phonon velocity is almost independent of the temperature and accordingly the short wavelength phonons are dominant.

I.3 - Phonon scattering mechanisms

Scattering of carriers and phonons are key events that have to be understood. Indeed, the electrical conductivity and the Seebeck coefficient values are directly affected by carrier scattering, whereas phonon scattering impacts on the thermal conductivity value of a given material. The major scattering mechanisms in thermoelectric materials are described below.

Every scattering mechanism limit the mean free path of carriers. Therefore, the total relaxation time, τ, is proportional to the sum of the inverse of every single scattering time, τ_i, from each source, and it can be written as[14]:

$$\frac{1}{\tau}=\frac{1}{\tau_1}+\frac{1}{\tau_2}+\ldots\frac{1}{\tau_i} \quad \text{(I.19)}$$

a. Carrier scattering

In a thermoelectric material, carriers can be either electrons, holes, or both. When moving, they are possibly scattered by various mechanisms such as interactions with impurities, phonons, defects, or other carriers[15]. The most important mechanism in metals and semiconductors is the electron-phonon scattering one[16]. In metals, most of the Brillouin zone is occupied by electrons. Thus, scattering takes place from one point to another one on the Fermi surface with large momentum changes. Whereas in semiconductors, this zone being mostly unoccupied, the change in momentum vector occurs only at small angles. It is why small angle scattering is critical in semiconductors.

The carrier-phonon scattering mechanism in a semiconductor depends on the probability that a carrier will move from an initial to a final position. Thus, it is proportional to the availability of energy states, to the probability of absorbing or emitting a phonon and to the strength of the carrier-phonon interaction. Others well-known carriers scattering processes are acoustic phonons scattering, dominating at room temperature, and optical phonon scattering, dominating at high temperatures.

b. Phonon-phonon scattering

In most semiconductors, phonons are predominantly scattered by other phonons. Peierls showed that the most important scattering process involves three phonons[13]: either two phonons combine to create a third one (normal situation), as shown in Figure I.7 (a), or one phonon breaks up into two phonons (Umklapp situation), as in Figure I.7 (b).

In the normal situation, the energy and momentum are conserved in the collision, all the phonons scatter with a wave vector conservation equation:

$$\overrightarrow{k_1}+\overrightarrow{k_2}=\overrightarrow{k_3} \quad \text{(I.20)}$$

The wave vector of the third phonon lies within the first Brillouin zone, like in Figure I.7 (a). Consequently there is a redistribution of phonons without any thermal resistance.

On the contrary, for the Umklapp situation, the energy is conserved but not the momentum, as shown in the following equation:

$$\overrightarrow{k_1}+\overrightarrow{k_2}=\overrightarrow{k_3}+\vec{G} \quad \text{(I.21)}$$

Here, $\overrightarrow{k_3}$ lies outside the Brillouin zone. It can be mapped back into this zone by adding the reciprocal lattice vector, $\vec{G}$, as in Figure I.7 (b). $\vec{G}$ contributes to the thermal resistance. Moreover, Peierls showed that the Umklapp situation is predominant at high temperatures and therefore it is responsible for lowering the lattice thermal conductivity of a given material.

From the second order perturbation theory, the relaxation time for three phonons in the Umklapp scattering situation, τ_U, above room temperature, is given by[17]:

$$\frac{1}{\tau_U} = 2\gamma^2 \frac{k_B\, T}{V_0\, \mu} \frac{\omega^2}{\omega_D} \qquad (I.22)$$

where μ is the shear modulus, V_0 is the volume per atom of the crystal lattice, ω_D is the Debye frequency and γ represents the Gruneisen parameter which measures the anharmonicity of the lattice vibrations.

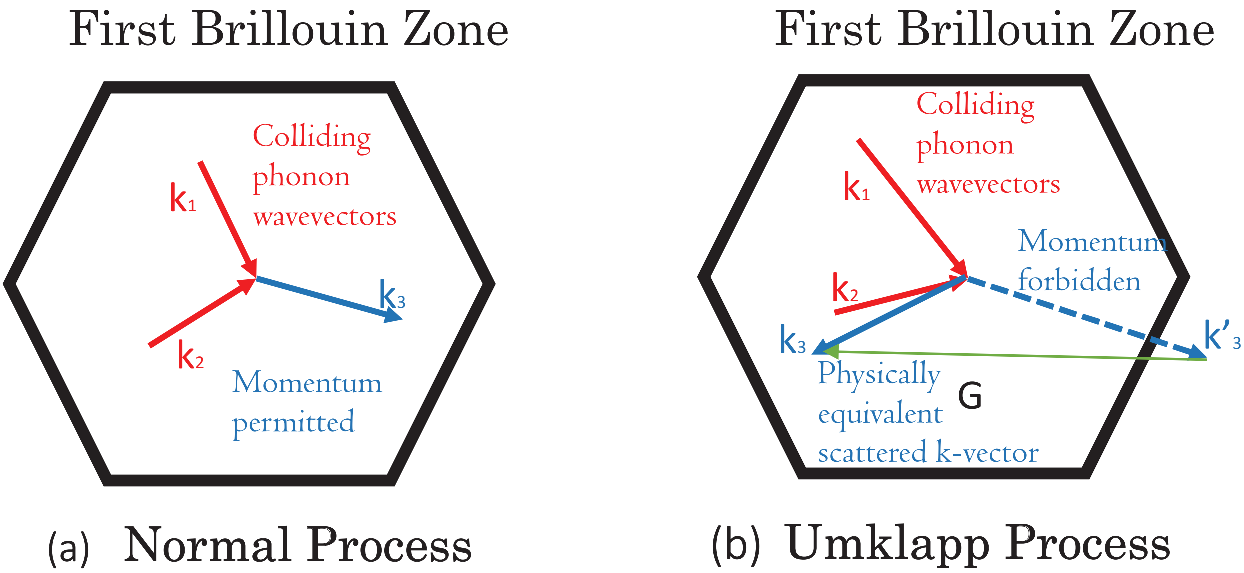

Figure I.7 : *Normal scattering (a), Umklapp scattering (b)*

c. Boundary scattering

For polycrystalline materials, another scattering mechanism involves grain boundaries. Boundary scattering is an important mechanism, especially at low temperatures and for long wavelength phonons. It depends typically on grain size.

The boundary scattering relaxation time, τ_B, is given by[18]:

$$\frac{1}{\tau_B} = \frac{v}{D}\,(1-p) \qquad (I.23)$$

with D the average grain diameter of a polycrystalline material, v the phonon velocity and p is the boundary specularity parameter. In fact $1-p$ represents the probability that the phonon undergoes diffusive scattering at the different interfaces (grain boundaries). In the case of very interacting interfaces (roughness, non-linearity for example), the scattering is purely diffusive and p=0, as in Figure I.8. Then equation (I.23) is reduced to the well-known Casimir limit[18]:

$$\frac{1}{\tau_B} = \frac{\nu}{D} \tag{I.24}$$

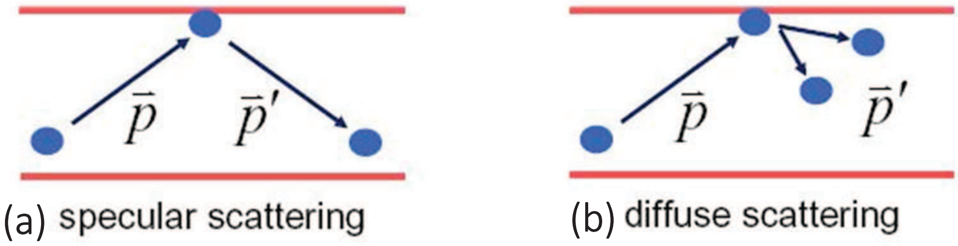

Figure I.8 : *Specular boundary scattering (a) and diffuse boundary scattering (b)*

The grain boundaries in a polycrystalline material can also scatter charge carriers, lowering the carrier's mobility and thus the electrical conductivity. Nevertheless, in most cases, the reduction of electrical conductivity due to carrier scattering is compensated by the reduction in thermal conductivity because of phonon scattering. Indeed, according to relation (I-23) a grain size reduction promotes an improvement of the thermoelectric performances of a given polycrystalline material[19].

d. Defects scattering

Defects scattering involves something locally in the crystal that is different from all the atoms that are surrounding it. For instance, it can be due to impurity sites, different isotopes, solid solutions or lattice vacancies in the host material[20]. The atom mass is possibly different from the host atoms and so it creates a point defect in the thermoelectric material, as in Figure I.9. At high temperatures, only the short wavelength phonons are strongly scattered by point defects in the lattice.

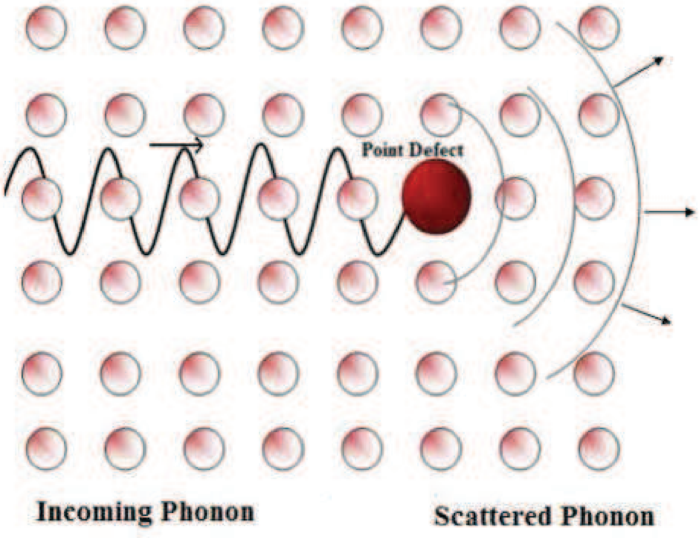

Figure I.9 : *Phonon scattering by a point defect.*

The phonon relaxation time, τ_D, for this scattering mechanism can be expressed as:

$$\frac{1}{\tau_D} = \frac{V_0 \Gamma \omega^4}{4\pi \nu^3} \qquad (I.25)$$

where: Γ is a disorder parameter proportional to the strength of the scattering point defect, V_0 is the volume per atom of the crystal lattice, ν and ω are respectively the phonon velocity and frequency.

Once again, this phenomenon can also affect carriers' motion, but phonons scattering is stronger in intensity and therefore it leads to a final improvement of the thermoelectric material performance by reducing strongly the lattice contribution to the thermal conductivity[21].

II - Thermoelectric materials and half-Heusler compounds

In this section, we are presenting the different families of thermoelectric materials that have been investigated in the literature. A focus is done on the half-Heusler group and we explain why this kind of alloys has been retained in the frame of the thesis.

II.1 - Materials for thermoelectric applications

a. Thermoelectric materials

Ioffe was the pioneer of thermoelectric materials investigations by introducing doped semiconductors in 1952[1]. For Ioffe, thermoelectric materials selection must follow these rules: having a high Seebeck coefficient value and a high value of the mean atomic mass of the atoms of the composition[22]. Few years later, Goldsmid and all. discovered Bi_2Te_3 as the first high-potential thermoelectric material for applications around room temperature[23]. In 1956, Ioffe and all. suggested the use of isomorphs solid solutions to create local mass fluctuations through the crystal lattice, in order to induce point defects and phonon scattering leading to significantly lower thermal conductivity values for the same kind of alloys[24].

After these preliminary developments, different classes of thermoelectric materials have developed. An overview is given in the following sub-sections.

- Chalcogenides.

Birkholz used the concept based on solid solutions of isomorphs by alloying the already promising Bi_2Te_3 to Sb_2Te_3 compounds[25]. Nowadays, the chalcogenides n-types $Bi_2Te_{3-x}Se_x$ and p-types $Bi_{2-x}Sb_xTe_3$

have exhibited ZT values around 1.4 at 100 °C and still remain basic materials groups for thermoelectric applications in the range 20-200 °C[26].

Lately, tin chalcogenides have attracted a great deal of interest. As an example, an outstandingly (and controversial) high ZT value of 2.6 at 650 °C has been reported for SnSe monocrystals according to peculiar orientations[27].

Other well-known chalcogenide-based materials are the ones belonging to the PbTe family. They have been used in practical applications since the 1950s[28]. N or p-type formulations have been developed, depending on the dopant used. Progresses have been made concerning this kind of materials by substituting Te with Sr, Sb or Sn generating enhanced p-type PbTe alloys with a ZT of 2.2 at 650 °C[29]. Despite high performance as thermoelectric materials, both kinds of formulation have a limited usage due to the rareness of Te and environmental or toxicity problems linked to Te and Pb elements.

Derived from a combination of Pb-Te and $AgSbTe_2$ systems, the LAST (lead, antimony, silver, telluride) have been shown to be n-type materials with a ZT value up to 2.2 at 530 °C[30]. And recently, another alternative compound, the p-type TAGS chalcogenide (Te-Ag-Ge-Sb) one, appeared to have interesting thermoelectrical properties, with a maximum ZT of 1.6 at 360 °C, obtained for the $Ge_{0.53}Ag_{0.13}Sb_{0.27}\square_{0.07}Te_1$ composition, □ representing a vacancy[31].

- Si based materials.

Using the same approach as the one described above, Abeles and all. synthesized a solid solution between silicon and germanium[32]. Even though both individual elements are bad thermoelectric materials, the solid solution Si-Ge presents good thermoelectric properties with, as an example, a ZT peak value around 0.95 at 900-950 °C for a p-type formulation[33]. Nowadays, germanium-poor Si-Ge alloys are attracting more and more attention due to the high cost of germanium.

In the range of temperatures going from 300 to 600 °C, the higher manganese silicides (HMS) are reported to have a ZT close to 0.7 at 500 °C for an Al-doped $MnSi_{1.73}$ composition[34]. To create thermoelectric generators with HMS, other silicides are used as an n-type material, as for example, $Mg_2Si_{1-x}Sn_{x\ (0.2<x<0.8)}$ alloys (Sb can be used as a dopant for this material). Thus ZT values as high as 1.4 at 510 °C have been obtained for an $Mg_2Si_{0.4}Sn_{0.6}$ composition[35].

- PGEC approach.

Another approach to achieve a maximum ZT value, known as the “phonon glass electron crystal” (PGEC) one was developed in 1979 by Slack[36]. The PGEC concept is to have a glass-like lattice thermal conductivity value coexisting with electronic properties associated to a good semiconductor. This features can be obtained by rattling motion of loosely bonded atoms within a large cage, generating strong scattering of lattice vibrations (phonons) but having a few impact on the electrons displacement.

Among the PGEC materials, skutterudites and clathrates have been investigated. Skutterudites, as for example $CoSb_3$ or $CoAs_3$, have a MX_3 generic formula, where M is a metal such as Co, Rh, Ir and X is P, As or Sb. This materials have been optimised, leading to the LM_4X_{12} chemical formula, where L is a rare earth element. Clathrates have a $X_8Y_{16}Z_{30}$ composition where X can be Ca, Sr or Ba; Y is Al or Ga and Z is Si, Ge or Sn. Skutterudites and clathrates possess a cage structure, where a large metal atom can be inserted in order to scatter phonons. Because the void-filling atoms can act as electron donors or acceptors and can be small and heavy, very good Seebeck coefficients can be obtained. In the same time, this specific structure promotes a large structural disorder, reducing the lattice thermal conductivity and leading to ZT values higher than 1. For example, a ZT peak value of 1.7 was reported in quadruple filled n-type skutterudites $Ba_{0.08}La_{0.05}Yb_{0.04}Co_4Sb_{12}$ at 580 °C[37] and a ZT around 1.35 at 630 °C was found for an n-type $Ba_8Ga_{16}Ge_{30}$ clathrate[38].

Other materials, as the half-Heusler group, exhibit an optimised complex crystalline structure and their chemical composition incorporate a large variety of atoms, limiting the mean free path of phonons. They appear to be good thermoelectric candidates, for temperatures going up to 600 °C, because of their chemical stability and also because they are easily synthetized. These materials will be described more precisely afterwards.

- Nanostructuration.

In the past 20 years, the thermoelectricity community realized about the importance of the low structure dimension for thermoelectric materials[39]. Indeed, simulations highlighted the effect of nanostructuration on the thermoelectric materials performances. In the case of polycrystalline materials, the nanostructuration consists of decreasing as much as possible the grain size, promoting phonon scattering at the increased amount of grain boundaries. Considering the phonon mean free path (100-200 nm at room temperature)[40], nanostructures are supposed to scatter phonons more efficiently than charge carriers (mean free path around 10-30 nm at room temperature). Therefore, nanostructuration reduces thermal conductivity more than electrical conductivity resulting in a ZT enhancement[41] [42].

A graph presenting the ZT of the materials exposed before is shown in Figure I.10. This part is only a quick and non-exclusive summary of the most known existing materials for thermoelectricity and more details can be found in the cited publications[43] [44] [45].

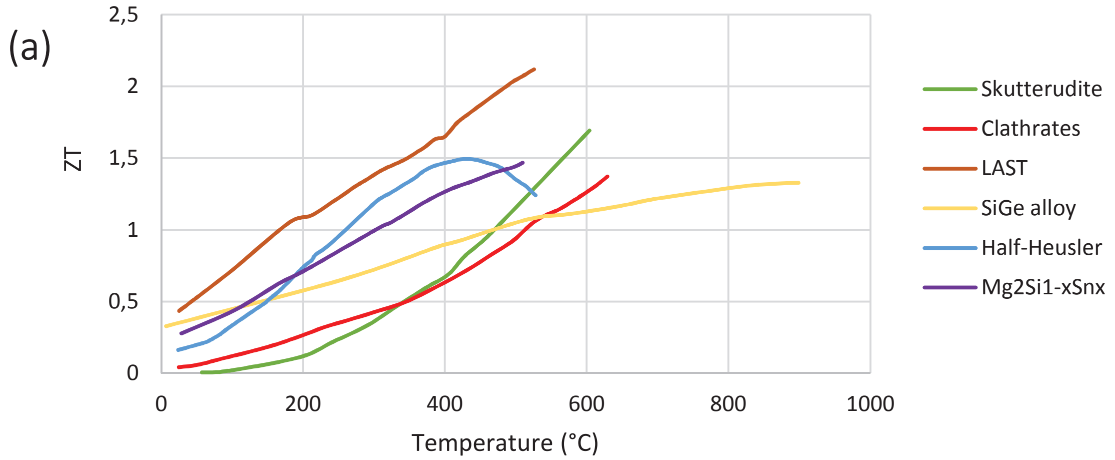

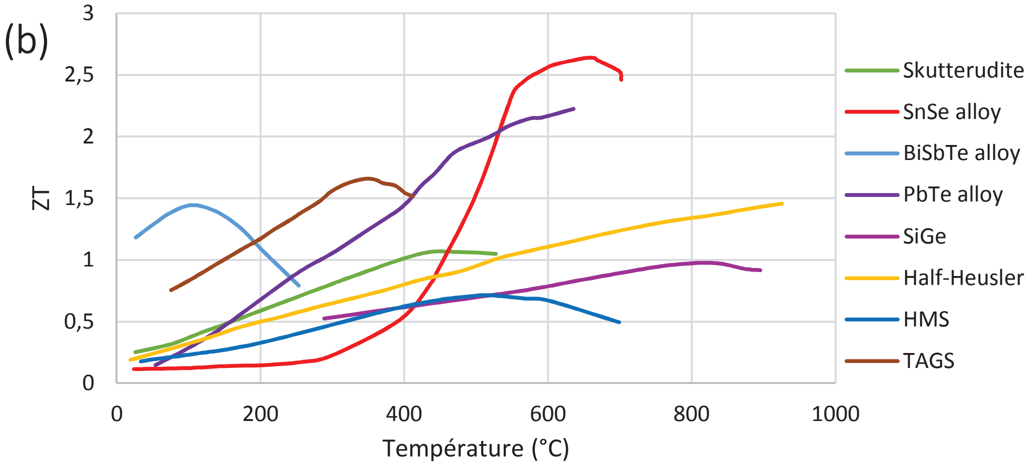

Figure I.10 : *Examples of (a) n and (b) p-types thermoelectric materials from the literature (References in the materials subsection presented before).*

b. Materials selection

As shown in the non-exclusive examples before, numerous thermoelectric materials systems have been investigated and developed over the last 20 years. Most of the already known class of thermoelectric materials have been improved and new classes have been developed, leading to a significant improvement of ZT values being optimum in different temperature ranges. In order to be efficient and to be viable for large scale production of power generators, a thermoelectric material has to fulfil several requirements, as resumed in Figure I.11. First, the raw materials chosen have to be non-toxic, cheap and abundant. Secondly, the manufacturing process should be robust and compatible with the production of a high volume of materials per day. Last but not least, the elaborated materials have to exhibit acceptable thermoelectric properties in the temperature range of interest for the final application. They must also have a long-term thermal stability in different kinds of environments and good mechanical properties.

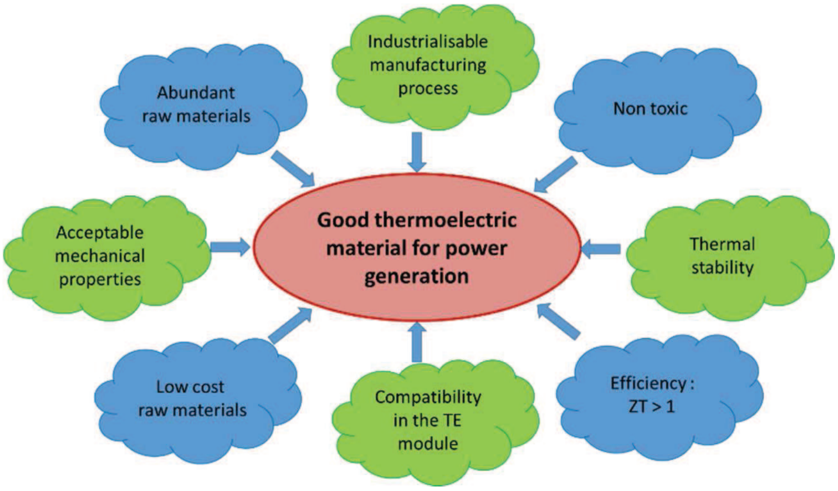

Figure I.11 : *Requirements for a good thermoelectric material.*

As shown in Figure I.12, the thermoelectric market for very high temperatures (600-1000 °C) is limited to space exploration. And the low temperatures segment (around room temperature) is mostly limited to domestic applications belonging to niche businesses. However, the transport segment accounts for 20 % of all carbon released in the atmosphere[46] and wasted-heat recovery in automotive and trucks is becoming a great deal. Thermoelectric materials potentially usable in such applications must have ZT values as high as possible and thermal stability in the temperature range 100 to 600 °C. Moreover, wasted-heat in industry (metallurgy/nuclear…) belongs also to this temperature domain. Accordingly, the most important challenge to address in a short future will be to find adequate thermoelectric materials efficient in the 300 to 500 °C temperature range.

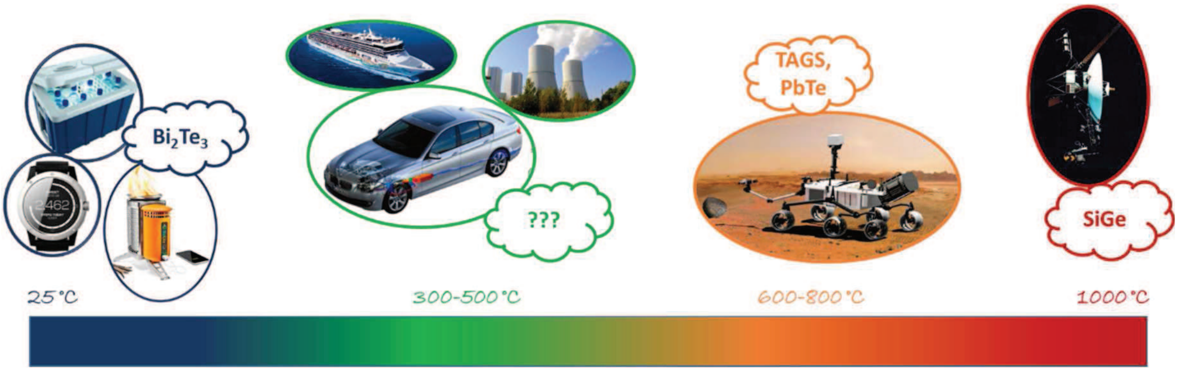

Figure I.12 : *Materials and applications depending on the service temperature.*

Figure I.13 shows the price versus crustal abundance of most of raw elements that can be used for the formulation of thermoelectric materials. Using this chart and the requirements present in Figure I.11, it is possible to target components that could be incorporated in viable thermoelectric materials. Accordingly, the chalcogenides (Bi_2Te_3, PbTe, Pb(Te,Se), Sb_2Te_3,…) group, the LAST formulations (based on the use of Te, Ag, Sb, Pb, Sn elements), the TAGS family (incorporating Te, Ag, Ge, Sb) and clathrates can be eliminated from a potential list of interest.

Due to the stoichiometric level accessible, it is interesting to point out that $Si_{0.8/0.92}Ge_{0.2/0.08}$ formulations are compatible with a selection method based on a cost/abundance filter and are passing through it. However, it has to be pointed out that the n-type is doped with As or P, which are toxic or hazardous elements. In addition, it has to be remained that the optimum temperature for the use of these kind of materials thermoelectric devices is around 800°C, the ZT values being too modest for the 300-500 °C temperature range.

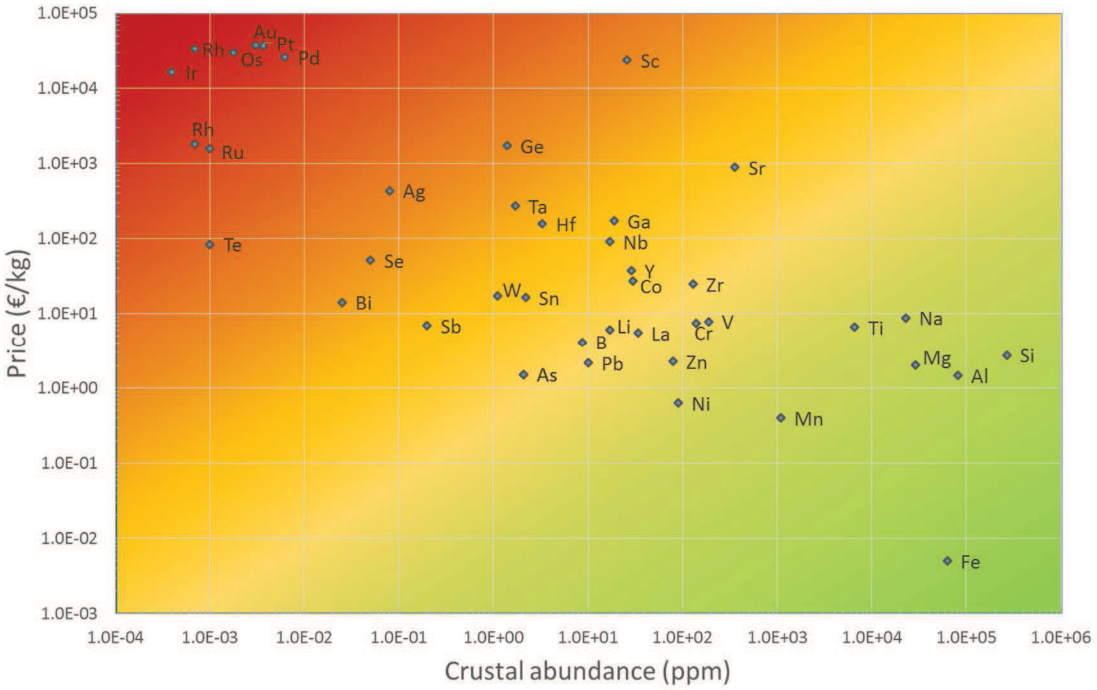

Figure I.13 : *Price vs crustal abundance of elements used in thermoelectric materials.*
(Data from [47and 48])

HMS and $Mg_2Si_{1-x}Sn_x$ alloys appear to be good candidates due to their chemical compositions and good thermoelectric properties around 500 °C. Nonetheless, joining problems (thermal expansion compatibility issues for the different components in presence) have still to be overcome before a robust and definitive implementation in thermoelectric modules. Consequently, skutterudites and half-Heusler compounds are the remaining possible solutions. However considering Figure I.11, skutterudites suffer from their mechanical brittleness, with fracture toughness values limited to 0.5 MPa.$m^{1/2}$ (lower than the one of a standard glass) at room temperature for an n-type In-doped Co_4Sb_{12} formulation[49]. Regarding the waste-heat recovery for automotive applications, which can go up to about 650 °C, skutterudites low thermal stability (tendency to oxidation[50]) is also a serious issue.

Then, half-Heusler alloys stand out and appear to be promising thermoelectric materials for mid-temperature power generation (ranging from 300 to 600 °C) [51]. Although they have a ZT lower than some other thermoelectric materials for medium-high temperatures, such as skutterdites or PbTe alloys, they have attracted increasing attention because of their relatively low cost, abundant components and their much better mechanical properties and thermal stability. Due to their semiconductor like band structure[52], these materials exhibit large Seebeck coefficient values going from -100 to -300 µV/°C and high electrical conductivity in the range 10^5-10^7 S.m^{-1}, both for a n-type formulation, as an example[53 54]. Unfortunately, half-Heusler alloys thermal conductivity is rather high (5-10 W.m^{-1}.K^{-1})[84]. Therefore, the main research efforts on half-Heusler formulations devoted to be used for thermoelectric applications have been focused on decreasing the thermal conductivity, while keeping a good electronic transport in the material.

II.2 - Half-Heusler compounds

a. Introduction

In 1903, Friedrich Heusler discovered the first Heusler alloy, Cu_2MnAl, which was surprisingly ferromagnetic, even though none of its elemental constituents are magnetic by themselves[55] [56].

This remarkable class of material includes more than 1500 compounds. Due to their promising properties they attracted great interest for potential spintronic applications and sustainable energy field, such as solar cells or thermoelectric devices.

The Heusler family is classified into two main groups: the full-Heusler compounds and the half or semi-Heusler ones. The full-Heusler are metallic compounds formulated as X_2YZ, where X and Y are usually transition metals and Z a metalloid or metal with a low melting point compared to X and Y, as shown in Figure I.14. They crystallize into the cubic crystal structure (space group 225, $Fm\underline{3}m$) [57]. The half-Heusler compounds will be described in the following section.

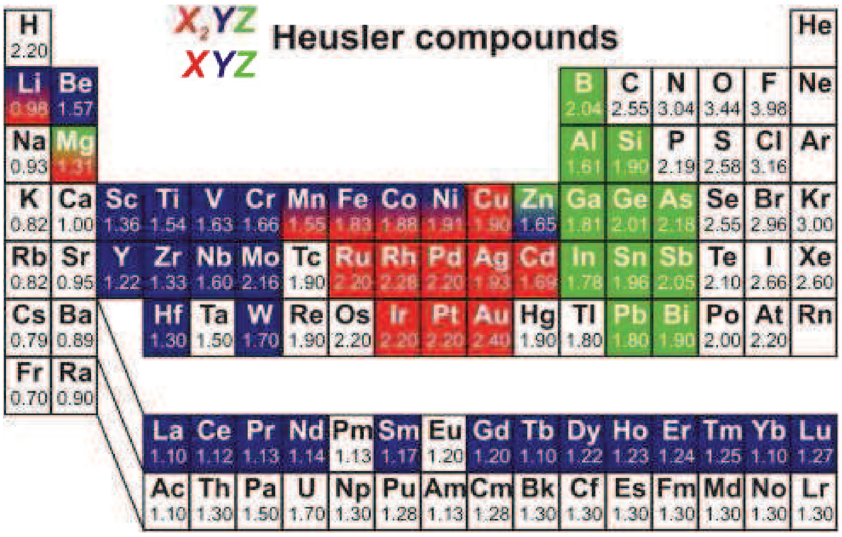

Figure I.14 : *Periodic table of the elements with the Heusler possible combinations.*

b. Half-Heusler compounds - Electronic and crystal structure

In order to understand the properties of these materials, the crystal structure and atom positions knowledge are necessary. Half-Heusler alloys are intermetallic compounds with a general formula XYZ. As for the Heusler materials, X and Y are transition metal (in some cases X can also be a rare-earth element) and Z is a main group element. The structure is analogous to the one of MgAgAs (space group 216, $F\underline{4}3m$). As presented in Figure I.15 it is made up of four face centered cubic sub-lattices, three being filled with the following Wyckoff positions : the Z atom is located at (0, 0, 0), the Y atom at (¼, ¼, ¼), and the X atom at (½, ½, ½) and the remaining one being vacant at (¾, ¾, ¾)[58].

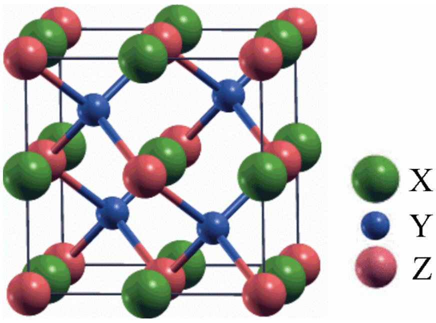

Figure I.15 : *Half-Heusler structure*

Half-Heusler materials for thermoelectricity exhibit a semiconducting behavior, mostly with an 18 valence electron count (VEC) character[59]. Nonetheless, some half-Heusler alloys, such as TiFeSb, got a VEC of 17, or 19, such as VCoSb[60], which doesn't change the good electronic properties of the material. It was determined by density of states calculations and experiments that half-Heulsers possess a band gap in the range 0 to 1.1 eV, near the Fermi energy level. Alieve measured the MNiSn (M = Hf, Ti, Zr) composition structure to have a narrow band gap of 0.1 to 0.2 eV[61]. Half-Heuslers narrow band gap usually provides a quite high Seebeck coefficient and a good electronic conductivity, leading to a high power factor.

Moreover, there is a high substitutability of the three lattice sites of the half-Heusler structure (X, Y and Z). Thus, it is possible to dope a half-Heusler compound on all three atom sites, allowing the tuning of electronic properties, changing the charge carrier concentration and introducing disorder to decrease the thermal conductivity of the material.

c. Synthesis of half-Heusler materials

Half-Heusler compounds contain high melting point elements, weighted in the desired stoechiometry, such as Hf (2233 °C), Zr (1855 °C), Ti (1668 °C), Ni (1455 °C) and Co (1495°C), as well as elements with lower melting points such as Sn (232 °C) and Sb (631°C).

- Powder synthesis using melting technics.

High temperature alloying methods are commonly used. The most widely applied one is the melting of raw materials by arc-melting in an Ar atmosphere[19, 60, and 72]. Others known melting technics to synthetized half-Heuslers used in literature are: induction melting by levitation or in a crucible[77 and 93], melt spinning[62] and optical floating zone melting[63]. Often, in the cases of arc melting and induction melting technics, the molten ingots are flipped and re-melt at least three times to ensure a good homogenization of the alloy composition. However, with theses high temperature melting technics it is important to note that for elements having a high vapour pressure, such as Sb, vaporization could be an issue. Accordingly, a typical method to compensate Sb evaporation is to add an extra 5 wt% of this element in the starting mix[64]. Impurity phases may be observed after the melting process. That is why, annealing of the ingot is often conducted afterward.

For that, the samples are typically vacuum sealed in quartz ampules and annealed around 900°C during 3 to 7 days, followed by a quenching step[77]. Then, usually, whatever they are quenched or not, ingots are reduced to powder by ball milling, commonly in a tape-sealed WC jar charged with WC balls in a glovebox, for few hours. However, considering an industrial application, this kind of global process is possibly time consuming.

- <u>Powder synthesis using solid state reaction.</u>

Another approach to avoid the material loss during manufacturing is to use solid state reactions. For Half-Heuslers synthesized using this route, the starting materials are preferably powders in order to facilitate the alloying process. The first solid state reaction technique used was by encapsulating the mixed powders of raw elements in a silica or quartz tube and heating it up to about 900°C[65]. However due to this low temperature, the alloying step takes time and can be up to two weeks for completion. Quite newly, microwave heating appeared to be an energy and time efficient method for solid state half-heusler synthesis[66] [67]. Also, even though mechanical alloying of half-Heuslers was first believed to be not successful due to the limited energy input (considering the high melting points of the used elements)[68], the $ZrNiSn_{1-x}Sb_{x\ (0<x<1)}$ formulation was successfully synthetized by Soon-Chul Ur, even though for now the obtained ZT is quite low (0.1 at 730 °C)[69]. Finally, mechanical alloying appears to be a good candidate to generate nano-sized powders of half-Heusler materials, but being potentially a difficult process to scale up.

- <u>Sintering.</u>

Finally, the collected powder has to be compacted and sintered to generate a bulk sample. In order to limit grain growth or preserve the nanosized features, the temperature and the time spends at high temperature have to be as low as possible. That is why a pressure assisted-sintering method using fast heating rates has to be used. Accordingly, most of the time spark plasma sintering[68], hot pressing[69] and shock consolidation[70] are preferably used to sinter half-Heusler compounds. Afterwards, half-heusler sintered pellets are polished and cut to be incorporated in a thermoelectric modulus or characterized.

d. Ways to improve half-Heusler thermoelectric properties

In this section a quick review of the considered ways in literature to improve half-Heusler thermoelectric properties is presented. More details can be found in the cited references.

- Reduction of thermal conductivity

The dominant drawback of half-Heusler materials is their high thermal conductivity. It explains why most of the works about optimisation of these materials have be driven by its reduction. Since the electronic thermal conductivity is related to the electrical conductivity, a general approach is to reduce the lattice thermal conductivity via effective phonon scattering. Several approaches are considered:

- Elemental substitution

Elemental substitution on the X site has been widely used in order to reduce the thermal conductivity. Indeed, alloying creates point defects that scatter phonons due to mass and size differences and interatomic coupling force differences (strain field fluctuations) between the host atoms and the impurity atoms[71]. For example, ternary or binary combinations of Hf, Ti and Zr on the M site of the MNiSn or MCoSb compositions, result in a thermal conductivity reduced by a factor 2-3 for different temperatures. Hereby, high ZT values of 1.5 at 425°C for an n-type $Hf_{0.25}Zr_{0.25}Ti_{0.5}NiSb_{0.002}Sn_{0.998}$[72] compound and of 1.0 at 525 °C for a p-type $Hf_{0.44}Zr_{0.44}Ti_{0.12}CoSb_{0.8}Sn_{0.2}$[73] formulation were obtained. Substitution on the Y site is also possible[74]. As an example, Ni can be substituted by Pt and Pb and Co by Rh, although, it is less common because of the dopants cost and rareness.

- Nano-structuration

As shown in part I.1, phonon scattering also happens at the grain boundaries in a polycrystalline material. To promote this behavior, it is necessary to increase the number density of grains boundaries, which can be done by reducing the grain size[75]. Over the past several years, nano-structuring has become one of the most investigated approach to improve the ZT of bulk thermoelectric materials[75].

Another way to create additional grain interfaces is by manufacturing nanocomposites including nano-sized precipitates or second phases that are homogeneously dispersed in a half-Heusler surrounding matrix. There are two sorts of possible inclusions: the ones obtained by in-situ formation via nucleation and growth during the synthesis of the material and the ones incorporated as a second phase, named ex-situ.

For example, Hsu and all. highlighted the in-situ formation of HfO_2 precipitates in a p-type $Zr_{0.5}Hf_{0.5}CoSb_{0.8}Sn_{0.2}$ composition, finding a maximum ZT of 0.75 at 620 °C[76]. Other groups add In in the half-Heusler composition to generate the in-situ formation of InSb nano-particles in the half-Heusler matrix, leading to a 160 % ZT improvement for n-type $Ti_{0.5}Zr_{0.25}Hf_{0.25}Co_{0.95}Ni_{0.05}Sb$ half-Heusler compositions (a ZT of 0.2 is measured at 550 °C for the InSb free composition against 0.51 for the composition including 1 at% of InSb nanoparticles). Indeed, moreover than acting as obstacles for phonon scattering, InSb inclusions can also “inject” electrons and thus increase the electrical conductivity, acting also as a potential energy barrier to scatter low energy electrons and improving the Seebeck coefficient[77].

Various sort of secondary phases have also been incorporated to a half-Heusler matrix to investigate the nano-composite approach. Among them, Al_2O_3[78], NiO[79], ZrO_2[80 84] have been used. A typical microstructure encountered using the nano-composite approach is presented in Figure I.16. Most of the time, the second phase is located at grain boundaries of the sintered polycrystal. For example, the thermal conductivity of a ZrNiSn-6 vol% ZrO_2 composite was reduced by 35 % in comparison to the ZrNiSn matrix alone, without a significant decrease of the electrical conductivity, leading to a 25 % ZT enhancement [81]. More precisions on nano-structured half-Heusler compounds can be found in the literature[82] [83].

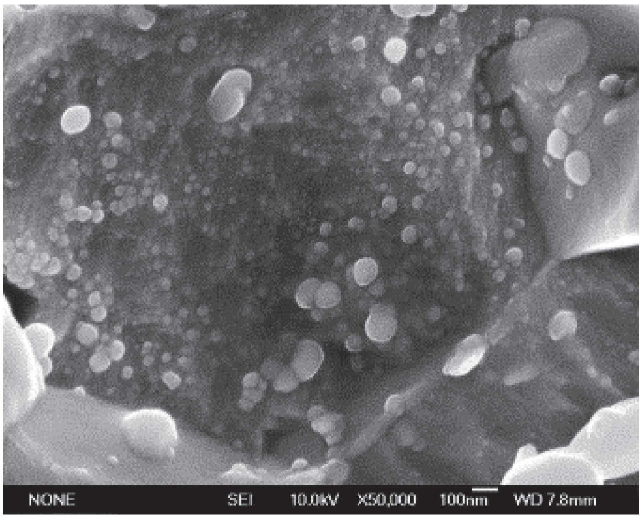

Figure I.16 : *SEM image of ZrNiSn/2 vol% ZrO_2 nanocomposite* [84]

Another approach is based on the half-Heusler/full-Heusler nanocomposite approach. Ni excess in a (Ti,Zr,Hf)NiSn generic composition leads to the formation of homogeneously dispersed full-Heusler nano-precipitates, having coherent interfaces with the half-Heusler surrounding matrix, as presented in Figure I.17[84]. As a result, the coherent boundaries act as a potential energy barrier to scatter low energy electrons and a Seebeck improvement is observed, as well as phonon scattering[85].

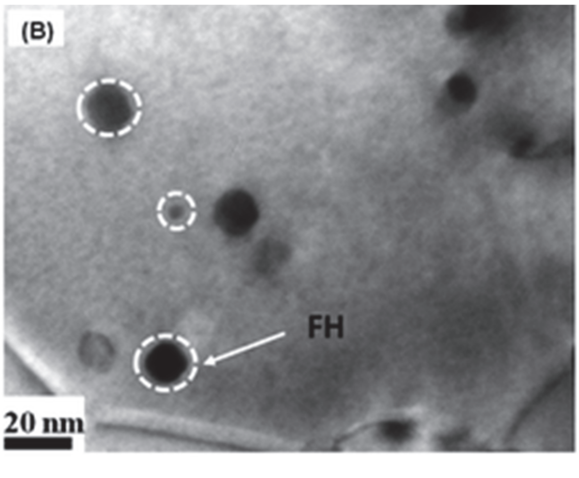

Figure I.17 : *TEM images of a half-Heusler$_{1-x}$/full-Heusler$_x$ (FH) bulk nanocomposite with $x = 0.3$* [86]

- Phase separation

Another way to decrease the thermal conductivity by structuration of a given material can be achieved by phase separation. Indeed, multicomponent half-Heusler compounds possess an intrinsic phase separation domain when they are solidified by quenching. As shown in Figure I.18, microstructures of n-type $Ti_{0.3}Zr_{0.35}Hf_{0.35}NiSn$ and p-type $Ti_{0.26}Sc_{0.04}Zr_{0.35}Hf_{0.35}NiSn$ compounds, mainly consist of two coexisting phases. The first occurring during eutectic solidification is the bright one. It is made of a low Ti-content half-Heusler phase. The second one to solidify during subsequent cooling is the darkest one. It is a Ti-rich half-Heusler phase, which is dendritically interlaced through the microstructure[87].

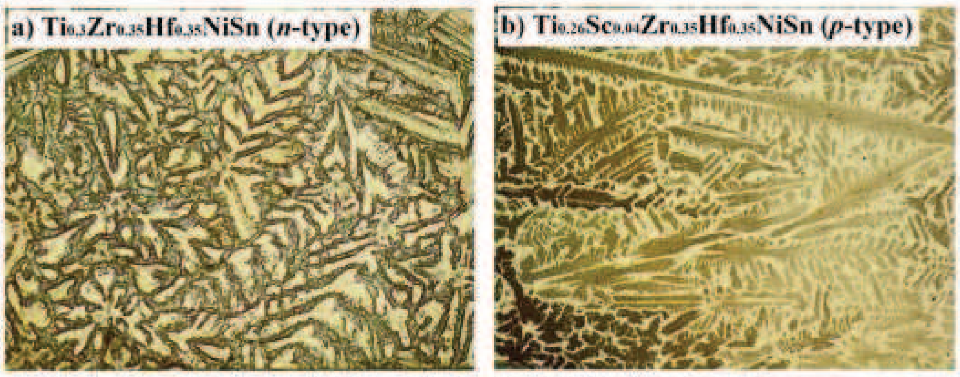

Figure I.18 : *Optical microscope image of a) n-type $Ti_{0.3}Zr_{0.35}Hf_{0.35}NiSn$ and b) p-type $Ti_{0.26}Sc_{0.04}Zr_{0.35}Hf_{0.35}NiSn$ half-Heusler compounds quenched*

Besides the scattering of high frequency phonons by the substitution of the half-Heusler X site, phase separation scatters effectively low and mid-frequency phonons at the multiple dendritic interfaces, decreasing efficiently the lattice thermal conductivity and leading to a ZT value around 0.65 at 500 °C for the n-type material and 0.3 at 500 °C for the p-type[87].

- Enhancement of the electronic properties

As discussed before the electronic properties of a thermoelectric material are linked to the carrier mobility and concentration. That is why one strategy to enhance the ZT of half-Heusler materials is by tuning the carrier concentration, via incorporating dopants into the elemental crystalline lattice.

However, as shown in Figure I.6, as the electrical conductivity is increasing with the carrier concentration, the Seebeck coefficient is decreasing. The optimum carrier concentration value was calculated to be between 10^{19} and 10^{21} carrier per cm^3 [5]. Indeed, electronic doping of small amounts of transition metals into the half-Heusler system introduces local features in the DOS (density of states) near to or within the band gap region. In the case of half-Heusler materials all the three positions in the XYZ cubic face centred crystal structure can be doped. The X site can be effectively doped with Ce, La, Nb, Ta and V (although Ti, Zr and Hf alloying in half-Heusler X site have been shown to impact the carrier concentration[5], it does not impact the VEC or the major type of carriers[88]). The Y site can be doped with Ni, Co, Cr, Cu and Fe. Finally, the electrical conductivity is reduced by doping the Z site with Sn, Sb, Ge, Pb or Bi. [88] [89] [90] Therefore half-Heusler formulations can become extremely complex.

e. Half-Heusler compounds today

The most investigated n-type half-Heusler composition is MNiSn (M = Ti, Zr, Hf), with Sn substituted by Sb (doping). For the p-type, the most popular one is MCoSb, where Co is substituted by Fe (doping) and/or Sb substituted by Sn (doping). However, more recently, calculations of the band structure has revealed that the MFeSb (M=V, Nb) p-type compound could be more effective as a thermoelectric materials because of its band structure[91]. Ti[92] and, recently, Hf[93] were found to be effective dopants and have the benefit of decreasing lattice thermal conductivity via point defect scattering. As an example, a high ZT around 1.5 at 930 °C was reported for the p-type $FeNb_{0.86\text{-}88}Hf_{0.12\text{-}0.14}Sb$ composition[93].

In 2015, Bartholomé et al, published on bulk half-Heusler alloys synthetized in large production scale (batches of several kilograms)[94]. The thermoelectric properties of the materials are in line with what was published at the lab scale on similar compositions. Then, thermoelectric modules were assembled from a $Zr_{0.4}Hf_{0.6}NiSn_{0.98}Sb_{0.02}$ n-type material having a ZT value around 0.8 at 500 °C and a $Zr_{0.5}Hf_{0.5}CoSb_{0.8}Sn_{0.2}$ p-type material having a ZT value around 0.5 at 500 °C, leading to a power output of 2.8 W.[94]

Nowadays, half-Heusler based thermoelectric generators have been developed and started to be commercialized. For example, since 2015, Isabellenhütte (Isabellenhütte Heusler GmbH & Co. KG, Dillenburg, D) is working on the development of thermoelectric modules incorporating two half-Heusler materials (one of the n-type and one of the p-type) for a conversion efficiency around 5 %[95]. GMZ Energy (recently acquired by Evident Thermoelectrics, Troy, NY, US), develop and commercialise modules incorporating bulk nanostructured half-Heusler compounds efficient for temperatures in the range 500°C to 700°C[96].

One of the critical issue to address now is the high hafnium content incorporated in the developed materials. Isabellenhütte and Evident Thermoelectrics are currently working on free or low hafnium-content compositions, in order to reduce significantly the cost of thermoelectric modules. Indeed, as hafnium is relatively expensive (around 160 €/kg) compared to other constituents (0.7 €/kg for nickel, for example), reducing its concentration in the well known MNiSn and MCoSb compounds, with M = Ti, Zr, Hf, is becoming one of the most important challenge. Last year, Gürth et al, obtained promising results with a hafnium free n-type half-Heusler formulation having a ZT value up to 1.2 at 530 °C[97].

Finally, the European project INTEGRAL (H2020-NMBP-PILOTS-2016) also targets the use of half-Heusler materials combining low thermal conductivities with low or without hafnium incorporation, for waste-heat recovery applications. For example, a part of this project focuses on the development of half-Heusler materials for thermoelectric generator in the automotive (partnership with Valeo Systèmes Thermiques SAS France) and heavy duty trucks (partnerships with Ricardo UK Limited and TitanX Engine Cooling Holding AB) industries[98].

f. Our approach

As shown before, half-Heuslers have a great potential as n and p-types thermoelectric materials for power generation in the temperature range 300 to 600 °C. Based on the material requirement presented in section II.1.b, in the frame of the PhD thesis, we decided to investigate half-Heusler compositions from the n-type MNiSn and p-type MCoSb (M = Ti, Zr, Hf) groups. Moreover having good thermoelectric properties, these compositions are the most respectful regarding non-toxicity, cheapness and abundance of raw constituents.

One of the best ZT values obtained up to now for this classes of materials were found for the n-type $Hf_{0.25}Zr_{0.25}Ti_{0.5}NiSb_{0.002}Sn_{0.998}$ composition (1.5 at 425 °C)[72] and for the p-type $Hf_{0.44}Zr_{0.44}Ti_{0.12}CoSb_{0.8}Sn_{0.2}$ (1.0 at 700 °C) one[73]. Accordingly, it has been decided to investigate these both stoichiometric compositions during the thesis.

It is a fact that there is a direct link between the thermoelectric properties of a material and its microstructure. Therefore, in order to improve the ZT parameter for a given temperature, it is essential to understand the relationships between the microstructure at a fine scale and the electrical/thermal properties of a thermoelectric material. That is why it has been decided to investigate the electrical/thermal properties of n-type and p-type samples sintered at different temperatures and exhibiting different microstructures. Accordingly, X-ray diffraction (XRD), scanning electron microscopy (SEM) and transmission electron microscopy (TEM) are essentials tools that have been used during our investigations.

Afterward, a second objective of the PhD thesis is to reduce the price per kilogram of the investigated materials and to simplify the manufacturing process, without having a detrimental impact on the thermoelectric properties. As mentioned before, the hafnium concentration is the main parameter affecting the cost of the generic formulations retained for our investigations. Therefore, we will try to reduce its concentration as much as possible and to evaluate, if it is possible, to replace it by the addition of oxide-based nano-particles. It is also well known that the presence of oxide-based precipitates in a given material promotes phonon scattering, leading to a decrease of thermal conductivity[81] [84]. Instead of adding oxide precipitates during manufacturing, we also propose to simplify the global process by synthetizing the materials under ambient atmosphere (air) to promote an in-situ precipitation in the sintered microstructure.

---

[1] Seebeck, T. J., Koenigl, A., Wiss, A., Magnetishe polarization der metalle and erze durck termeratur differenz, 1822, 265

[2] Peltier, J.C., Chim, A., Nouvelles expériences sur la caloriecete des courants electriques, LVI, 1834, 371.

[3] Thomson, W., in Proceeding Royal Society, 1851, 91.

[4] Thermoelectricité : des principes aux appklications. Technique de l'ingénieur

[5] Jeffrey Snyder, G., Eric, S., Toberer, Complex thermoelectric materials, Nature Materials, 2008, 7, 105-114

[6] Yaqub, R., Thermoelectric properties of $Zr_{0.5}Hf_{0.5}Ni_{1-x}Pd_xSn_{0.99}Sb_{0.01}$ and effect of nanoinclusions on transport properties of half-Heuslers, phD in philosophy in engineering and applied sciences, University of New Orleans, 2011

[7] MacDonald, D. K. C., Thermoelectricity: An Introduction to the Principles. Dover Books, N. Y., 2006.

[8] Je-Hyeong Bahk Birc k, Electron energy filtering by a nonplanar potential to enhance the thermoelectric power factor in bulk materials, Nanotechnology Center, Purdue University

[9] Heremans J. P., Thrush C. M., Morelli D. T., Physical Review, 2004, 70, 115334

[10] Wiedemann G., Franz R., Über die Wärme-Leitungsfähigkeit der Metalle, Annalen der Physik und Chemie, 1853, 139, 8

[11] Kittel, C., Introduction to solid state physics. John Wiley & Sons, Inc, 2005.

[12] Balaguru, R. J. B. and Jeyaprakash, B. G., Lattice Vibrations, Phonons, Specific Heat Capacity, Thermal Conductivity, NPTEL – Electrical & Electronics Engineering – Semiconductor Nanodevices

[13] R. E. Peierls, Ann. Physik 3, 1929, 1055

[14] Matthiessen, A.; Vogt, C., On the Influence of Temperature on the Electric Conducting-Power of Alloys, Philosophical Transactions of the Royal Society of London., 1868 154: 167.

[15] Ashcroft, N. W. and Mermin, D.N. Solid State Physics. Brooks/coles, 1976

[16] J. F. Nye, Physical properties of crystals, Clarendon Press, 1979

[17] Sommerfeld, A. Z. Phys ., 1928, 47,1.

[18] Casimir, H.B.G, Note on the Conduction of Heat in Crystals, Physica, 1938, 5, 6, 495

[19] Xie, W, Weidenkaff, A, Tang, X, Zhang, Q, Poon, J, Tritt, T.M., Recent Advances in Nanostructured Thermoelectric Half-Heusler Compounds, Nanomaterials 2012, 2(4), 379-412

[20] Narayanamurti, V. et al. Physical review Letters 1979,43 , 2012.

[21] Goldsmid H., Electronic Refrigeration, Pion Ltd., London, 1986

[22] Goldsmid H., Proceedings of the Physical Society. Section B, 1954.67,360

[23] Goldsmid H., Douglas R W, British Journal of Applied Physics, 1954, 5(11), 386

[24] Ioffe A., Airepetyants S., Kolomoets N., Stilbans L., Dokl. Akad. Naitk. USSR, 1956,106,981

[25] Birkholz, U. Untersuchung der intermetallischen Verbindung Bi_2Te_3 sowie der festen Lösungen $Bi_{2-x}Sb_xTe_3$ und $Bi_2Te_{3-x}Se_x$hinsichtlich ihrer Eignung als Material für Halbleiter-Thermoelemente. Z. Naturforsch. A 13, 780–792 (1958).

[26] Poudel, B.; Hao, Q.; Ma, Y.; Lan, Y.; Minnich, A.; Yu, B.; Yan, X.; Wang, D.; Muto, A.; Vashaee, D.; et al. High-Thermoelectric Performance of Nanostructured Bismuth Antimony Telluride, Bulk Alloys. Science, 2008, 320, 634−638.

[27] Zhao L.-D., Lo S.-H., Zhang Y., Sun H., Tan G., Uher C., Wolverton C., Dravid V. P., Kanatzidis M. G., Ultralow thermal conductivity and high thermoelectric figure of merit in SnSe crystals, Nature, 2014,508(7496), 373–377

[28] Cadoff I. B., Miller E., Thermoelectric materials and devices, Reinhold Pub. Corp, 1960.

[29] Biswas, K.; He, J.; Blum, I. D.; Wu, C.-I.; Hogan, T. P.; Seidman, D. N.; Dravid, V. P.; Kanatzidis, M. G. High-Performance Bulk Thermoelectrics with All-Scale Hierarchical Architectures. Nature, 2012, 489, 414−418.

[30] Hsu, K. F.; Loo, S.; Guo, F.; Chen, W.; Dyck, J. S.; Uher, C.; Hogan, T.; Polychroniadis, E.; Kanatzidis, M. G. Cubic AgPbmSbTe2+m: Bulk Thermoelectric Materials with High Figure of Merit. Science, 2004, 303, 818−821.

[31] Schro¨der T., Rosenthal T., Giesbrecht N., Nentwig M., and Maier S., Nanostructures in Te/Sb/Ge/Ag (TAGS) thermoelectric materials induced by phase transitions associated with vacancy ordering, Inorg. Chem., 2014 53, 7722

[32] Abeles B., Beers D. S., Cody G. D., Dismukes J. P., Phys. Rev., 1962, 125(1), 44

---

[33] Joshi, G.; Lee, H.; Lan, Y.; Wang, X.; Zhu, G.; Wang, D.; Gould, R. W.; Cuff, D. C.; Tang, M. Y.; Dresselhaus, M. S.; et al. Enhanced Thermoelectric Figure-of-Merit in Nanostructured P-Type Silicon Germanium Bulk Alloys. Nano Lett. 2008, 8, 4670−4674

[34] Bernard-Granger, G., Soulier, M., Ihou-Mouko, H., Navone, C., Boidot, M., Leforestier, J., Simon, J., Microstructure investigations and thermoelectrical properties of a P-type polycrystalline higher manganese silicide material sintered from a gas-phase atomized powder, Journal of Alloys and Compounds, 618 (2015) 403–412

[35] Bernard-Granger, G., Navone, C., Leforestier, J., H., Boidot, M., Krunoslav, R., Carrete, J., Simon, J., Microstructure investigations and thermoelectrical properties of an N-type magnesium–silicon–tin alloy sintered from a gas-phase atomized powder, Acta Materialia, 96 (2015) 437–451

[36] G. Slack Solid State Physics, 1979, 34, 1

[37] Shi, X.; Yang, J.; Salvador, J. R.; Chi, M.; Cho, J. Y.; Wang, H.; Bai, S.; Yang, J.; Zhang, W.; Chen, L. Multiple-Filled Skutterudites: High Thermoelectric Figure of Merit through Separately Optimizing Electrical and Thermal Transports. J. Am. Chem. Soc. 2011, 133, 7837−7846.

[38] Saramat A., Svensson G., and Palmqvist A. E. C., Large thermoelectric figure of merit at high temperature in Czochralski-grown clathrate Ba8Ga16Ge30, Journal of Applied Physics, 2006, 99, 023708

[39] Hicks L D and Dresselhaus M S 1993 Phys. Rev. B 47 12727

[40] Chen, G. Journal of Heat Transfer 1997, 119, 220.

[41] Satyala N., Norouzzadeh P., Vashaee D., Nano bulk thermoelectrics: Concepts, techniques, and modeling, Nanoscale Thermoelectrics, 2014, 141–183.

[42] Joshi, Giri Raj. Study of Thermoelectric Properties of Nanostructured P-Type Si-Ge, Bi-Te, Bi-Sb, and Half-Heusler Bulk Materials, PhD, Boston College, 2010.

[43] Antonio P., Gonçalves, Godart C., New promising bulk thermoelectrics: intermetallics, pnictides and chalcogenides, Eur. Phys. J. B ,2014, 87: 42

[44] Hébert S , Berthebaud D , Daou R , Bréard Y , Pelloquin D , Guilmeau E , Gascoin F , Lebedev O , Maignan A , Searching for new thermoelectric materials: some examples among oxides, sulfides and selenides, J. Phys.: Condens. Matter, 2016, 28, 013001

[45] Sootsman J.R., Chung D.Y., Kanatzidis M.G., New and old concepts in thermoelectric materials, Angew Chem Int Ed, 2009, 48, 8616–8639

[46] Simens. Iea wolrd energy outlook, vattenfall. 2012

[47] https://www.webelements.com/periodicity/abundance_crust/

[48] https://www.metalprices.com

[49] Eilertsen, J., Subramanian, M.A., Kruzic, J.J., Fracture toughness of Co_4Sb_{12} and $I_{n0.1}Co_4Sb_{12}$ thermoelectric skutterudites, Journal of Alloys and Compounds 552 (2013) 492–498

[50] Xia, X., Qiu, P., Shi, X. et al. High-Temperature Oxidation Behavior of Filled Skutterudites $Yb_yCo_4Sb_{12}$, Journal of Elec Materi, 2012, 41: 2225.

[51] Poon S. J., Recent Trends in Thermoelectric Materials Research II, Semi-conductors and Semimetals, ed. T. M. Tritt, Academic, New York, 2001, 70, 37.

[52] Aliev, F.G., Kozyrkov, V.V., Moshchalkov, V.V. et al. Z. Physik B - Condensed Matter, 1990, 80: 353.

[53] C. Uher, J. Yang, S. Hu, D. T. Morelli, and G. P. Meisner, Transport properties of pure and doped MNiSn (M=Zr, Hf), Phys. Rev. B 59, 8615 – Published 1 April 1999

[54] Poon, S.J.; Tritt, T.M.; Xi, Y.; Bhattacharya, S.; Ponnambalam, V.; Pope, A.L.; Littleton, R.T.; Browning, V.M. Bandgap Features and Thermoelectric Properties of Ti-Based Half-Heusler Alloys. In Proceedings of Eighteenth International Conference on Thermoelectrics, Maryland, MD, USA, 1999; pp. 45–51.

[55] Heusler F. Verhandlungen der Deutschen Physikalischen Gesellschaft,5:219, 1903.

[56] Heusler F, W Starck, and E. Haupt. Verhandlungen der Deutschen Physikalischen Gesellschaft, 5:220{223, 1903.

[57] Graf, T., Felser, C., Parkin, S. S. P., Simple rules for the understanding of Heusler compounds. Progress in Solid State Chemistry, 2011, 39(1), 1-50.

[58] Graf, T., Felser, C., Parkin, S. S. P., Simple rules for the understanding of Heusler compounds. Progress in Solid State Chemistry, 2011, 39(1), 1-50.

---

[59] Casper F, Graf T, Chadov S, Balke B, Felser C, Half-Heusler compounds: novel materials for energy and spintronic applications, Semicond. Sci. Technol., 2012, 27 063001

[60] Zhang H., Wang Y., Huang L., Chen S., Dahal H., Wang D., Ren Z., Synthesis and thermoelectric properties of n-type half-Heusler compound VCoSb with valence electron count of 19, Journal of Alloys and Compounds, 2016, 654, 321-326

[61] Aliev F. G. , Kozyrkov V. V. , Moshchalkov V. V. , Scolozdra R. V. , Durczewski K. , Narrow band in the intermetallic compounds MNiSn (M=Ti, Zr, Hf), Z. Physik B - Condensed Matter, 1990, 80: 353.

[62] Yu, C., Zhu, T.-J., Xiao, K., Jin, J., Shen J.-J., Yang S.-H., Zhao, X.-B., Microstructure of ZrNiSn-base Half-Heusler Thermoelectric Materials Prepared by Melt-spinning, journal of Inorganic materials, 2010, 6, 569-572

[63] Kimura, Y., Kuji, T., Zama, A., Shibata, Y., Mishima, Y., High-Performance of Half-Heusler MNiSn (M=Hf,Zr) Single-Phase Thermoelectric Alloys Fabricated using Optical Floating Zone Melting, 2005, 886,

[64] Chen, S., Ren, Z., Recent progress of half-Heusler for moderate temperature thermoelectric applications, Maretials Today, 2013, 16, 10 387–395

[65] Shen, Q., Zhang, L., Chen, Li., Goto, T., Hirai, T., Thermoelectric properties of ZrNiSn-based half-Heusler compounds by solid state reaction method, Journal of Materials Science Letters. 2001, 20(24), 2197-2199,.

[66] Christina S. Birkel, Wolfgang G. Zeier, Jason E. Douglas, Bethany R. Lettiere, Carolyn E. Mills, Gareth Seward, Alexander Birkel, Matthew L. Snedaker, Yichi Zhang, G. Jeffrey Snyder, Tresa M. Pollock, Ram Seshadri, and Galen D. Stucky*, Rapid Microwave Preparation of Thermoelectric TiNiSn and TiCoSb Half-Heusler Compounds, Chem. Mater., 2012, 24 (13), pp 2558–2565

[67] Li Y., Cheng C., Lei Y., Wang M., Wan R. D., Ultra-fast preparation of high-performance thermoelectric bulk $TiNiSb_{0.05}Sn_{0.95}$ by microwave synthesis, Dalton Trans., 2017, 46, 33-38

[68] Zou M., Li J.-F., Du B., Liu D., Kita T., Fabrication and thermoelectric properties of fine-grained TiNiSn compounds, J. of Solid State Chem., 2009, 182, 3138

[69] Soon-Chul U., Thermoelectric Properties of Half-Heusler ZrNiSn1-xSbx Synthesized by Mechanical Alloying Process and Vacuum Hot Pressing, Journal of Korean Powder Metallurgy Institute, 2011, 18, 5

[70] Bhattacharya, S.; Tritt, T.M.; Xia, Y.; Ponnambalam, V.; Poon, S.J.; Thadhani, N. Grain structure effects on the lattice thermal conductivity of Ti-based half-heusler alloys. Appl. Phys. Lett. 2002, 81, 43–45.

[71] Yang, J., Meisner, G. P., Strain field fluctuation effects on lattice thermal conductivity of ZrNiSnZrNiSn-based thermoelectric compounds, Appl. Phys. Lett., 2004, 85, 1140

[72] Sakurada, S.; Shutoh, N., Effect of Ti substitution on the thermoelectric properties of (Zr,Hf)NiSn half-Heusler compounds, Appl. Phys. Lett., 2005 86, 2105

[73] Yan X., Liu W., Chen S., Wang H., Zhang Q., Chen G., Ren Z., Thermoelectric Property Study of Nanostructured p-Type Half-Heuslers (Hf, Zr, Ti)$CoSb_{0.8}Sn_{0.2}$, Adv. Energy Mater., 2013, 3, 1195

[74] Shen Q., Chen L., Goto T., Hirai T., Yang J., Meisner G. P., and Uher C., Effects of partial substitution of Ni by Pd on the thermoelectric properties of ZrNiSn-based half-Heusler compounds, Appl. Phys. Lett., 2001, 79, 4165

[75] Bhattacharya, S., Tritt, T.M., Xia, Y., Ponnambalam, V.; Poon, S.J.; Thadhani, N. Grain structure effects on the lattice thermal conductivity of Ti-based half-heusler alloys. Appl. Phys. Lett. 2002, 81, 43–45.

[76] Chia-Cheng H., Yion-Ni L., Hsiao-Kang M., Effect of the $Zr_{0.5}Hf_{0.5}CoSb_{1-x}Sn_x/HfO_2$ half-Heusler nanocomposites on the ZT value, Journal of Alloys and Compounds, 2014, 597, 217–222

[77] Xie, W.J.; He, J.; Zhu, S.; Su, X.L.; Wang, S.Y.; Holgate, T.; Graff, J.W.; Ponnambalam, V.; Poon, S.J.; Tang, X.F.; Zhang, Q.J.; Tritt, T,M. Simultaneously optimizing the independent thermoelectric properties in (Ti,Zr,Hf)(Co,Ni)Sb alloy by in situ forming InSb nanoinclusions, Acta Mater,. 2010, 58, 4705–4713.

[78] Huang, X.Y.; Xu, Z.; Chen, L.D.; Tang, X.F. Effect of γ-Al_2O_3 content on the thermoelectric performance of ZrNiSn/γ-Al_2O_3 composites. Key Eng. Mater., 2003, 249, 79–82

[79] Yaqub, R.; Sahoo, P.; Makongo, J.P.A.; Takas, N.; Poudeu, P.F.P.; Stokes, K.L. Investigation of the effect of NiO nanoparticles on the transport properties of $Zr_{0.5}Hf_{0.5}Ni_{1-x}Pd_xSn_{0.99}Sb_{0.01}$ (x = 0 and 0.2). Sci. Adv. Mater. 2011, 3, 633–638

[80] Poon, S.J.; Wu, D.; Zhu, S.; Xie, W.; Tritt, T.M.; Thomas, P.; Venkatasubramanian, R. Half-Heusler phases and nanocomposites as emerging high-ZT thermoelectric materials, J. Mater. Res., 2011, 26, 2795–2802.

[81] Huang, X.Y.; Xu, Z.; Chen, L.D. The thermoelectric performance of ZrNiSn-ZrO_2 composites. Solid State Commun, 2004, 130, 181–185.

---

[82] Xie, W, Weidenkaff, A, Tang, X, Zhang, Q, Poon, J, Tritt, T.M., Recent Advances in Nanostructured Thermoelectric Half-Heusler Compounds, Nanomaterials 2012, 2(4), 379-412

[83] Chen Z.-G., Han G., Yang L., Cheng L. & Zou J., Nanostructured thermoelectric materials: Current research and future challenge. Prog. Nat. Sci.: Mater. Int., 2012, 22, 535–549

[84] Chai, Y.W.; Kimura, Y. Nanosized precipitates in half-Heusler TiNiSn alloy. Appl. Phys. Lett. ,2012, 100, 033114.

[85] Makongo, J.P.A.; Misra, D.K.; Salvador, J.R.; Takas, N.J.; Wang, G.; Shabetai, M.R.; Pant, A.; Paudel, P.; Uher, C.; Stokes, K.L.; et al. Thermal and electronic charge transport in bulk nanostructured $Zr_{0.25}Hf_{0.75}NiSn$ composites with full-Heusler inclusions. J. Solid State Chem. 2011, 184, 2948–2960.

[86] Makongo, J.P.A.; Misra, D.K.; Zhou, X.; Pant, A.; Shabetai, M.R.; Su, X.; Uher, C.; Stokes, K.L.; Poudeu, P.F.P. Simultaneous large enhancements in thermopower and electrical conductivity of bulk nanostructured half-Heusler alloys. J. Am. Chem. Soc. 2011, 133, 18843–18852.

[87] Krez J, Thermoelectric properties in phase-separated half-Heusler materials, phD, 2014

[88] Hohl, H, Ramirez, P, Goldmann, C, Ernst G, Wölfing, B, Bucher E, Efficient dopants for ZrNiSn-based thermoelectric materials, Journal of Physics: Condensed Matter, 11, N7

[89] Li X.G., Huo D.X., He C.J., Zhao S.C., Lu Y.F., Effect of Rare-earth Doping on the Thermoelectric Properties of the Tin-based Half-Heusler Alloys,J. Inorg. Mater., 2010, 25, 573

[90] Uher C., Yang J., Hu S., Morelli D. T., and Meisner G. P., Transport properties of pure and doped MNiSn (M=Zr, Hf), Phys. Rev., 1999, B 59, 8615

[91] Jodin L., Tobola J., Pecheur P., Scherrer H., Kaprzyk S., Effect of substitutions and defects in half-Heusler FeVSb studied by electron transport measurements and KKR-CPA electronic structure calculations, Phys Rev B, 2004, 70,. 184207

[92] Fu C.G., Zhu T.J., Liu Y.T., Xie H.H., Zhao X.B., Band engineering of high performance p-type FeNbSb based half-Heusler thermoelectric materials for figure of merit zT > 1, Energ Environ Sci, 2015, 8, 216–220

[93] Fu C.G., S.Q. Bai, Liu Y.T., Tang Y.S., Chen L.D., Zhao X.B., et al., Realizing high figure of merit in heavy-band p-type half-Heusler thermoelectric materials, Nat Commun, 2015, 6, 8144

[94] Bartholomé, K, Balke, B, Zuckermann, D, Köhne, M, Müller, M,, Tarantik, K, König, J, Thermoelectric Modules Based on Half-Heusler Materials Produced in Large Quantities, Journal of Electronic Materials, 2014, 43, 6, 1775–1781

[95] http://www.isabellenhuette.de/

[96] http://evidentthermo.com/

[97] Gürth, M., Rogl, G., Romaka, V.V., Grytsiv, A., Bauer, E., Rogl, P., Thermoelectric high ZT half-Heusler alloys $Ti_{1-x-y}Zr_xHf_yNiSn$ ($0 \le x \le 1$; $0 \le y \le 1$), Acta Materialia, 2016, 104, 210–222

[98] http://www.cea.fr/english/Pages/News/salvaging-waste-heat-into-electricity-INTEGRAL-thermoelectric-materials.aspx

Chapter II

Materials synthesis and characterisation

I - Manufacturing of the half-Heusler sintered pellets

I.1 - Cold crucible levitation melting induction furnace

a. Introduction to cold crucible levitation melting induction furnace

Induction furnaces use joule heating effect to heat up and melt metals. Indeed, an alternative current passes through a copper coil, inducing an alternating magnetic field. If a conductive material is placed in a crucible, inside the coil, an electric current will be generated. The material is then heated up by Joule effect until melting. This approach ensures a rapid heat transfer into the sample and provides a good temperature homogeneity[1].

Another effect is that the current induced in the material, positioned at the center of the coil, will generate its own magnetic field, this later developing charge lines opposite to the copper's ones. Consequently, the piece of melted material will "levitate". Moreover, a metallic crucible (in order to provide electromagnetic transparency for the magnetic field, the crucible is segmented and every section is electrically isolated from another one) is used and water-cooled. The melt material solidifies immediately when coming into contact with the cold crucible walls. This configuration prevents the obtained ingot from contamination[2].

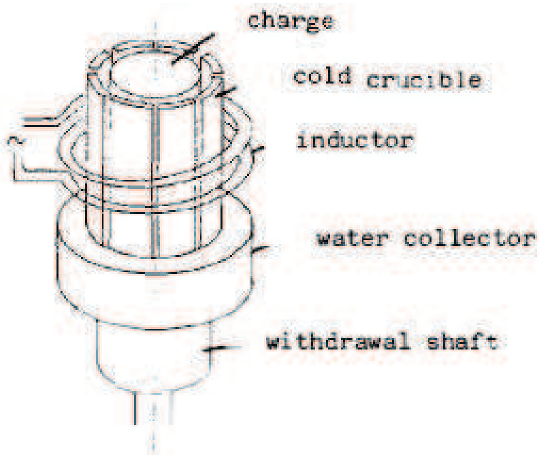

Figure II.1 : *Cold crucible induction furnace*[3].

b. Solution to avoid volatility of the compounds

The half-Heusler formulations that will be investigated contain elements with quite different melting points. For instance, the n-type $Zr_{0.25}Hf_{0.25}Ti_{0.5}NiSn_{0.994}Sb_{0.006}$ formulation involves high melting point elements as Hf (2233°C) and Zr (1855°C) but also low melting point elements as Sb (dopant, 631 °C) and Sn (232 °C). In addition, Sb has a boiling point around 1587°C. Evaporation of a component during the melting step would lead to a modification of the stoichiometry of the final material.

First of all, to limit components volatility in the crucible and to avoid oxidation, melting is done preferably under argon rather than under vacuum. During the PhD thesis, two different cold crucibles induction furnaces were used, with two different ways to limit Sb evaporation. The first one, adopted at INAC (CEA, Grenoble, F) and also widely extoled in the literature, is to add an extra 5 wt% of Sb[4 and 5]. The second one, used at Neel Institute (Grenoble, F), was to first melt a mix of the weighted Ti, Zr, Hf, and Ni compounds in order to reduce the melting temperature of the system. Then, a pellet made by cold pressing of the Sn and Sb raw elements, is added in the cold crucible induction furnace. All the elements are then re-melt together.

c. Experimental procedure used

The starting materials (shots from 1 to 3 mm for antimony and slugs from 3 to 6 mm for all other elements) used to elaborate the ingots were the same for the whole PhD thesis. The purity of the starting materials (Neyco, Vanves, F) are presented in Table II.1. The different elements were weighed in the desired stoichiometric ratio to obtain in-fine 50 g ingots of the target n and p-types half-Heusler compositions.

Materials from Neyco
Zirconium 99.95%
Hafnium 99.95%
Titanium 99.99%
Cobalt 99.98+%
Nickel 99.99%
Tin 99.99%
Antimony 99.999%

Table II.1 : *Purity of the starting materials.*

As an example, the furnace and a typical melt bath during induction melting at Néel Institute are shown in Figure II.2 and Figure II.3. All the ingots were prepared in a purified argon atmosphere, flipped and re-melt three times in order to ensure a good homogeneity.

The furnaces were operating with a high frequency generator (around 100 kHz). The power delivered (around 50 kW) was controlled, so that as soon as melting appeared, heating was stopped to avoid evaporation.

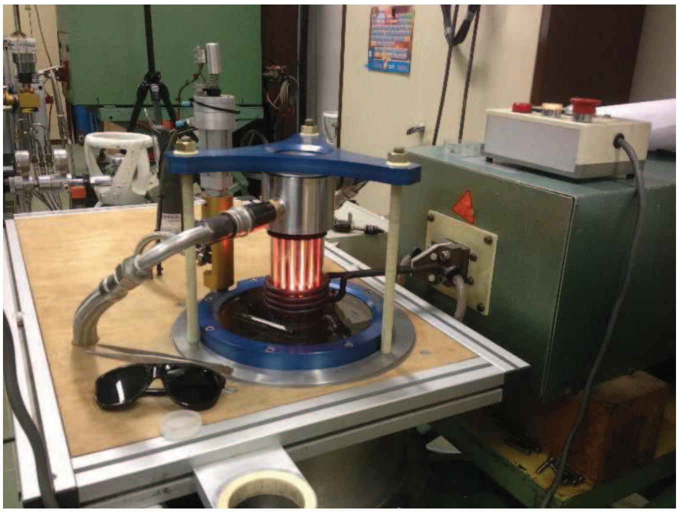

Figure II.2 : *Cold crucible induction furnace (Néel Institute).*

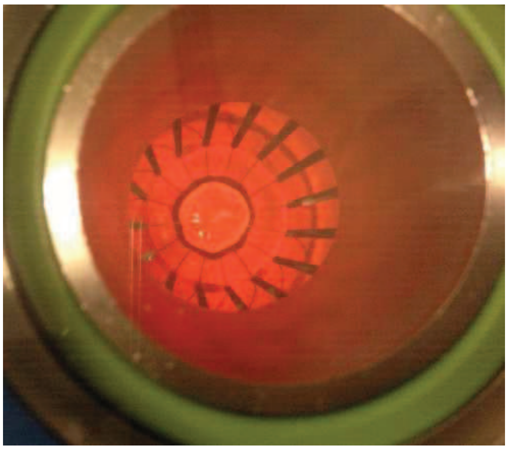

Figure II.3 : *Melt material into the levitation melting induction furnace cold crucible (Néel Insititute).*

I.2 - Ball milling

Once the 50 g ingots were obtained, they were grinded in order to obtain fine powders.

a. Introduction to the planetary ball mill

In order to obtain powders, a planetary ball mill was used. The ball milling technique is based on mechanical forces to transfer energy from the milling tools to the material. The material to grind is placed in a grinding jar, usually made of hardened steel or tungsten carbide, with different grinding balls having different diameters. The grinding jars and the balls used during this work were made of tungsten carbide to avoid any contamination from the jar. Then the jar was attached to the planetary ball mill disk, which rotated around a central axis while the jar was simultaneously rotating around its own axis, as shown in Figure II.4.[6]

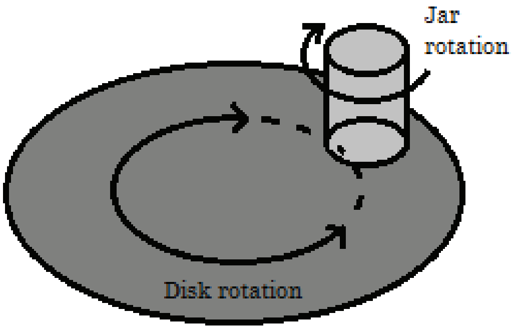

Figure II.4 : *Rotation and revolution – Planetary ball milling.*

During the jar motion, the material to grind is trapped and crushed between the moving balls. The size reduction occurs through a sequence of collisions inside the ball miller.[7] Moreover, several parameters can be controlled. For example, the revolution speed, the milling time, the balls and jar sizes and the ball to powder filling ratio can be tailored. All these parameters can change the intensity of the impacts and so the energy transferred to the material inside[8].

Even though ball milling is an easy, quick and contamination free process some disadvantages are also noticed. Indeed, after a long processing time the grinded material might become amorphous and stick on the jar wall. To prevent these phenomenons, lubricants can be added. However, it has to be noted that no lubricant were added during our investigations to limit as much as possible contamination.

b. Experimental procedure

For this work, a PM100 planetary ball mill (Retsch France, Eragny sur Oise, F), shown in Figure II.5, was used.

Figure II.5 : *PM100 planetary ball mill.*

Firstly, in order to break the collected bulk ingots, a 50 mL tungsten carbide jar loaded with tungsten carbide 5 and 10 mm diameter balls (ball to solid ration around 3), filled under argon atmosphere is used. The jar is then hermetically closed and sealed with tape to ensure the whole milling step being completed under argon. Then the jar is placed and tied up into the planetary ball mill. Grinding is completed with a revolution speed set to 500 rpm during 2 min.

Afterward, the jar is opened into a glove box (argon atmosphere) and the weakened collected material is crushed manually with a mortar into pieces smaller than 2 mm. Then, 10 g of the collected fragments are introduced into the grinding jar, loaded with 40 g of a mix of 3 and 5 mm diameter balls, providing a ball to powder mass ratio about 4.

The planetary ball mill was set with a revolution speed of 250 rpm during 2 h. Then, the grinded powder was collected and rubbed through a 56 µm sieve. The powder that was not passing through the sieve was grinded again, in the same conditions, until no remaining was left after sieving.

X-ray diffraction (XRD, the technique will be described in section III.3 of the present chapter) analyses were completed in order to control that the crystalline structure was not affected by grinding (amorphization, for example). Moreover, laser granulometry (the technique will be described in section III.1 of the present chapter) was used to check the particle size distribution at the end of the grinding process.

42Spark Plasma Sintering

Spark plasma sintering (SPS) is a standard sintering process used to sinter half-Heusler or other thermoelectric materials[9] [10] [11]. As a fast process, powder densifies while avoiding grain coarsening, if the experimental parameters are tailored[11]. That is why SPS has been used for this work.

a. Introduction to SPS

SPS also named field-assisted sintering technique (FAST) is a pressure-assisted sintering method, where the atmosphere can be controlled. A pulsed current, characterized by a low voltage and a high intensity, is imposed between two electrodes to a stack made of graphite punches, spacers and a pressing die, leading to Joule heating of the powder introduced into the die, as shown in Figure II.6[12]. In the same time, the powder bed is compacted using the controlled displacement of the graphite punches. Such a configuration enables heating rates ranging from 1 to 600 °C/min to be achieved. Regarding the cooling rate, it can be easily tailored.

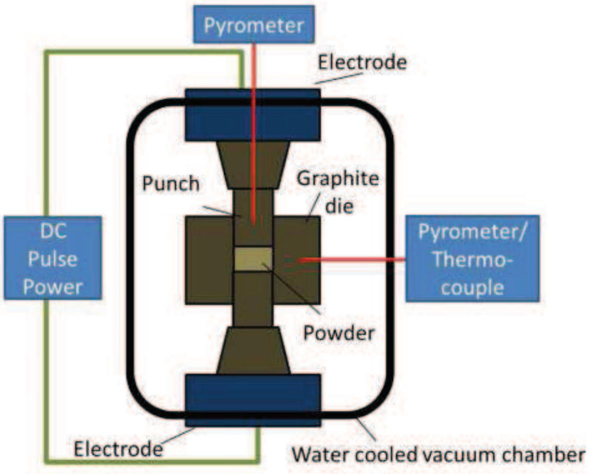

<u>Figure II.6 :</u> *Detailed illustration of the SPS configuration*

b. Experimental procedure

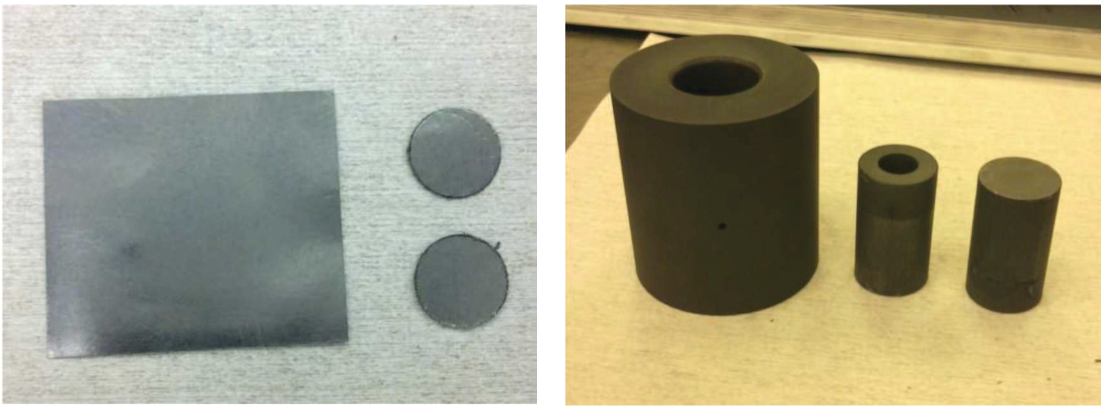

<u>Figure II.7 :</u> *Papyex foils and graphite dies used for the SPS experiments.*

Approximately 7 g of powder was loaded into a graphite die (15 mm thickness and internal diameter of 20 mm). As presented in Figure II.7 graphite foils are positioned inside the die and at the powder/punches interfaces. Then the die containing the powder is placed into the SPS equipment (HPD-25 equipment, FCT Systeme GmbH, Rauenstein, D) shown in Figure II.8.

A compaction pressure of 40 MPa was imposed to the powder bed at room temperature and kept during the sintering cycle. The heating rate was fixed to 50 °C.min^{-1} and the standard 12:2 pulse sequence for the DC current was adopted.[13] The soak time was fixed to 5 min for all samples. At the end of the soak, cooling was controlled and completed using an adapted pressure release profile. The whole SPS cycle has been completed under a 1010 hPa argon pressure. After sintering, the pellets were approximately 20 mm in diameter and 3 mm thick.

Figure II.8 : *HPD-25 SPS equipment used during the PhD thesis.*

During all the SPS test (heating, soak and cooling), it is possible to measure very precisely the height variation of the powder bed ($\Delta L = L - L_0 < 0$, where *L* is the instantaneous height and L_0 the initial height of the powder bed when the pressure is applied at room temperature). Each test is also corrected to account for the dimension changes related to the SPS equipment (a blind test is performed and then subtracted to the "real" test result). Finally, it is easy to show that the instantaneous sample height variation and its instantaneous relative density are linked by the following relationship:

$$D = \left(\frac{L_f}{L}\right) D_f \qquad \text{(II.1)}$$

where: *D* is the instantaneous relative density, L_f is the final height, *L* is the instantaneous height and D_f is the final relative density.

The apparent density of the sintered samples was measured using the Archimedes method with absolute ethanol (dry, wet and humid masses were measured). Then, the final relative density, D_f, is obtained using a theoretical volume mass adapted for each formulation investigated.

II - Measurement of thermoelectric properties for the sintered samples

II.1. Introduction

As seen in the first chapter, the efficiency of a thermoelectric material is characterized by a dimensionless figure of merit defined as:

$$ZT = \frac{S^2\sigma T}{\kappa} = \frac{S^2 T}{\rho\kappa} \qquad \text{(II.2)}$$

where S is the Seebeck coefficient, σ the electrical conductivity, ρ the electrical resistivity, κ the thermal conductivity and, T the absolute temperature.

The thermal conductivity of a material, is given by the relationship:

$$\kappa = \rho C_p \alpha \qquad \text{(II.3)}$$

with ρ is the density of the sample, C_p its specific heat at constant pressure and α its thermal diffusivity.

As explained in Chapter I, the thermal conductivity is the addition of two contributions: the lattice thermal conductivity, κ_l (heat transfer occuring through elastic vibration of the lattice, also called phonons), the other phenomena is the electronic thermal conductivity, κ_e (heat is transferred by the carriers).

The electronic thermal conductivity is given by

$$\kappa_e = L\sigma T \qquad \text{(II.4)}$$

where L is the Lorenz number, widely used to estimate κ_E from σ measurements.

It is a common practice to treat L as a universal factor with a value of 2.44 × 10^{-8} W.Ω.K^{-2}. However, significant deviations from the degenerated limit are known to occur for non-degenerated semiconductors where L converges to 1.5 × 10^{-8} WΩK^{-2} for acoustic phonon scattering. The decrease in L is correlated with an increase in thermopower (absolute value of Seebeck coefficient). Thus, a first order correction to the degenerated limit of L can be based on the measured thermopower, $|S|$, independent of temperature or doping. Kim and all. defined the Lorentz number as [14]:

$$L = 1.5 + e^{-\frac{|S|}{116}} \qquad \text{(II.5)}$$

where *L* is in 10^{-8} W.Ω.K^{-2} and *S* in µV/K. The expression (II.5) was used to calculate the electronic contribution to thermal conductivity when needed during our investigations.

The ZT value can be directly obtained by a ZT-meter method[15]. However, a precise measurement of each individual parameter, in function of temperature, is of prime interest to understand the relationships between the microstructure and the thermoelectric properties of a given material.

For this reason, in the sections bellow, the three different methods used to characterize the individual electric and thermal properties of the sintered pellets, in function of temperature, are described.

II.2. Cutting and samples polishing

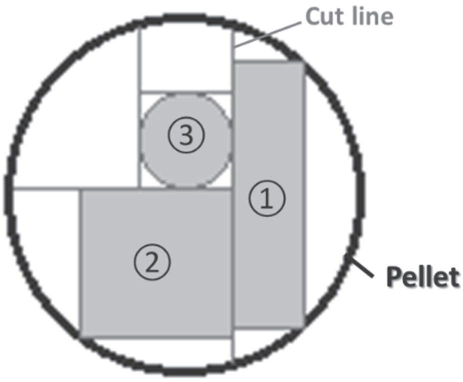

Figure II.9 : Samples cut from a SPS pellet for the characterization of thermoelectric properties

Firstly, three samples are cut, as shown in Figure II.9

Figure II.9, from the bulk of a sintered pellet by using a precision saw (IsoMet 1000 Precision Saw, Buehler, Dardilly, F) equipped with a rotary diamond blade. A cutting speed of 250 rpm was used. For each sintered pellets, the following samples are finally obtained: ① a rectangular bar (10 x4x2.5 mm^3), ② a square (9.5x9.5x2.25 mm^3) and ③ a disc (diameter of 5.2 mm and thickness of 0.5 mm).

Then, all samples have been polished under water, with SiC grinding papers going from grade 180# up to grade 800#, using a Mechatech 234 (Presi, Eybens, F) polishing equipment.

II.3. Electrical conductivity and Seebeck coefficient measurements

a. Introduction

The electrical conductivity, σ, is the inverse of the electrical resistivity, ρ. The four-probe method is widely used to measure the electrical resistivity of a given material. With this technique, it is possible to measure and eliminate the contribution of contact resistances between the electrodes and the sample. Basically, a current is sent through the sample positioned between one set of metal (nickel) electrodes and the difference of potential in the sample is measured using two temperature sensors (C-type thermocouple), as shown in Figure II.10.

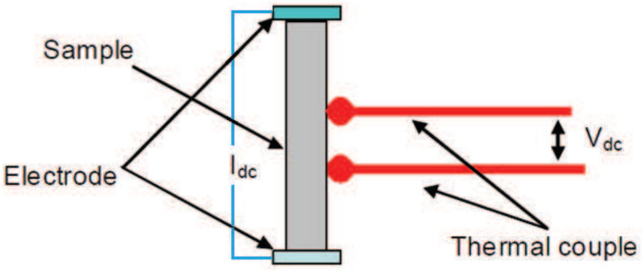

<u>Figure II.10 :</u> *Measurement of the electrical conductivity.*

Knowing the sample dimensions, the electrical resistivity and accordingly the electrical conductivity can be calculated using the equation:

$$\rho = \frac{1}{\sigma} = \frac{A}{L}\frac{V}{I} \qquad \text{(II.6)}$$

with A the cross-section area of the sample, L the distance between the thermocouples and V the voltage generated when the current I is flowing through the sample at each imposed temperature.

Even though the measurement is supposed to be taken when the probes are at a constant temperature, in the case of a thermoelectric material, Peltier effect may add a Seebeck voltage to the measured one and lead to an error in the electrical resistivity measurement. To minimise this phenomenon a direct current switching technique, or a an alternative current, is used.

The Seebeck coefficient is related to the difference of potential between two probes, while introducing a temperature difference between these ones. Therefore, Seebeck coefficient can be measured as shown in Figure II.11.

Seebeck coefficient (S), difference of potential (ΔV) and temperature gradient (ΔT) are linked as follows:

$$S = \frac{\Delta V}{\Delta T} = \frac{V_2 - V_1}{T_2 - T_1} \qquad \text{(II.7)}$$

Moreover, as explained in Chapter I, depending on the sign of *S*, it is possible to conclude on the nature of the main carriers (electrons or holes) circulating in the characterized material.

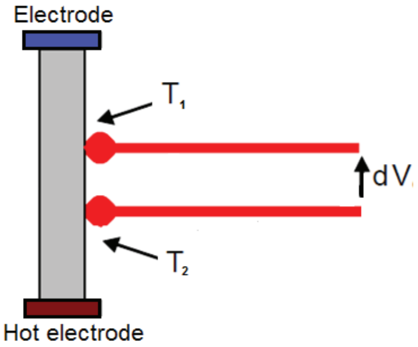

Figure II.11 : *Measurement of the Seebeck coefficient.*

b. ZEM-3 equipment

Figure II.12 : *ZEM-3 equipment from ULVAC Technologies Inc.*

A ZEM-3 equipment (ULVAC Technologies Inc, Methuen, MA, US), is used to measure simultaneously electrical conductivity and Seebeck coefficient (Figure II.12).

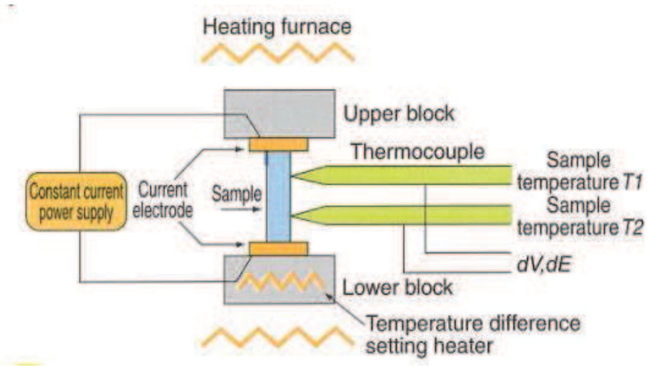

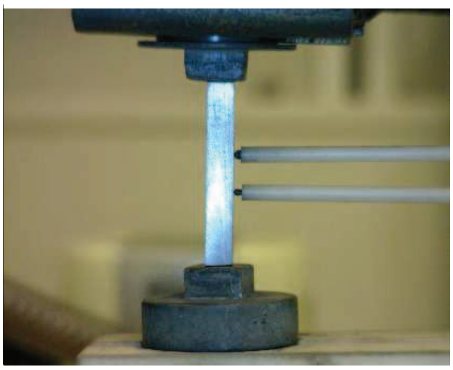

Figure II.13 : *ZEM-3 experimental configuration.*

Figure II.14 : *Picture of the sample holder with the sample.*

First of all, the sample is mounted on the sample holder as shown in Figure II.13 and held firmly between the nickel electrodes to ensure good electrical and thermal contacts between electrodes and the top/bottom sample surfaces. The thermocouples are slightly pressed against one of the lateral sample surfaces to ensure good temperature and difference of potential measurements. The sample dimensions were measured with a micrometer with a 0.001 mm precision. The distance between the thermocouple probes was measured using a camera. All these values were reported into the ZEM-3 software.

First, an I-V curve is acquired, its linearity confirming the good contacts on the four points. Then the sample holder is enclosed in a furnace able to work into specific atmospheric conditions. In our case, all the measurements were carried out in helium atmosphere (0.5 MPa) to avoid any oxidation of the samples exposed at high temperatures.

As mentioned in the previous paragraph, a direct current switching technique is used in order to minimise contribution of a parasitic Peltier effect. Indeed, the correct resistance is calculated by combining data from currents in opposite directions.

To measure the Seebeck coefficient, no current is applied to the sample, but a temperature gradient is generated by heating the lower electrode. A temperature difference of 10, 20 and 50 °C is imposed for each fixed temperature. In this manner, the Seebeck coefficient is determined from the ΔV vs. ΔT plot, giving a much more precise value. The Seebeck value related to the calibrated thermocouples is subtracted. Finally, the collected data of the material investigated are treated by the software piloting the ZEM-3 equipment to obtain an average value of the Seebeck coefficient at a given temperature.

II.4. Thermal diffusivity measurement

a. Thermal diffusivity using the laser flash method

The thermal diffusivity of the sintered samples was determined using a laser flash method[16 and 17]. It is difficult parameter to evaluate correctly due to surface heat loss and laser flash method has been proved to give more precise results. During such a measurement, the front surface of a parallelepipedic sample is heated by a laser pulse, while the temperature emerging from the rear surface is measured using an infra-red detector, as shown in Figure II.15.

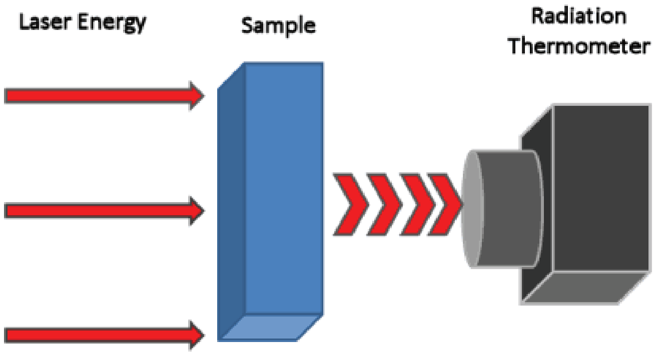

Figure II.15 : *Laser flash method*

The temperature vs time graph is plotted. Eventually, the temperature increase to a limit T_{max}. The thermal diffusivity, α, is then determined using the expression:[18]

$$\alpha = \frac{1.37}{t_{1/2}} \frac{d^2}{\pi^2} \qquad \text{(II.8)}$$

where d is the sample thickness and $t_{1/2}$ is the time needed by the rear surface to reach the temperature $T_{max}/2$, T_{max} beeing the maximum temperature recorded by the IR detector from the rear surface.

It is important to notice that the laser flash apparatus can also be used to measure the specific heat at constant pressure[16]. However, for this phD, Differential Scanning Calorimetry (DSC) will be used, as described below.

b. Thermal diffusivity measurement

For our investigations, square samples of 10*10 mm² and from 1 to 2 mm thickness, were entirely covered by a thin carbon layer, in order to avoid laser reflection during the measurements.

Afterwards, they were mounted on a SiC sample holder and placed into a LFA-457 MicroFlash apparatus (Figure II.16, Netzsch-Geratebau GmbH, Dardilly, F). All the measurements were completed under argon atmosphere. The samples were heated up to 500°C with the following temperature sequence: until 100°C the heating rate was 1°C/min, up to 200°C the heating rate was 2°C/min, up to 300°C the heating rate was fixed to 5°C/min and up to 500°C it was set to 10°C/min.

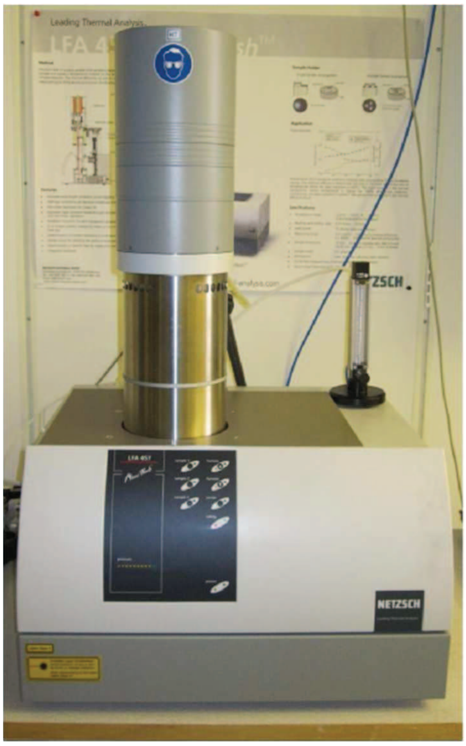

Figure II.16 : *LFA 457 MicroFlash equipment*

The analysis software available on the equipment proposes various models to fit the experimental data to determine a precise value of the $t_{1/2}$ parameter. In our case the Cape-Lehman theoretical model is used[17].

II.5. Heat capacity measurement

a. Heat capacity measurement by differential scanning calorimetry

Differential scanning calorimetry (DSC) is a thermo-analytical method frequently used to characterize how heat flows into a given sample as a result of heating. By comparing the heat flow rate between a reference sample and the analysed one, as a function of time and temperature, this technique can be used to characterize nearly all energetic effects occurring in a solid or a liquid during a thermal treatment.

In order to obtain accurate data to calculate a specific heat value at constant pressue for a given sample, three measurements are required: baseline, reference sample and analysed sample. All these measurements have to be performed with the exact same conditions: same crucible position, same measurement program and the same day.

The signal differences between the reference sample and the analysed one are recorded as a function of time and temperature. And the sample heat capacity at constant pressure is finally calculated as:

$$C_p = \frac{m_{reference} * \, signal\ difference\ (sample - baselise)}{m_{sample} * \, signal\ difference\ (reference - baselise)} \, C_{p\ (reference)} \qquad \text{(II.9)}$$

b. Heat capacity at constant pressure measurements

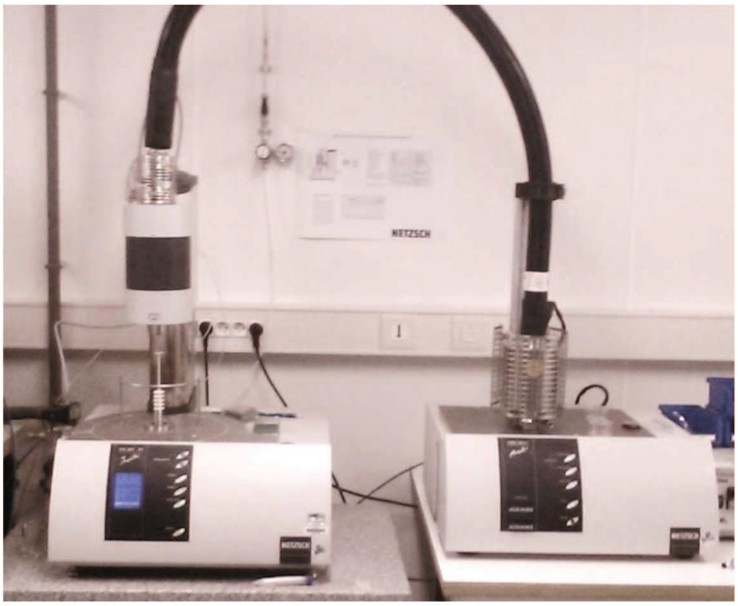

Figure II.17 : *DSC 404 F1 Pegasus equipment.*

The equipment used for our investigations was a DSC 404 F1 Pegasus (Netzsch–Geratebau GmbH, Dardilly, F), shown on Figure II.17. For these analyses, disk samples with a 5.2 mm diameter and a 0.5 mm thickness (polished and having parallel faces to ensure a good heat exchange between the sample and the crucible) were used. Measurements were done with two platinum crucibles with a coating of alumina (Figure II.18). Coating prevents interactions between the sample and the crucible. Both are marked with a tweezer in order to keep the same positions during the measurements.

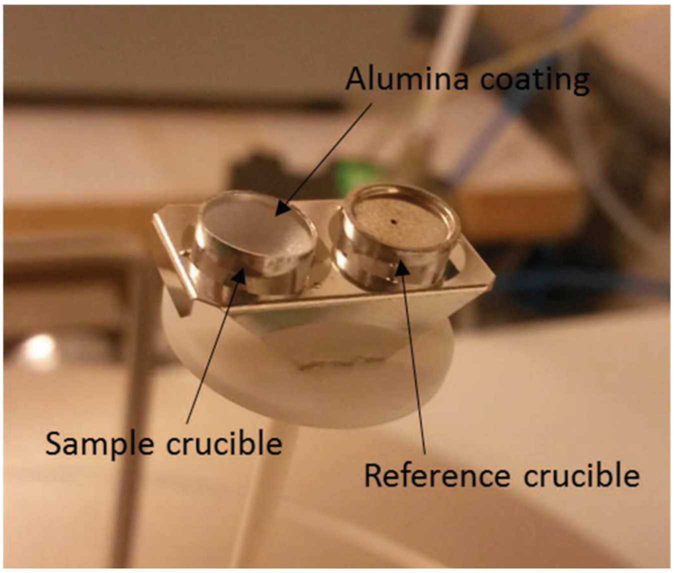

Figure II.18 : *Platinum crucibles used in the DSC configuration.*

All the measurements were done under an argon stream, with a heating rate of 20 °C/min. Firstly, for the baseline measurement, the sample crucibles was kept empty in the DSC equipment. Afterward, an 88 mg sapphire reference sample is placed in the sample crucible for the reference measurement. And finally, the investigated sample is placed in the sample crucible. For all the three measurements the reference crucible was kept empty and untouched.

II.6. Uncertainties

Once we have performed electrical and thermal properties measurements, we are able to calculate the figure of merit ($ZT = \sigma S^2/\kappa$, where σ is the electrical conductivity, S is the Seebeck coefficient, and κ is the thermal conductivity). However, the uncertainty of this calculation is very important. These uncertainties depend on the equipment that is used for the measurements.

Therefore, ZEM-3 equipment has uncertainties of $\pm$ 3% and $\pm$ 1.5 % when measuring electrical conductivity and Seebeck coefficient, respectively. Total uncertainty from the thermal conductivity measurements are contributed by two devices (thermal diffusivity measurement on LFA-457 MicroFlash and heat capacity measurement on DSC 404 F1 Pegasus) and its value amasses to $\pm$ 6%.

Finally, we have the total uncertainty value for the figure of merit, ZT, of $\pm$11.5 % that is represented by the sum of all uncertainties. Additionally, it is very rare to see in publications the uncertainty of the published results, which, depending on the equipment, can be as high as $\pm$21 %.

III - Characterization of raw powders and sintered samples

For powdered or sintered materials, we used different tools to characterize the microstructure at a fine scale. We will present all the kinds of equipments used, how the samples were prepared for such analyses and the methods applied to obtain quantitative results for key parameters when needed (average grain size of the sintered materials, chemical compositions of different phases dispersed in the sintered microstructure, for example).

II.1. Laser diffraction

Laser diffraction was used to investigate the size distribution of the raw powders (synthesized from a melting process, as described in section I of the present chapter) selected to sinter the different thermoelectric materials investigated during our work. A Mastersizer 2000 equipment (Malvern Instruments SA, Vénissieux, F) was employed. The laser wavelength was 633 nm and the Fraunhofer mode was selected (only the diffraction of the laser light by the particles was considered, not the diffusion, the refractive index of the investigated materials are not required). A small quantity of powder is dispersed in water (refractive index of 1.33 at 633 nm, no absorption) and analysed by the equipment using the wet configuration.

II.2. Density measurements by Archimedes method

This is a precise method which easily calculates the apparent density of the as-sintered samples. A special kit is used for measurements (figure II.19).

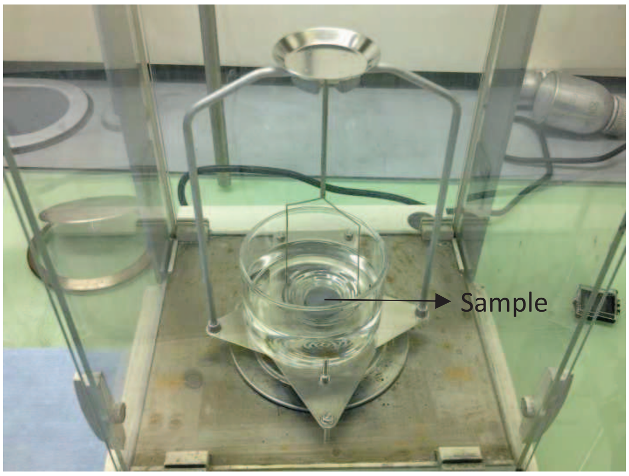

Figure II.19: *Density measurement kit.*

The weight of the sample is measured three times (scale used is a LA310s model, Sartorius France SAS, Dourdan, F). First, mass is measured in air, obtaining the mass m_1. A second measure is done for the sample that is submerged into absolute ethanol and second mass value, m_2 is measured. After that, the submerged sample is removed from the ethanol and wiped. Then, it's mass in air is measured again, obtaining the third mass value, m_3. Knowing these three masses, we can calculate the density of the material:

$$\rho_{sample} = \frac{m_{total}}{V_{total}} = \frac{m_1}{m_3 - m_2} \cdot \rho_{ethanol} \qquad \text{(II.10)}$$

where $\rho_{ethanol}$ represents the density of ethanol ($\rho_{ethanol} = 0.7893$ g/cm^3). It is necessary to compare the sample density with theoretical density to see if the densification process has been fully completed.

II.3. X-ray diffraction

X-ray diffraction is a technique for analysing a wide range of materials, identifying crystalline phases and determining the parameters of the crystal structure. Measurements on the powders we synthesized and on the as-sintered samples were performed on a BRÜKER D8 advance device (sample holder/detector have a θ/2θ configuration). A copper anticathode ($\lambda_{K\alpha1} = 1.54056$ Å and $\lambda_{K\alpha2} = 1.54439$ Å) and nickel filters that allow the elimination of K_β rays were used.

Powders were placed in a glass holder with a hole in the middle, so that the powder bed surface is in the same plane as the glass holder. Due to the glass holder, at lower angles some noise is noticed (shown in later chapters). Sintered samples are placed on a normal holder, while kept in the plane of reference. Analyses were performed in the domain of existence of most of the diffraction peaks belonging to a half-Heusler formulation, which is between 20 and 80 °.

II.4. Scanning electron microscopy (SEM)

A scanning electron microscope is able to produce images of a surface sample by scanning it with a focused beam of electrons. The electrons interact with atoms in the sample and SEM gathers various detectable signals which give the information about the sample's surface topography and composition. Detector may catch the secondary electrons that emit from the surface of the samples. These secondary electrons form a topographic image of the surface of the sample.

The microscope we used to investigate our powders and sintered samples was mainly a LEO 1530VP Gemini, (LEO Elektronenmikroskopie GmbH). It is equipped to perform energy dispersion X-ray spectroscopy (EDS) analyses. This method is used to investigate the chemical homogeneity of the samples.

Before SEM observations, solid samples were polished (SiC polishing papers 320, 800, 1200, 2000 mesh) and cleaned by cloth. Tools were also used to break the samples. Complementary observations were done on freshly broken surfaces. In this manner, it was easy to see the grain shape, porosity levels (if any) and second phases/precipitates if they are big enough. The investigated powders were placed on an adhesive graphite circular shaped tape. Due to their fast oxidation when exposed in air, this was performed few minutes before observations. In all cases, no metallization was used, all the powders and samples being sufficiently electrically conducting to avoid parasitic charging phenomenons during the observations. Acquisitions were made with a 5-10 mm working distance with an electron high tension (EHT) of 5-15 kV.

II.5. Transmission electron microscopy (TEM)

a. Sample preparation by FIB

Focused ion beam (FIB) is a technique used for specific analysis, deposition, and ablation of materials. It looks like SEM, but instead of using a focused beam of electrons to make an image, FIB uses a focused beam of ions.

To investigate the microstructure of our different as-sintered samples, each one was cut from its center part, put on a holder and introduced into the FIB equipment (Strata DB 235, FEI, Eindhoven, NL, beam of Ga). Then thin-foils, having a thicknesses ranging from 70 to 100 nm, where cut and glued onto a cupper grid (Figure II.20).

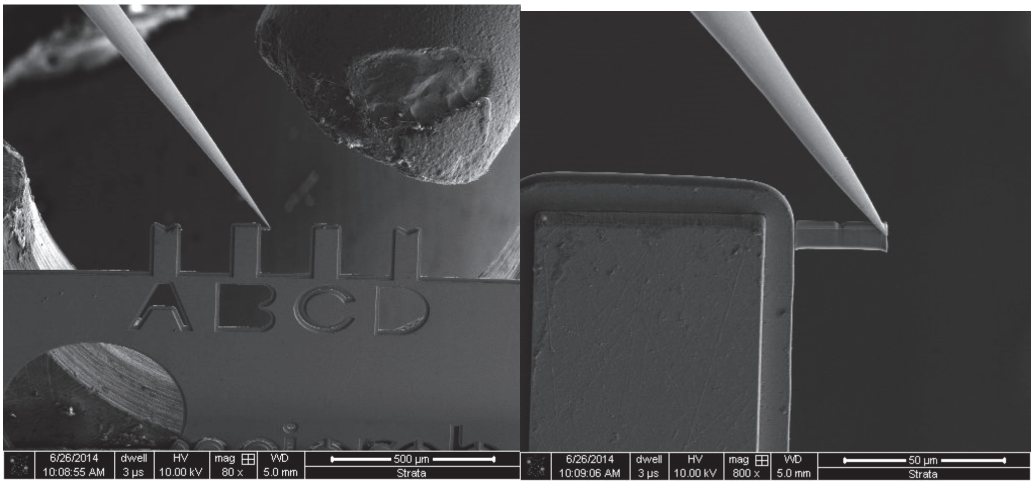

Figure II.20: *Image of thin foil for TEM observation in FIB equipment.*

b. TEM observations

Transmission electron microscopy (TEM) is a microscopy technique in which a beam of electrons is transmitted through an ultra-thin specimen, interacting with it as it passes through. Image is formed from the interaction of the electrons transmitted with the specimen. The image is magnified and focused onto an imaging device, such as a fluorescent screen, on a layer of a photographic film or is detected by a sensor, such as a CCD camera.

TEM uses the small de-Broglie wavelength of electrons and can create high resolution images.

Characterization of samples using TEM was performed on a Tecnai Osiris microscope (acceleration voltage of 200 kV, line resolution of 1.02 Å, point to point resolution of 2.5 Å). It is an analytical TEM instrument optimised for high speed and high sensitivity EDS measurements in STEM mode. With a high brightness XFEG gun, EDS maps can be acquired very fast. It has BF (bright field), ADF (annular dark-field imaging) and HAADF (high angle annular dark field) detectors that provide a wide range of diffraction and Z-contrast conditions for STEM imaging and analyses. Tecnai Osiris has a 1.8 Å point to point resolution in HAADF/STEM mode.

II.6. SEM and TEM data analysis

The obtained SEM and TEM images are treated by ImageJ software to determine the average grain size or precipitate size of the as-sintered samples. Statistic analysis is done on a surface containing 100 to 300 precipitates and around 500 grains. For a SEM polished surface and TEM images, apparent grain/precipitate sizes, *g/p*, can be approximated by spheres that have a diameter G/P. Using the three-dimensional correction factor of 1.2, the real grain/precipitate size, G/P is given by[19]:

$$G/P \approx 1.2g/p \qquad \text{(II.11)}$$

This correction factor is not used to calculate the precipitate size from a SEM fracture surface observation as the entire precipitate is observed.

Quantification of the chemical elements that are found in the sintered samples was done using ESPRIT software (BRUKER, version 1.9). Mapping was done using Hypermap mode, where every pixel of the image corresponds to an EDS spectrum. Sometimes, acquisitions in point-mode were also done in phases of interest. Quantification is done using a Gaussian deconvolution of peaks that are associated to each element. Afterwards, the patterns were quantified using the Cliff-Lorimer method[20], which can determine the relative concentration of different elements based on the intensity of the peaks. For a binary system, it can be written as:

$$\frac{C_A}{C_B} = k_{AB}\frac{I_A}{I_B} \qquad \text{(II.12)}$$

where C_A is the atomic fraction of the element A, C_B is the atomic fraction of the element B, I_A and I_B correspond to the intensity of the peaks for elements A and B, respectively and k_{ab} is the Cliff-Lorimer factor or *k*-factor. The Cliff-Lorimer factor is defined as:

$$k_{AB} = \frac{(Q\omega a)_A A_B \varepsilon_A}{(Q\omega a)_B A_A \varepsilon_B} \qquad \text{(II.13)}$$

where A is the atomic weight, Q is the ionization cross section (how easily a particular atom is ionized by a particular electron), ω is the fluorescence yield (ionization fraction resulting in X-ray emission), a is the relative intensity factor (fraction of the total measured *K* line intensity of an element) and ε the detector efficiency for a measured element. The sum of all atomic fractions for a binary system (A, B) is written with expression $C_A + C_B = 100\%$.

In ternary and higher order systems, the intensities of all the elements, whose mass concentrations are unknown, must be measured, or the weight fraction of a particular element in the sample must be known in advance of the analysis[21]. For a three-element analysis:

$$\frac{C_A}{C_B} = k_{AB}\frac{I_A}{I_B} \qquad \text{(II.13)}$$

And

$$\frac{C_B}{C_C} = k_{BC}\frac{I_B}{I_C} \qquad \text{(II.14)}$$

where C_C is the atomic percent of the element C. The sum of all atomic fractions for a ternary system (A, B and C) is written as $C_A + C_B + C_C = 100\%$.

The k-factors are usually calculated from experiments, by using standards where the concentration of elements of interest are known. But they may also be theoretically calculated using equation II.13. In our case, the k-factors used for our quantifications have been theoretically calculated using Esprit software, by introducing the key parameters related to the Osiris TEM equipment used.

---

[1] Gopalakrishnan, S., Sengar, P.S., Cold crucible induction melting technology for vitrification oh high level waste : development and Status in India, WM2008 Conference, Pheanix AZ, 2008

[2] Starck, A., Mühlbauer ,A., Kramer, C., Handbook of Thermoprocessing Technologies: Fundamentals, Processes ..,392

[3] Gagnoud, A., Leclercq, I.,Electromagnetic modelling of induction melting devices in clod crucible, transactions on magnetics, 1988, 24, 1, 573

[4] Chen, S., Ren, Z., Recent progress of half-Heusler for moderate temperature thermoelectric applications, Maretials Today, 2013, 16, 10 387–395

[5] Xia Y., Ponnambalam V., Bhattacharya S., Pope A.L. , Poon S.J., Tritt T.M., Electrical transport properties of TiCoSb half-Heusler phases that exhibit high resistivity,J. Phys. Condens. Matter, 2001, 13, 77-89

[6] Friederike Burmeister, C., Kwade, A., Process engineering with planetary ball mills, Chem. Soc. Rev., 2013, 42, 7660-7667

[7] Costa, P., Nanomatériaux, structure et elaboration, Technique de l'ingénieur, 2001, M4026 V1

[8] Abdellaoui M., Gaffet E., Mechanical alloying in a planetary ball mill : kinematic description., J. Phys. IV France, 1994, 04

[9] Zou, M., Li, J.-F., Du, B, Liu, D., Kita, T., Fabrication and thermoelectric properties of fine-grained TiNiSn compounds, J. of Solid State Chem., 2009, 182, 3138

[10] Bernard-Granger G. , Soulier M. , Ihou-Mouko I. , Navone C. , Boidot M., Leforestier J. , Simon J. , Microstructure investigations and thermoelectrical properties of a P-type polycrystalline higher manganese silicide material sintered from a gas-phase atomized powder, J. Alloys Compd., 2015, 618 , 403

[11] Guillon,O., Gonzalez-Julian, J., Dargatz, B., Kessel, T., Schierning, G., Rathel, J., and Herrmann, M., Field-Assisted Sintering Technology/ Spark Plasma Sintering: Mechanisms, Materials, and Technology Developments

[12] Estournes, C., Mise en forme de matériaux par frittage flash, Techniques de l'ingénieur, 2006, IN56 V1

[13] Shen Z, Johnsson M, Zhao Z, Nygren M., Spark Plasma Sintering of Alumina, J Am Ceram Soc, 2002, 85, 1921

[14] Kim, H.-S., Gibbs, Z. M., Tang, Y., Wang, H., Snyder, G. J., Characterization of Lorenz number with Seebeck coefficient measurement, APL Materials, 2015 3, 041506

[15] Harman, T.C., Special Techniques for Measurement of Thermoelectric Properties, J. Appl. Phys., 1958, 29, 1373

[16] Parker, W. J., Jenkins, R. J., Butler, C. P., Abbott, G. L., Flash Method of Determining Thermal Diffusivity, Heat Capacity, and Thermal Conductivity, J. Appl. Phys., 1961, 32, 1679

[17] Cape J. and Lehman, G., Temperature and finite pulse-time effects in the flash method for measuring thermal diffusivity, J. App. Physics, 1963, 34, 7, 1909-1913.

[18] R. Taylor in CRC Handbook of Thermoelectrics (ed. D. M. Rowe) 170-172 (CRC, Boca Raton, 1995).

[19] Bernard-Granger, G, Guizard, C, Addad, A, Influence of Co-Doping on the Sintering Path and on the Optical Properties of a Submicronic Alumina Material, Journal of the American Ceramic Society 91 (5), 1703-1706

[20] Longo, D. M., Howe, J. M., and Johnson, W. C. Experimental method for determining Cliff-Lorimer factors in transmission electron microscopy (TEM) utilizing stepped wedge-shaped specimens prepared by focused ion beam (FIB) thinning, Ultramicroscopy, 1998, 80, 85-97.

[21] Joy, D. C., Romig, A. D., and Goldstein, J. Principles of Analytical Electron Microscopy. Springer Science & Business Media, 1986. ;

Chapter III

Microstructure and thermoelectric properties of the $Zr_{0.25}Hf_{0.25}Ti_{0.5}NiSn_{0.994}Sb_{0.006}$ n-type material

The N type half-Heusler $Zr_{0.25}Hf_{0.25}Ti_{0.5}NiSn_{0.994}Sb_{0.006}$ composition got the highest ZT of 1.5 at 430 °C ever reported in the literature.[1]Even if it was never reproduced despite numerous attempts since the publication from Sakurada and Shutoh in 2005[2, 3 and],[4] Schwall and Blake shown that this value could be possibly achieved[5]. To them, phase separation in the material, lowering the thermal conductivity, is a key step. However, if perfunctory X-ray diffraction (XRD) and energy dispersive spectroscopy (EDS) analysis from scanning electron microscopy (SEM) observations are presented in some of the publication cited before, no detailed microstructure investigation was completed. Indeed, no paper is reporting on the use of a strict microstructure analysis to understand the thermoelectric properties of the half-Heusler $Zr_{0.25}Hf_{0.25}Ti_{0.5}NiSn_{0.994}Sb_{0.006}$ composition and more generally of most of the thermoelectric materials, whatever the family they are belonging to.

The link between microstructure and thermoelectric properties is an essential point to address to be able to understand how to improve the thermoelectric properties of a given material. Accordingly, in this chapter, pellets of an n-type polycrystalline material, having the composition $Zr_{0.25}Hf_{0.25}Ti_{0.5}NiSn_{0.994}Sb_{0.006}$ have been sintered at different temperatures using the manufacturing process exposed in Chapter II. Then, the microstructure of the sintered samples has been characterised using SEM and TEM and the thermoelectric properties have been investigated. Finally, results are discussed in order to establish a link between the microstructure and the thermoelectric properties of the investigated material.

I - Analysis of the manufacturing steps

In this section, the microstructure of the investigated composition is analysed at each step of the manufacturing process.

II.1 - Melted ingot analysis

An ingot with the target $Zr_{0.25}Hf_{0.25}Ti_{0.5}NiSn_{0.994}Sb_{0.006}$ stoichiometry was manufactured by levitation melting under argon atmosphere. The obtained ingot was then crushed manually with an agate mortar into a glovebox operating under argon. The microstructure of the ingot has been investigated through XRD analysis and SEM coupled to EDS mapping.

The XRD diffractogram, presented in Figure III.1, reveals that the half-Heusler phase, with a $C1_b$ structure (space group 216, $F\underline{4}3m$), is obtained. In addition to the half-Heusler phase indexed, pure Sn-β[6] and a Ti-Sn[7] compound were also identified. Moreover, looking at the peaks observed at high diffraction angle values, it appears that those related to the half-Heusler phase are not symmetrical. They seem to be enlarged at the right side. Such a shoulder on the right side of diffraction peaks was also observed, even though not explained, in an arc melted ingot having the $Zr_{0.4}Hf_{0.3}Ti_{0.3}NiSn$ composition, as reported by Kurosaki and all[8].

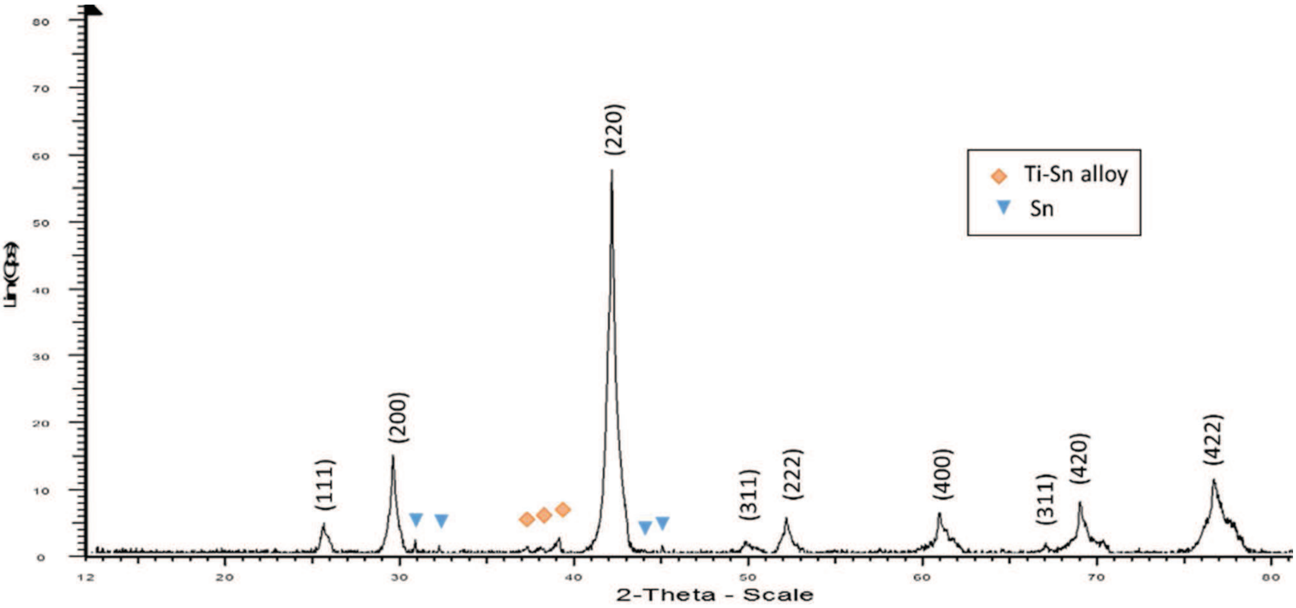

Figure III.1 : *XRD diffractogram of the* $Zr_{0.25}Hf_{0.25}Ti_{0.5}NiSn_{0.994}Sb_{0.006}$ *ingot synthetized by levitation melting*

A fresh fracture surface of the ingot, is shown in Figure III.2.a) and b) (SEM, secondary electron mode). The EDS maps for the different constituting elements are also shown on the Figure III.2.c). From Figure III.2.a) and b), it seems that two different phases may be present (different brightness contrast). Complementary quantitative EDS analyses have shown that it is not the case. The difference of contrast in then attributed to topographic and orientation factors. The average composition of the investigated area has been determined to be $Zr_{0.25}Hf_{0.24}Ti_{0.52}Ni_{1.07}Sn_{0.92}Sb_{0.006}$, in good agreement <ith the target composition.

From the element maps shows in Figure III.2.c), it as to be noticed that the dark areas, outlined by white arrows, are link to EDS signal absorption due to surface’s irregularities and are not related to chemical composition variation. The Zr, Ni and Hf contents are constant throughout the observed area. In the same time, Figure III.2.c) also highlights the presence of a Ti-Sn enriched areas located where defects seem to be present in the ingot microstructure, for example at grain boundaries. This observation is in agreement with the Ti-Sn phase detected using XRD in Figure III.1. It is interesting to notice that a Ti-Sn based alloy was also observed at grain boundaries in $Zr_{0.4}Hf_{0.3}Ti_{0.3}NiSn$ ingots manufactured using arc melting by Kurosaki all.[8].

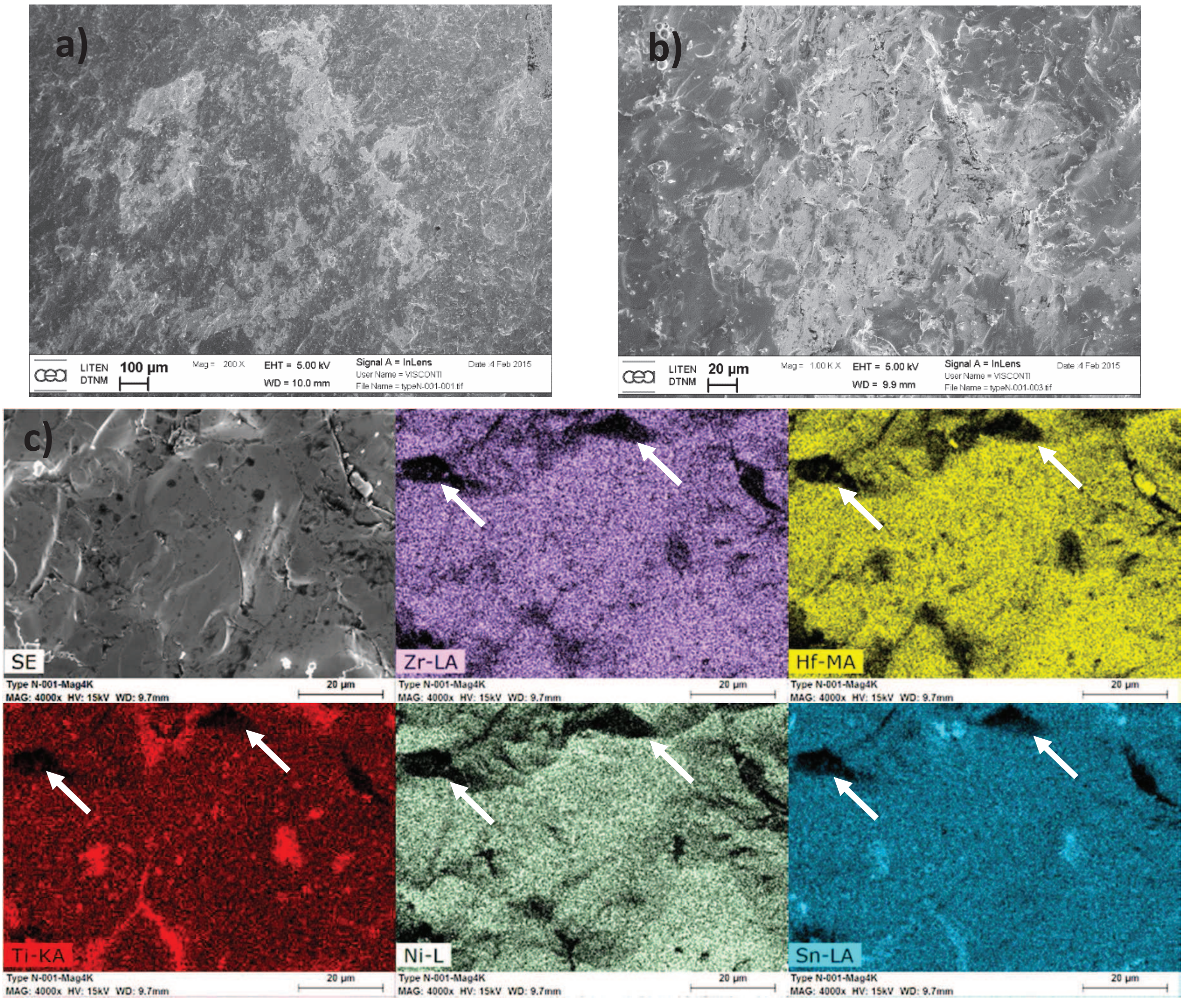

Figure III.2 : *a) and b) SEM images and c) EDS mapping of the ingot*

II.2 - Powder analysis

After synthesis by levitation melting, the ingot is milled under argon atmosphere. Then, the collected powder is rubbed through a 56 µm sieve. The particle size distribution presented in Figure III.2 is not monomodal and presents a non-negligible fraction of fine particles. For information, the global volume diameter ($D_{4,3}$) is around 16 µm.

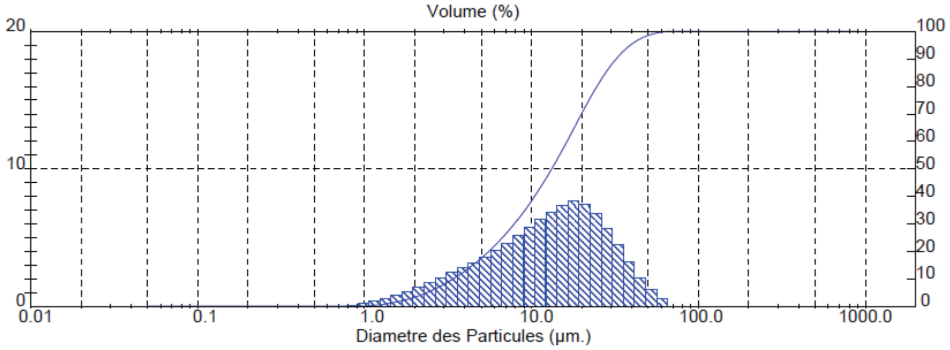

Figure III.3 : *Particle size distribution of the* $Zr_{0.25}Hf_{0.25}Ti_{0.5}NiSn_{0.994}Sb_{0.006}$ *powder*

By looking at the SEM images in Figure III.4, collected from the sieved powder, there are only a few particles with an average diameter larger than 10 µm. As shown in Figure III.4.c), most of the particles seem to have a diameter in the range from 1 to 3 µm.

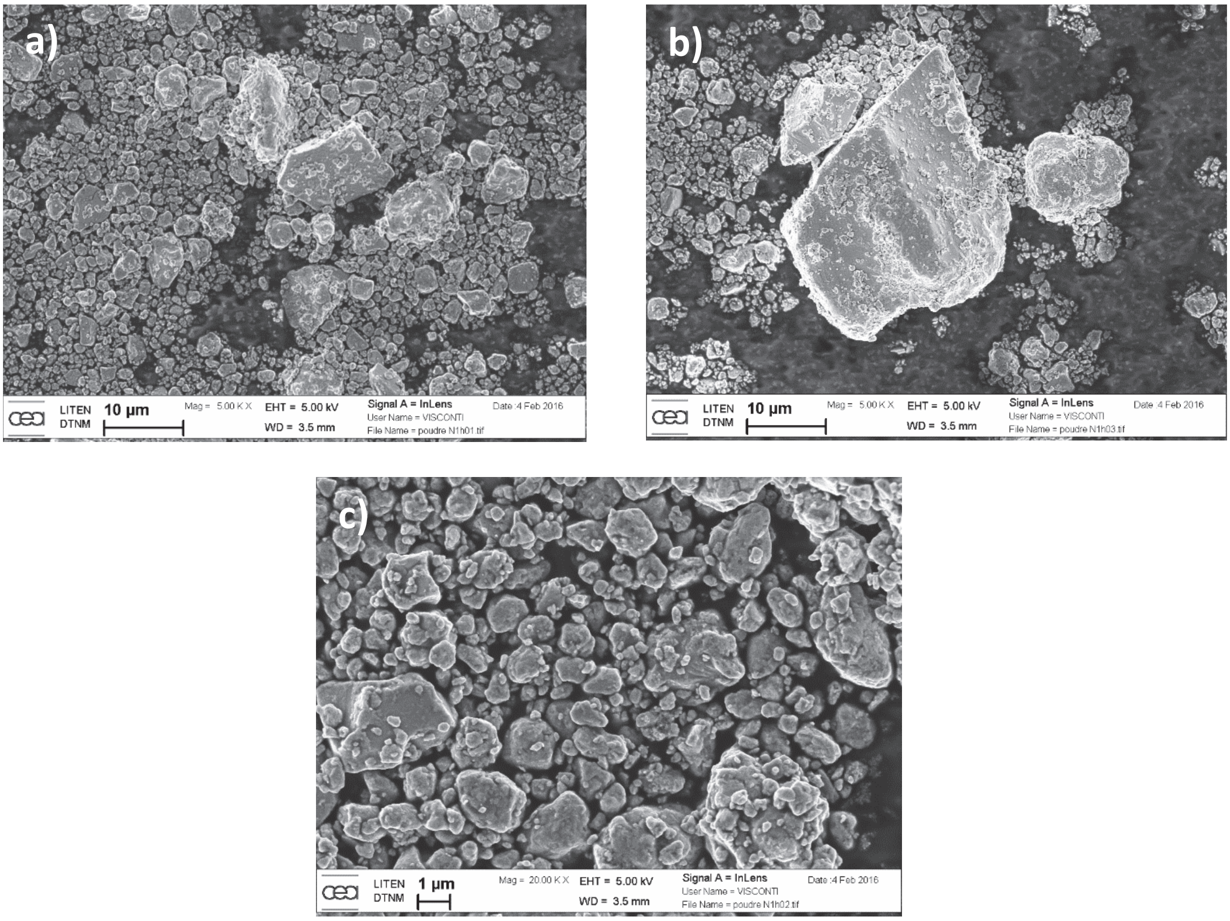

<u>Figure III.4 :</u> *SEM imaging of the* $Zr_{0.25}Hf_{0.25}Ti_{0.5}NiSn_{0.994}Sb_{0.006}$ *powder.*

An XRD analysis of the $Zr_{0.25}Hf_{0.25}Ti_{0.5}NiSn_{0.994}Sb_{0.006}$ sieved powder has been completed to control structure and crystallinity. Figure III.5 shows only peaks matching to the half-Heusler composition (JCPDS 04-012-9150 file, lattice parameter of 6.08 Å). However, as already noticed for the melted ingot, peaks are not symmetrical. They are larger at the right side, possibly because of composition gradients in the powder.

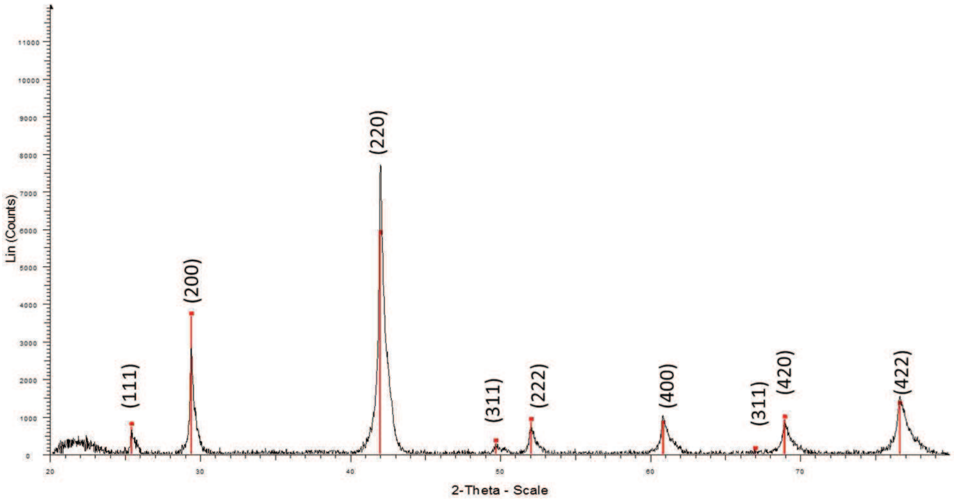

Figure III.5 : *XRD spectrum of a $Zr_{0.25}Hf_{0.25}Ti_{0.5}NiSn_{0.994}Sb_{0.006}$ powder synthetized by levitation melting and ball milling.*

As what was observed on the ingot, Ti and Sn repartition maps, presented in Figure III.6, show that few grains are enriched in both elements. In conclusion, ball milling used to crush the ingot has no influence on the chemical elements repartition.

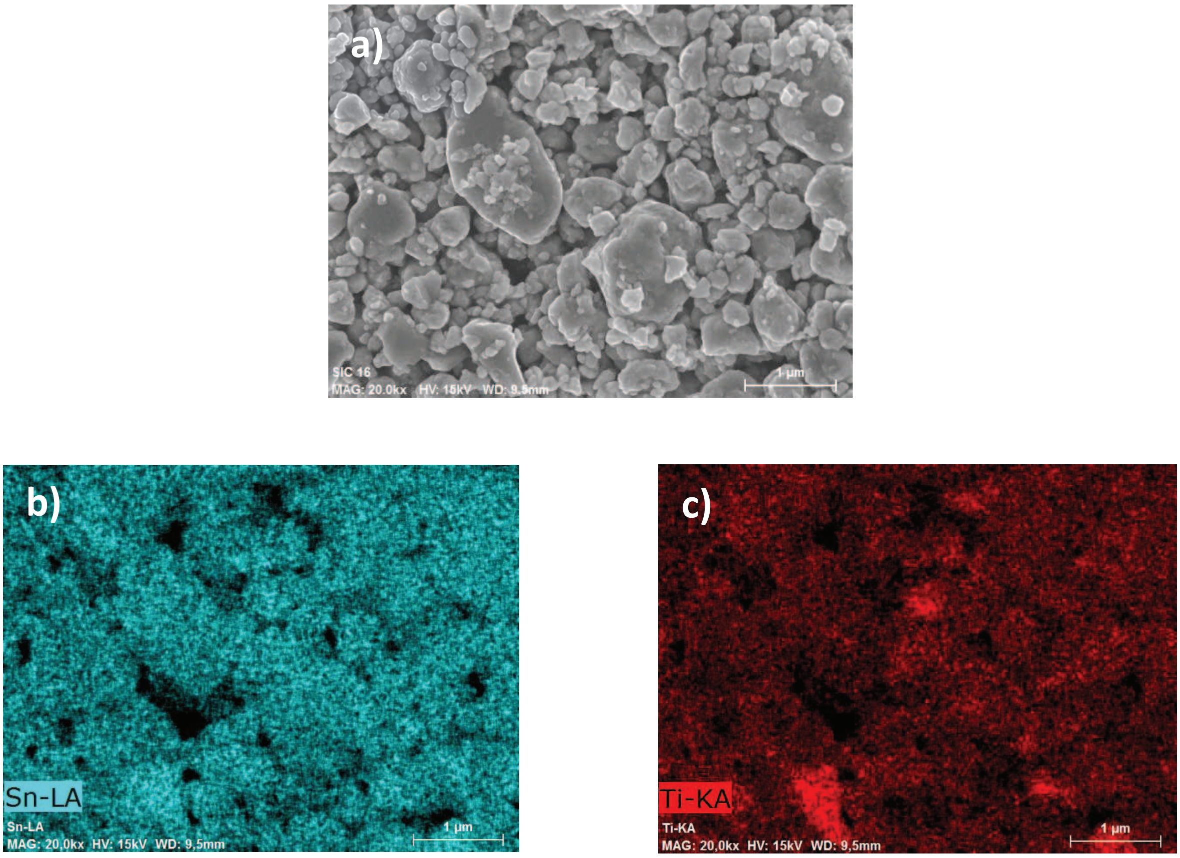

Figure III.6 : *a) EDS and b) Sn and c) Ti mapping of the $Zr_{0.25}Hf_{0.25}Ti_{0.5}NiSn_{0.994}Sb_{0.006}$ powder synthetized*

II.3 - Determination of the sintering temperature

In order to determine the accurate sintering temperature to obtain a highly dense material and therefore good thermoelectric properties, the powder sintering window has to be determined. To this aim, a first SPS run was completed and the densification rate was analysed and reported in Figure III.7, from room temperature up to 1150 °C. As claimed for other thermoelectric powders[9] [10], the densification rate in function of temperature exhibits a standard bell-shaped curve with a maximum value measured for a temperature of 990 °C. Accordingly, three sintering temperatures have been retained for further tests: 990 °C which is the temperature where the densification rate value is at maximum, 1050 °C corresponding to the temperature regime where the densification rate decreases from its maximum value towards zero and, finally, 1140 °C which is the temperature where the densification rate approaches zero. For each sintering temperature, the soak time was fixed to 5 min, and all other sintering parameters are summarized in Chapter II.

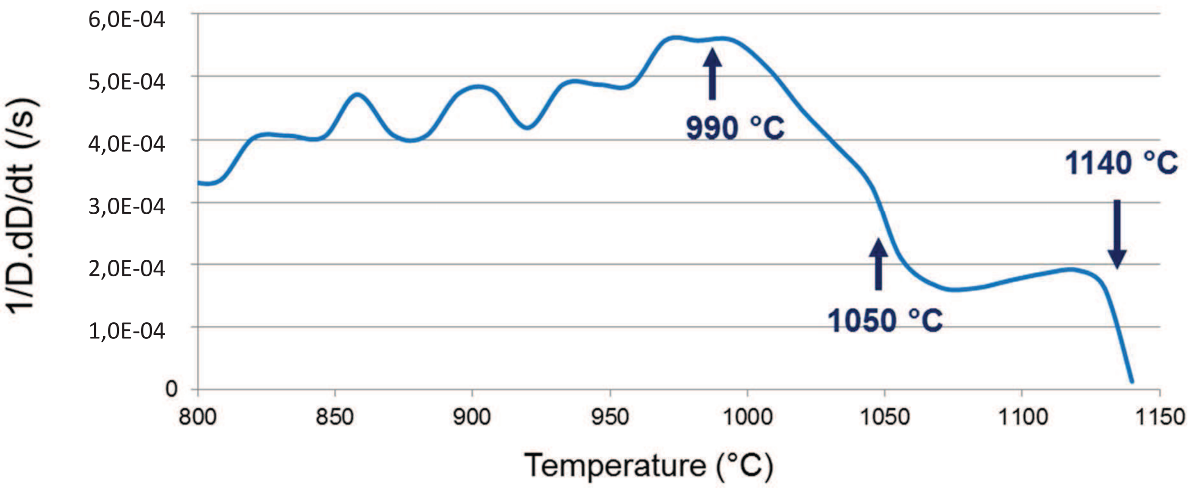

Figure III.7 : *Densification rate of the* $Zr_{0.25}Hf_{0.25}Ti_{0.5}NiSn_{0.994}Sb_{0.006}$ *material.*

II - Microstructure analyses of the sintered pellets

Three $Zr_{0.25}Hf_{0.25}Ti_{0.5}NiSn_{0.994}Sb_{0.006}$ pellets were synthetized by SPS at 990 °C, 1050 °C and 1140 °C. Afterward, a detailed microstructure analysis is performed.

II.1 - SEM observations and XRD analysis

- Residual porosity.

The apparent density of the sintered samples was measured using the Archimedes method with absolute ethanol. The theoretical density calculated for the $Zr_{0.25}Hf_{0.25}Ti_{0.5}NiSn_{0.994}Sb_{0.006}$ target composition was 8.25 g.cm^{-3}. The measured densities of the samples sintered at 990, 1050 and 1140 °C were respectively 95, 96 and 98 %, as reported in Table III.1.

Figure III.8 presents a SEM general view, in secondary electron mode, of fresh fracture surfaces for the three investigated samples. The ones sintered at 990 °C and 1050 °C are not fully dense as residual pores, materialized with red arrows, are detected. Whereas the sample sintered at 1140 °C appears devoid of any residual pore.

The porosity evolution observed on the SEM images concords with the density one. The higher the sintering temperature, the higher the sintered relative density, the lower the number of residual pores.

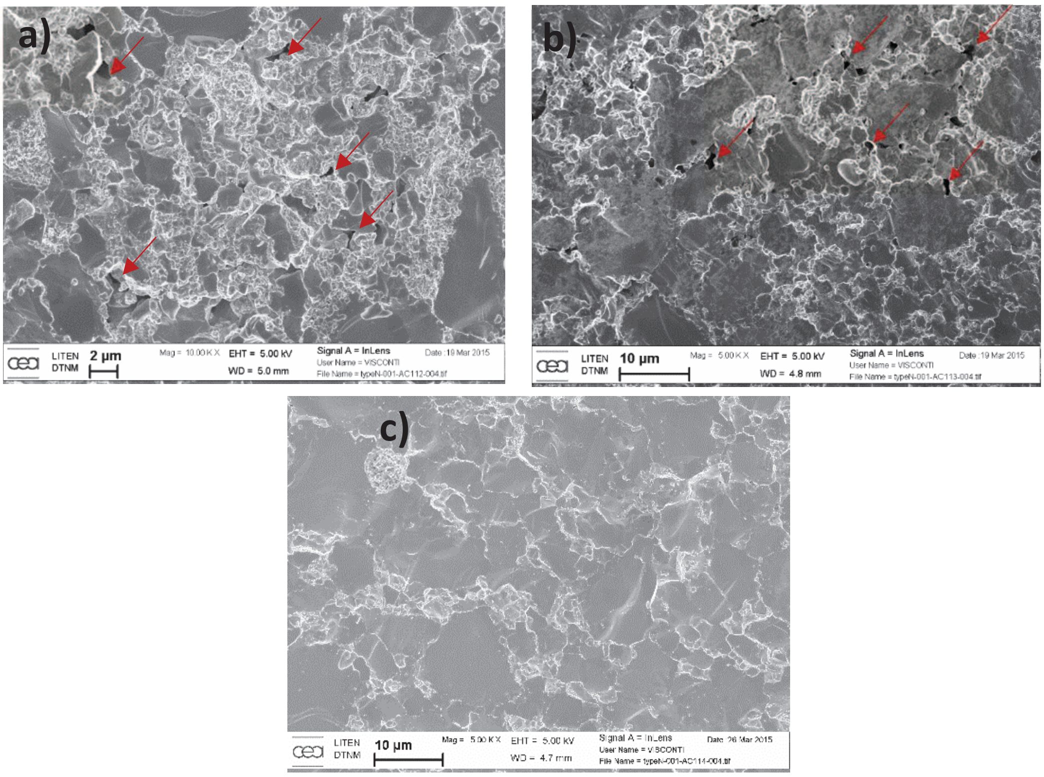

Figure III.8 : *SEM images of a fracture surface of the sample sintered at a) 990 °C, b) 1050 °C and c) 1140 °C.*

- XRD analyses.

X-ray diffraction patterns collected on the powder and each sintered sample is shown in Figure III.9. In all cases the half-Heusler phase, with a $C1_b$ structure (216, $F\underline{4}3m$), is detected.

It is important to notice that there is an evolution of the main lattice parameter before and after sintering. The lattice parameter evaluated for the ingot and the grinded powder was 6.08 Å, as reported in parts I.1 and I.2. When looking at the different sintered samples, the lattice parameter corresponding to the main peaks is calculated to be 6.01 Å. This change can be attributed to internal stresses. Indeed, it is possible that internal stresses appear during ingot casting and are still present in the powder after grinding. Then, during sintering at high temperature, internal stresses may relax modifying the value of the lattice parameter of the main half-Heusler phase. Unfortunately, up to now, this point has not been scrupulously addressed during our investigations.

Additionally, a significant broadening of the peaks is also observed in each XRD spectrum of the sintered samples. Indeed, shoulders located on left side of the main diffraction peaks are also noticed. This peak broadening can possibly be linked to a composition fluctuation inside the samples. The covalent radius of titanium is around 160 pm, whereas the zirconium and hafnium ones are about 175 pm. Accordingly, the lattice parameter of the ternary half-Heusler compounds TiNiSn[11], HfNiSn[12] and ZrNiSn[13] is 5.94 Å, 6.10 Å and 6.12 Å, respectively. Therefore, it is possible to estimate the qualitative phase contend in Ti and Zr/Hf in the investigated samples[14]. The broadening on the left side of the main peak is probably related to the presence of a phase depleted in Ti and enriched in Zr and Hf. In contrary, the main peaks, characterized by a lower lattice parameter, are probably related to the occurrence of another phase enriched in Ti. Moreover, shoulders width is decreasing when increasing the sintering temperature. Therefore, it signifies, that the sintered sample are more homogenous when increasing the sintering temperature[15].

Additional peaks are also detected for all sintered samples. First of all, a carbon peak is found for the sample sintered at 1050 °C. This is simply due to remaining graphite at the pellet surface from the SPS process. Small amounts of elemental Sn-β (metallic form, stable at room temperature) [6] residues are also detected in all the sintered samples. Downie *and all* noticed this impurity in a (Ti, Zr, Hf)NiSn material sintered by SPS. A Sn-deficient composition could avoid the apparition of the Sn impurity phase[16] [17]. Moreover, another phase detected by XRD is monoclinic HfO_2[18].

Finally, it is interesting to notice that the Ti/Sn phase found in the ingot (Figure III.1) and on the EDS analysis of the powder (Figure III.6) is not detected anymore. This phase must have disappear during the sintering step.

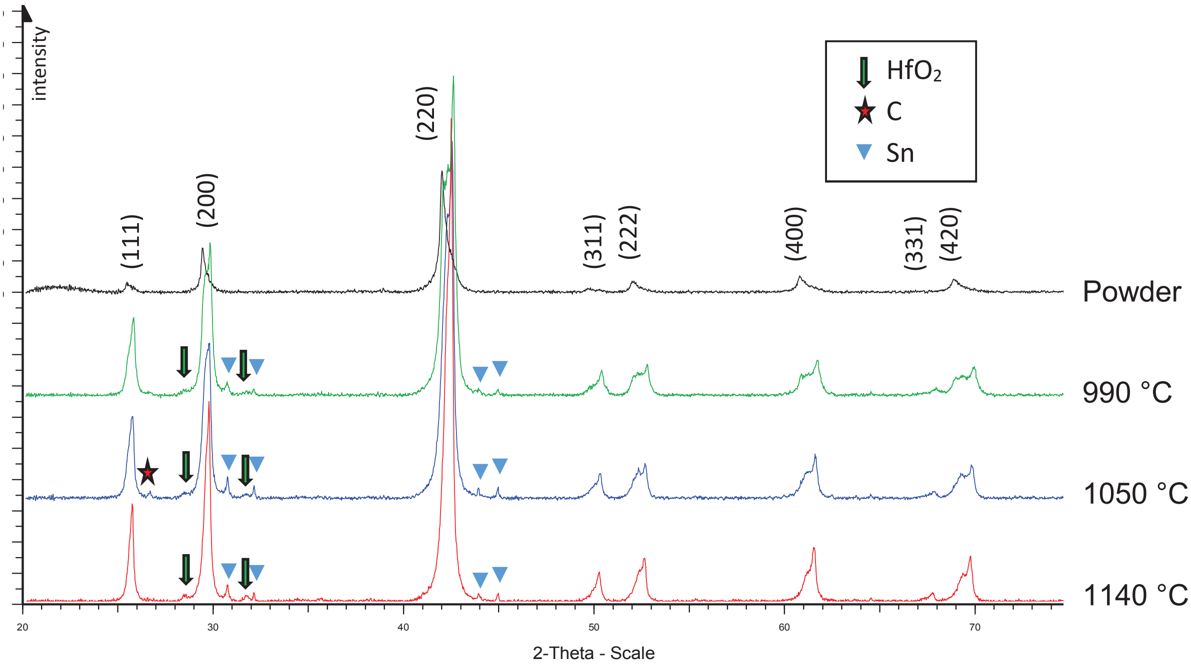

Figure III.9: *XRD patterns of the $Zr_{0.25}Hf_{0.25}Ti_{0.5}NiSn_{0.994}Sb_{0.006}$ powder, and the samples sintered at 990°C, 1050°C and 1140°C.*

- Precipitates and grain size analysis.

From the SEM pictures in back scattered electrons mode on polished sections presented in Figure III.10, it was possible to calculate an average grain size for each sintered sample. For that, the two-dimensional surface of each grain appearing in the observation plan is measured out of more than 500 grains and the diameter of a corresponding disc, having the same surface value is calculated for each grain using a tridimensional correction factor of 1.2[19]. The calculated average grain diameters for the three different sintered samples are presented in Table III.1. The average grain size grows from 3.1 to 3.5 and 3.8 µm with the sintering temperature increasing from 990 to 1050 and 1140 °C.

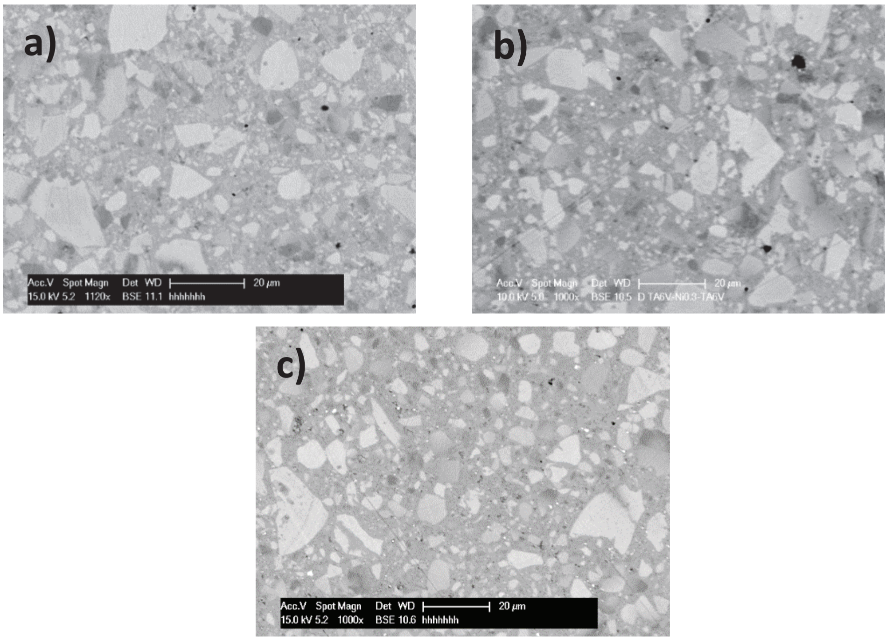

Figure III.10 : *SEM back scattering electron analysis of a polished surface of the sample sintered at a) 990 °C, b) 1050 °C and c) 1140 °C*

SEM images in secondary electron mode of fractures surfaces of three samples at different magnifications are present in Figure III.16. The presence of numerous tiny bright precipitates is noticed at higher magnifications for all the investigated samples. For the samples sintered at 990 and 1050 °C, the precipitates appear to be located at grain boundaries. Indeed, in Figure III.11.a) and b), the fracture path is transgranular in some grains, for example the ones with a red arrow, and in that case no precipitate is detected. For the sample sintered at 1140 °C, it can be noticed in Figure III.11.c), that some bright precipitates are now entrapped in the elemental grains constituting the sintered polycrystal, as shown in the red ellipse.

As for the grain size, for each sample, the surface of each individual precipitate observed from fracture surfaces reported in Figure III.11.d), e) and f) is measured. A corresponding mean diameter is calculated and reported in Table III.1. It has to be outlined that in this case, no tridimensional correction factor was applied. As for the grain size, the precipitate diameter increases with the sintering temperature. Indeed, the average precipitate diameter grows from 32 to 52 and finally to 104 nm.

Accordingly, a precipitate size distribution, made out of more than 100 precipitates for each investigated soak temperature, is shown in Figure III.12. It shows that the higher the sintering temperature the larger the distribution.

Additionally, looking at Figure III.11.d), e) and f), it can be noticed, by eyes inspection, that the number of precipitate per surface unit decreases when the sintering temperature increases. This observation possibly proves that precipitates are coalescing when the sintering temperature increases.

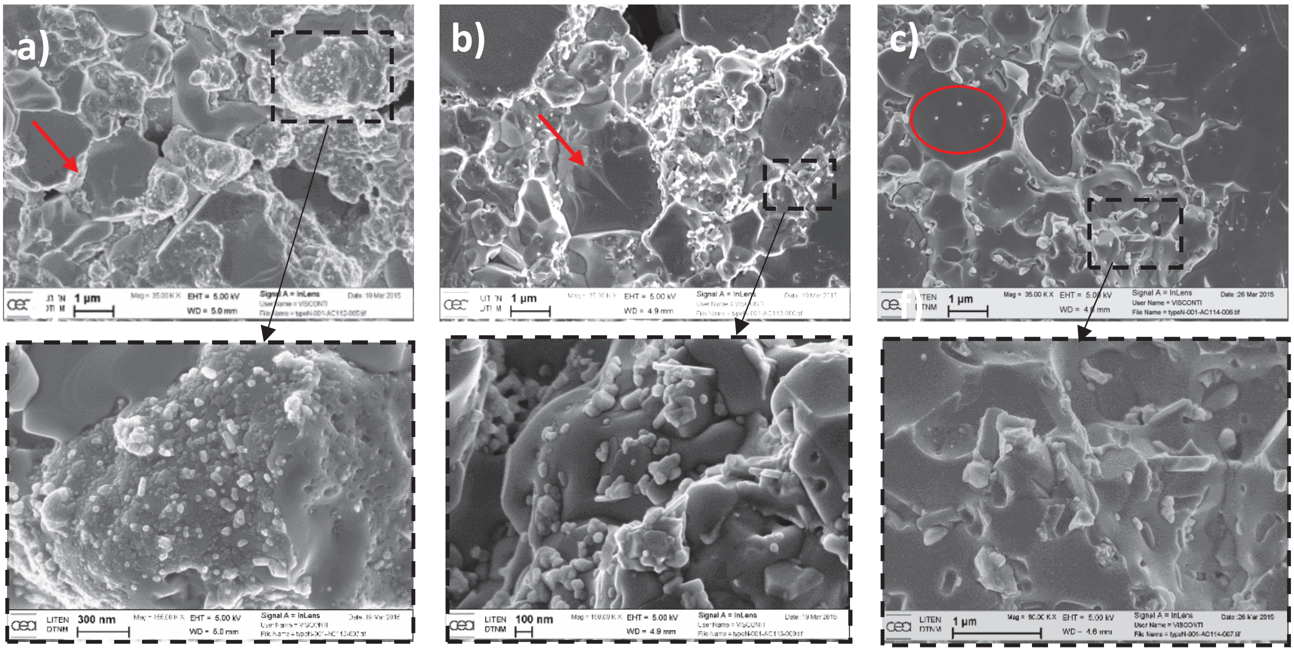

Figure III.11 : *SEM images of a fracture surface of the sample sintered at a) 990 °C, b) 1050 °C and c) 1140 °C. d), e) and f) are the same samples at higher magnification*

Soak temperature (°C)	990	1050	1140
Relative sintered density (%)	95	96	98
Average grain size (µm)	3.1	3.5	3.8
Average precipitate diameter (nm)	32	52	104

Table III.1 : *Density, average grain size and precipitate diameter depending on the soak temperature.*

Finally, looking at Figure III.13, it is interesting to point out that, for sintering temperatures ranging from 990 to 1140 °C, the grain size and precipitate diameter seem to be linear functions of the sintering temperature.

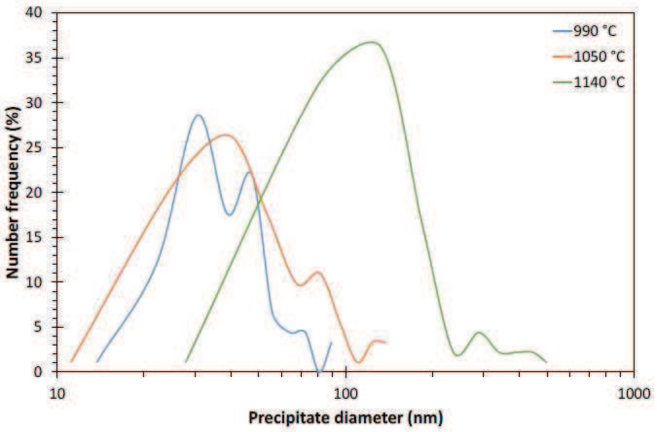

Figure III.12 : *Size distribution of the precipitates for different sintering temperature.*

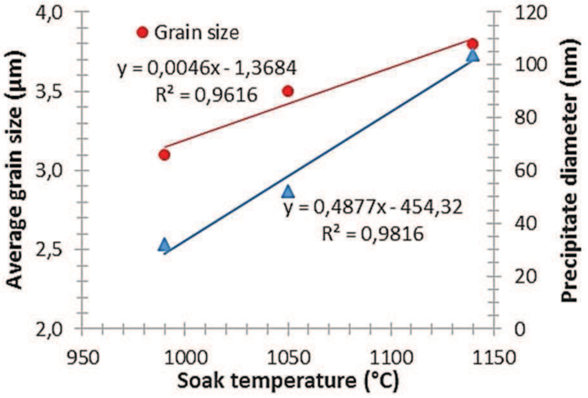

Figure III.13 : *Evolution of the grain and precipitate size depending on the soak temperature*

- EDS analyses.

EDS analyses have been completed on fresh fractures surfaces of the three sintered samples. In all cases, EDS maps of each constituting elements look similar. A typical example is shown in Figure III.14 for the sample sintered at 1140 °C. Ni and Sn repartitions seem quite homogeneous throughout the sample. On the contrary, Ti and Hf/Zr maps appear to behave complementary. As the larger grains are depleted in Ti, they seem enriched in Hf and Zr. This tendency is clearly imaged by the grain surrounded with white dots.

The global composition of the samples sintered at 990 °C, 1050 °C and 1140 °C were determined to be, respectively, $Zr_{0.23}Hf_{0.23}Ti_{0.56}Ni_{0.97}Sn_{1.01}$, $Zr_{0.26}Hf_{0.23}Ti_{0.56}Ni_{0.97}Sn_{0.98}$, and $Zr_{0.26}Hf_{0.23}Ti_{0.56}Ni_{0.97}Sn_{0.98}$. These composition values are in good agreement with the targeted one, proving that there is no significant loss of matter during the sintering step.

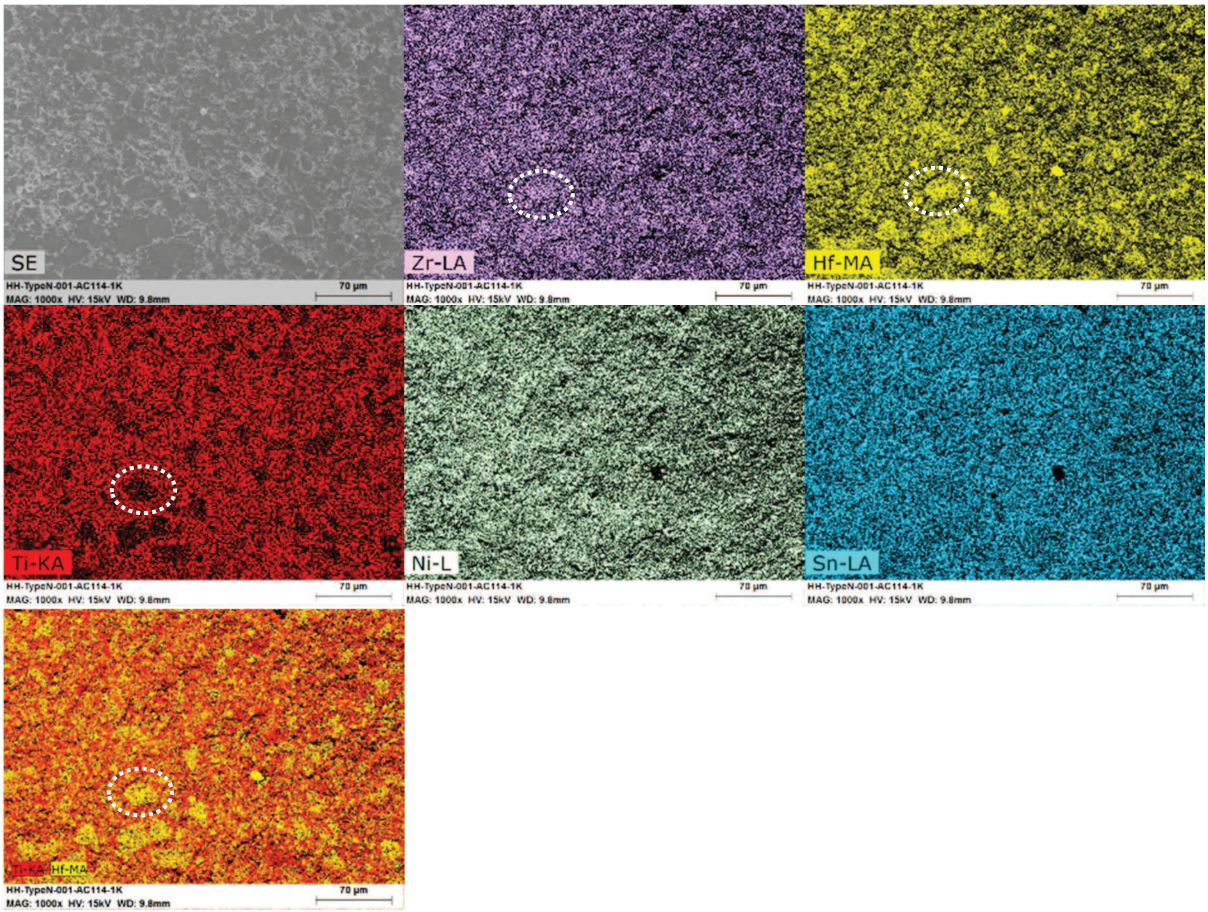

Figure III.14 : *EDS mapping of the sample sintered at 1140 °C.*

As before, only the EDS maps of each constituting element of the sample sintered at 1050 °C are now presented at a higher magnification in Figure III.15. As already observed at lower magnification in Figure III.14, it is confirmed that the biggest grains are depleted in Ti while enriched in Hf and Zr. Moreover, this tendency seems to be the opposite for smaller grains. Complementary investigations have shown that these two phases have the following compositions: $Zr_{0.3}Hf_{0.4}Ti_{0.3}Ni_{1.1}Sn_{0.9}$ and $Zr_{0.2}Hf_{0.1}Ti_{0.7}Ni_{1.0}Sn_{1.0}$.These results confirm what has been proposed for the XRD patterns interpretation before.

Another point to notice is the presence of bright narrow bands within the Sn map, suggesting slight Sn segregation at grain boundaries. Such a trend was also noticed by Downie and all. when investigating a $Ti_{0.5}Zr_{0.5}NiSn$ sintered polycrystalline material[16]. This phase most probably corresponds to Sn-β residues detected using XRD analysis.

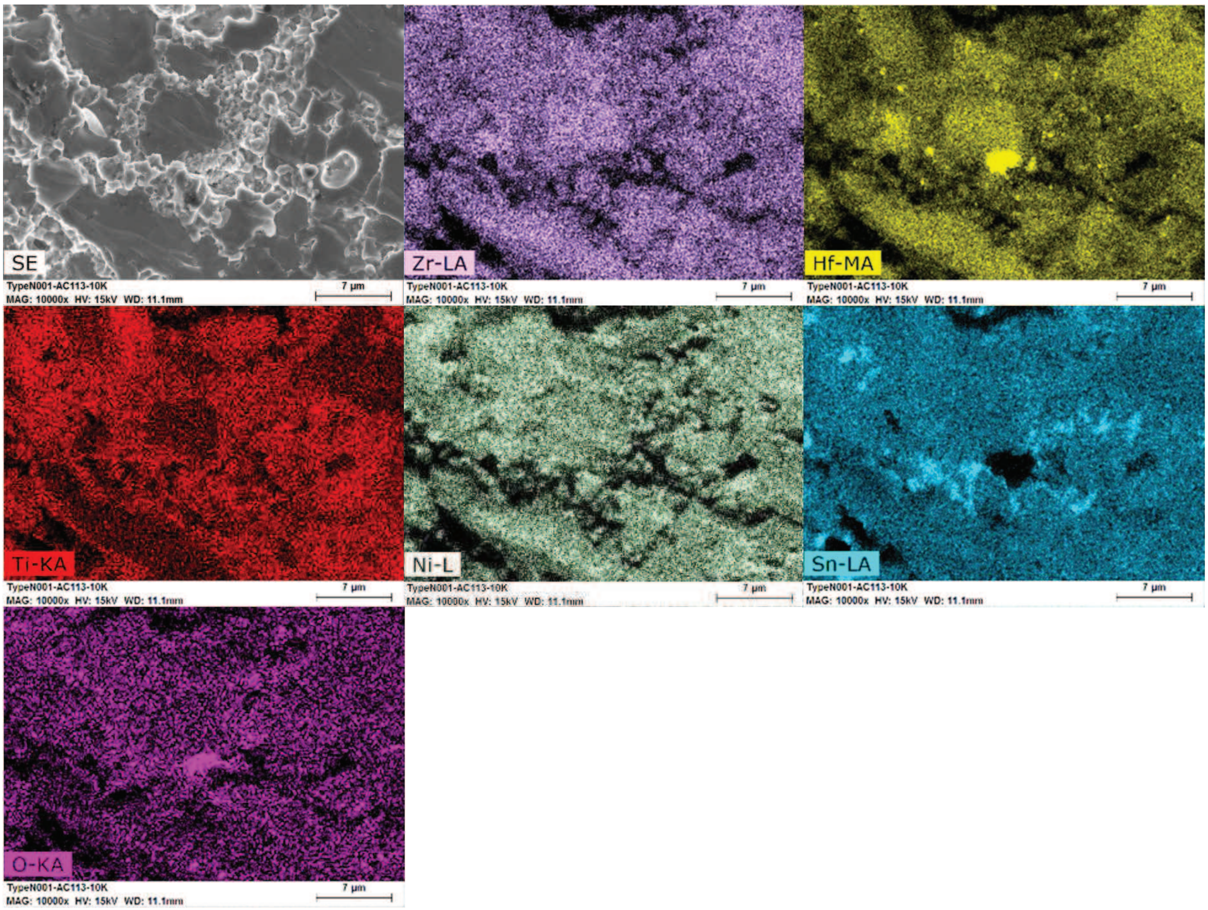

<u>Figure III.15 :</u> *EDS mapping of the sample sintered at 1140 °C.*

Finally, an EDS spectrum has been acquired from the matrix and a precipitate for the sample sintered at 990 °C (Figure III.16). Once again, the results are similar for the three samples.

It appears that the precipitates are enriched in Hf and O and impoverished in other elements when compared to the surrounding matrix. Accordingly, precipitates are made of a hafnium-based oxide, in agreement to the XRD analysis reported before.

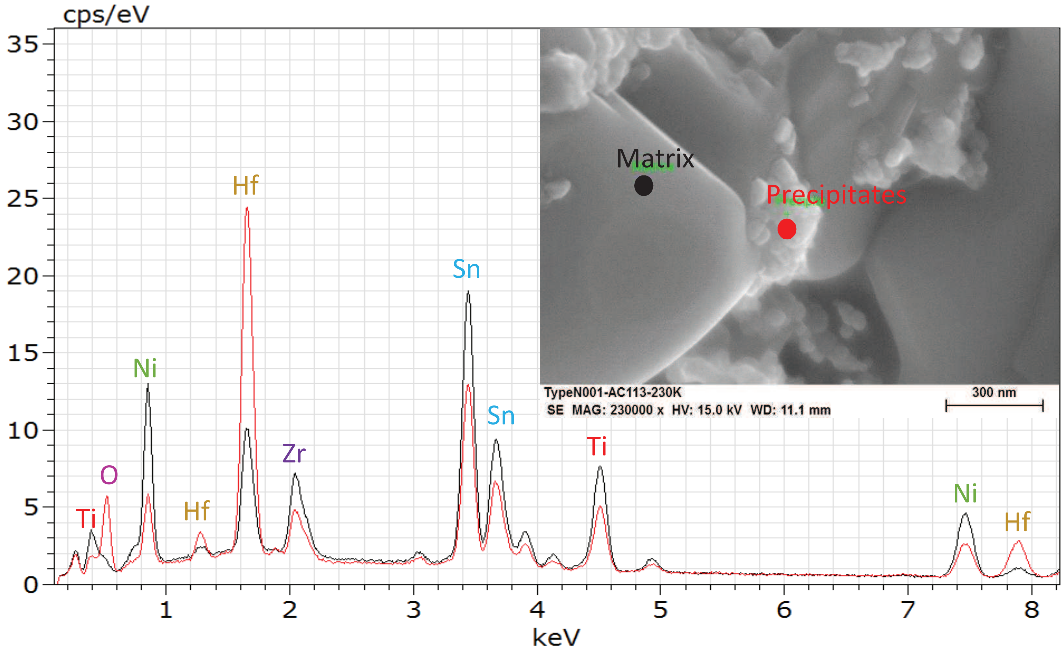

Figure III.16 : *EDS spectrum from the matrix and the precipitate of sample sintered at 1050 °C.*

II.2 - TEM observations

A thin foil of the sample sintered at 1140 °C was prepared using focus ion beam for further microstructure observations. The foil (confined to minimise contacts with air) was observed with the TEM/STEM apparatus presented in Chapter II.

Using the STEM/HAADF mode, two types of precipitates are observed in the sintered microstructure, as shown in Figure III.17. Numerous bright and dark nanometer-sized precipitates seem to be entrapped in individual grains constituting the sintered polycrystal. The dark ones are very numerous and about 10 nm diameter. EDS analysis were performed in STEM mode, with a probe size around 4 nm, on both type of precipitates and on the surrounding matrix.

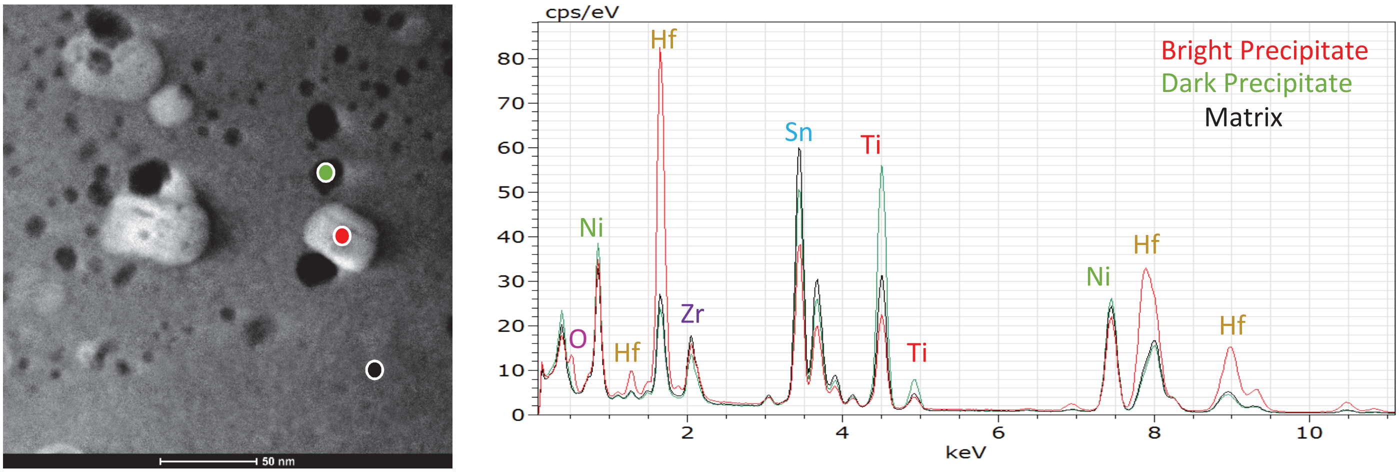

Figure III.17 : *STEM/HAADF spectrum from the matrix and the white and black precipitates of sample sintered at 1140 °C.*

As shown in Figure III.17, the bright precipitates are impoverished in Ti, Sn and enriched in Hf and O in comparison to the surrounding matrix. They are indeed the bright precipitates that were detected using SEM observations on fresh fracture surfaces taken from the sintered samples. The dark precipitates are enriched in Ti and slightly impoverished in Sn in comparison to the matrix. However, it has to be outlined that the thin foil thickness is around 100 nm. The dark precipitate average diameter being around 10 nm a contribution to the surrounding material to the EDS signal is not excluded. The main differences between the bright and dark precipitates are: a much higher Hf content for the bright ones, dark ones do not contain O element and dark ones are enriched in Ti in comparison to the bright ones. Precise determinations of the bright/dark precipitates and of the surrounding matrix compositions, using quantitative EDS analyses performed in STEM mode, are still to be done.

Figure III.18.a) and b) show images made with the HRTEM mode of a dark Ti enriched precipitate and a bright Hf oxide-based one, respectively. Lattice fringes can be seen in both kinds of precipitates attesting of the crystalline nature for both.

The Fast Fourier Transformation (FFT) of the selected areas of the HRTEM images are then calculated. The distance in the reciprocal lattice between the central spot and the first neighbour one is 3.545 nm^{-1} and 4.150 nm^{-1} for the dark and bright precipitates of interest, respectively. Then, the inter-plane distance in the direct lattice is calculated to be 2.821 Å and 2.410 Å for the dark and bright precipitates, respectively. Up to now no strict identification of the crystalline structure of the dark and bright precipitates have been established.

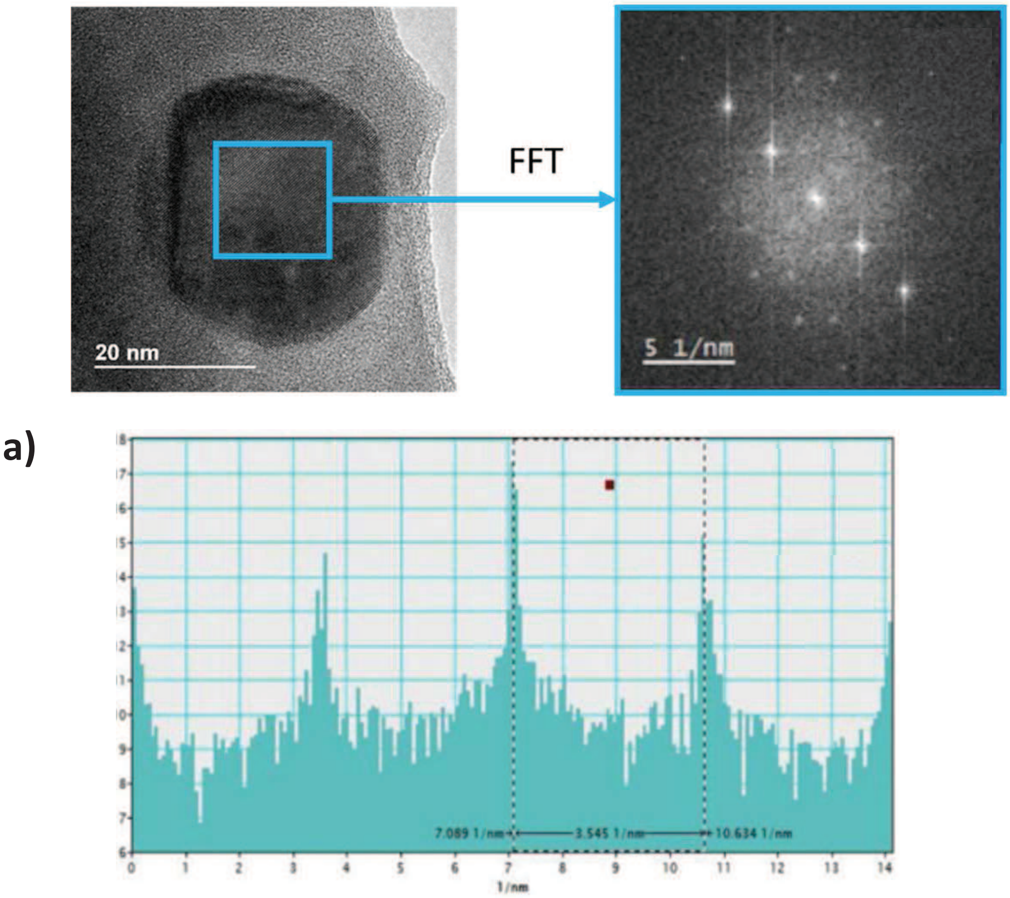

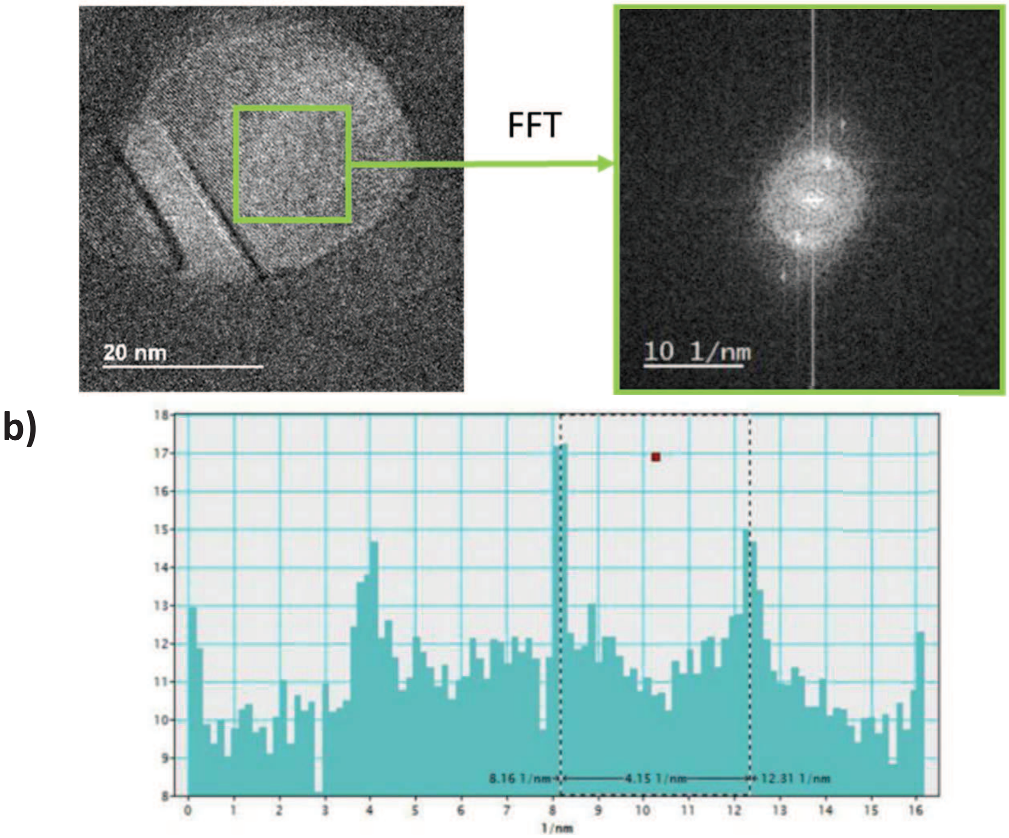

Figure III.18 : *STEM/HAADF image and FFT transformation of the a) Ti and b) Hf/O enriched particles analysed.*

To put it in a nutshell, the Hf oxide-based precipitates nature has not been determined precisely using HRTEM mode. Nevertheless, XRD pattern clearly highlights the presence of an HfO_2 phase. Currently, other HRTEM analysis are running. A possible explanation is that other elements from the matrix substitute to Hf in the HfO_2 formulation. For example, as Hf and Zr covalent radius is the same one, it is possible that a small substitution of Zr occurs in such precipitates. Therefore their composition could possibly be $Hf_{1-x}Zr_xO_2$ with $0>x>0.2$

III - Thermoelectric properties and relationship to the microstructure

As explained in Chapter II, each pellet is cut and polished in order to investigate the different thermoelectric properties in the temperature range going from 100 °C to 600 °C. Each contribution to the ZT value is compared to the data reported by Sakurada and all[1], Joshi and all[3] and Yu and all[4]. By using such comparisons, it is important to keep in mind that compositions and manufacturing processes were not the same as the one adopted during our investigations. To summarize, Joshi used ball-milling from an $Hf_{0.75}Zr_{0.25}NiSn_{0.99}Sb_{0.01}$ ingots to obtained nanopowders that were shaped and sintered using hot-pressing. Sakurada used the same process to manufacture a sintered sample of the $Zr_{0.25}Hf_{0.25}Ti_{0.5}NiSn_{0.994}Sb_{0.006}$ composition (the same as the one retained for our investigation). And finally, Yu used levitation melting and spark-plasma sintering to a manufacture $Hf_{0.6}Zr_{0.4}NiSn_{0.98}Sb_{0.02}$ dense samples.

Comparing our results to the ones previously published[1 3 4] is not an easy task because most authors did not perform careful microstructure investigations of the samples they characterized from a thermoelectric aspect.

II.1 - Electrical conductivity

The evolutions of the electrical conductivity in function of temperature of the as-sintered samples investigated are shown in Figure III.19. They are typical of degenerated semiconductors. Whatever the investigated temperature, the higher the sintering temperature, the higher the electrical conductivity. Thus, the best result is obtained for the pellet sintered at 1140 °C, with an electrical conductivity going from 180,000 S/m at 100 °C to 150,000 S/m at 600 °C. The obtained values are in good agreement with the literature, where our experimental results are parts of a global envelop delimited by the experimental values of Yu and Sarukada.

It is also interesting to notice that Joshi's material electrical conductivity values are quite close from the ones obtained in our work, even though he reported a sintered microstructure typical of a submicronic polycrystal. In our case, all the sintered samples exhibit a micronic average grain size, as shown in Table III.1.

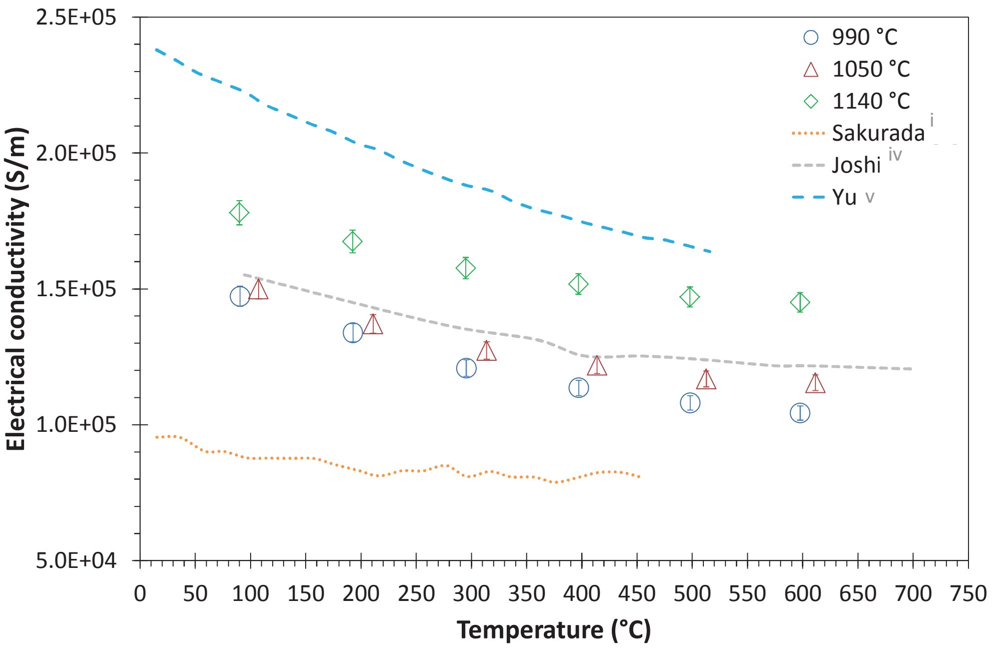

Figure III.19 : *Electrical conductivity of the as-sintered samples in function of the temperature*

Moreover, the evolutions of the electrical conductivity in function of temperature are in good agreement with experimental relative densities and grain sizes measured for the different sintered samples. Indeed, residual pores and grain boundaries are obstacles for main carriers' motion (trapping effect). Then a low residual porosity level and a high grain size are in favour of a high electrical conductivity, whereas a higher porosity level and small grain size will scatter electrons, whatever the temperature of interest.

II.2 - Seebeck coefficient

Figure III.20 shows that all the as-sintered samples investigated exhibit the desired N-type conduction with a negative Seebeck coefficient. With a Seebeck coefficient between –140 µV/°C and -185 µV/°C, on the temperature range going from 200 to 600 °C, the three samples investigated exhibit similar values than the ones reported by Joshi and Yu. However the Seebeck coefficient value reported by Sakurada is much better with a Seebeck coefficient mean value around -250 µV/°C from 20 to 450 °C. Up to now it was not possible for us to complete charge carrier concentration measurements. Such data could help to explain the differences between our values and the one reported by Sakurada.

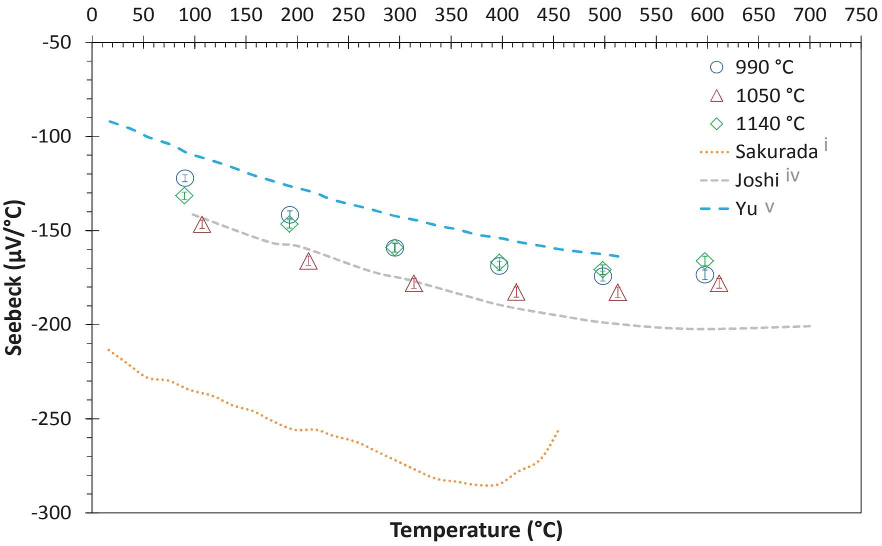

Figure III.20 : *Seebeck coefficient of the as-sintered samples in function of the temperature*

II.3 - Thermal conductivity

The evolution of the thermal conductivity in function of the temperature for the as-sintered samples investigated is reported in Figure III.21. First of all, it is interesting to notice than the samples sintered at 990 °C and 1050 °C exhibit a similar thermal conductivity value. These ones are quite close, even though slightly lower, than the one reported by Joshi, whatever the temperature of interest. However, the sample sintered at 1140 °C appears to have the lowest thermal conductivity of the three samples investigated, with a mean value around 3.6 W/mK. In the same temperature range, Sakurada's material possess a very low thermal conductivity, around 2.7 W/mK.

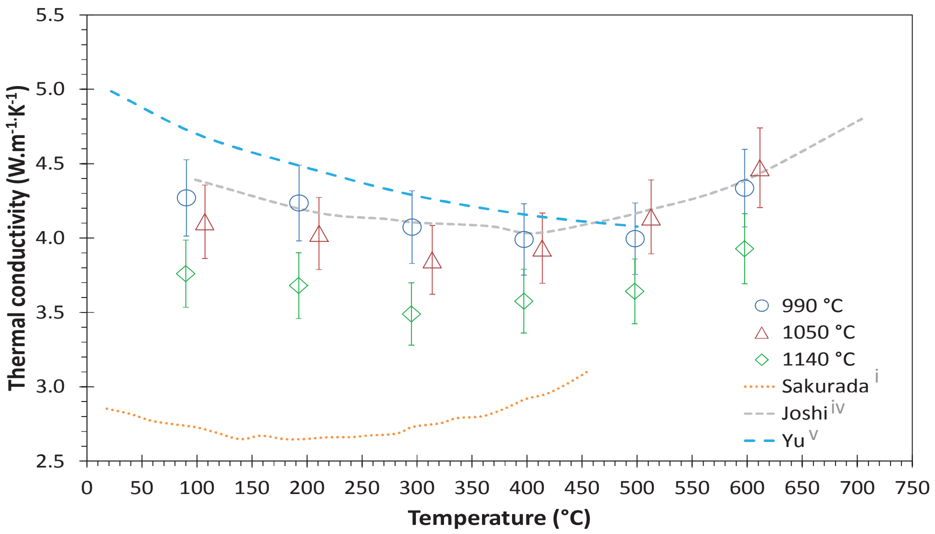

Figure III.21 : *Thermal conductivity of the as-sintered samples in function of the temperature*

For our investigated samples, the calculated Lorentz number is around 1.75x10^{-8} W.Ω.K^{-2}. Electronic and lattice thermal conductivity contributions are then calculated. These values are presented in Figure III.22. As expected, the electronic part is growing with the temperature, whereas the phonon part decreases when increasing the sintering temperature. Another point, is that the sample sintered at 1140 °C is the only one having the electronic part exceeding the lattice one above 400 °C.

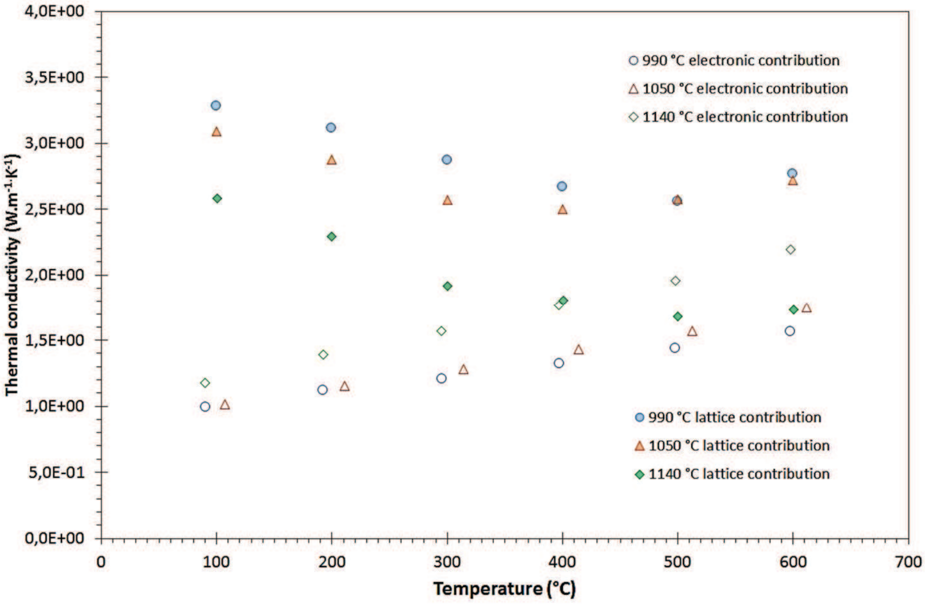

Figure III.22 : *Contribution of the electronic and thermal parts of the thermal conductivity of the as-sintered samples in function of the temperature*

The thermal conductivity of the investigated samples exposed in Figure III.21 is lower than the one reported from Joshi, whatever the temperature of interest, even though his material got a submicronic polycrystalline microstructure. Which means that another microstructural parameter than grain size is governing phonon scattering.

First, the high concentration of nanometer-sized hafnium-based oxide and Ti-rich precipitates dispersed in the sintered microstructures, is thought to perturb lattice vibrations, lowering the thermal diffusivity and so directly the thermal conductivity. This point is confirmed by looking at the lattice thermal conductivity in Figure III.22. Indeed, the one related to the sample sintered at 1140 °C is much lower than the ones for others samples, which signifies that microstructure directly impacts on the total thermal conductivity. Secondly, the phase separation detected using SEM and TEM observations promotes additional phonon scattering.

The electronic contribution to thermal conductivity is more important for the sample sintered at 1140 °C, than for the two other investigated samples. This trend is directly related to its higher electrical conductivity in all the temperature range of interest, as presented in Figure III.19.

For the investigated samples, if the electric conductivity is decreasing when increasing the temperature, the electronic contribution to the thermal conductivity is increasing in the same time (Figure III.19. and Figure III.22).

This trend is related to the fact that electronic thermal conductivity is also proportional to the temperature. Indeed, hot electrons from higher energy states carry more thermal energy than cold ones, while electrical conductivity is rather insensitive to the energy distribution of carriers. The amount of charge that electrons carry does not depend on their energy. This is the physical reason for the greater sensitivity of electronic thermal conductivity to the energy dependence of density of states and relaxation time.

It is also interesting to point out that the thermal conductivity of the different samples we investigated and also from the materials characterized in the literature, increases when the temperature becomes higher than a critical value (around 450 °C for the samples we investigated). This result is related to the addition of both lattice and electronic contributions to the thermal conductivity.

II.4 - ZT parameter

Finally, Figure III.23 represents the evolution of the ZT parameter in function the temperature for the different samples investigated. The best ZT value obtained is around 0.9 at 500 °C for the sample sintered at 1140 °C. This value is 15 % higher than the one obtained for the sample sintered at 990°C. In comparison to the literature, this maximum value is similar to the one reported by Joshi at the same temperature. At temperatures higher than 500 °C, the thermoelectric performance of our material starts to degrade slowly.

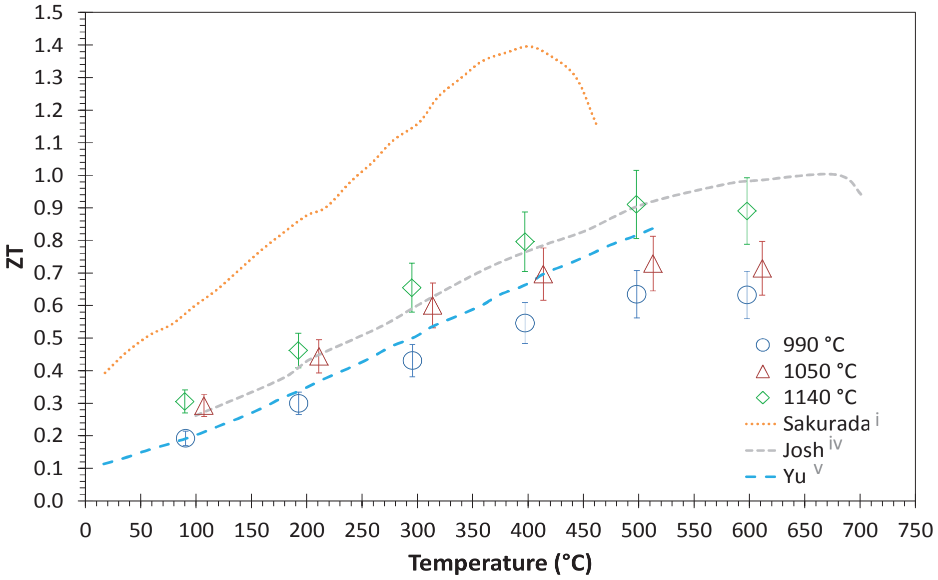

Figure III.23 : *ZT of the as-sintered samples in function of the temperature*

The excellent results reported by Sakurada are very different to the ones reported by us, Joshi and Yu. The material he investigated exhibits unconventional very low electrical and thermal conductivities and very high negative Seebeck coefficient values, whatever the temperature of interest. Sakurada did not complete a detailed microstructure investigation on the material he was focused on. Accordingly, from this point of view, it is not possible to compare his material to the one we investigated.

IV - Conclusion

In this section, n-type $Zr_{0.25}Hf_{0.25}Ti_{0.5}NiSn_{0.994}Sb_{0.006}$ dense polycrystalline pellets have been sintering by spark plasma sintering at different temperatures from a powder directly prepared by levitation melting from the raw elements. The microstructure and thermoelectric properties of the pellets have been deeply investigated and an optimum sintering temperature of 1140 °C was determined. For the three sintering temperature considered, the higher the sintering temperature, the lower the number of residual pores and the higher the grain size (going from 3 to 4 µm, depending on the sintering temperature). As residual pores and grain boundaries have act as obstacles for main carriers' motion they directly impact on the electrical conductivity of the considered material. Therefore a low residual porosity level and a high grain size are in favor of a high electrical conductivity, whereas higher porosity and small grain size will scatter electrons, whatever the temperature of interest.

SEM and TEM observations enabled to detect a phase separation in the half-Heusler sintered microstructure. Large grains constituting the polycrystal appear enriched in Hf and Zr, while, the smaller ones are enriched in Ti. Finally, whatever the sintering temperature, numerous tiny hafnium oxide-based precipitates mainly located at the grain boundaries are also detected. XRD analyses show that they are probably made of monoclinic HfO_2. Moreover, the higher the sintering temperature, the bigger the precipitates and the higher the HfO_2 phase concentration. These precipitates are thought to have a positive impact of thermoelectric properties by scattering lattice vibrations, leading to a dimensionless-thermoelectric figure of merit (ZT) around 0.9 at 500 °C for the sample sintered at 1140 °C.

---

[1] Sakurada, S.; Shutoh, N., Effect of Ti substitution on the thermoelectric properties of (Zr,Hf)NiSn half-Heusler compounds, Appl. Phys. Lett., 2005, 86, 2105

[2] Chen, S., Ren, Z., Recent progress of half-Heusler for moderate temperature thermoelectric applications, Maretials Today, 2013, 16, 10 387–395

[3] Joshi, G., Yan, X., Wang, H., Liu, W., Chen, G. and Ren, Z., Enhancement in Thermoelectric Figure-Of-Merit of an N-Type Half-Heusler Compound by the Nanocomposite Approach, Adv. Energy Mater., 2011, 1, 643–647.

[4] Yu C, Zhu TJ, Shi RZ, Zhang Y, Zhao XB, He J, High-performance half-Heusler thermoelectric materials $Hf_{1-x}Zr_xNiSn_{1-y}Sb_y$ prepared by levitation melting and spark plasma sintering, Acta Mater, 2009; 57:2757

[5] Schwall M., Blake B., Phase separation as a key to a thermoelectric high efficiency, Phys. Chem. Chem. Phys., 2013, 15, 1868

[6] JCPDS file 04-004-7747

[7] JCPDS file 03-065-2564

[8] Kurosaki, K.; Maekawa, T.; Muta, H.; Yamanaka, S. Effect of spark plasma sintering temperature on thermoelectric properties of (Ti,Zr,Hf)NiSn half-Heusler compounds. J. Alloy. Compd. 2005, 397, 296–299

[9] Favier K, Bernard-Granger G, Navone C, Soulier M, Boidot M, Leforestier J, Simon J, Tedenac J C, Ravot D, Influence of in situ formed $MoSi_2$ inclusions on the thermoelectrical properties of an N-type silicon–germanium alloy, Acta Mater, 2014; 64:429

[10] Bernard-Granger, G, Navone, C, Leforestier, J, Boidot, M, Romanjek, K, Carrete, J, Simon, J, Microstructure investigations and thermoelectrical properties of an N-type magnesium-silicon-tin alloy sintered from a gas-phase atomized powder, Acta Mater 2015; 96:437

[11] JCPDS file 00-023-1281

[12] JCPDS file 00-043-2564

[13] JCPDS file 04-002-1779

[14] R.D. Shannon, Acta Ctyst. A 32 (1976) 751.

[15] Gürth, M., Rogl, G., Romaka, V.V., Grytsiv, A., Bauer, E., Thermoelectric high ZT half-Heusler alloys Ti1−x−yZrxHfyNiSn ($0 \leq x \leq 1$; $0 \leq y \leq 1$) Acta Materialia; 2016, 104, 210-222

[16] Downie R. A., MacLaren D. A., Bos J.-W. G., Thermoelectric performance of multiphase XNiSn (X = Ti, Zr, Hf) half-Heusler alloys, Journal of materials chemistry A, 2014, 17

[17] Downie, R.A., Popuri, S.R., Ning, H., Reece, M.J.,Bos, J.W.G., Effect of spark plasma sintering on the structure and properties of Ti1-xZrxNiSn half-heusler alloys, Marerials, 2014, 7, 7093.

[18] JCPDS file 00-043-1017

[19] Bernard-Granger, G., Guizard, C., Addad, A., Influence of Co-Doping on the Sintering Path and on the Optical Properties of a Submicronic Alumina Material, Journal of the American Ceramic Society, 91, 5, 1703-1706

Chapter IV

Cost reduction and simplification of the manufacturing process for n-type half-Heusler based thermoelectric materials

One of the challenges for thermoelectric devices commercialisation, made from half-Heusler alloys, is the cost reduction and the simplification of the manufacturing process of the n and p-types legs.

Chapter IV explores the ways to reduce the price per kilogram of an n-type half-Heusler alloy, without introducing any detrimental effect on the thermoelectric properties. By using the link between the presence of oxide-based precipitates and good thermoelectric properties, in the 100 to 500 °C temperature range, for the n-type $Hf_{0.25}Zr_{0.25}Ti_{0.5}NiSb_{0.006}Sn_{0.994}$ composition investigated in Chapter III, two approaches have been retained.

The first one, consists of lowering as much as possible the metallic Hf content incorporated in the half-Heusler composition of interest. Indeed, Hf is much more expensive than other constituents and lowering its concentration is a key challenge[1, 2, 3]. Therefore, pellets of a composite material are elaborated, by mixing a hafnium free n-type $Zr_{0.5}Ti_{0.5}NiSb_{0.006}Sn_{0.994}$ powder with HfO_2 nano-particles. The second approach consists of simplifying the global manufacturing process, by doing some critical steps under ambient atmosphere (air) and not in inert glove boxes. The objective is to promote the formation of in-situ oxide-based precipitates in the sintered pellet to decrease the thermal conductivity, while simplifying strongly the handling operations.

In order to simplify the notations in the following serctions, the n-type $Hf_{0.25}Zr_{0.25}Ti_{0.5}NiSb_{0.006}Sn_{0.994}$ composition synthetized under argon atmosphere that was investigated in Chapter III will be referenced as “standard” composition. In the same way, the n-type $Zr_{0.5}Ti_{0.5}NiSb_{0.006}Sn_{0.994}$ composition will be referenced as “composite” composition, whereas HfO_2 is incorporated or not. Finally, the samples put in contact with ambient atmosphere during the manufacturing process will be refers as “oxidized”

I - Reduction of the metallic Hf content – Incorporation of HfO_2 nanoparticles

With a price around 160 €/kg[4], Hf is much more expensive than other elements present in the $Hf_{0.25}Zr_{0.25}Ti_{0.5}NiSb_{0.006}Sn_{0.994}$ formulation. A straightforward calculation shows that it represents about 72% of the price for one kilogram of raw material, see Figure IV.1. Based on this fact, lowering as much as possible the Hf content is becoming an important challenge for half-Heusler materials[1,2,3].

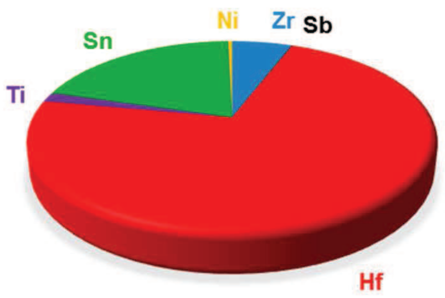

Figure IV.1 : *Contribution of each constituent on the* $Hf_{0.25}Zr_{0.25}Ti_{0.5}NiSb_{0.006}Sn_{0.994}$ *composition cost.*

In the first chapter, we recalled that an Hf substitution on the M site of the MNiSn or MCoSb half-Heulser compositions, resulted in a thermal conductivity reduction. The formation of hafnium oxide-based precipitates, dispersed in the matrix of the $Hf_{0.25}Zr_{0.25}Ti_{0.5}NiSb_{0.006}Sn_{0.994}$ half-Heusler composition, has been shown in Chapter III to decrease the lattice contribution of the thermal conductivity. Both considerations are then thought to be essential in order to keep good thermoelectric properties.

Hf and Zr have the same covalent radius (about 175 pm). Thus, it is reasonable to postulate that replacing Hf by Zr in the investigated half-Heusler composition will still lead to a similar substitution effect. That is why, we have chosen to compensate the Hf suppression by an increase of the Zr content in order to keep the half-Heusler stoichiometry. Secondly, in order to keep the benefits linked to the formation of HfO_2 precipitates, observed in Chapter III, we propose to directly add some HfO_2 nanoparticles in an n-type Hf-free $Zr_{0.5}Ti_{0.5}NiSb_{0.006}Sn_{0.994}$ matrix. Other authors in the literature have already tried to add oxide-based particles to a half-heusler powder in order to improve the sintered material thermoelectric properties. For example, Huang and all. incorporated ZrO_2[5] or Al_2O_3[6] nanoparticles to a ZrNiSn powder. They observed a 25 % increase of the ZT parameter attributed to a strong decrease of the thermal conductivity related to the presence of the oxide nanoparticles.

I.1 - Analysis of the manufacturing steps

A $Zr_{0.5}Ti_{0.5}NiSb_{0.006}Sn_{0.994}$ ingot is synthetized by levitation melting under argon atmosphere. Afterward, the ingot is ball milled under argon and the powder is rubbed through a 56 µm sieve, as explained in Chapter II. For the ingot and the collected grinded powder, the same trends as the ones reported for the "standard" composition are observed.

a. Addition of the HfO_2 powder

The $Zr_{0.5}Ti_{0.5}NiSb_{0.006}Sn_{0.994}$ powder is milled into a 50 ml tungsten carbide jar (5 and 10 mm tungsten carbide balls), filled under argon atmosphere, with 0, 1, 1.5 or 2 %wt of HfO_2 particles (Sigma Aldrich, Lyon, France, 99.95% purity) during 1 h at 250 rpm, with a planetary ball mill.

As shown using SEM observations in Figure IV.2, the HfO_2 powder is made of elemental crystallites agglomerated, having a polygonal shape and a diameter around 100 nm. Laser diffraction analysis, reported in Figure IV.3, confirms the agglomeration of the particles. Indeed, almost no individual 100 nm diameter particles are detected. Two sizes of agglomerates are measured: one centred around 300 nm and the other one around 5 µm.

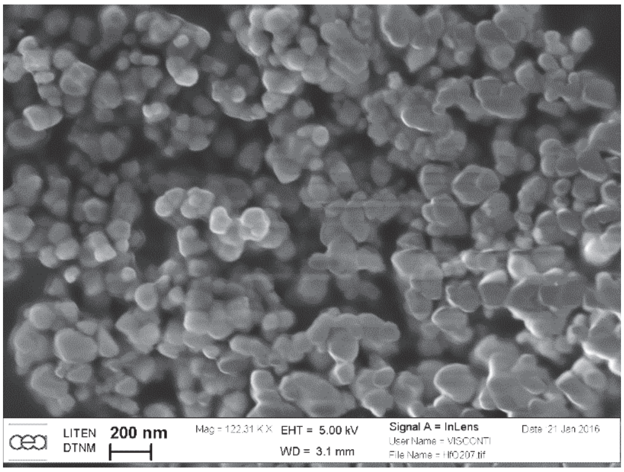

Figure IV.2 : *SEM images of the* HfO_2 *powder used*

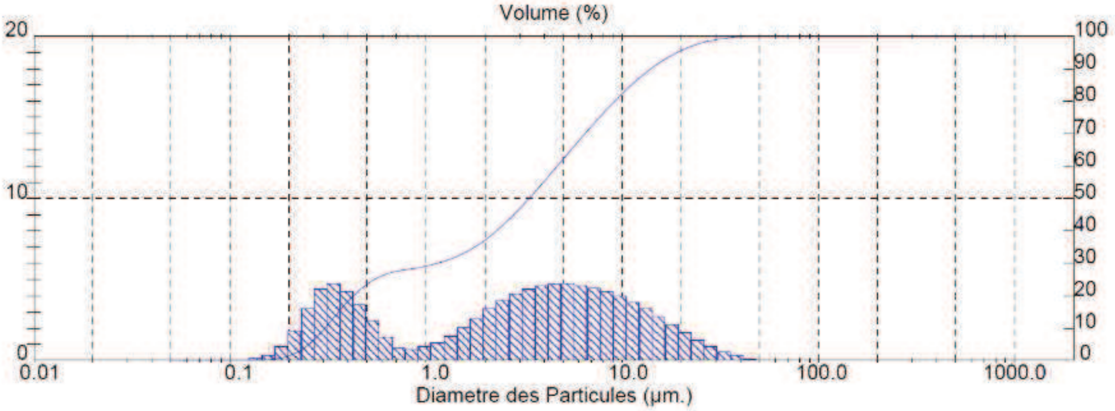

Figure IV.3 : *Particle size distribution of the commercial* HfO_2 *powder*

b. Determination of the sintering temperature

For the “standard” $Zr_{0.25}Hf_{0.25}Ti_{0.5}NiSn_{0.994}Sb_{0.006}$ composition, the optimum sintering temperature was determined to be 1140 °C. It corresponds to the temperature of the last plateau, just before the densification rate vanishes.

However, with the composition change, it is possible that the optimum sintering temperature shifts to a different value. To address this point, a SPS run was completed with the $Zr_{0.5}Ti_{0.5}NiSn_{0.994}Sb_{0.006}$ composition, from room temperature up to 1250 °C. The densification rate measured in function of temperature is presented in Figure IV.4. The curve still exhibits the standard bell-shape. However, it is shifted about 60 °C towards higher temperature values. Accordingly, the sintering temperature retained for sintering the “composite” formulation is 1200 °C, whatever the amount of HfO_2 incorporated. All the others experimental sintering parameters are the same as the ones retained for the “standard” material, as exposed in Chapter II.

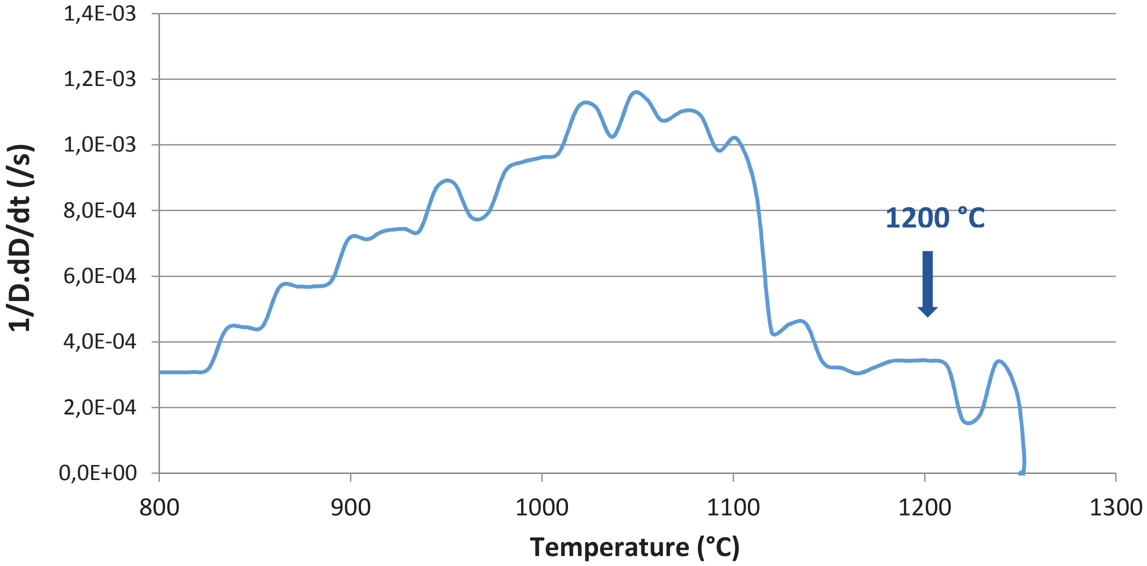

Figure IV.4 : *Densification rate of the* $Zr_{0.5}Ti_{0.5}NiSn_{0.994}Sb_{0.006}$ *material.*

I.2 - Thermoelectric properties

The thermoelectric properties of the four samples (containing 0, 1, 1.5 or 2 %wt of HfO_2 particles) are investigated in the temperature range going from 100 to 500 °C. In this section, the thermoelectric properties will be discussed and compared to the ones reported by Gürth and all. For a Hf-free coumpound[7]. It has to be noticed that Gürth introduced a small fraction of a secondary phase, named “DA” (for densification additives) in the n-type $Zr_{0.5}Ti_{0.5}NiSn_{0.98}Sb_{0.02}$ formulation he investigated.

Figure IV.5.a) shows the evolution of the electrical conductivity depending on the temperature. Except for the “DA” labeled composition from Gürth, all samples exhibit a behavior that is typical of degenerated semiconductors. All the investigated “composite” samples have very close electrical conductivity values, going from $1.5.10^5$ to $1.7.10^5$ S/m, whatever the temperature. Nonetheless, the sample incorporating 1.5 %wt of HfO_2 is slightly better than the other ones. The $Zr_{0.5}Ti_{0.5}NiSn_{0.98}Sb_{0.02}$ composition from Gürth without “DA” exhibits better electrical conductivities, in comparison to the $Zr_{0.5}Ti_{0.5}NiSn_{0.994}Sb_{0.006}$ one, for all the temperature range. It is possibly due to the larger amount of Sb dopant he incorporated. Finally, the composite with “DA” from Gürth exhibits a drastically different behaviour: the electrical conductivity increase slightly with the increasing temperature, as for a non-doped semi-conductor.

The Seebeck values exposed in Figure IV.5.b) confirm the desired N type conduction, with electrons as charge carriers, with a negative Seebeck coefficient. Whatever the temperature, the Seebeck values are very close for all the "composite" samples. However, once again, Seebeck absolute coefficient values from Gürth samples are quite different. In comparison to our samples, he obtained very low values for the sample without "DA" and higher ones for the sample incorporating "DA".

Figure IV.5.c) shows the evolution of thermal conductivity in function of temperature. All the thermal conductivity values of the investigated "composites" are in the range of 3.5 ± 0.5 W/mK, whatever the temperature. Considering the samples with 0, 1 and 2 %wt of HfO_2, the higher the HfO_2 particles incorporated, the lower the thermal conductivity. This is probably due to the presence of the HfO_2 particles dispersed in the half-Heusler matrix. Indeed, as exposed before, oxide-based precipitates scatter lattice vibrations and therefore decrease the thermal conductivity. However, no clear explanation has been found to explain that the sample incorporating 1.5 %wt of HfO_2 has a lower thermal conductivity than the other ones. It is possible that an optimum concentration in HfO_2 particles incorporated exists. Up to now this point has not been addressed. For the four "composite" samples, the evolution of the thermal conductivity in function of the temperature is similar. First, the thermal conductivity decreases slowly with the temperature and then it starts going up again around 350 °C. This trend is in favor of a bipolar contribution. This tendency is not observed for Gürth's samples, where thermal conductivity continuously decreases with the temperature increase. The addition of "DA" drops the thermal conductivity of about 25 % for all temperatures of interest.

Finally, the evolution of the ZT parameter in function of temperature is reported in Figure IV.5.d). Whatever the temperature, the best ZT values are found for the sample containing 1.5 %wt of HfO_2. A maximum ZT around 1.0 is obtained at 500 °C. This result is probably due to more favourable values of electrical and thermal conductivities, despite a slightly lower absolute value of the Seebeck coefficient. For comparison, the sample that does not contain HfO_2 particles exhibits a ZT of 0.85 at 500 °C. Accordingly, 18 % increase of the ZT parameter is obtained by the incorporation of 1.5 %wt of HfO_2 nanoparticles.

The curve profile of the ZT obtained by Gürth are different from those related to the "composite" samples investigated. Indeed, in our samples the ZT parameter reaches a plateau value at a temperature around 400-500 °C, whereas, Gürth values continue to increase for these temperatures. This tendency is probably due to the continuous decrease of thermal conductivity values recorded for Gürth's samples.

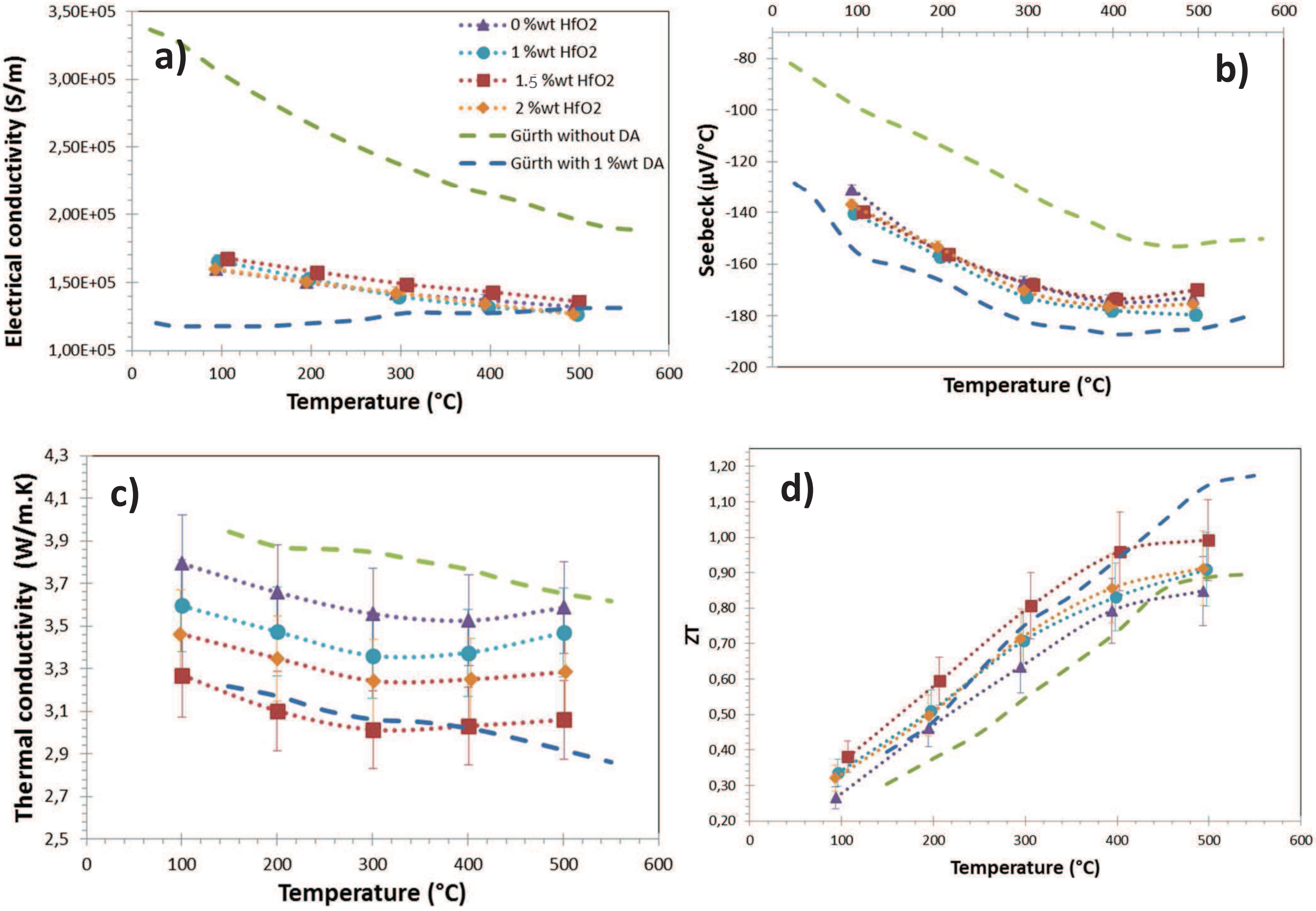

Figure IV.5 : *Thermoelectric properties in function of temperature for the as-sintered $Zr_{0.5}Ti_{0.5}NiSn_{0.994}Sb_{0.006}$ samples incorporating 0, 1, 1.5 and 2 %wt of HfO_2.*
a) Electrical conductivity; b) Seebeck coefficient; c) Thermal conductivity and d) ZT parameter.

I.3 - Microstructure analysis of the sintered pellets

Pellets of $Zr_{0.5}Ti_{0.5}NiSn_{0.994}Sb_{0.006}$ with 0, 1, 1.5 and 2 %wt of HfO_2 were synthetized and SEM observations have been completed for each sample. TEM investigations have been performed for the sample containing 1.5 %wt of HfO_2. All the samples exhibit a quite similar microstructure. Accordingly, the pictures of all the samples are not shown. The microstructure views presented in this chapter are typical of all the samples.

a. SEM observations and DRX analysis

- XRD analyses.

In the same way, only X-ray diffraction of the sample containing 1.5 %wt of HfO_2 is presented in Figure IV.6. For comparison, the XRD pattern of the "standard" sample is also recalled. Both diffractograms are similar. The different peaks are characteristic of the half-Heusler $C1_b$ structure (space group 216, F$\underline{4}$3m). For both samples, the same lattice parameter is calculated to be around 6.01 Å and left shoulders appear to be about the same width in both cases.

The Sn-β[8] peaks are still detected in the "composite" materials. When looking closer around the diffraction angles 28.5 and 31.7 °, it appears that peaks related to the monoclinic HfO_2[9] observed in the "standard" sample are slightly shifted towards lower diffraction angles. Therefore, the peaks of the "composite" sample match with a monoclinic ZrO_2[10] phase. Moreover, the ZrO_2 peaks appear to be more intense which indicate a higher amount of this phase in the material.

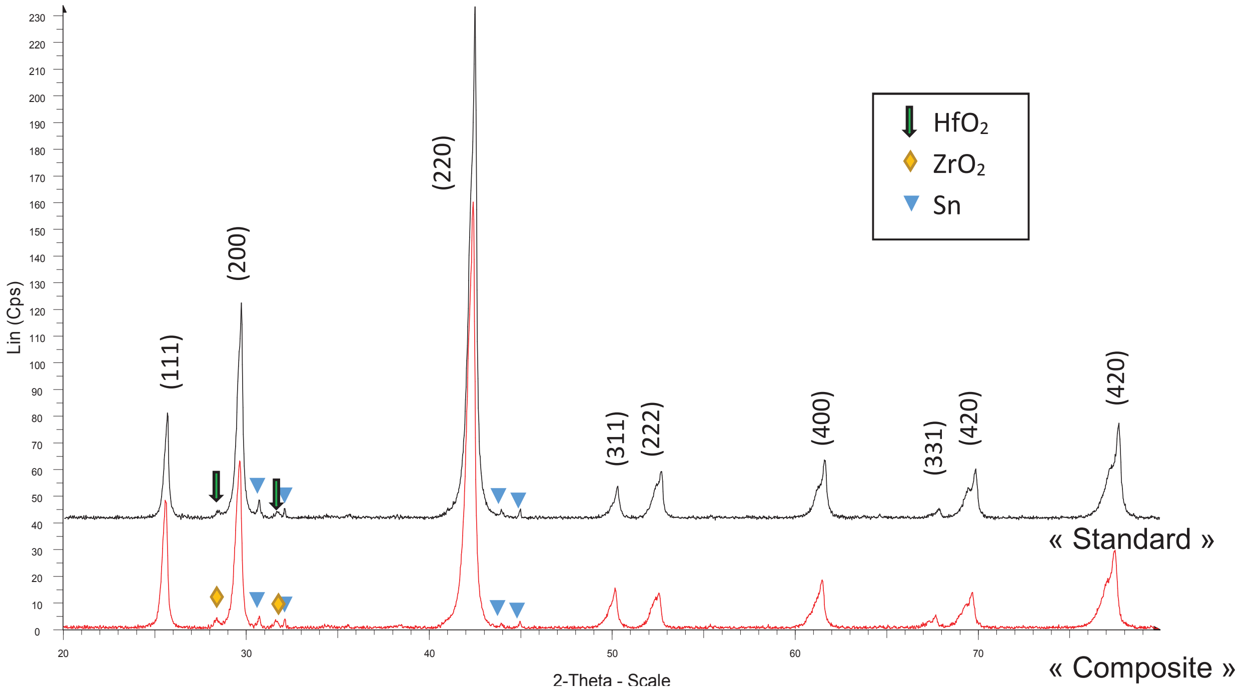

<u>Figure IV.6 :</u> *XRD patterns of the $Zr_{0.5}Ti_{0.5}NiSn_{0.994}Sb_{0.006}$ composition containing1.5 %wt of HfO_2 and the "standard" sampler sintered at 1140°C.*

- <u>SEM observations.</u>

A general view from a fracture surface of the $Zr_{0.5}Ti_{0.5}NiSn_{0.994}Sb_{0.006}$ matrix, without HfO_2 incorporation, is presented in Figure IV.7.a). The material appears to be densely packed as no porosity can be seen. This result is in good agreement with the relative density of the four sintered samples that was measured to be around 97 ± 1 %.

The matrix grain size is not uniform, it is composed of large grains, from 2 to 10 µm, and smaller ones, with a diameter below 1 µm. Indeed, complementary analyses have shown that the small and large grains are made of a half-Heusler phase. Nonetheless, as observed for the "standard" sample in Chapter III, the larger grains are enriched in Zr and depleted in Ti. This point will be confirmed using TEM observations latter.

In the samples where HfO_2 particles have been added, agglomerates (around 5 µm diameter) of smaller particles are observed, as highlighted with a blue ellipse in Figure IV.7.b).

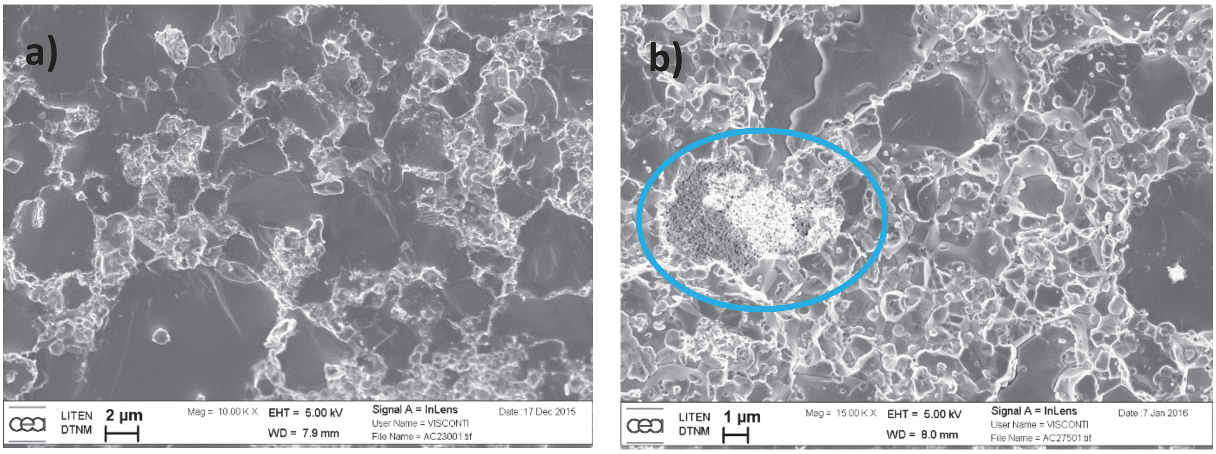

Figure IV.7 : *SEM images of the samples with a $Zr_{0.5}Ti_{0.5}NiSn_{0.994}Sb_{0.006}$ composition containing a) 0 %wt and b) 1.5 %wt of HfO_2.*

Higher magnification views of the "composite" sample containing 1.5 %wt oh HfO_2 are shown in Figure IV.8. Two different type of precipitates are detected in the material. The firsts ones, surrounded by blue circles, are the same as the ones forming agglomerates in Figure IV.7.b) and Figure IV.8.a). They have an elemental diameter around 100 nm and a polygonal shape. The second ones, surrounded by green circles, appear located at the matrix grain boundaries. They have a rounded shape and a diameter about 200 nm.

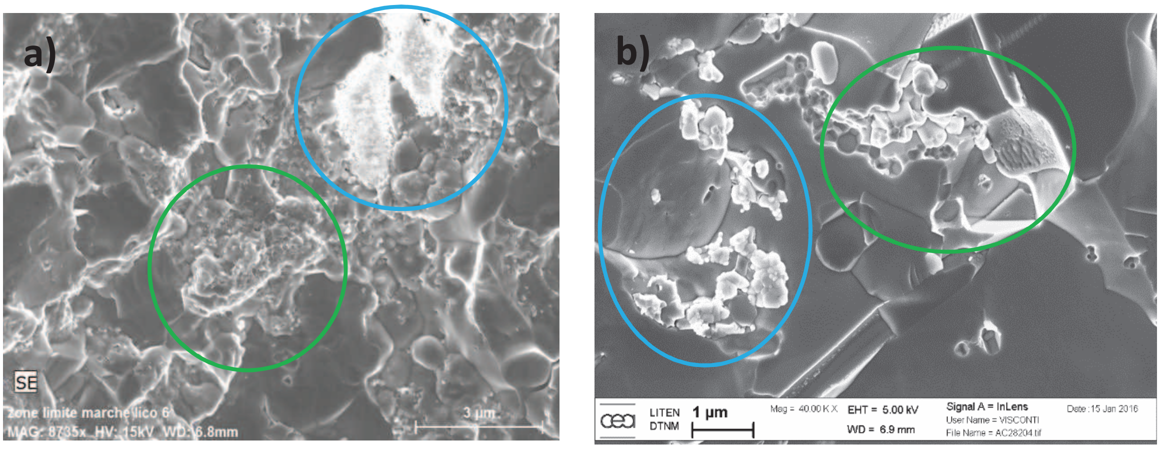

Figure IV.8 : *SEM images of the sample with a $Zr_{0.5}Ti_{0.5}NiSn_{0.994}Sb_{0.006}$ + 1.5 %wt HfO_2.*

EDS analyses have been completed in order to determine the chemical composition of both kinds of precipitates. Fresh fracture surfaces and the corresponding EDS maps of the "composite" samples, incorporating 0, 1.5 and 2 %wt HfO_2 are present in Figure IV.9.a), b) and c), respectively. For the three samples, numerous lenticular particles are detected, outlined by green ellipses. They have typically the same size than numerous craters that are also easily discernable throughout the samples. Accordingly, the craters probably form by lenticular particles pull-out during the generation of the fracture surface. From the EDS maps, it appears that these lenticular particles are made of Zr and O.

EDS maps acquired on the aggregates of very fine particles, highlighted with blue circles Figure IV.9. b) and c), show that they are made of Hf and O. They are indeed residual aggregates constituting the HfO_2 raw powder added when elaborating the “composite” formulation. Such relics prove that the approach used to manufacture the “composite” material is not optimal.

Additionally, very fine isolated particles, some examples being outlined by blue-dotted ellipses in Figure IV.9. b), are also detected. Some seem entrapped in the bulk of elemental grains, others seem to be located at the triple points and at grain boundaries. Such particles have typically the same dimension as the ones that are segregated in the micrometer-sized aggregates. Higher magnifications EDS mapping proved that the very fine isolated particles are made of Hf and O. They are most probably HfO_2 individual particles that were effectively separated from the aggregates constituting the HfO_2 raw powder added when elaborating the “composite” formulation.

Finally, it is interesting to point out that, without considering the different kind of precipitates, the distributions of Ti, Sn and Ni are similar and homogeneous in all the samples.

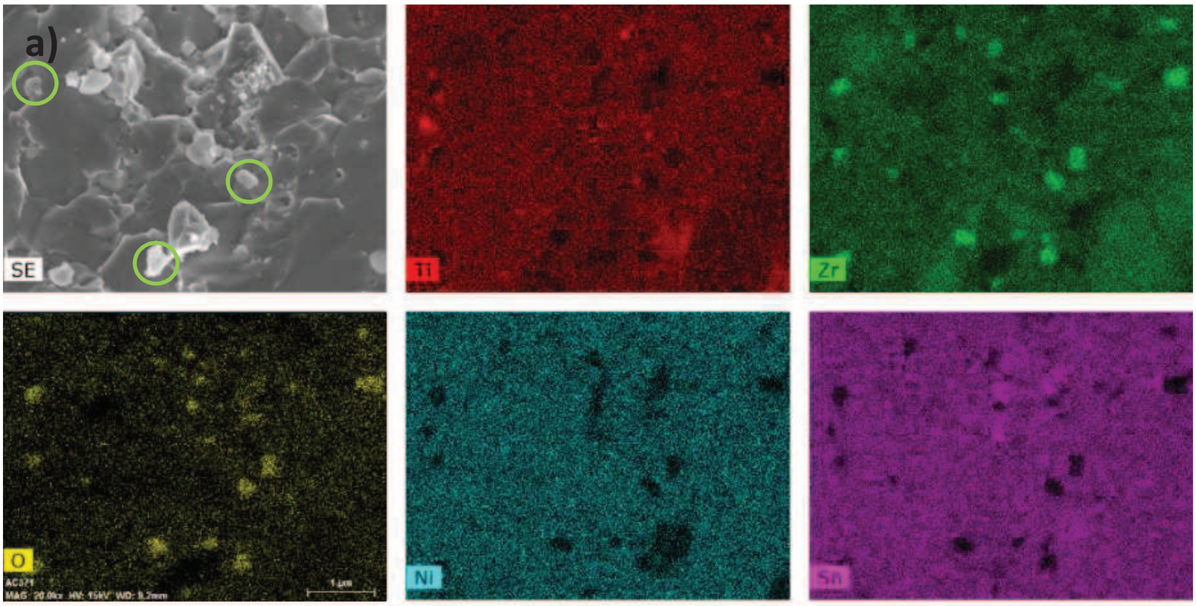

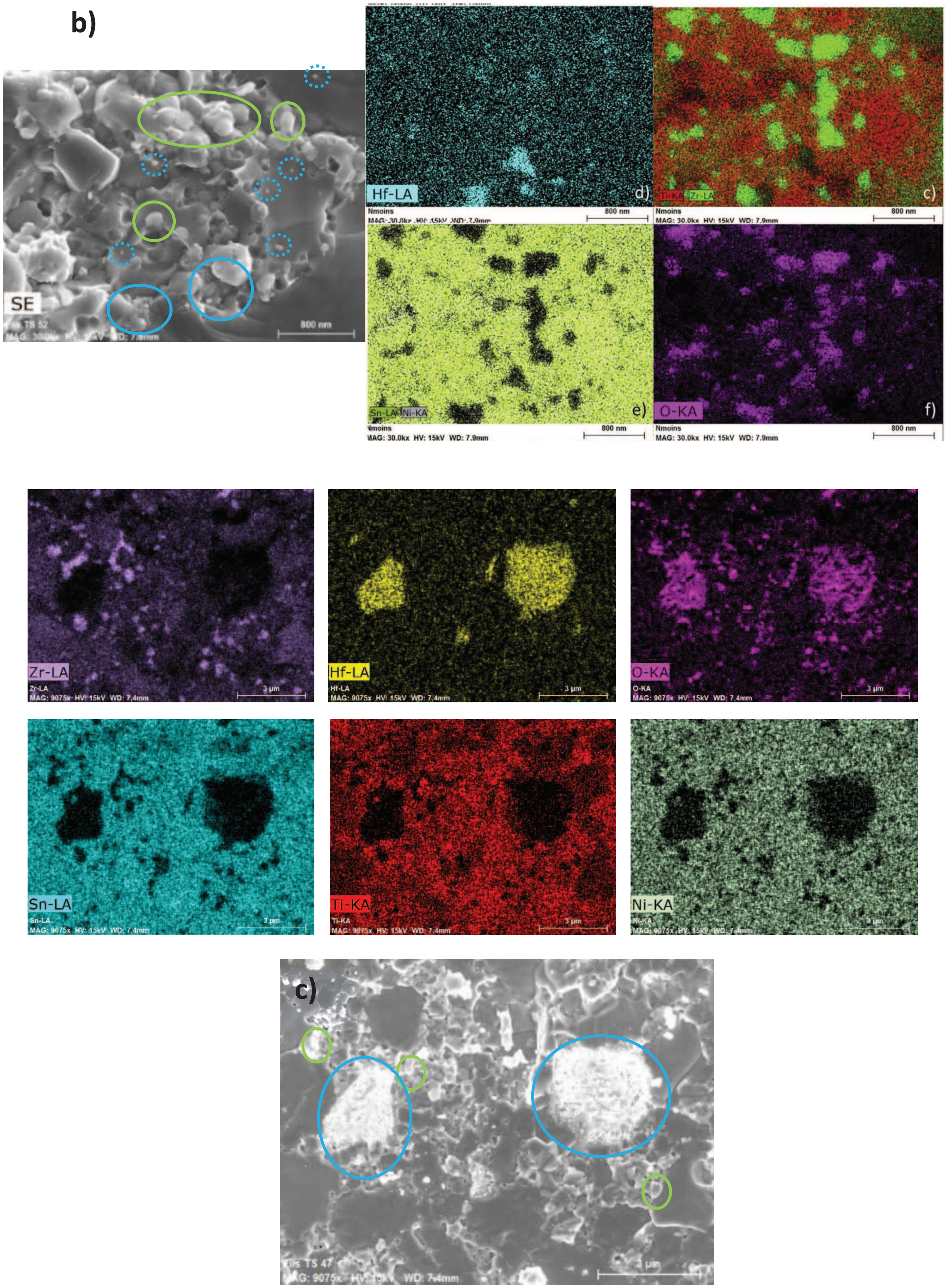

Figure IV.9 : *Element mapping of the samples with a $Zr_{0.5}Ti_{0.5}NiSn_{0.994}Sb_{0.006}$ composition containing a) 0 %wt, b) 1.5 %wt and c) 2 %wt of HfO_2,* The surface of each individual Zr oxide-based precipitate observed from a fracture surface of the sample containing 1.5 %w of HfO_2 is measured. A corresponding mean diameter is calculated to be around 340 nm (500 precipitates considered). Their size distribution is shown in Figure IV.10.

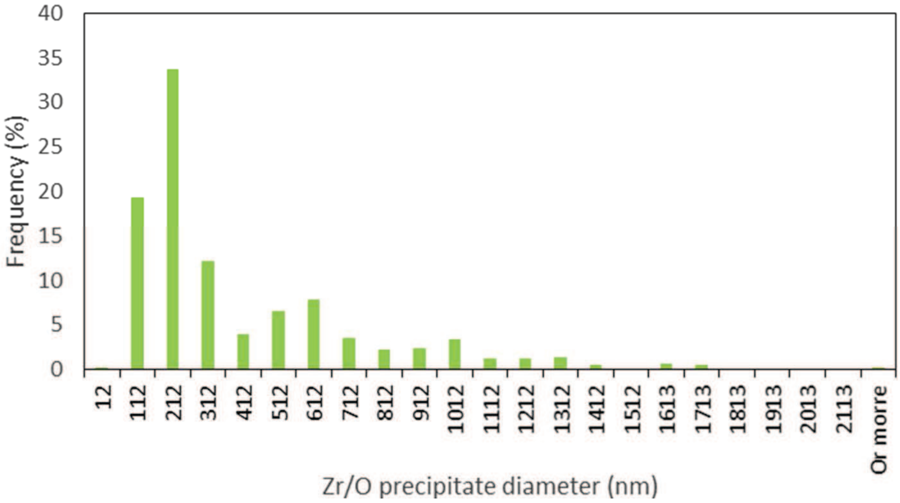

Figure IV.10 : *Zr/O precipitate size distribution in the* $Zr_{0.5}Ti_{0.5}NiSn_{0.994}Sb_{0.006}$ *with 1.5 %wt* HfO_2

b. TEM observations

A thin foil of the sample, having the composition $Zr_{0.5}Ti_{0.5}NiSb_{0.006}Sn_{0.994}$ + 1.5 %wt HfO_2, was observed by TEM. A general STEM/HAADF view and the associated elemental maps of Zr, Hf, Ti and O are presented in Figure IV.11. These images highlight the presence of two types of precipitates. Grey ones, as the one outlined by a green dotted circle, having a diameter going from 100 to 500 nm, are composed of Zr and O. They correspond to the lenticular precipitates detected using SEM and EDS examinations before. The other ones, brighter, are highlighted by blue arrows. They have a diameter about 100 nm and are composed of Hf and O. They are the isolated particles, probably made of HfO_2, that were also already observed by SEM. It is interesting to point out that this particles look imbricated in the Zr/O ones. Finally, as observed before, the biggest matrix grains appear to be enriched in Zr and depleted in Ti.

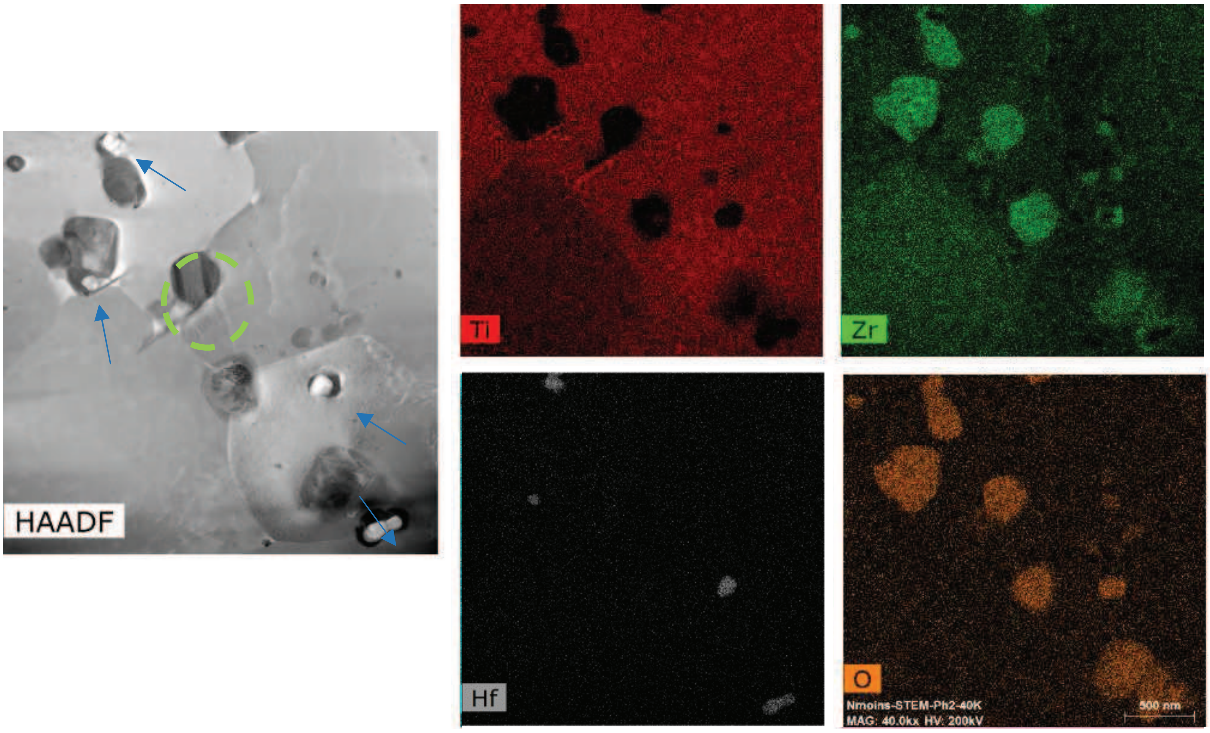

Figure IV.11 : *STEM/HAADF image of the* $Zr_{0.5}Ti_{0.5}NiSb_{0.006}Sn_{0.994}$ *+ 1.5 %wt* HfO_2 *sample with Ti, Zr, Hf and OEDS map*

A higher magnification STEM/HAADF view is shown in Figure IV.12.a). A third type of precipitate is detected. They have a dark contrast and a diameter ranging from 2 to 80 nm, such size explaining why they were not observed by SEM. They appear to be entrapped in individual grains constituting the sintered polycrystal. A Ti map, acquired on one of these dark precipitates, presented in Figure IV.12.b), shows that they are mostly constituted of Ti.

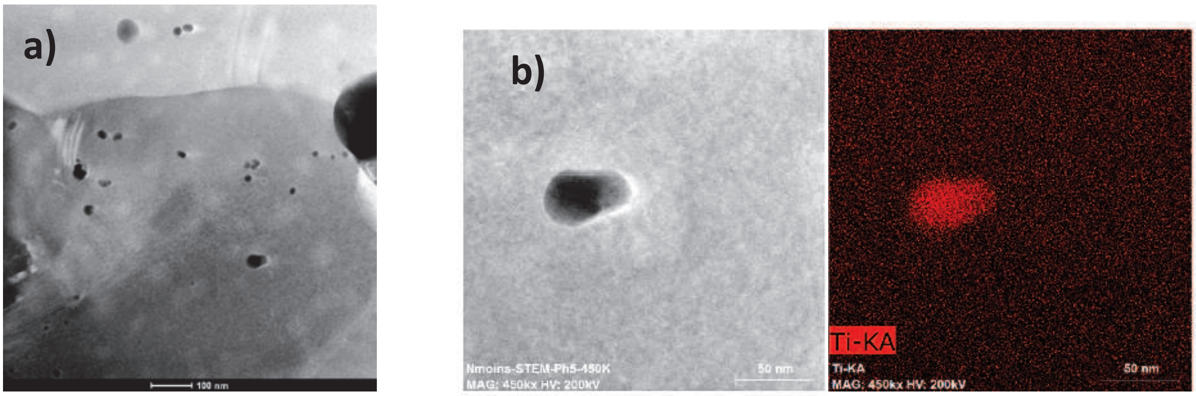

Figure IV.12 : *STEM/HAADF image of the a) fine dark precipitates and b) higher magnification view with Ti mapping of the* $Zr_{0.5}Ti_{0.5}NiSb_{0.006}Sn_{0.994}$ *+ 1.5 %wt* HfO_2 *sample General view with fine grey precipitates.*

Figure IV.13 shows a detailed STEM/HAADF view of grey and bright precipitates. In that case, it appears that the hafnium oxide-based precipitates are imbricated into the Zr/O enriched ones. Moreover, EDS spectra of the grey (A) and bright (B) precipitates with the corresponding quantitative analyses, with a foil thickness measured to be around 100 nm, are also presented. Accordingly it is concluded that the grey lenticular particles are mainly made of ZrO_2. A small amount of Hf is also detected. The Hf can come from a partial substitution of Zr by Hf. In the same way, the quantitative analysis confirm that the bright precipitates have the HfO_2 composition, with a small amount of Zr also detected. This is possibly due to a partial substitution of Hf by Zr or to a superposition with the ZrO_2 precipitates surrounding the HfO_2 one.

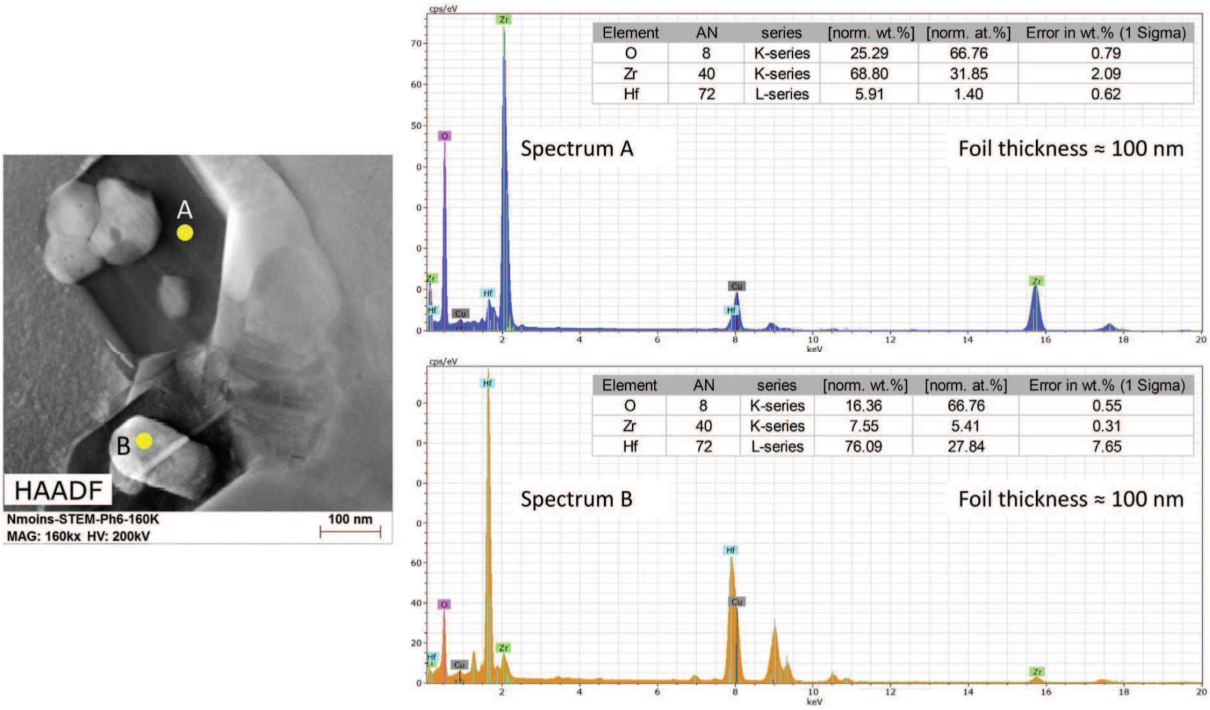

Element	AN	series	[norm. wt.%]	[norm. at.%]	Error in wt.% (1 Sigma)
O	8	K-series	25.29	66.76	0.79
Zr	40	K-series	68.80	31.85	2.09
Hf	72	L-series	5.91	1.40	0.62

Element	AN	series	[norm. wt.%]	[norm. at.%]	Error in wt.% (1 Sigma)
O	8	K-series	16.36	66.76	0.55
Zr	40	K-series	7.55	5.41	0.31
Hf	72	L-series	76.09	27.84	7.65

Figure IV.13 : *STEM/HAADF image of the* $Zr_{0.5}Ti_{0.5}NiSb_{0.006}Sn_{0.994}$ *+ 1.5 %wt* HfO_2 *sample with EDS spectra and quantitative analysis of the grey and white precipitates.*

To go further, HRTEM observations (Figure IV.14.a) have been completed on a typical lenticular grey particle constituted of Zr and O. A twin structure, as shown in Figure IV.14.b), is observed. It is characteristic of monoclinic ZrO_2[11]. Additionally, a Fast Fourier Transformation (FFT) of the selected zone of the HRTEM image was calculated. The distance in the reciprocal lattice between the central spot and the first neighbours, in the directions $\vec{a}, \overrightarrow{b}$ and $\vec{c}$, are 1.9598 nm^{-1}, 4.3860 nm^{-1} and 4.5940 nm^{-1}, respectively. Then, the inter-plane distances in the direct lattice are calculated to be 5.082, 2.308 and 2.177 Å. This indexation of the different spots and the angle values between the different directions confirm that the precipitate is made of the monoclinic zirconia specie[10].

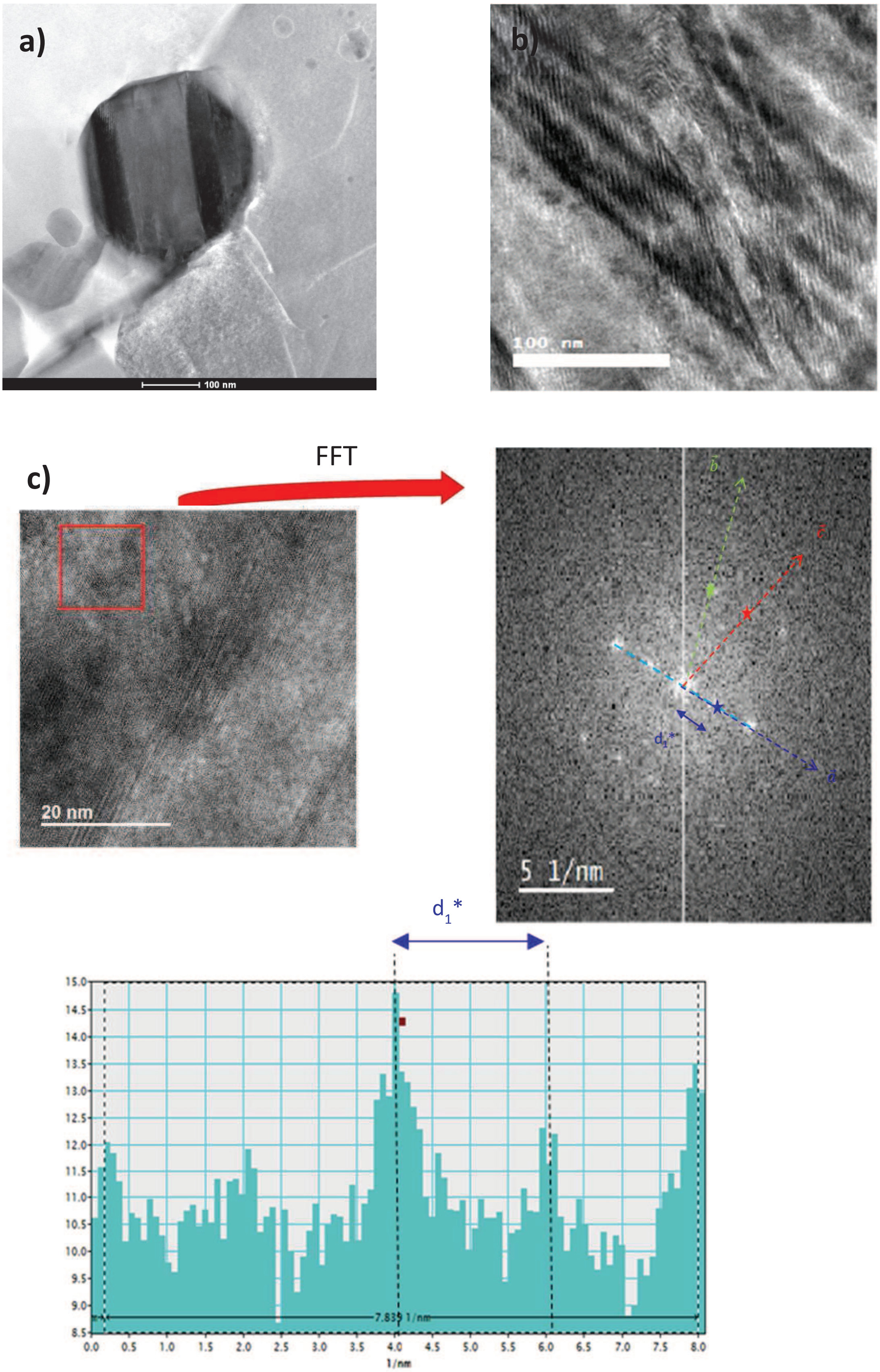

<u>Figure IV.14 :</u> a) STEM/HAADF image, b) characteristic twins, c) HRTEM and FFT transformation of the Zr/O particule analysed.

At this point, two complementary hypotheses may be advanced to explain the formation of numerous lenticular zirconia-based particles. To elaborate the investigated samples, the atomic content of suppressed Hf was compensated by increasing in the same proportion the Zr content. Moreover the formation of hafnium oxide-based precipitates in the “standard” $Zr_{0.25}Hf_{0.25}Ti_{0.5}NiSn_{0.994}Sb_{0.006}$ composition demonstrate the fact that oxygen is present in a significant amount throughout the microstructure and proves that the manufacturing process used is not preventing completely oxidation. Also oxygen is present in the powder before SPS, because of a partial oxidation that it was not possible to completely avoid with the manufacturing process adopted and also because of the addition of HfO_2 particles. The first hypothesis is that, during sintering, Zr from the matrix grains situated close to grain boundaries is pumped to react with the oxidation layer entrapped between the grains. This leads to the formation of zirconia precipitates. The second one is that Zr at the interfaces between the matrix grains and the HfO_2 precipitates pumps oxygen from the HfO_2 particles, added during the manufacturing process, and reacts with it to form ZrO_2 (the Gibbs energy of formation of ZrO_2 is lower than the one of HfO_2[12]).

I.4 - Microstructure and thermoelectric properties comparison for the “standard” and “composite” materials

The microstructure and thermoelectric properties of the sample having the composition $Zr_{0.5}Ti_{0.5}NiSn_{0.994}Sb_{0.006}$ + 1.5 %wt HfO_2 (“composite”), is compared to the $Zr_{0.25}Hf_{0.25}Ti_{0.5}NiSn_{0.994}Sb_{0.006}$ one (“standard”) sintered at 1140 °C, investigated in Chapter III.

a. Microstructure comparison

Both “standard” and “composite” samples investigated can be described as almost fully dense polycrystalline materials. In addition, different half-Heusler phases are observed in both materials. Indeed, the bigger grains are enriched in Zr (and Hf in the case of the $Hf_{0.25}Zr_{0.25}Ti_{0.5}NiSb_{0.006}Sn_{0.994}$ composition) and depleted in Ti, whereas the opposite is observed for smaller grains.

However, their average grain size is different. Indeed the “composite” average grain size is about 9 µm. This value is 130 % higher than the one obtained for the “standard” composition (around 4 µm). Moreover, as presented in Figure IV.15, the grain size distribution is larger for the “composite” material. The possible explanation to justify this trend is that the “composite” material is sintered at a higher temperature (1200 °C for the “composite” material vs. 1140 °C for the “standard” sample”), which promotes grain growth.

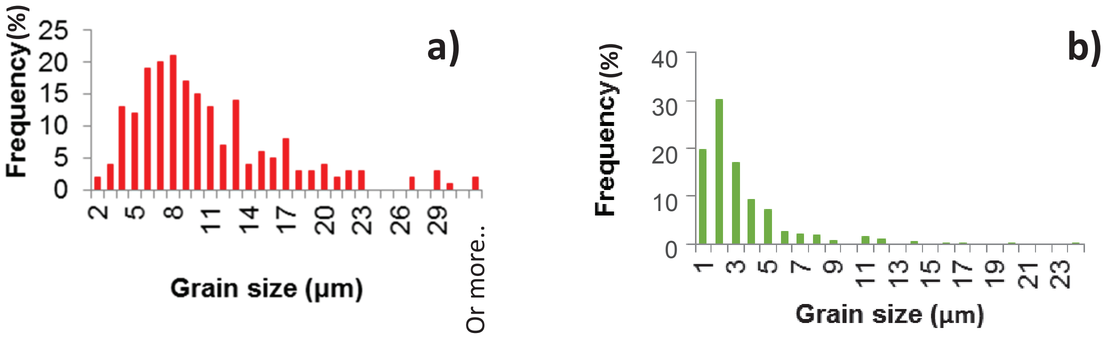

__Figure IV.15 :__ Grain size distribution of a) the $Zr_{0.5}Ti_{0.5}NiSb_{0.006}Sn_{0.994}$ + 1.5 %wt HfO_2 and b) the $Hf_{0.25}Zr_{0.25}Ti_{0.5}NiSb_{0.006}Sn_{0.994}$ samples

Another point to discuss is the presence of precipitates in both materials. Three types of precipitates are detected in the "composite" sample: numerous lenticular shaped particle made of monoclinic zirconia (averaged diameter around 340 nm), fine particles enriched in Ti (diameter in the range 2 to 80 nm) entrapped in the bulk of elemental grains and finally, the added HfO_2 particles (diameter around 100 nm) which are agglomerated or isolated (entrapped in individual grains or positioned at multiple grain junctions). In comparison, the "standard" sample investigated in Chapter III exhibits only two kinds of precipitates, both formed in-situ: HfO_2 ones (about 100 nm diameter) and Ti enriched ones (diameter around 10 nm) entrapped in the individual grains.

All the results are summarised in Table IV.1 and compared to the "standard" sample.

Material composition	**Soak temperature**	**Relative sintered density**	**Average grain size**	**Precipitates**	
				Enriched in	Average diameter (nm)
$Zr_{0.25}Hf_{0.25}Ti_{0.5}NiSn_{0.994}Sb_{0.006}$	1140 °C	98 %	3.8 µm	HfO_2	104
				Ti	5-20
$Zr_{0.5}Ti_{0.5}NiSn_{0.994}Sb_{0.006}$ + 1.5 %wt HfO_2	1200 °C	98 %	9 µm	ZrO_2	340
				Ti	2-80
				HfO_2	100

__Table IV.1 :__ Soak temperature, density, average grain size and precipitate nature and diameter of the as-sintered $Zr_{0.5}Ti_{0.5}NiSn_{0.994}Sb_{0.006}$ with 1.5 %wt of HfO_2 and the "standard" $Zr_{0.25}Hf_{0.25}Ti_{0.5}NiSn_{0.994}Sb_{0.006}$ samples

b. Thermoelectric properties comparison

The thermoelectric properties of the $Zr_{0.5}Ti_{0.5}NiSn_{0.994}Sb_{0.006}$ + 1.5 %wt HfO_2 sample is compared to the "standard" $Zr_{0.25}Hf_{0.25}Ti_{0.5}NiSn_{0.994}Sb_{0.006}$ one sintered at 1140 °C, in the 100 to 500 °C temperature range. Results are presented in Figure IV.16.

As shown in Figure IV.16.a), whatever the temperature, the $Zr_{0.5}Ti_{0.5}NiSn_{0.994}Sb_{0.006}$ + 1.5 %wt HfO_2 material has the lowest electrical conductivity, despite a significant higher grain size. Indeed, for a polycrystalline material, grain boundaries are potential obstacles to charge carriers motion. The lower the density of grain boundaries, the higher the electrical conductivity should be. This trend is possibly linked to the presence of numerous zirconia lenticular particles dispersed throughout the microstructure, zirconia being well known to be an insulating material at low temperatures. These numerous lenticular particles have an average diameter around 340 nm, they can possibly promote electron scattering more efficiently than the smaller precipitates present in the "standard" material.

The absolute values of the Seebeck coefficient, in Figure IV.16.b), show that both samples exhibit the desired N-type conduction. Even though the ones of the "composite" sample are slightly better, Seebeck coefficient values are very close from one sample to the other one. These values are probably close due to the fact that Sb doping on the Z site of the half-Heusler structure is the same for both compositions.

Figure IV.16.c) presents the evolution of the thermal conductivity in function of temperature for both samples. Whatever the temperature, the "composite" sample exhibits a significantly lower thermal conductivity than the "standard" one, despite a much higher grain size. The three kinds of precipitates detected in the sintered microstructure of the "composite" sample are thought to be more effective to scatter lattice vibrations than the two sorts of precipitates detected in the microstructure of the "standard" sample. Moreover, it has been shown by XRD analyses, that the ZrO_2 amount in the "composite" sample is higher than the HfO_2 of the "standard" one, decreasing even more the phonon mean free path.

Lastly, the evolution of the ZT parameter in function of temperature is shown in Figure IV.16.d) for both samples. A maximum ZT around 1.0 at 500 °C is obtained for the "composite" material, against 0.9 at the same temperature for the "standard" composition. Therefore an increase of 11 to 23 % of the ZT value is obtained in the 200 to 500 °C temperature range.

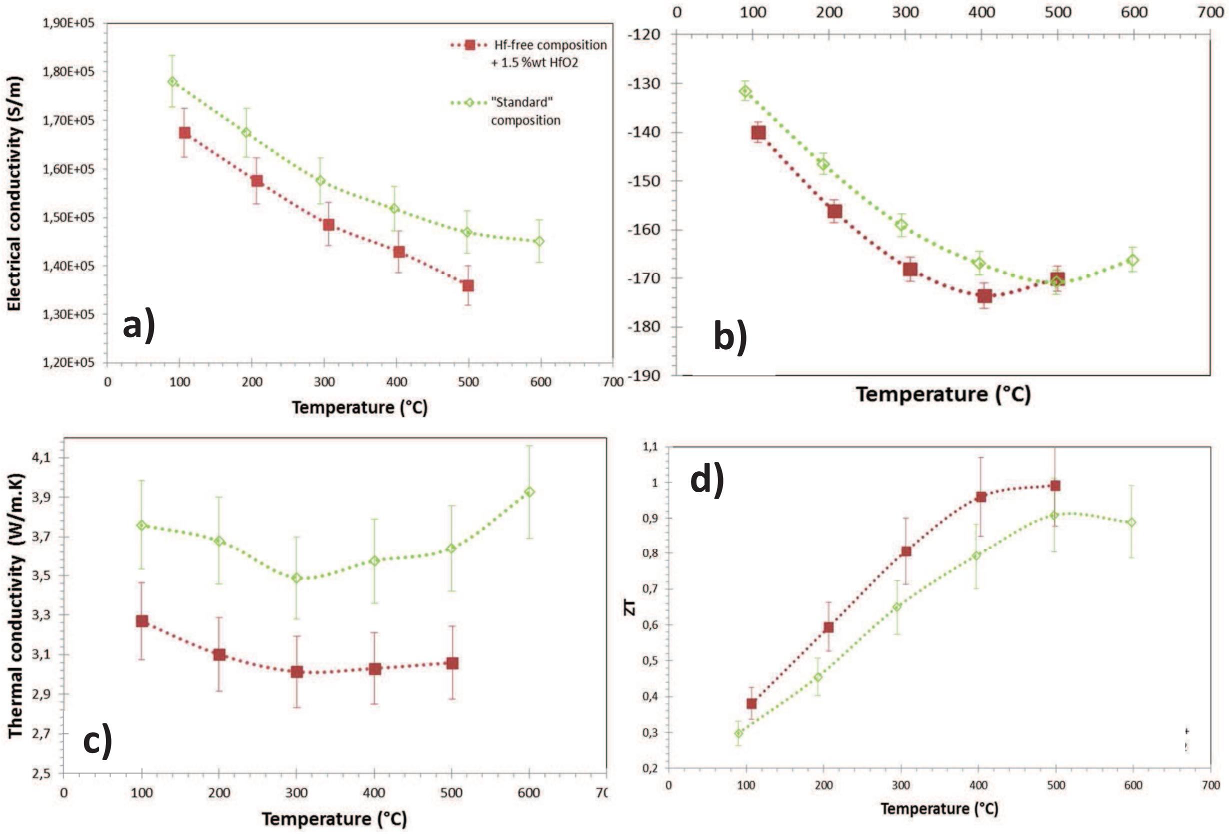

Figure IV.16 : *Thermoelectric properties in function of temperature for the as-sintered $Zr_{0.5}Ti_{0.5}NiSn_{0.994}Sb_{0.006}$ with 1.5 %wt of HfO_2 and the "standard" $Zr_{0.25}Hf_{0.25}Ti_{0.5}NiSn_{0.994}Sb_{0.006}$ samples.*
a) Electrical conductivity; b) Seebeck coefficient; c) Thermal conductivity; d) ZT parameter.

I.5 - Conclusion

In order to reduce the material cost, a $Zr_{0.5}Ti_{0.5}NiSn_{0.994}Sb_{0.006}$ composition incorporating HfO_2 nanoparticles has been investigated. A maximum ZT value around 1.0 was obtained at 500 °C for a material incorporating 1.5 %wt of HfO_2. It represents an increase of 11 to 23 % of the ZT value, in the 200 to 500 °C temperature range, compared to the $Hf_{0.25}Zr_{0.25}Ti_{0.5}NiSb_{0.006}Sn_{0.994}$ composition. Indeed, due to the addition of HfO_2 nanoparticles and also to the formation of ZrO_2 precipitates at the grain boundaries of the half-Heusler grains constituting the sintered polycrystal, thermal conductivity is reduced from 15 to 20%.

Such thermoelectric properties improvements are combined to a 50 to 60 % reduction of the cost per kilogram of material, as shown in Figure IV.17.

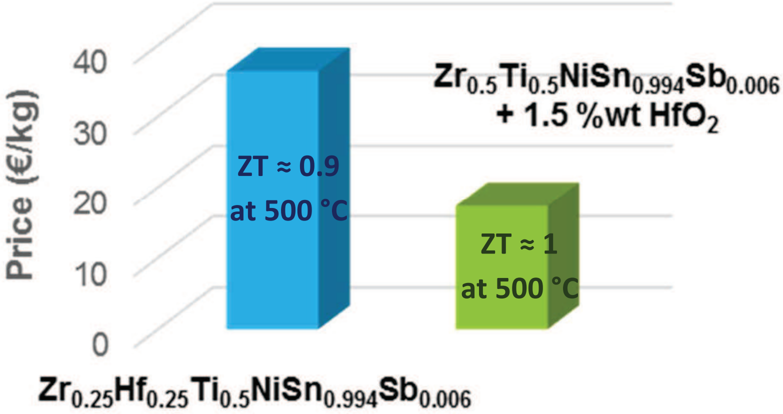

*<u>**Figure IV.17 :**</u> Price comparison between the* $Zr_{0.5}Ti_{0.5}NiSn_{0.994}Sb_{0.006}$ *with 1.5 %wt of* HfO_2 *and the "standard"* $Zr_{0.25}Hf_{0.25}Ti_{0.5}NiSn_{0.994}Sb_{0.006}$ *raw material compositions*

II - Synthesis of the half-Heusler powder under ambient atmosphere

Usually, oxygen is not desired when manufacturing half-Heusler (or whatever thermoelectric material) powders. Indeed, it has been shown in literature that oxidation is detrimental to the thermoelectric properties of a given material. That is why, all the powder manipulations between the different manufacturing steps (powder transfer into the grinding jar, loading into the sintering die…) and powder storage are done under reduced atmosphere, in most cases using glove boxes filled with argon.

As noticed in Chapter III and Section IV.I, oxide-based precipitates in the sintered material are scattering phonons, enabling low thermal conductivity values to be achieved and promoting the increase of the ZT parameter. For this reason, it is reasonable to postulate that a direct oxidation of the n-type $Hf_{0.25}Zr_{0.25}Ti_{0.5}NiSb_{0.006}Sn_{0.994}$ powder will lead to the formation of numerous in-situ oxide-based precipitates in the sintered material. Therefore, in comparison to a material elaborated from a non-oxidized powder, the thermal conductivity will be lower, while simplifying strongly the handling operations.

In this chapter, the half-Heusler powder is stored and ball-milled under ambient air. Then, pellets are sintered by SPS as explained in Chapter II. The effect of powder oxidation on the sintered pellet microstructure and thermoelectric properties will be discussed.

II.1 - Microstructure analysis of the “oxidized” sintered pellet

As for the “standard” material, an n-type $Hf_{0.25}Zr_{0.25}Ti_{0.5}NiSb_{0.006}Sn_{0.994}$ ingot is synthetized by levitation melting under argon atmosphere. Then the ingot is manually crushed and ball milled under ambient air. Then the powder is passed through a 56 µm sieve and sintered at 1140 °C under argon atmosphere, as for the “standard” sample (same heating rate, soak time and cooling rate).

Afterward, XRD, SEM and TEM observations have been completed. A detailed microstructure analysis of the “oxidized” sample and a comparison with the “standard” one are performed.

a. Analysis of the sintering curve

First of all, the height variation of the pellet during sintering is measured and the densification rate of the “oxidized” sample, depending on the temperature, is calculated. The results are reported in Figure V.18 and compared to the densification curve of the “standard” sample. In both cases, the standard bell-shape curve is observed. However, it appears that the maximum densification rate is shifted about 50 °C towards lower temperature values for the “oxidized” sample.

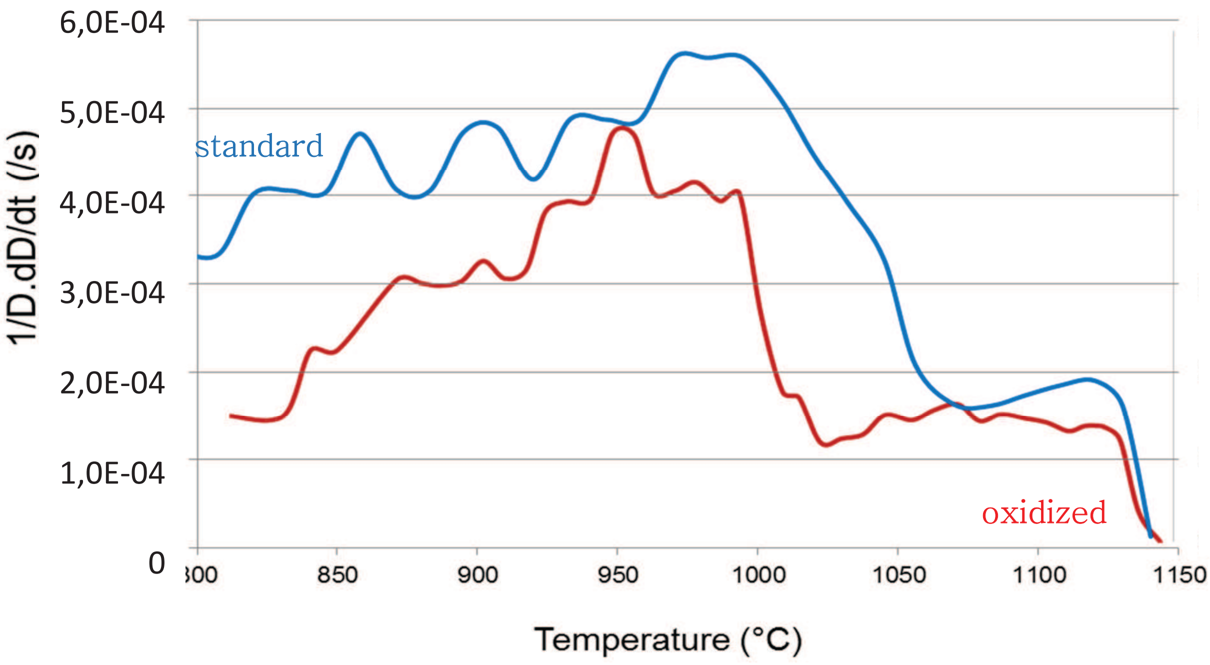

Figure V.18 : *Densification rate of the “oxidized” and “standard” materials.*

b. SEM observations and XRD analysis

- XRD analyses.

X-ray diffraction of the “oxidized” sintered samples has been completed, as shown in Figure IV.19. For comparison, the XRD pattern of the “standard” sample is also recalled. Both diffractograms are similar. The different peaks are characteristic of the half-Heusler C1$_b$ structure (space group 216, F$\underline{4}$3m).

For both samples, the same lattice parameter is calculated to be around 6.01 Å. However, left shoulders are less pronounced for the “oxidized” sintered sample. This probably means that the half-Heusler matrix grains are more homogeneous in composition. This trend is possibly linked to the shift of the densification rate in function of temperature, as exposed above. Indeed, it has been shown in Chapter III, that the higher the sintering temperature, the sharper the half-Heusler diffraction peaks. The “oxidized” material sinters globally at a lower temperature in comparison to the “standard” one. This means that for the same sintering temperature of 1140 °C, microstructure development is more advanced for the “oxidized” material, explaining the decrease of the left shoulders appearing on the diffractogram.

Additional peaks are also detected for both samples. As explained in Chapter III, the carbon peak detected for the “oxidized” sample is due to remaining graphite from the SPS sintering process. Sn-β[13] diffraction peaks are no longer observed for the “oxidized” sample. However, it doesn’t mean that there is no free Sn remaining in the sample. A very small amount of Sn can present but not detected due to the XRD apparatus resolution.

Finally, diffraction peaks due to the presence of HfO_2 are observed for both samples. They appear to be more intense for the “oxidized” one. This is a strong indication for the presence of a higher amount of HfO_2[9] in the sample which has been oxidized during the powder preparation.

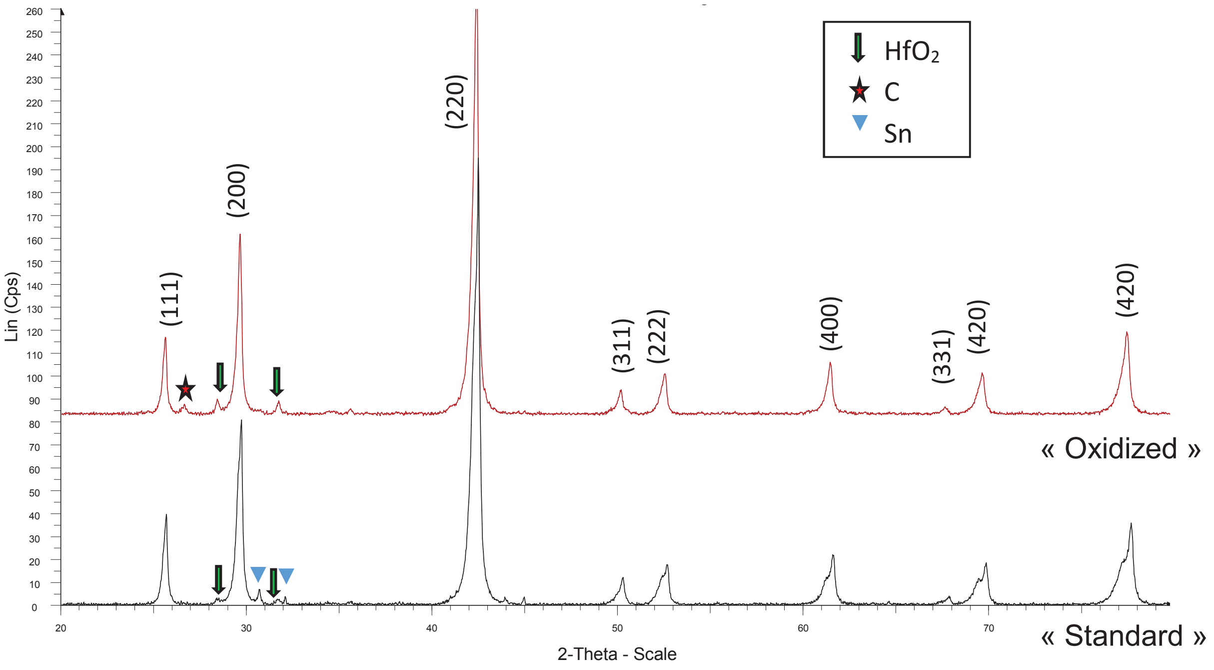

Figure IV.19 : *XRD patterns of the* $Zr_{0.25}Hf_{0.25}Ti_{0.5}NiSn_{0.994}Sb_{0.006}$ *“standard” and “oxidized” sample sintered at 1140°C.*

- SEM observations.

At low magnification, fracture surface of the “oxidized” sample, shown in Figure IV.20, exhibits a quite similar microstructure than the “standard” one already presented in Figure III.8.c. The “oxidized” sintering pellet appears to be depleted of any residual porosity. This observation confirms the relative density value calculated to be 98 %.

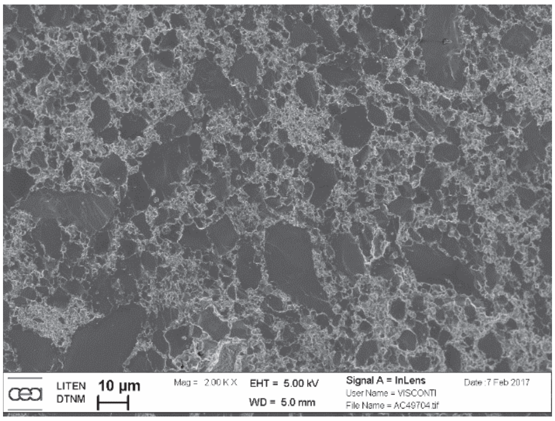

Figure IV.20 : *SEM image of the of the* $Zr_{0.25}Hf_{0.25}Ti_{0.5}NiSn_{0.994}Sb_{0.006}$ *“oxidized” sample*

The observations of a polished surface of the “oxidized” sample are presented in Figure IV.21. It is possible to notice the presence of a lot of white particles located at the grain boundaries vicinity. Black dots observed in Figure IV.4.b) are porosities due to particles pulled-out during polishing.

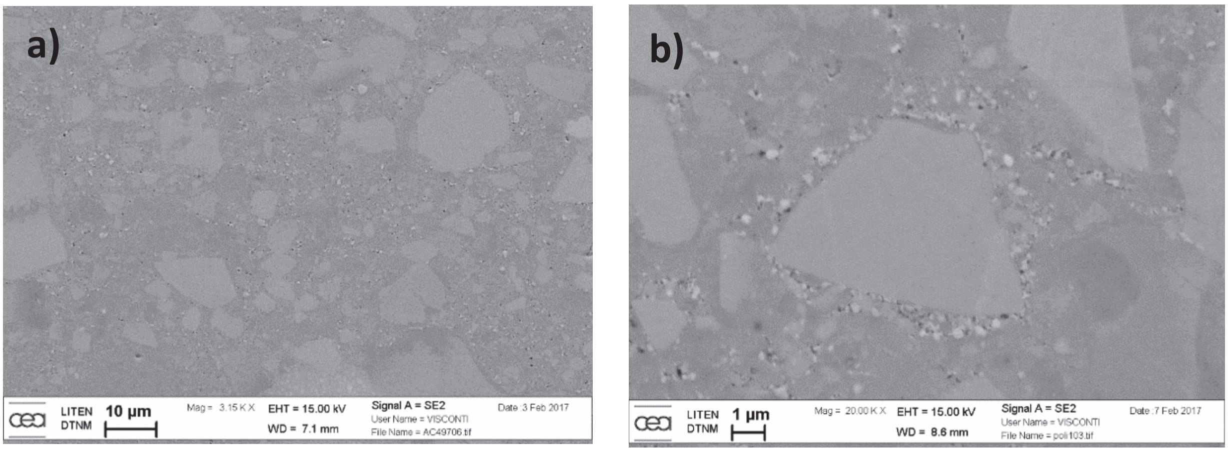

Figure IV.21 : *a) and b) SEM images of a polished surface of the “oxidized” sample sintered at 1140 °C.*

Moreover, from these images, a corresponding diameter was calculated for more than 200 grains belonging to the “oxidized” sample. The grain size distribution is presented in Figure IV.22 (with the one related to the “standard” sample) and the average grain size is calculated to be around 3.6 µm. This value is slightly lower than the one measured for the “standard” sample (3.8 µm). In the same time, the grain size distributions are similar for both materials.

Even though the densification rate versus temperature curve of the "oxidized" sample is shifted towards higher temperatures, the average grain size measured is slightly lower than the one of the "standard" sample. This trend can be due to the presence of more oxide precipitates at the grain boundaries restraining grain growth during sintering (Zener effect[14]).

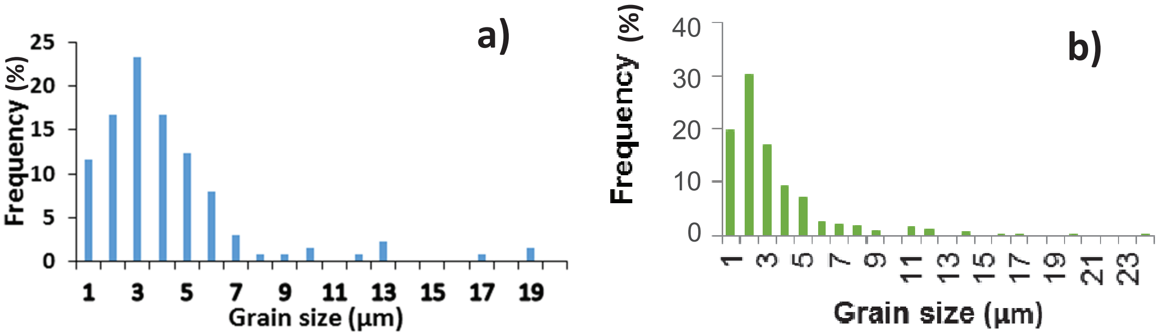

Figure IV.22 : *Grain size distribution of a) the* $Hf_{0.25}Zr_{0.25}Ti_{0.5}NiSb_{0.006}Sn_{0.994}$ *"oxidized" sample and b) the* $Hf_{0.25}Zr_{0.25}Ti_{0.5}NiSb_{0.006}Sn_{0.994}$ *"standard" sample*

SEM observations in secondary electron mode of fractures surfaces at higher magnifications are presented in Figure IV.23. As noticed before for the "standard" sample, numerous tiny bright precipitates can be seen. Even though most of them appear to be located at the grain boundaries, some seem to be entrapped in the matrix elemental grains, as outlined for examples by the red ellipses. They have the same aspect than the ones observed for the "standard" sample.

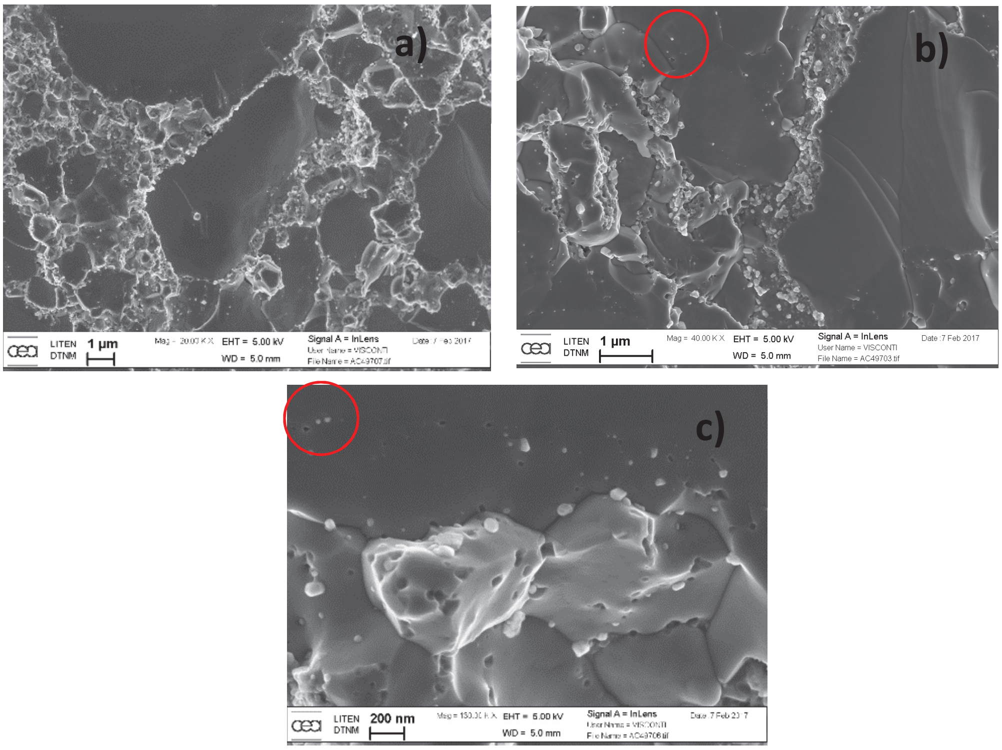

Figure IV.23 : *a), b), and c) SEM images at different magnification of a fracture surface of the "oxidized" sample sintered at 1140 °C*

Eye inspection of this SEM images and comparison to the ones obtained on the “standard” sample (Figure III.10) show that the white precipitates in the “oxidized” sintered sample are much smaller and numerous. Unfortunately, at this point, no strict determination of the precipitates concentration in the different samples has been completed.

By taking into account more than 500 precipitates, an average diameter has been calculated to be 49 nm for the “oxidized” sample. For the “standard” one, the precipitate average diameter was 104 nm.

- <u>EDS analyses.</u>

EDS analyses on a polished sintered section of the “oxidized” sample is presented in Figure IV.24.

As observed for the “standard” sample in Chapter III, large grains of the “oxidized” one are clearly depleted in Ti while enriched in Zr and Hf. Between the large grains, the material is composed of smaller grains enriched in Ti and of some oxide-based precipitates located mainly at the grain boundaries of the large grains.

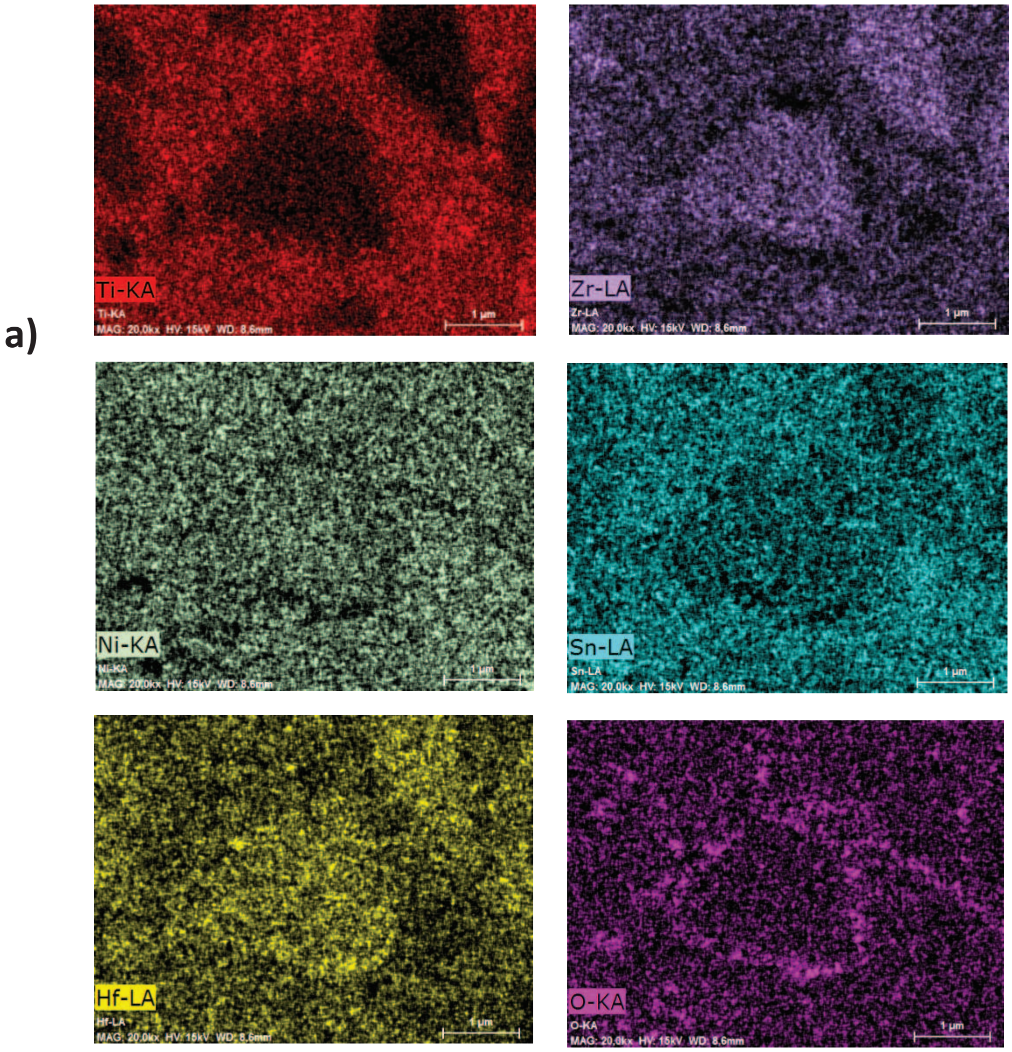

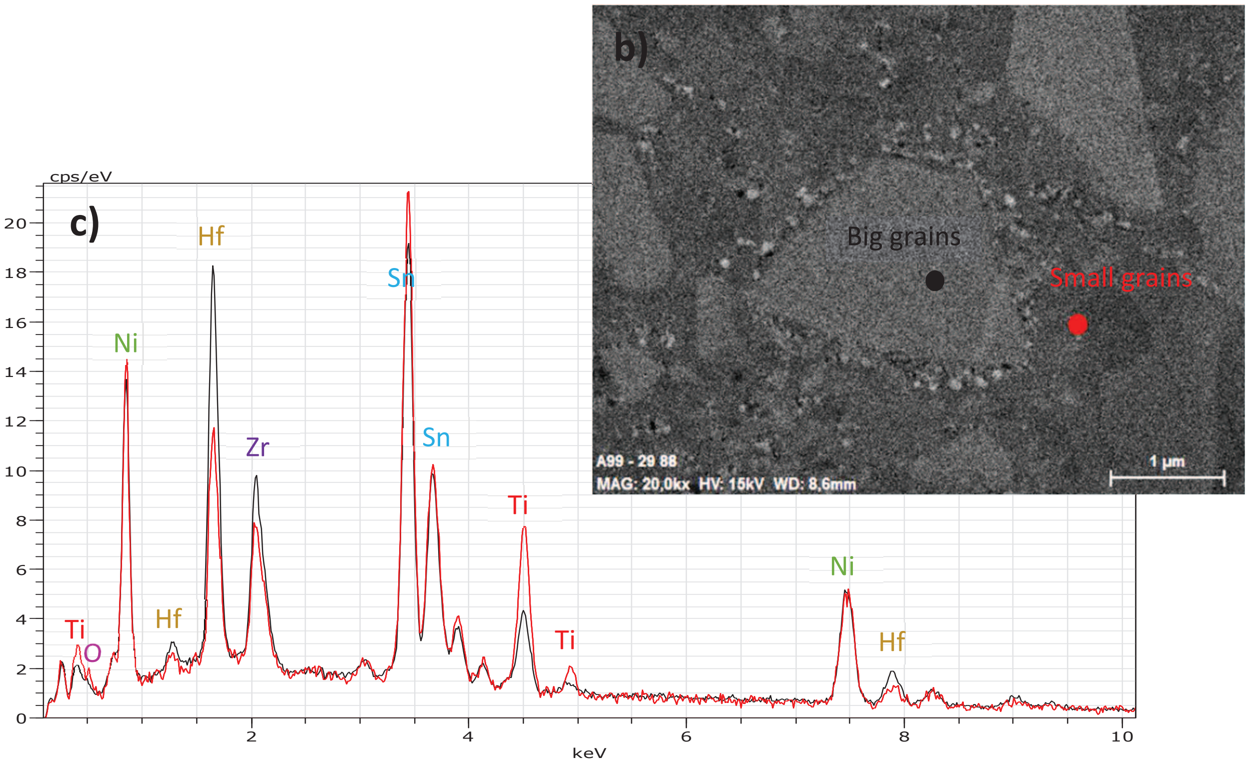

<u>Figure IV.24 :</u> *a) EDS mapping and c) EDS Spectrum of b) a polished surface of the "oxidized" sample.*

An EDS mapping acquired on a fracture surface at higher magnification, shown in Figure IV.25, highlights that there is actually two different types of precipitates. The first ones, outlined by a blue circle, appear to be enriched in Hf and O. They probably correspond to the HfO_2 phase detected using XRD analyses. Moreover, they are also possibly the same kind of precipitates as the ones observed for the "standard" sample. Secondly, some Ti-enriched precipitates are also observed. They are highlighted by a red circle.

Despite coupling with EDS analyses, it is impossible to distinguish both kinds of precipitates only by observing SEM images. Indeed, both appear to be located at the grain boundaries or triple points and have about the same shape and average diameter. Accordingly, the mean diameter of 49 nm calculated from SEM pictures corresponds to the contribution of Hf/O and Ti enriched precipitates.

Despite of the precipitates and the shadow artefacts due to the surface irregularities, all the elements constituting the matrix appear to be homogeneously distributed in the investigated area.

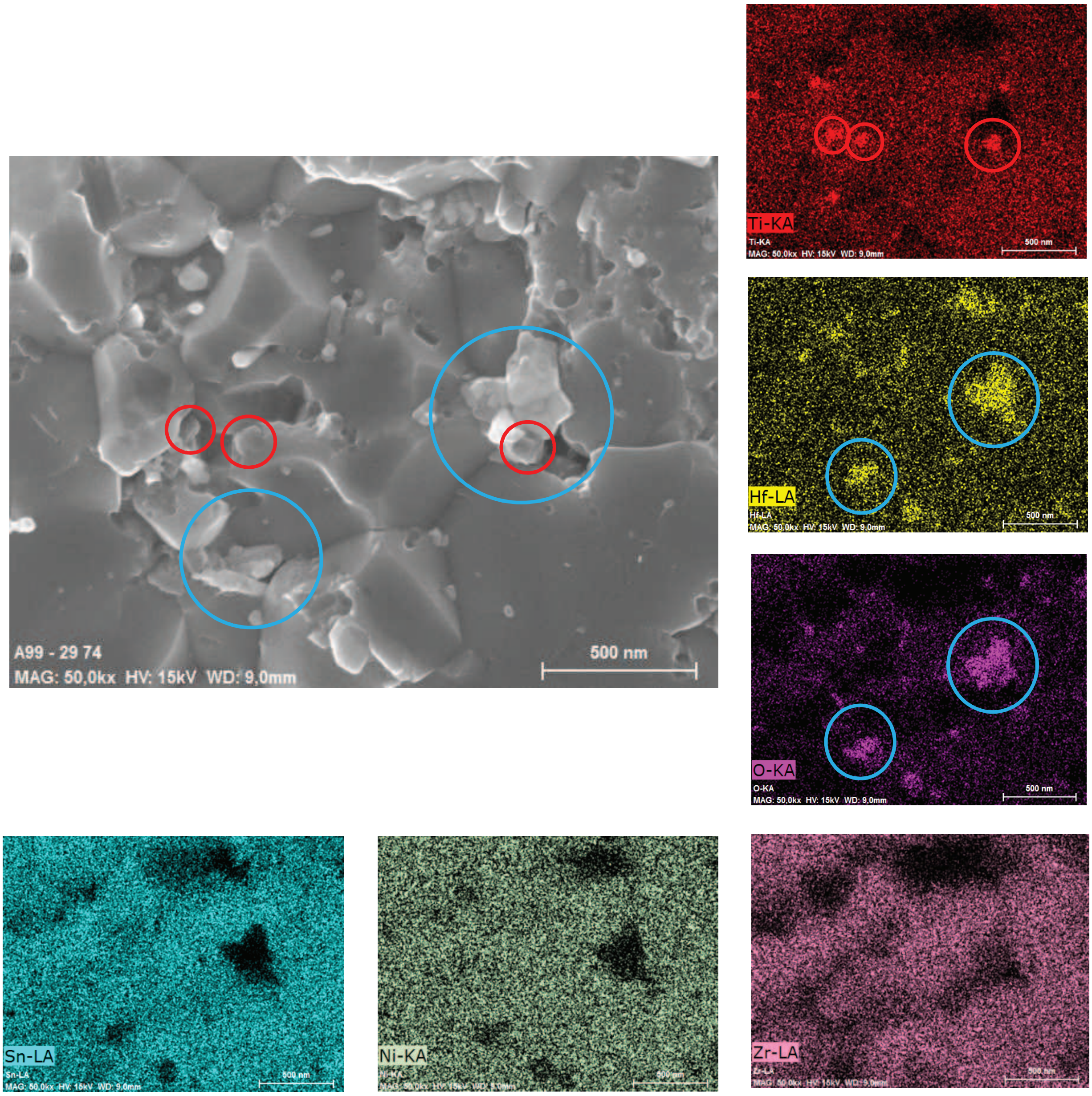

Figure IV.25 : *EDS mapping of the "oxidized" sample sintered at 1140 °C.*

c. TEM observations

STEM/HAADF observations have been quickly performed on a thin foil machined from the bulk of the "oxidized" as-sintered sample. Results are presented in Figure IV.26. According to the EDS mapping, it is confirmed that Ni and Sn seem to be equally distributed throughout the half-Heusler matrix grains. Moreover, hafnium-based oxide (white) and Ti-riched (dark) precipitates are also clearly imaged, confirming what has been reported using SEM investigations.

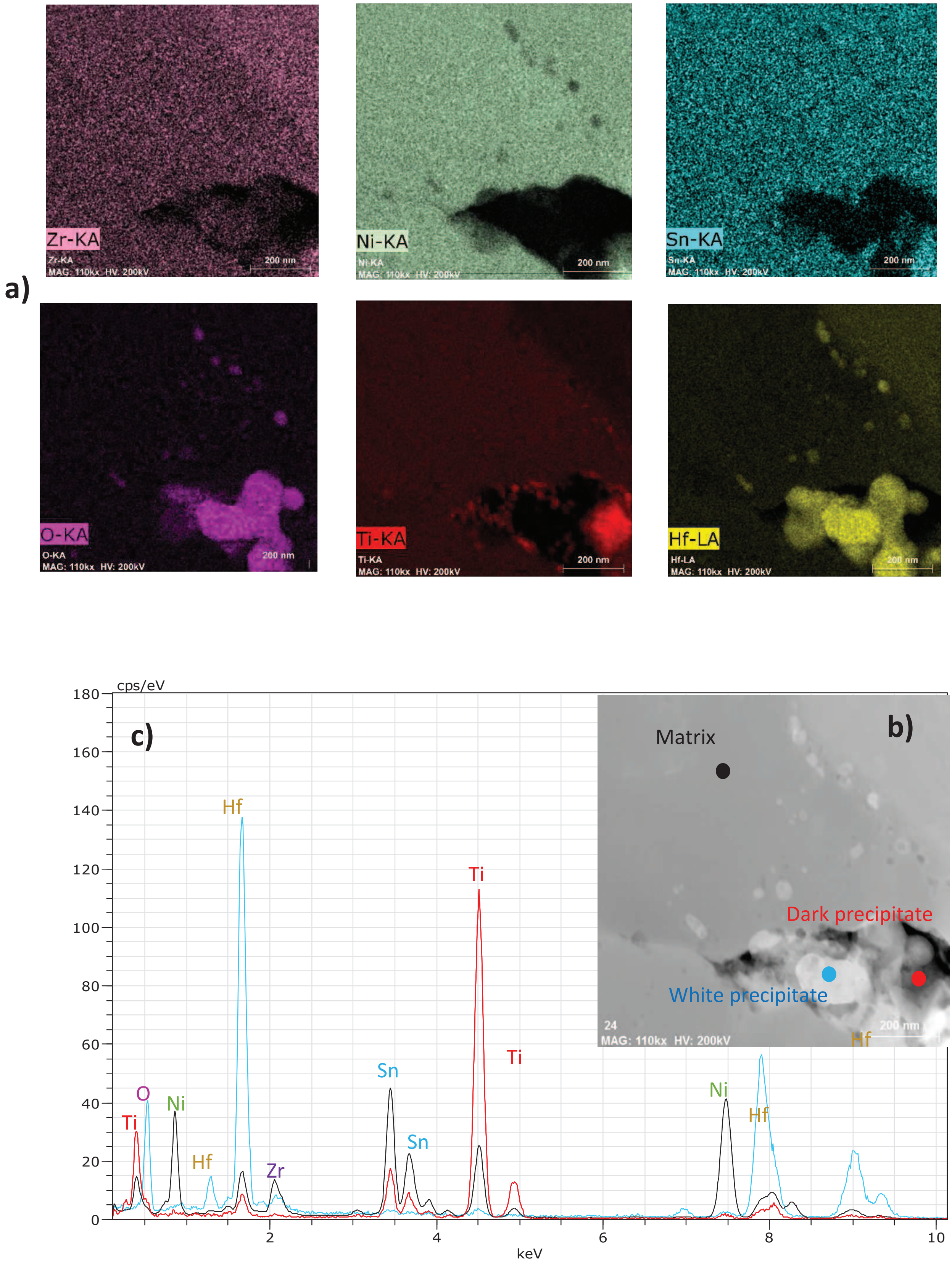

Figure IV.26 : *a) STEM/HAAD mapping and c) spectrum of b) the "oxidized" sample.*

All the results are summarised in Table IV.2 and compared to the “standard” sample.

Material composition	**Soak temperature**	**Relative sintered density**	**Average grain size**	**Precipitates**	
				Enriched in	Average diameter (nm)
$Zr_{0.25}Hf_{0.25}Ti_{0.5}NiSn_{0.994}Sb_{0.006}$	1140 °C	98 %	3.8 µm	HfO_2	104
				Ti	5-20
“oxidized” $Zr_{0.25}Hf_{0.25}Ti_{0.5}NiSn_{0.994}Sb_{0.006}$	1140 °C	98 %	3.6 µm	Ti	~49
				HfO_2	~49

<u>Table IV.2 :</u> *Soak temperature, density, average grain size and precipitate nature and diameter of the as-sintered ”oxidized” and the “standard” samples with the* $Zr_{0.25}Hf_{0.25}Ti_{0.5}NiSn_{0.994}Sb_{0.006}$*composition*

II.2 - Thermoelectric properties

The thermoelectric properties of the “oxidized” sample are measured and compared to the “standard” ones in the 100 to 500 °C temperature range, as presented in Figure IV.27.

First, the evolution of the electrical conductivity in function of the temperature is shown in Figure IV.27.a). The “oxidized” material has an electrical conductivity reduced of about 10 % on all the temperature range, when compared to the “standard” sample values. This trend can be due to the presence of more oxide-based precipitates at the grain boundaries of the “oxidized” sample, preventing charge carrier motion due to their insulating nature.

The absolute values of the Seebeck coefficient (Figure IV.27.b) show that both samples exhibit the desired N-type conduction. Even though Seebeck coefficient values are close for both samples, it decreases faster with the increase of temperature for the “oxidized” sample. For this reason, the Seebeck coefficient is slightly larger for the “oxidized” sample in the 200 to 540 °C temperature range.

As shown in Figure IV.27.c), whatever the temperature, the “oxidized” sample exhibits a significantly lower thermal conductivity than the “standard” one. The presence of more oxide-based precipitates in the sintered microstructure perturb lattice vibrations, lowering directly the thermal conductivity.

To finish, the evolution of the ZT parameter in function of temperature is shown in Figure IV.27.d) for both samples. A maximum ZT around 1.0 is obtained at 500 °C for the “oxidized” material in comparison to 0.9 for the “standard” one. Moreover, the ZT values of the “oxidized” sample are always higher than the ones of the “standard” material in the 200 to 500 °C temperature range of interest.

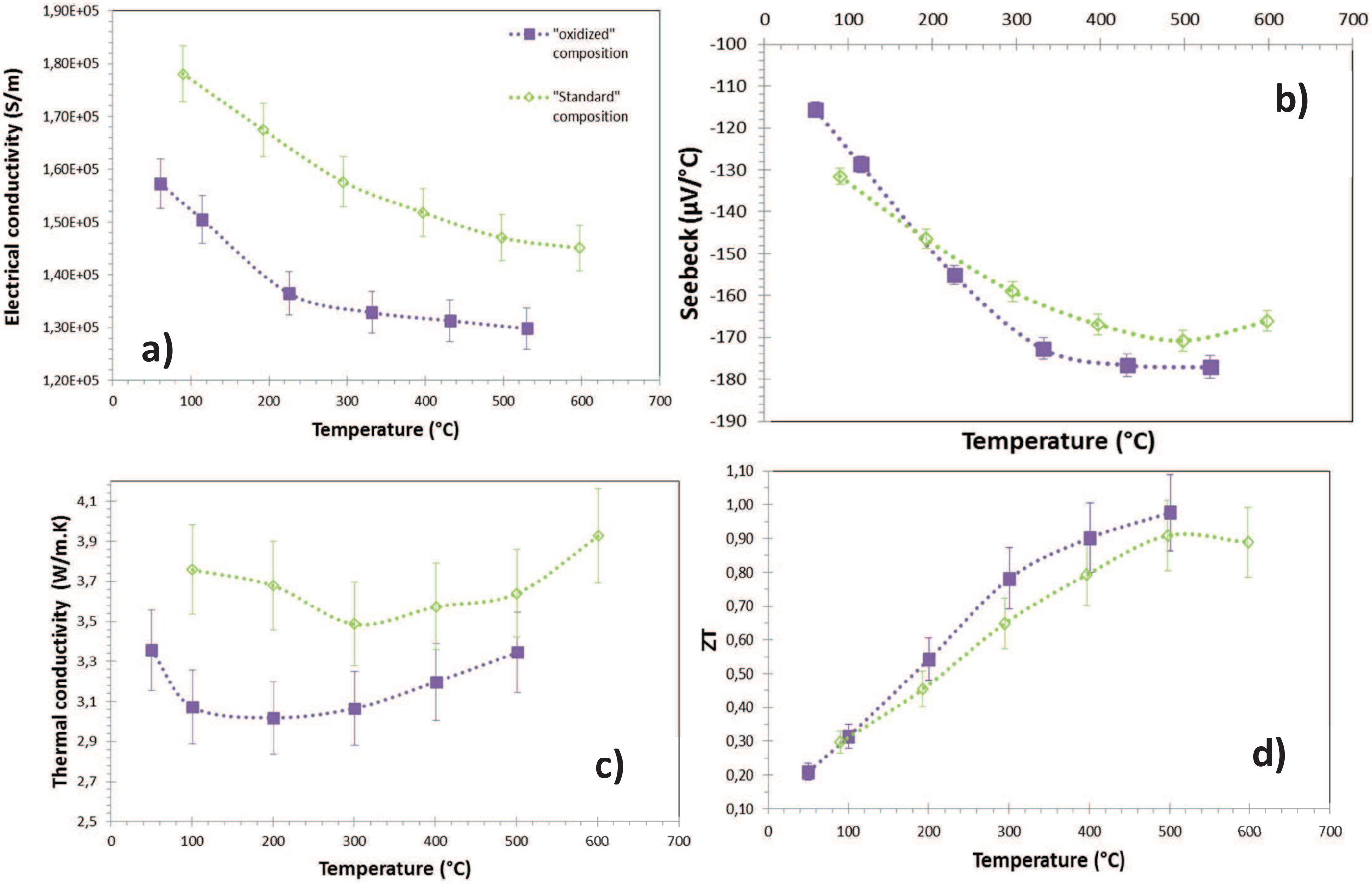

<u>Figure IV.27 :</u> *Thermoelectric properties in function of temperature for the as-sintered "oxidized" and the "standard" samples with the* $Zr_{0.25}Hf_{0.25}Ti_{0.5}NiSn_{0.994}Sb_{0.006}$*composition.*
a) Electrical conductivity; b) Seebeck coefficient; c) Thermal conductivity; d) ZT parameter.

III - Conclusion

Two solutions have been highlighted to reduce the price per kilogram for the n-type $Hf_{0.25}Zr_{0.25}Ti_{0.5}NiSb_{0.006}Sn_{0.994}$ alloy investigated, without introducing any detrimental effect onto the thermoelectric properties in the 20-500 °C temperature range.

The first one is focused on suppressing the incorporation of metallic Hf from the alloy formulation. An hafnium-free n-type $Zr_{0.5}Ti_{0.5}NiSb_{0.006}Sn_{0.994}$ powder is mixed with HfO_2 nano-particles before sintering in order to decrease the thermal conductivity, while maintaining the electrical conductivity and the Seebeck coefficient to a good level. The addition of 1.5 %wt of HfO_2 was founded to be optimal in order to improve the thermoelectric properties, especially the ZT parameter.

The second way consists of milling and stocking the n-type $Hf_{0.25}Zr_{0.25}Ti_{0.5}NiSb_{0.006}Sn_{0.994}$ powder under ambient atmosphere (air), to promote the formation of in-situ oxide-based precipitates in the sintered microstructure. This approach is time saving for the operator and simplifies strongly the manufacturing process.

Both approaches lead to a significant decrease of the thermal conductivity in the temperature range of interest, due to the presence of oxides-based precipitates. An increase of 11 to 23% of the ZT value is observed when compared to the “standard” material, in the 200 to 500 °C temperature range. Whatever the solution adopted, maximum ZT values around 1.0 were obtained at 500 °C.

Therefore, a cost reduction about 55% of the raw material and a simplification of the manufacturing process have been obtained, while further improving the n-type material thermoelectric properties. A further improvement way could be to combine both investigated approaches.

---

[1] Downie, R.A., Popuri, S.R., Ning, H., Reece, M.J.,Bos, J.W.G., Effect of spark plasma sintering on the structure and properties of Ti1-xZrxNiSn half-heusler alloys, Marerials, 2014, 7, 7093.

[2] Downie, R.A.; MacLaren, D.A.; Smith, R.I.; Bos, J.W.G. Enhanced thermoelectric performance in TiNiSn-based half-Heuslers, Chem. Commun., 2013, 49, 4184–4186.

[3] Chen, S., Lukas, K. C., Liu, W., Opeil, C. P., Chen, G. and Ren, Z., Effect of Hf Concentration on Thermoelectric Properties of Nanostructured N-Type Half-Heusler Materials $Hf_xZr_{1-x}NiSn_{0.99}Sb_{0.01}$. Adv. Energy Mater., 2013, 3: 1210–1214.

[4] https://www.metalprices.com.

[5] Huang, X. Y., Xu, Z. and Chen, L. D., The thermoelectric performance of ZrNiSn/ZrO2 composites, Solid State Communications, 2004, 130, 5, 181-185

[6] Huang, X. Y., Xu, Z. and Chen, L. D., Tang, X.F., Effect of y-Al2O3 content on the thermoelectric performance of ZrNiSn/y-Al2O3 composites, Key Engineering Materials, 2003, 249, 5, 79-82

[7] Gürth, M., Rogl, G., Romaka, V.V., Grytsiv, A., Bauer, E., Thermoelectric high ZT half-Heusler alloys Ti1−x−yZrxHfyNiSn (0 ≤ x ≤ 1; 0 ≤ y ≤ 1), Acta Materialia; 2016, 104, 210-222

[8] JCPDS file 04-004-7747

[9] JCPDS file 00-043-1017

[10] JCPDS file 04-004-7747

[11] Bischoff, E., Manfred, R., Journal of the American Ceramic Society, 2006, 66(2), 123-127

[12] Reed, T.B., Free Energy of Formation of Binary Compounds: an Atlas of Charts for High-temperature Chemical Calculations, MIT Press, Cambridge, 1971.

[13] JCPDS file 04-004-7747

[14] Smith, C.S., Introduction to grain, phases and interfaces : An interpretation of microstructure, Transactions of the American institute of Mining Engineers, 1948, 175, 15-51

Chapter V

Microstructure, thermoelectric properties, cost reduction and simplification of the manufacturing process of a p-type $Zr_{0.44}Hf_{0.44}Ti_{0.12}CoSn_{0.2}Sb_{0.8}$ material

In a thermoelectric device, n and p-types legs incorporated must have closest thermoelectric and thermomechanical properties as possible. Moreover, it is essential that the thermoelectric properties of the n and p-type materials are optimised in the same temperature range of interest. Finally, both materials must also have coefficient of thermal expansion, young modulus and Poisson's ratio as close as possible in order to limit internal stresses from thermal origin at the contacts with the metallic connectors.

For this reason, we have chosen to investigate a p-type half-Heusler formulation, with a composition very close to the n-type one investigated in the previous chapters. Once again, the link between microstructure and thermoelectric properties will be examined, in order to obtain the best thermoelectric properties as possible. Finally, with the need to further reduce the price of the sintered pellets, without compromising the thermoelectric properties, the same strategy as the one adopted for the n-type material in Chapter IV has been retained: suppression of metallic Hf from the based-formulation with addition of HfO_2 particles and promotion of the powder oxidation before the sintering step.

I - Microstructure and thermoelectric properties of a p-type $Zr_{0.44}Hf_{0.44}Ti_{0.12}NiSb_{0.8}Sn_{0.2}$ material

The p-type half-Heusler $Zr_{0.44}Hf_{0.44}Ti_{0.12}CoSbn_{0.8}Sn_{0.2}$ composition has been shown to be one of the most promising p-type (Ti, Zr, Hf)Co(Sn, Sb) half-Heusler material with a ZT of 1.0 at 700 °C[1]. Accordingly, it has been decided to investigate this stoichiometric composition in this chapter.

As for the n-type formulation, pellets of a polycrystalline material, having the composition $Zr_{0.44}Hf_{0.44}Ti_{0.12}CoSbn_{0.8}Sn_{0.2}$ have been sintered at different temperatures, using the manufacturing process exposed in Chapter II. Then, the microstructure of the samples has been characterized using XRD and SEM. In parallel, the thermoelectric properties have been investigated. Finally, results are discussed in order to establish a link between the sintered microstructure and the thermoelectric properties.

II.1 - Determination of the sintering temperature

A first SPS run was completed from room temperature to 1500 °C, in order to determine the powder sintering window. The densification rate with the evolution of temperature is calculated and results are presents in Figure V.1.

As for the N-type materials previously investigated, the densification rate in function of temperature exhibits a standard bell-shaped curve. However, it is shifted towards higher temperature compared to the N-type $Zr_{0.25}Hf_{0.25}Ti_{0.5}NiSn_{0.994}Sb_{0.006}$ composition. The maximum densification rate is achieved for a temperature of 1250 °C. This shift is possibly due to the fact that the stoichiometry of the p-type material contains higher amounts of Hf, Zr and Sb, having high melting points, compared to the n-type composition investigated in Chapter III that incorporates higher amounts of Ti and Sn.

Then, the densification rate reaches a plateau for temperatures ranging from 1300 to 1400 °C. Afterward, the densification rate drops suddenly and increases back to the plateau value. This phenomenon is due to the software used for the data treatment and has been already observed on other materials investigated in the lab (microstructure investigations and thermoelectric properties measurements will confirm that no phase change is detected between a samples sintered at 1400 °C and another one at 1500 °C, see below). Finally, the densification rate increases drastically before 1500 °C, which corresponds to material melting.

Accordingly, three sintering temperatures have been retained for further tests: 1250 °C which is the temperature where the densification rate value is at maximum, 1300 °C corresponding to the temperature following the bell-shape and, finally, 1400 °C which is the temperature where the densification rate approaches zero. For each sintering temperature, the soak time was fixed to 5 min, and all other sintering parameters are the same as the ones resumed in Chapter II. The sintered sample used to determine the sintering window (heated until 1500 °C) has been also collected and characterized.

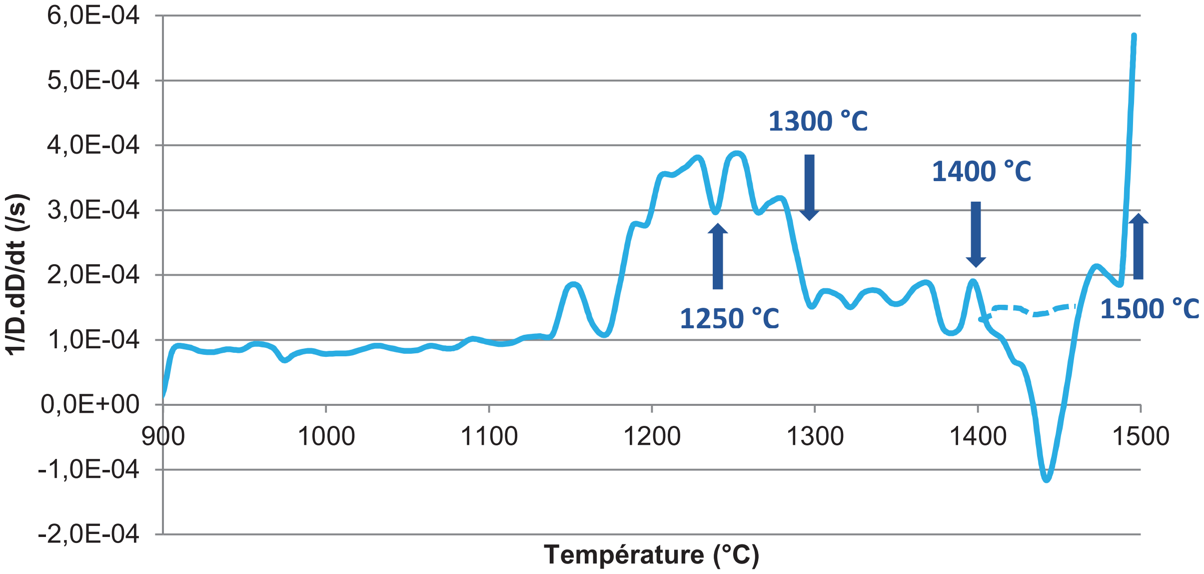

Figure V.1 : *Densification rate of the* $Zr_{0.44}Hf_{0.44}Ti_{0.12}CoSbn_{0.98}Sn_{0.02}$ *material.*

II.2 - Microstructure analysis of the sintered pellets

For each sample retained, XRD and SEM observations have been completed and results have been compared and discussed.

- Residual porosity.

The theoretical density calculated for the $Zr_{0.44}Hf_{0.44}Ti_{0.12}CoSbn_{0.98}Sn_{0.02}$ composition is 9.31 g.cm^{-3}. The calculated relative densities for the samples sintered at 1300, 1400 and 1500 °C were higher than 99 %. However, the relative density of the sample sintered at 1250 °C is only about 94 %.

SEM images in secondary electron mode of fresh fracture surfaces of the investigated samples are presented in Figure V.2. Samples sintered at a temperature higher than 1300 °C appear to be densely packed. Indeed, no residual porosity is detected in Figure V.2.a), b) and c). However, as outlined by the red arrows, porosities are clearly present in the sample sintered at 1250 °C. These results are in good agreement with the relative density values measured by Archimedes method.

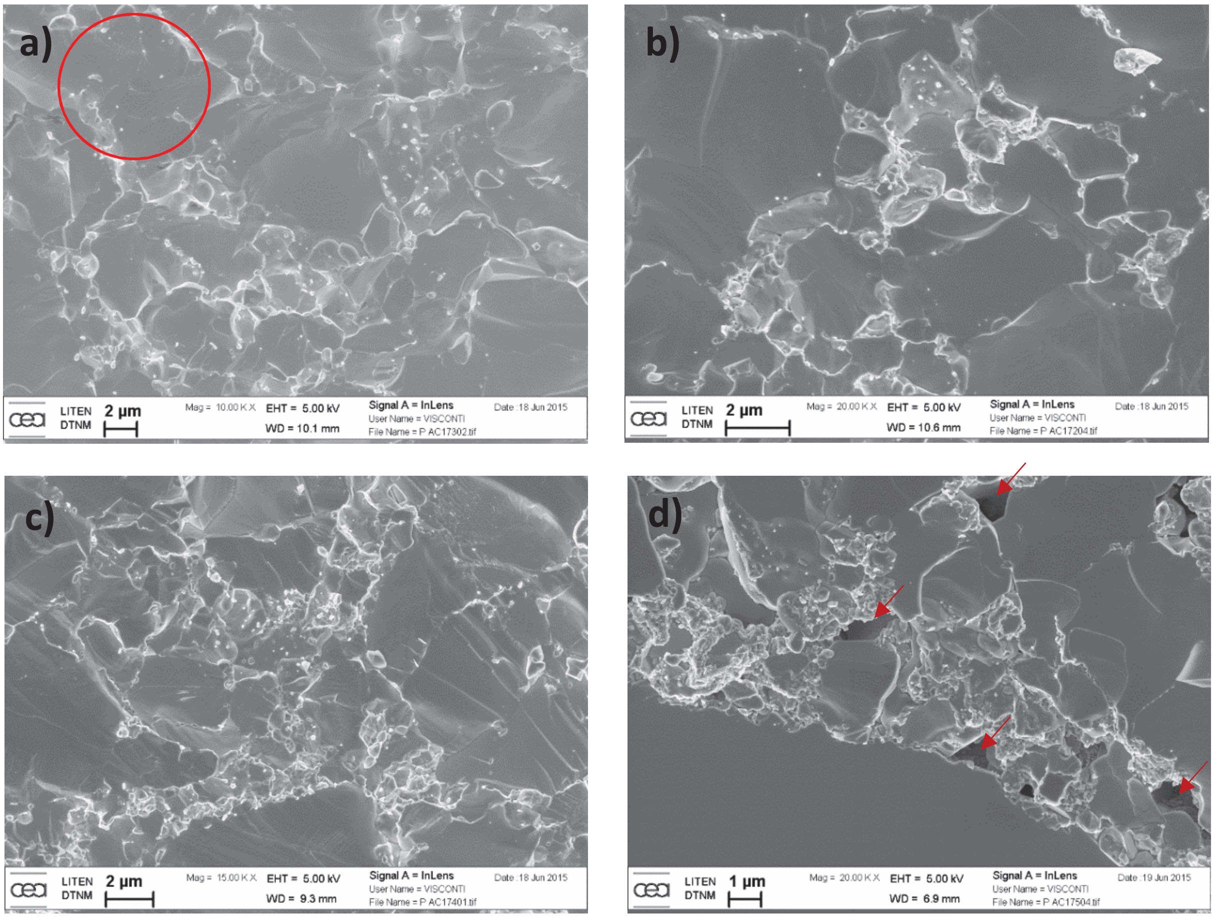

Figure V.2 : *SEM images of a fracture surface of the sample sintered at a) 1500 °C, b) 1400 °C, c) 1300 °C and d) 1250 °C*

It is interesting to point out that almost fully dense samples are the ones sintered at temperatures where the densification rate is positioned on the plateau shown in Figure V.1. In comparison, the sample sintered at a temperature below the one corresponding to the end of the densification rate bell-shape part remains porous. The same trend was also observed in Chapter III, where only the n-type sample sintered at 1140 °C was densely packed and devoted of any residual porosity.

Finally, small white precipitates can be observed for all the investigated samples. They mostly appear located at the grain boundaries, except for the sample sintered at 1500 °C where some of them may be entrapped in the bulk of individual grains (red circle, Figure V.2.a).

- XRD analyses.

X-ray diffractograms, presented in Figure V.3, indicate the formation of the major half-Heusler phase for each sintered sample. Indeed, whatever the sintering temperature, the $C1_b$ structure is detected, as for the previous n-type materials investigated. The lattice parameter is calculated to be 6.05 Å for all the samples. However, the half-Heusler peaks of the sample sintered at 1500 °C appear to be sharper than for the other samples sintered at lower temperatures. As shown in Figure V.1, the sintering temperature of this sample corresponds to the beginning of the material melting. Therefore the sample composition is possibly more homogeneous, a small fraction of liquid phase promoting atomic diffusion and redistribution of the different chemical species.

Few additional peaks are also observed. A carbon peak, linked to graphite remaining at the pellet surface, is noted for the sample sintered at 1300 °C. Also, slight monoclinic HfO_2[2] peaks are observed for all the investigated samples. The HfO_2 phase was also detected for the "standard" n-type composition. However the peaks intensity is much lower for the p-type material, attesting a lower content of HfO_2. Unfortunately, up to now, no strict calculations of the HfO_2 content, for example by using Rietveld analysis, has been completed.

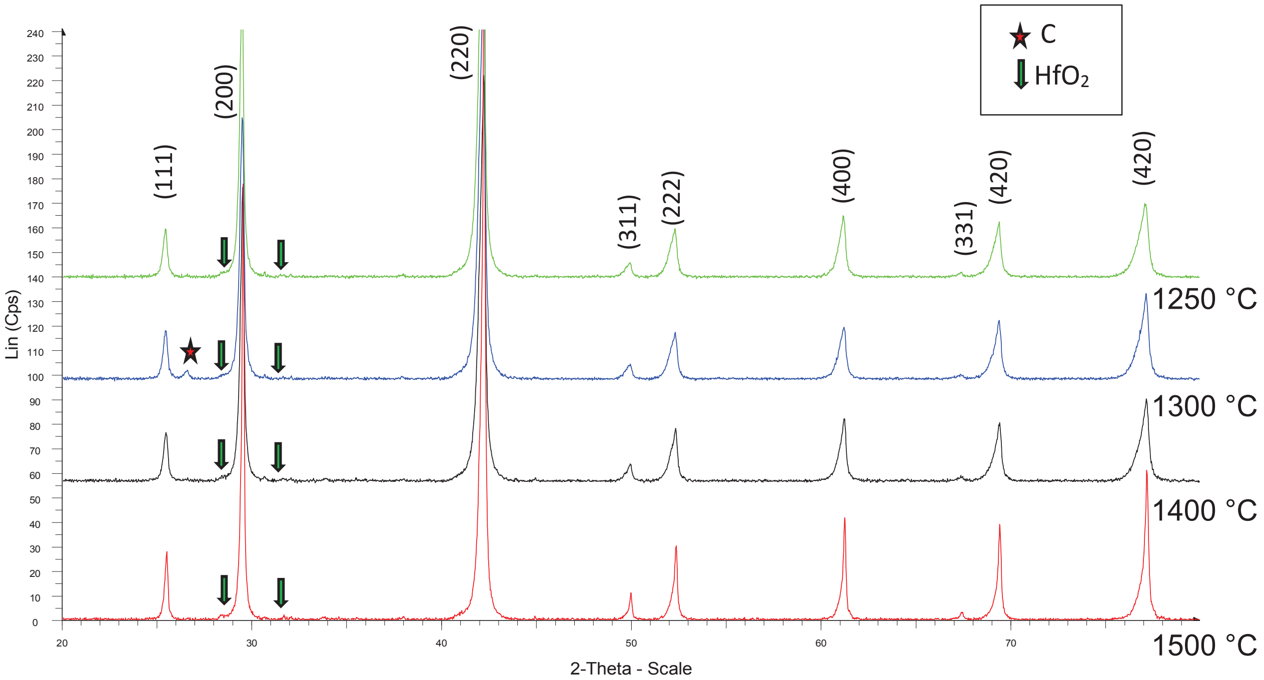

Figure V.3 : *XRD patterns of the* $Zr_{0.44}Hf_{0.44}Ti_{0.12}CoSbn_{0.98}Sn_{0.02}$ *samples sintered at 1250°C, 1300°C, 1400°C and 1500°C.*

- Precipitates and grain size analysis

SEM pictures, in back scattered electrons mode, on polished sections, were acquired for all four sintered samples. As an example, a polished section of the sample sintered at 1300 °C is presented in Figure V.4. It was possible to calculate an average grain size for each sample on more than 200 grains, as presented in Table V.1. The average grain size calculated was 3.5, 4.2, 4.5 and 5.4 µm for the samples sintered at 1250, 1300, 1400 and 1500°C, respectively. As expected, the higher the sintering temperature, the higher the grain size.

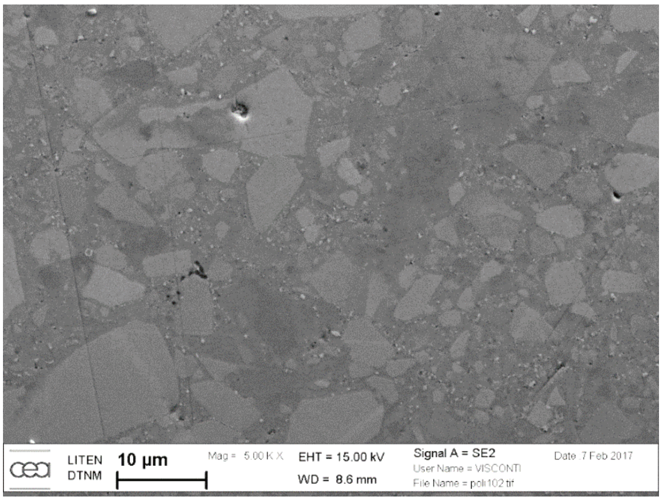

Figure V.4 : *SEM back scattering electron analysis of a polished surface of the sample sintered at 1300 °C*

Moreover, in Figure V.4, it is possible to notice small white dot at the grain boundaries (black dots are particles pulled out during the polishing step). They probably correspond to the precipitates observed on fracture surfaces, as shown in Figure V.2.

Fractures surfaces of all samples were observed using SEM in secondary electron mode, in order to measure the size of such precipitates. Images are present in Figure V.5. Taking into account more than 200 objects, the average precipitate diameter is calculated for each sample and reported in Table V.1. The average precipitate diameter increases with the sintering temperature. However, this evolution is not linear. Indeed, the average precipitate diameter in almost similar (around 60 nm) for the samples sintered at 1300 °C and 1400 °C.

A possible explanation for such a trend is that HfO_2 precipitates nucleate and grow for sintering temperatures where the densification rate exhibits the bell shape. Then, when the plateau is reached, precipitates growth is limited because of the dense microstructure achieved and short sintering times, preventing atomic migration and coalescence. Then, when the material starts melting, the precipitate size increases again drastically, assisted by the formation of a liquid phase.

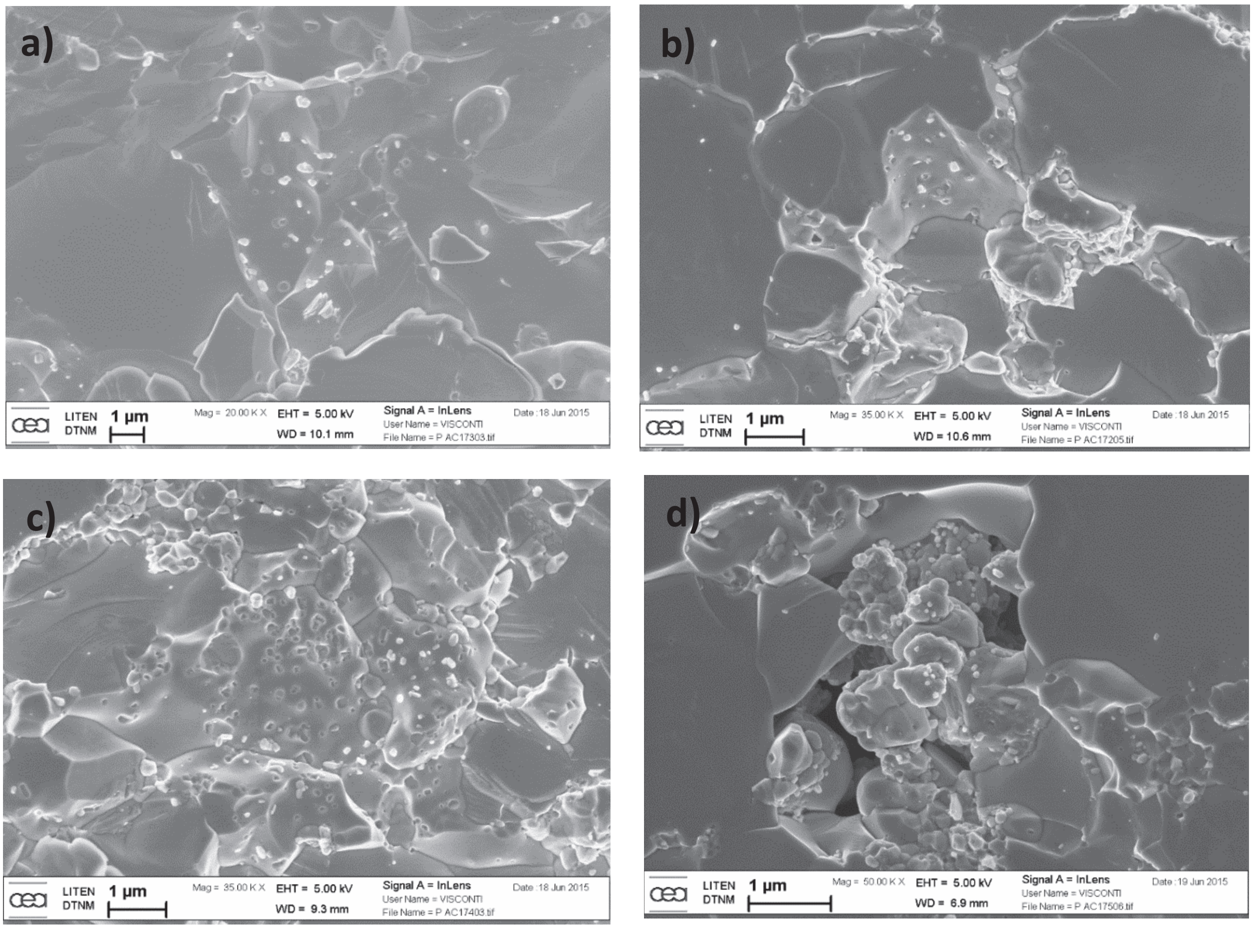

Figure V.5 : *SEM images of a fracture surface of the sample sintered at a) 1500 °C, b) 1400 °C, c) 1300 °C and d) 1250 °C*

Soak temperature (°C)	**1250**	**1300**	**1400**	**1500**
Relative sintered density (%)	94	>99	>99	>99
Average grain size (µm)	3.5	4.2	4.5	5.4
Average precipitate diameter (nm)	40	60	63	156

Table V.1 : *Density, average grain size and precipitate diameter depending on the soak temperature.*

EDS analyses on fresh fracture surfaces of the four investigated sintered samples have been completed. EDS maps of each constituting elements appear to be similar for all the considered samples. A typical example is presented in Figure V.6 for the sample sintered at 1400 °C. On the contrary to the n-type materials investigate previously, Zr, Ti and Hf elements seem to be homogeneously distributed throughout the individual matrix grains constituting the polycrystal. Accordingly no phase separation is detected in the samples.

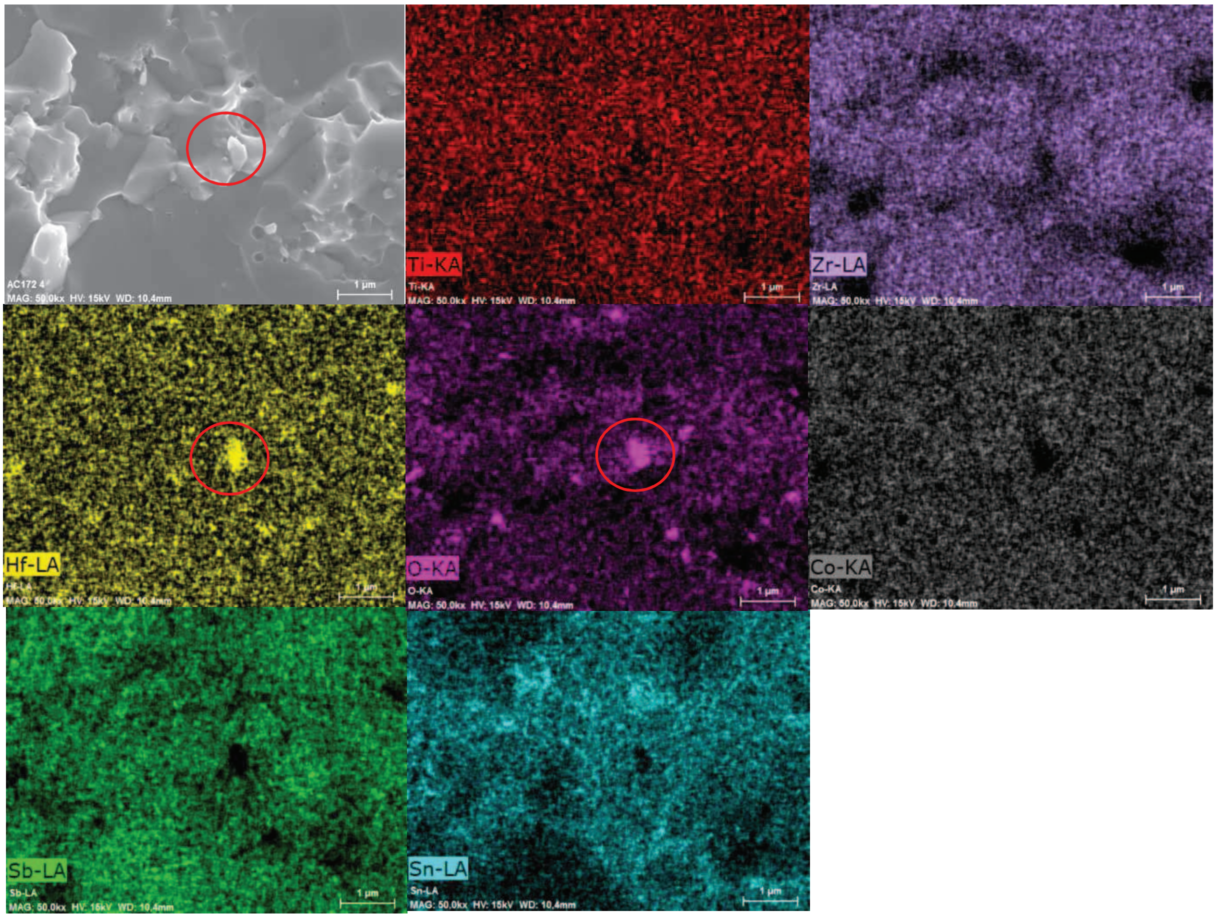

Figure V.6 : EDS maps of a fracture surface of the sample sintered at 1400 °C.

Moreover, a very slight Sn segregation can be noticed at the grain boundaries. The precipitate materialized by the red circle in Figure V.6 appears to be enriched in Hf and O while depleted in the other constituents.

The EDS spectra acquired from the matrix and a white precipitate confirms this point. Indeed Figure V.7 highlights that the white precipitate is made of a hafnium-based oxide, which is in agreement to the XRD analysis reported before.

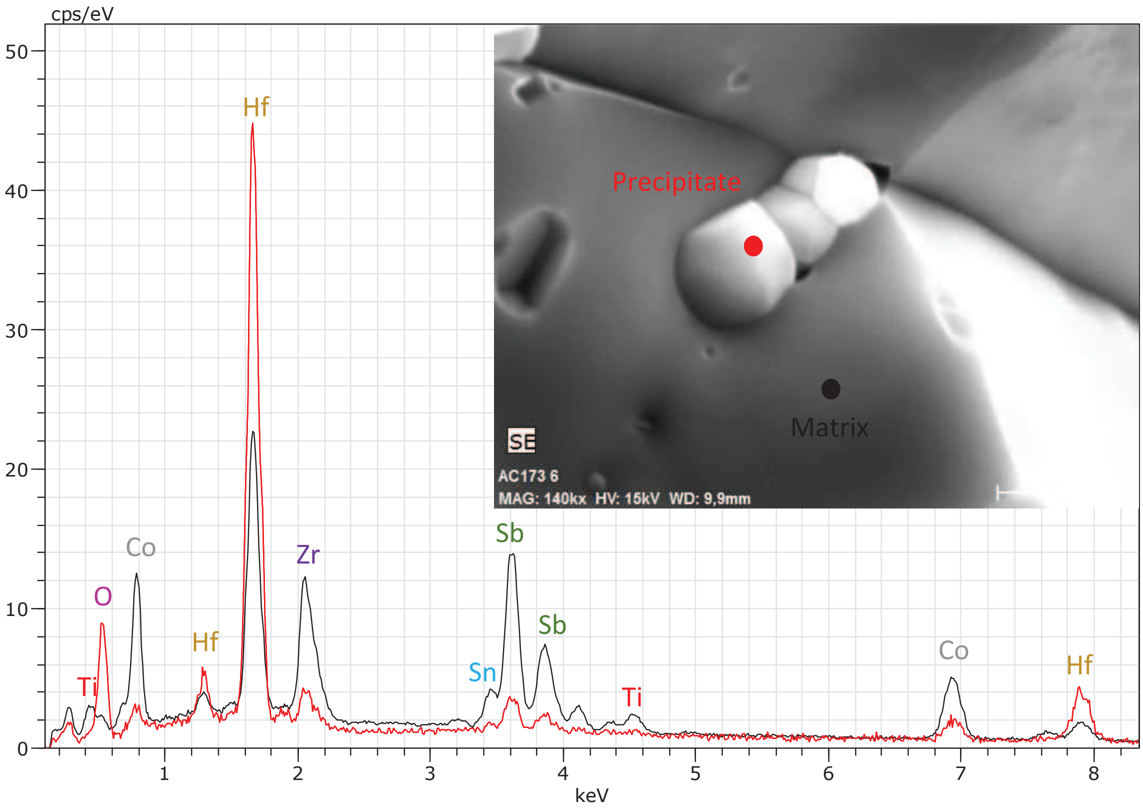

Figure V.7 : *EDS spectrum from the matrix and the precipitate for the sample sintered at 1500 °C.*

II.3 - Thermoelectric properties and relationship to the microstructure

The thermoelectric properties of each pellet is measured in the temperature range going from 100 °C to 500 °C. Results are presented in Figure V.8 and compared to the data reported by Yan and all.[1] on samples having the same p-type $Hf_{0.44}Zr_{0.44}Ti_{0.12}CoSb_{0.8}Sn_{0.2}$ composition as the one investigated in this chapter. For information Yan used arc melting, ball milling and hot pressing to obtain nanostructured dense pellets. It is also important to notice that Yan thermoelectric properties values are reported from 100 to 700 °C, whereas in our case the thermoelectric properties have been measured from 50 to 500 °C only.

The evolution of the electrical conductivity in function of temperature, presented in Figure V.8.a), is typical of degenerated semiconductors. Values go from 100,000 $S.m^{-1}$ at 50 °C to 60,000 $S.m^{-1}$ at 500 °C for all the investigated samples. The ones sintered at 1300 and 1400 °C exhibit similar values of electric conductivity, whereas the sample sintered at 1500 °C conducts electricity more efficiently (specially at lower temperatures) and the sample sintered at 1250 °C exhibits lower electrical conductivity values, whatever the temperature of interest.

It was shown that the grains of the sample sintered at 1500 °C are larger than the ones constituting the other sintered samples. This can explain its better electrical conductivity, whatever the temperature of interest, as grain boundaries are obstacles for carriers' motion. In the same way, the sample sintered at 1250 °C has a smaller grain size and is not totally dense, which is in favour of a lower electrical conductivity for all the temperature range of interest. On the contrary, the samples sintered at 1300 °C and 1400 °C are both totally dense and they exhibit a similar average grain size that is intermediate between the ones measured for the samples sintered at 1250 and 1500 °C. Finally, it can be also noticed that Yan's material exhibits lower electrical conductivity values than the ones measured for our investigated samples for all the temperature range of interest. This is probably linked to the fact that Yan's material is a nanosized-polycrystal (more grain boundaries having a detrimental effect on the main carriers' motion).

The positive Seebeck coefficient values of the all the as sintered samples are characteristic of a p-type conduction, as shown in Figure V.8.b). Seebeck values are quite close for all the samples, whatever the considered temperature. They go from 160 µV/°C at 50 °C to 220 µV/°C at 500 °C. Yan's material exhibits slightly better Seebeck coefficient values for all the temperature range of interest. It is possible that the charge carrier concentration is different between the samples we investigated and the ones from Yan, according to a possible Sb vaporization during the pellet manufacturing[3 and 4].

Figure V.8.c) presents the evolution of the thermal conductivity in function of temperature. For all the investigated samples, it decreases significantly with the increase of temperature, which is probably due to the electronic contribution to thermal conductivity. Indeed, as it is shown in Figure V.8.a) the electric conductivity decreases strongly when increasing the temperature and with the presence of nanometer-sized precipitates dispersed in the sintered microstructure. The lower thermal conductivities are observed for the sample sintered at 1300 °C, with values going from 3.4 W/m.K at 100 °C to 2.9 W/m.K at 500 °C. Differences of thermal conductivity values for the samples sintered at 1300 °C and 1400 °C are surprising, as the microstructure are quite similar (relative density, grain size and precipitate diameters). In the same way, for all the temperature range of interest, the sample sintered at 1250 °C has higher thermal conductivity values than the two previous ones, although exhibiting smaller grain and precipitate sizes. Finally, the sample sintered at 1500 °C has the highest thermal conductivity values of all the investigated samples. It is probably due to the higher grains and precipitates dimensions (less grain boundaries and possibly too large precipitates to scatter efficiently phonons). Yan's sample thermal conductivity is lower than the ones of our different sintered pellets, whatever the temperature of interest, in good agreement with the nanometer grain size of the material he investigated.

Finally, the ZT parameter depending on the temperature for the different samples investigated is presented in Figure V.8.d). All ZT values for the four samples are quite close. However, the ones for the sample sintered at 1300 °C are slightly better, with a maximum ZT value around 0.8 at 500 °C. This is possibly due to its lower thermal conductivity, whatever the considered temperature. It is interesting to point out that Yan's material ZT values are very close to the ones obtained for our different samples in the 200 to 500 °C temperature range.

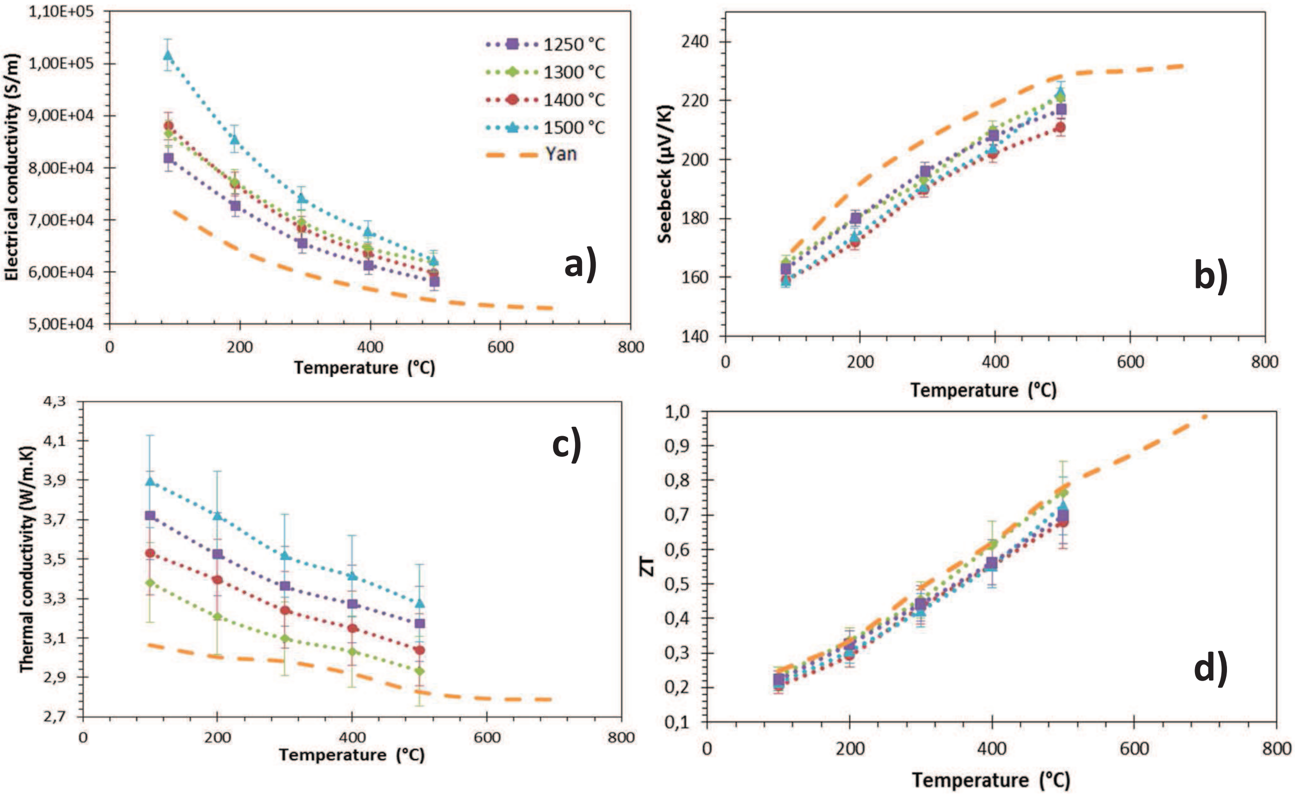

<u>Figure V.8 :</u> *Thermoelectric properties in function of temperature of the as-sintered* $Zr_{0.44}Hf_{0.44}Ti_{0.12}CoSn_{0.2}Sb_{0.8}$ *samples a) Electrical conductivity; b) Seebeck coefficient; c) Thermal conductivity; d) ZT parameter.*

The ZT values are still increasing at 500 °C for all our samples (in opposite to the "standard" n-type material, where a maximum of ZT was reached at 500 °C followed by a decrease for higher temperatures, see Chapter III). Therefore it is reasonable to suppose that a ZT value of 1.0 can be obtained at a higher temperatures, as for Yan's sample.

II - Cost reduction and simplification of the manufacturing process for p-type half-Heusler thermoelectric materials

As explained in Chapter IV, material cost is a key issue for the development of half-Heusler materials related to practical applications. With a price around 53 €/kg[5], the p-type $Hf_{0.44}Zr_{0.44}Ti_{0.12}CoSb_{0.8}Sn_{0.2}$ composition remains expensive for commercial applications. In order to reduce the price, two options are considered in the literature. First, NbFeSb-based p-type half-Heusler formulations are developed. As an example, Joshi and all. reported a ZT around 1.0 at 700 °C for an $Nb_{0.6}Ti_{0.4}FeSb_{0.95}Sn_{0.05}$ composition, being six times cheaper than the standard p-type $Hf_{0.44}Zr_{0.44}Ti_{0.12}CoSb_{0.8}Sn_{0.2}$ one[6]. Moreover, Zang and all. calculated that a ZT around 1.4 could be achieved at 530 °C for an NbFeSb composition[7]. A second option is to reduce the Hf content incorporated into the previously investigated p-type $Hf_{0.44}Zr_{0.44}Ti_{0.12}CoSb_{0.8}Sn_{0.2}$ composition.

As explained in the introduction of this chapter, in order to have an acceptable matching for the thermomechanical properties of the n and p-types legs incorporated in a device, this work focused on the second option, consisting of the reduction of the Hf content for a p-type material belonging to the (Ti, Zr, Hf)Co(Sb, Sn) family. Indeed, as for the n-type composition investigated in Chapter III, Hf is responsible of most of the raw material price. The Hf contribution represents more than 77 % of the total raw material cost, as shown in Figure V.9.

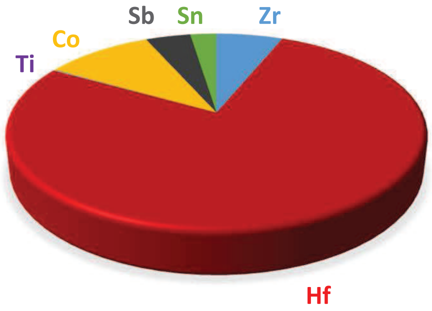

Figure V.9 : *Contribution of each constituent to the* $Hf_{0.44}Zr_{0.44}Ti_{0.12}CoSb_{0.8}Sn_{0.2}$ *composition cost.*

II.1 - Experimental protocol

As explained in Chapter I, theoretically, the lattice thermal conductivity can be reduced by large differences in the atomic mass and size for the atoms belonging to the crystal structure. Yan and all. investigated the $Hf_{1-x}Ti_xCoSb_{0.8}Sn_{0.2}$ composition and obtained the lowest thermal conductivity and the higher ZT values for x=0.2[1]. Considering that the atomic sizes of Hf and Zr are almost the same (covalent radius about 175 pm for both), we choose to investigate the $Zr_{0.8}Ti_{0.2}CoSb_{0.8}Sn_{0.2}$ composition.

In order to maintain the ZT parameter as high as possible, with the need to further reduce the Hf content and therefore decrease the material price as much as possible, the same solutions as the ones retained for the n-type material investigated in Chapter IV were combined and used. Accordingly, a $Zr_{0.8}Ti_{0.2}CoSb_{0.8}Sn_{0.2}$ ingot was synthetized by induction melting. Then, the powder is ball milled and stocked under ambient atmosphere (air). After sieving though a 56 µm sieve, 1.5 %wt of HfO_2 particles (Sigma Aldrich, Lyon, France, 99.95% purity, same as the one described in Section IV.I) were incorporated into a tungsten carbide jar, filled under ambient air, containing the $Zr_{0.8}Ti_{0.2}CoSb_{0.8}Sn_{0.2}$ collected powder. The mix is then milled during 1h at 250 rpm with a planetary ball mill. Finally, the composite powder is sintered by SPS at 1300 °C, all other parameters being the same as exposed in Chapter II.

As for the n-type material investigated in Chapter IV, the p-type $Hf_{0.44}Zr_{0.44}Ti_{0.12}CoSb_{0.8}Sn_{0.2}$ composition will be named "standard" composition and the p-type $Zr_{0.8}Ti_{0.2}CoSb_{0.8}Sn_{0.2}$ + 1.5 %wt HfO_2 one will be named "oxidized" $Zr_{0.8}Ti_{0.2}CoSb_{0.8}Sn_{0.2}$ + 1.5 %wt HfO_2 sample.

II.2 - Microstructure analysis of the sintered pellet

- Sintering curve.

First of all, the height variation of the pellet during the sintering is measured and the densification rate of the "oxidized" $Zr_{0.8}Ti_{0.2}CoSb_{0.8}Sn_{0.2}$ + 1.5 %wt HfO_2 sample, depending on the temperature, is calculated. The results are reported in Figure V.10. As for the "standard" material densification rate curve, the standard bell-shape is observed. However, it appears that the maximum densification rate is shifted about 100 °C towards lower temperature values for the "oxidized" $Zr_{0.8}Ti_{0.2}CoSb_{0.8}Sn_{0.2}$ + 1.5 %wt HfO_2 sample.The same phenomenon was observed for the "oxidized" n-type composition investigated in Section IV.II.

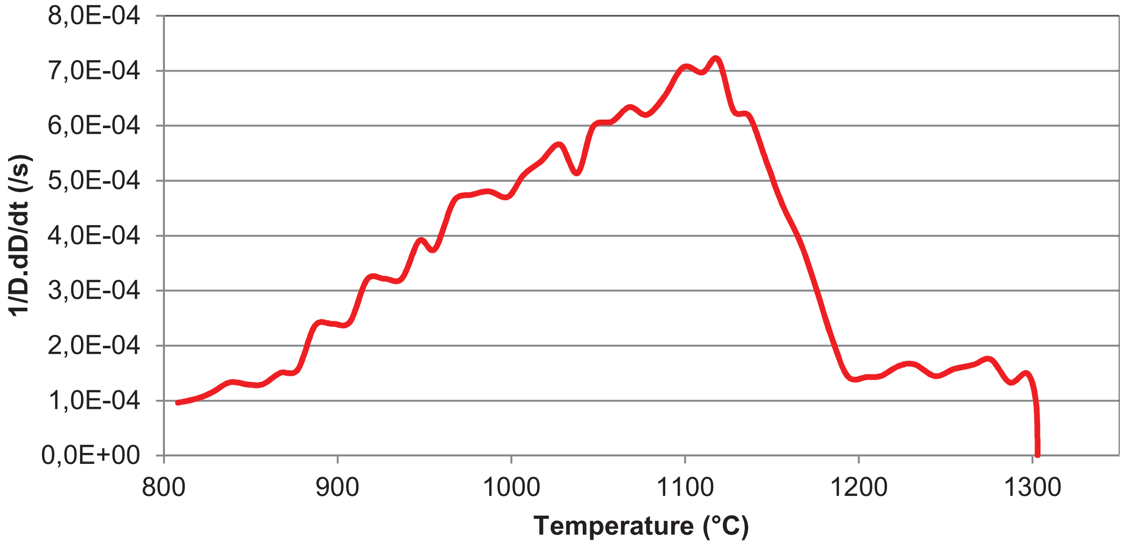

*<u>**Figure V.10 :**</u> Densification rate of the "oxidized" material.*

- X-ray diffraction.

In order to confirm the half-Heusler structure of the sample, X-ray diffraction has been completed as presented in Figure V.11. The XRD pattern of the “standard” composition sintered at 1300 °C has been recalled for comparison. The “oxidized” $Zr_{0.8}Ti_{0.2}CoSb_{0.8}Sn_{0.2}$ + 1.5 %wt HfO_2 sample exhibits peaks of two main half-Heusler phases with a typical $C1_b$ structure (space group 216, $F\bar{4}3m$). The first one exhibits a main lattice parameter around 6.04 Å and the second one is shifted toward the right side and has a main lattice parameter around 6.01 Å. These results suggest that the sintered microstructure incorporates a phase enriched in Zr, with the larger lattice parameter, and another one, with a higher Ti content, with a smaller lattice parameter.

In addition to the half-Heusler phases, additional peaks are also observed. First, peaks due to the presence HfO_2[2] cannot be detected for the “oxidized” $Zr_{0.8}Ti_{0.2}CoSb_{0.8}Sn_{0.2}$ + 1.5 %wt HfO_2 sample. However, peaks from a monoclinic zirconia[8] phase are detected. Secondly, a Sn-β[9] metallic phase is detected in the “oxidized” sintered material.

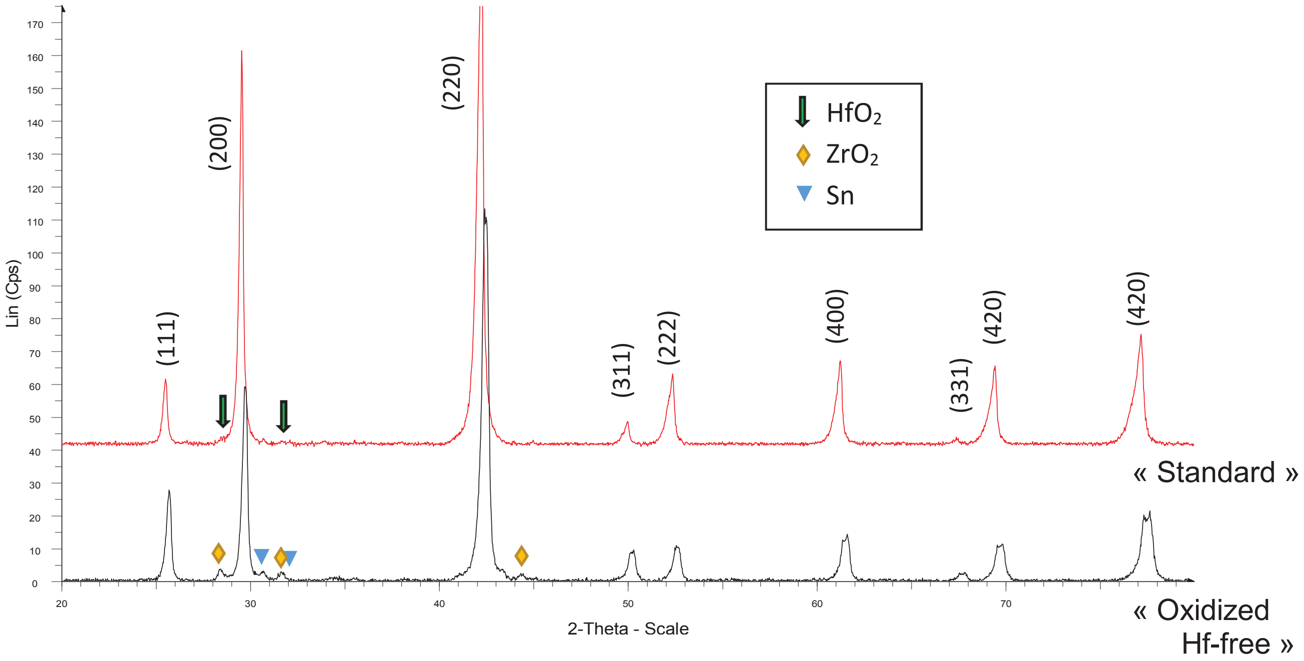

Figure V.11 : *XRD patterns of the $Hf_{0.44}Zr_{0.44}Ti_{0.12}CoSb_{0.8}Sn_{0.2}$ composition and $Zr_{0.8}Ti_{0.2}CoSb_{0.8}Sn_{0.2}$ + 1.5 %wt HfO_2 oxidized sample.*

- SEM analyses.

The apparent density of the sintered sample was measured to be around 95 %.

Microstructure analysis is performed by SEM observations on a fresh fracture surface, in secondary electron mode. Images at different magnifications are presented in Figure V.12. The microstructure is clearly different from the ones observed for all the previous investigated materials. The sintered material is now composed of large grains surrounded by smaller ones. From the SEM images a corresponding diameter around 2.9 µm was calculated for more than 300 large grains belonging to the "oxidized" $Zr_{0.8}Ti_{0.2}CoSb_{0.8}Sn_{0.2}$ + 1.5 %wt HfO_2 composition.

Views at higher magnifications, reported in Figure V.12.b and c) show that two types of smaller grains can be observed in the sample. The first ones, very numerous, have a lenticular morphology with a diameter around 450 nm. They constitute most of the mater surrounding the large grains. The second ones, outlined by blue ellipses, are small polygonal shaped particles around 100 nm in diameter, forming large agglomerates (around 3 µm diameter). Considering the observations made on the n type "composite" materials in Section IV.I, they most probably correspond to the HfO_2 commercial powder incorporated into the formulation before sintering.

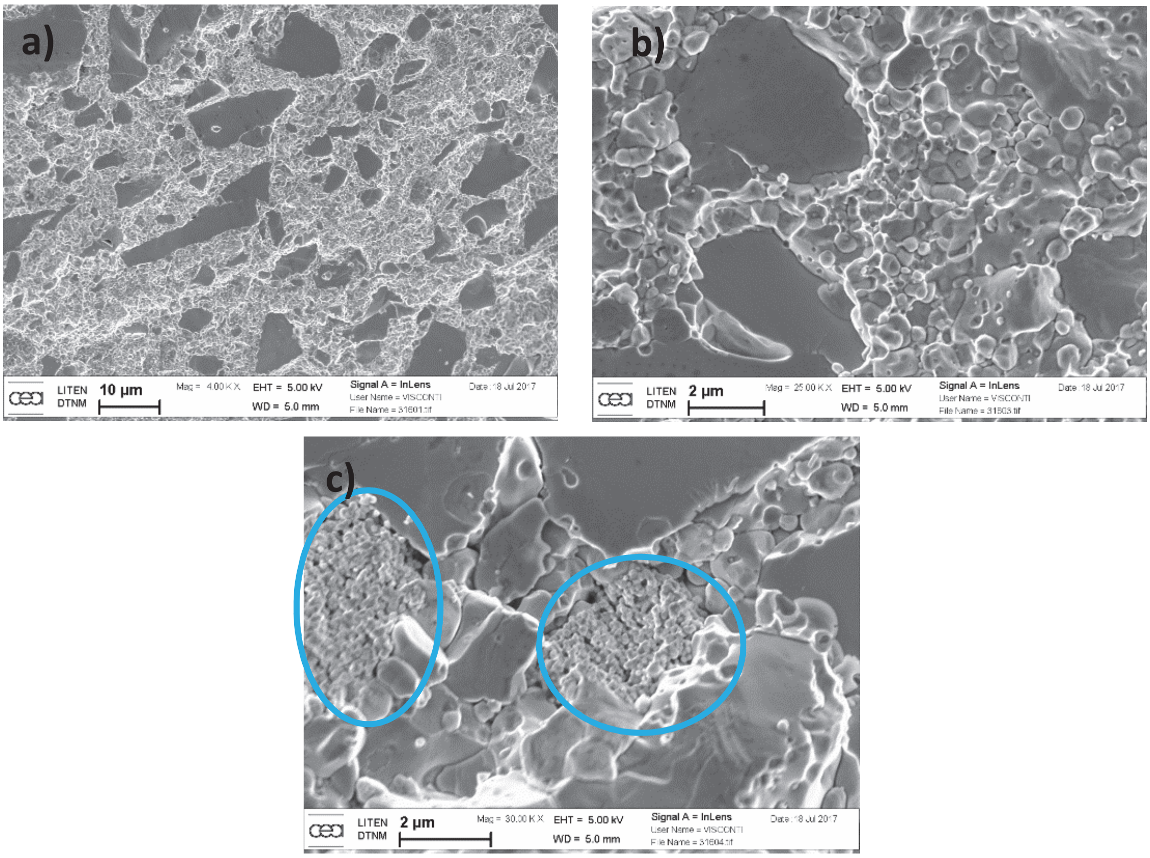

Figure V.12 : *SEM images of a fracture surface of the $Zr_{0.8}Ti_{0.2}CoSb_{0.8}Sn_{0.2}$ + 1.5 %wt HfO_2 oxidized sample at different magnifications.*

In order to check the grains compositions, EDS analyses, presented in Figure V.13, have been completed at different magnifications on a fresh fracture surface of the "oxidized" $Zr_{0.8}Ti_{0.2}CoSb_{0.8}Sn_{0.2}$ + 1.5 %wt HfO_2 sample.

EDS mapping of the general view is presented in Figure V.13.a). A quantitative analysis shows that the global composition is very close to the target one, proving that there is no significant loss of matter during the sintering step. Moreover, it is noticed that the large grains are enriched in Co, Zr and Sb, whereas smaller grains seem richer in Ti. Rausch and all. Made the same observation for a $Hf_{0.35}Zr_{0.35}Ti_{0.3}CoSb_{1-x}Sn_x$ material[10]. The quantified compositions are $Zr_{0.9}Ti_{0.1}Co_{1.1}Sb_{0.9}Sn_{0.1}$ and $Zr_{0.7}Ti_{0.3}Co_{0.9}Sb_{0.8}Sn_{0.2}$, for large and small grains, respectively. These observations are in agreement with the XRD results. Also, from these maps it is also possible to discern Hf and Zr oxide-based compounds and Sn segregation.

As shown in Figure V.13.b), observations at higher magnifications highlight that the small lenticular grains are constituted by three types of particles: half-Heusler small grains (black ellipse) and two types of precipitates. Indeed, as outlined by red doted circles, Ti-rich precipitates are present in the material. The other kind of precipitates detected are Zr oxide-based (surrounded by green broken lines in the picture). These results are confirmed by the EDS spectrum shown in Figure V.13.c). Moreover, Sn segregation can still be observed.

Finally, as outlined by blue circles in Figure V.13.b and d), it is confirmed that the small polygonal shaped agglomerated particles are enriched in Hf and O. Accordingly, they correspond to the HfO_2 particles incorporated in the material formulation.

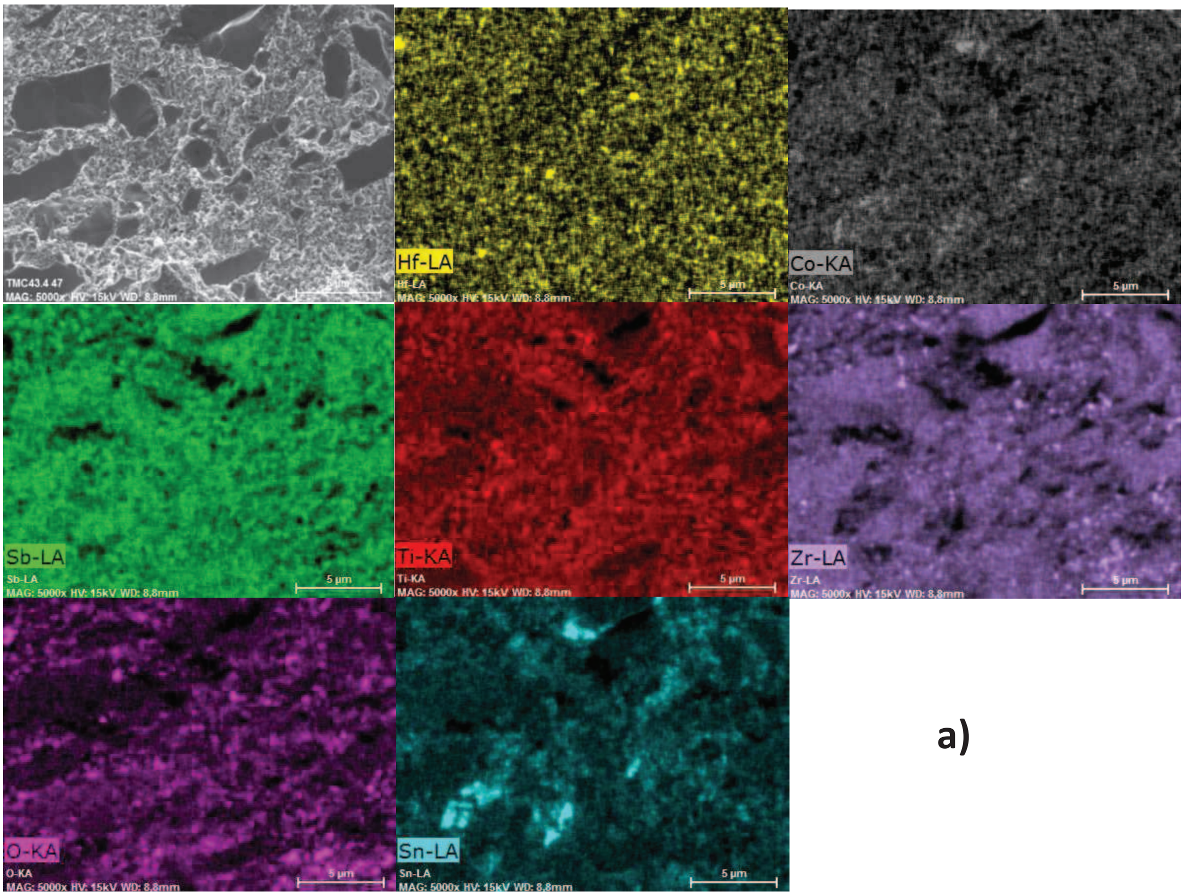

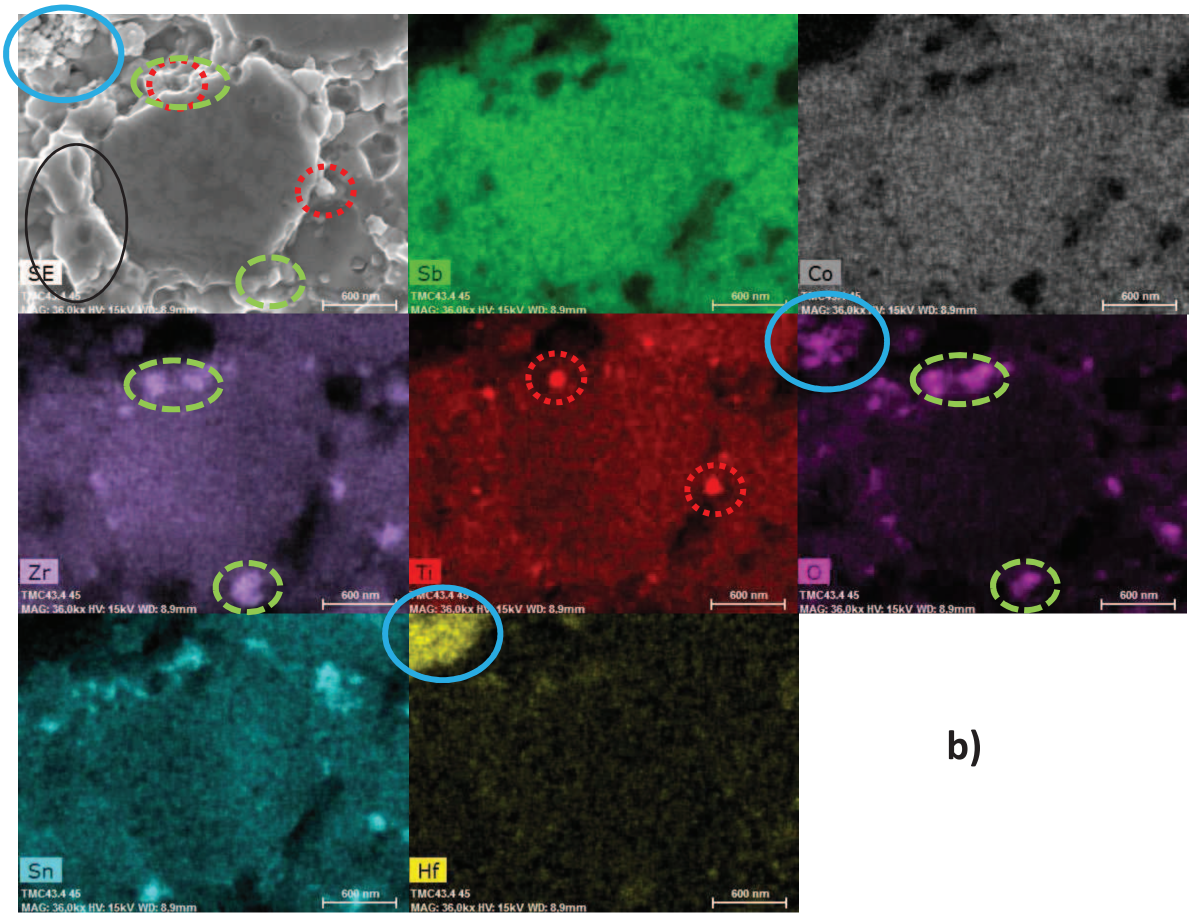
SE
Sb
Co
Zr
Ti
O
Sn
Hf
TMC43.4 45
MAG: 36.0kx HV: 15kV WD: 8.9mm
600 nm

b)

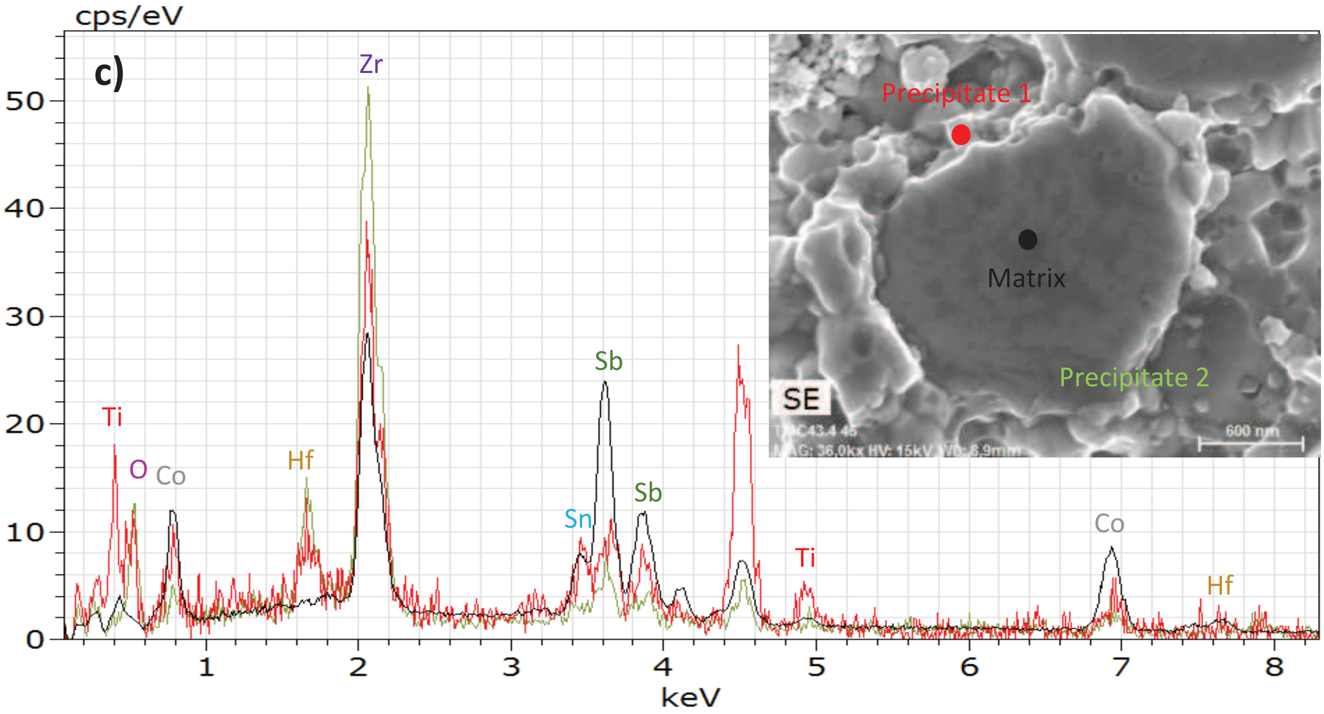
cps/eV
0
10
20
30
40
50
1
2
3
4
5
6
7
8
keV
Ti
O
Co
Hf
Zr
Sn
Sb
Sb
Ti
Co
Hf
Precipitate 1
Matrix
Precipitate 2
SE
TMC43.4 45
MAG: 36.0kx HV: 15kV WD: 8.9mm
600 nm

c)

d)

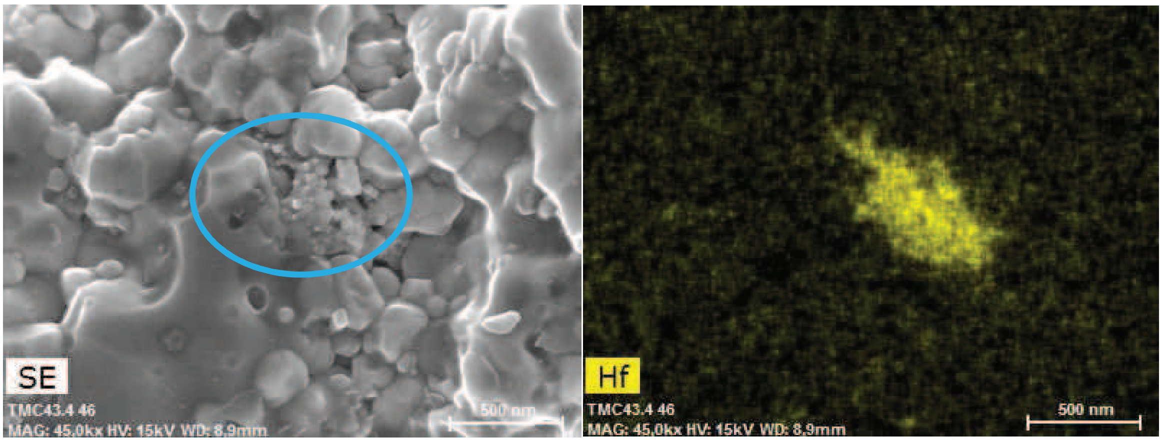

Figure V.13 : *a), b) and d) EDS maps of a fracture surface and c) spectrum on the different type of precipitates in the sintered* $Zr_{0.8}Ti_{0.2}CoSb_{0.8}Sn_{0.2}$ *+ 1.5 %wt* HfO_2 *oxidized sample*

Microstructures of the “standard” and the “oxidized” $Zr_{0.8}Ti_{0.2}CoSb_{0.8}Sn_{0.2}$ + 1.5 %wt HfO_2 samples are very different. Moreover the difference in the nature of the oxide precipitates observed in the sintered microstructures, the grain size is much lower for the second composition. This is possibly linked to the presence of oxygen in the powder before sintering (leading to the formation of in-situ precipitates at grain boundaries during sintering) and to the HfO_2 ex-situ nanoparticles incorporated in the formulation. Indeed, oxide-based precipitates are believed to exert a Zener pinning effect on grain boundaries, limiting grain growth[11].

II.3 - Thermoelectric properties

The thermoelectric properties of the “oxidized” $Zr_{0.8}Ti_{0.2}CoSb_{0.8}Sn_{0.2}$ + 1.5 %wt HfO_2 sample have been measured and discussed in the 100 to 500 °C temperature range of interest. As presented in Figure V.14, results are compared to the one of the “standard” material sintered at 1300 °C and to the data reported by He and all.[12] and Rausch and all.[13]. He synthetized a $Hf_{0.19}Zr_{0.76}Ti_{0.05}CoSb_{0.8}Sn_{0.2}$ material using arc melting, ball milling and hot pressing to obtain a nanostructured dense pellet. Rausch used arc melting followed by annealing at 900 °C for 7 days and finally quenching to synthetized a $Zr_{0.5}Ti_{0.5}CoSb_{0.8}Sn_{0.2}$ material. Rausch observed a phase separation (areas enriched in Zr and other enriched in Ti) into the individual grains of the sample she investigated.

Figure V.14.a) shows the evolution of the electrical conductivity in function of temperature. The electrical conductivity values for the “oxidized” $Zr_{0.8}Ti_{0.2}CoSb_{0.8}Sn_{0.2}$ + 1.5 %wt HfO_2 sample are very low. Indeed, values are going from 47,000 S/m at 50 °C to 35,000 S/m at 500 °C. It represents a 50 % decrease compared with the electric conductivity values observed for the “standard” p-type sample, whatever the temperature of interest. This trend can be explained by the difference of density and microstructure for both sintered materials. Indeed, the “oxidized” $Zr_{0.8}Ti_{0.2}CoSb_{0.8}Sn_{0.2}$ + 1.5 %wt HfO_2 sample is not fully dense (95 %) and exhibits a nanostructured matrix phase, with numerous oxide precipitates. All these factors are in favour of decreasing the carriers’ motion and increasing the electrical resistivity of a material. He's material electrical conductivity values are close to the ones of our "standard" p-type composition, whereas Rausch's ones are similar to the ones of our "oxidized" $Zr_{0.8}Ti_{0.2}CoSb_{0.8}Sn_{0.2}$ + 1.5 %wt HfO_2 sample. Rausch's manufacturing process is based on ingot quenching without using a powder/sintering approach. Such a manufacturing way probably promotes the formation of numerous cracks into the material that are detrimental to the electrical conductivity. He's material values of electrical conductivity are quite surprising considering that it is a nanosized polycrystal, numerous grain boundaries possibly acting as charge carriers motion obstacles. Nonetheless, the good electrical conductivity values obtained by He, in comparison to our ones, is probably linked to the fact that the grain boundaries in his material are possibly perfect (low energy configuration) and that the insulating nature of oxide precipitates located at grain boundaries in our materials prevent carriers motion.

The positive Seebeck coefficient values in Figure V.14.b) demonstrate the p-type nature of all the as sintered samples. Seebeck coefficient values of the "oxidized" $Zr_{0.8}Ti_{0.2}CoSb_{0.8}Sn_{0.2}$ + 1.5 %wt HfO_2 material is 5 to 10 % higher than the one of the "standard" composition in the 100 to 500 °C temperature range. Results from He and Rausch are parts of a global envelop delimited by our experimental values of Seebeck coefficients. Theoretically, the dopant level is supposed to be the same for all the four material exposed, with a 80/20 proportion of Sb/Sn. However, it is possible that Sb vaporization occurs during the pellet manufacturing step, modifying the main carrier concentration in the sintered samples[3 and 4]. Indeed, it can be interesting to notice that the "oxidized" $Zr_{0.8}Ti_{0.2}CoSb_{0.8}Sn_{0.2}$ + 1.5 %wt HfO_2 sample was synthetized adding an extra percentage of Sb to offset the vaporization during levitation melting in the induction furnace. In the same way, Rausch compensated the weight loss during arc melting by adding the appropriate amount of Sb in the ingot. On the contrary, no Sb compensation has been done for the "standard" and He's samples.

The evolution of thermal conductivity with temperature is presented in Figure V.14.c). With values ranging from 4.3 W/m.K at 100 °C to 3.5 W/m.K at 500 °C, the thermal conductivity is around 20 % higher for the "oxidized" $Zr_{0.8}Ti_{0.2}CoSb_{0.8}Sn_{0.2}$ + 1.5 %wt HfO_2 sample than for the "standard" one. He's material thermal conductivity values are situated in the middle of both, whereas Rausch material exhibits higher thermal conductivity values, especially at low temperatures. This trend can be explained by the lack of Hf in the half-Heulser structure of the "oxidized" $Zr_{0.8}Ti_{0.2}CoSb_{0.8}Sn_{0.2}$ + 1.5 %wt HfO_2 and $Zr_{0.5}Ti_{0.5}CoSb_{0.8}Sn_{0.2}$ materials. Indeed, Hf present in the half-Heusler matrix lowers thermal conductivity as a result of a heavier atomic mass compared to other elements. The substitution effect, promoting phonons scattering, appears to be less efficient without Hf incorporation in the formulation. Thus, for the "standard" material, He's one and the "oxidized" $Zr_{0.8}Ti_{0.2}CoSb_{0.8}Sn_{0.2}$ + 1.5 %wt HfO_2 one, the higher the Hf content, the lowest the thermal conductivity, whatever the temperature of interest and the microstructure of the sintered samples. Differences of thermal conductivity between Rausch and our Hf-free material is probably linked to the microstructure difference. Indeed, our material has a finer microstructure and contains oxide-based precipitates, both effects promoting more phonon scattering.

To finish, Figure V.14.d) presents the evolution of the ZT parameter depending on the temperature for the different samples considered. A maximum ZT around 0.7 at 500 °C was obtained for the "oxidized" $Zr_{0.8}Ti_{0.2}CoSb_{0.8}Sn_{0.2}$ + 1.5 %wt HfO_2 sample. Additionally, values are close to the ones of the "standard" and He's samples in the temperature range of interest. In comparison, Rausch's ZT values are more than 50 % lower than the ones calculated for ours samples, whatever the temperature of interest.

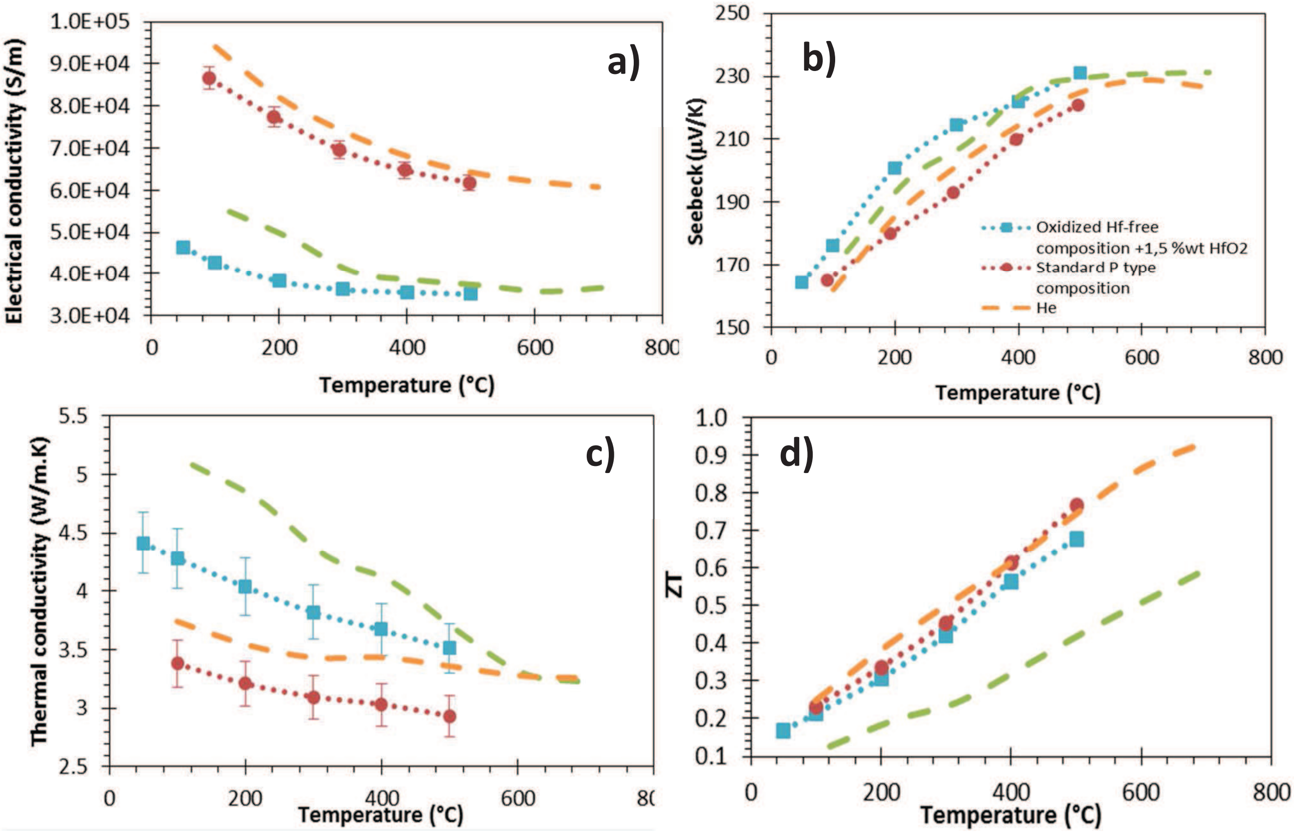

Figure V.14 : *Thermoelectric properties in function of temperature of the as-sintered* $Zr_{0.8}Ti_{0.2}CoSb_{0.8}Sn_{0.2}$ + 1.5 %wt HfO_2 oxidized sample *compared to the* $Zr_{0.44}Hf_{0.44}Ti_{0.12}CoSn_{0.2}Sb_{0.8}$ *"standard", He's and Rausch's ones a) Electrical conductivity; b) Seebeck coefficient; c) Thermal conductivity; d) ZT parameter.*

III - Conclusion

Surprisingly, a very different microstructure was noticed between the “standard” and the “oxidized” $Zr_{0.8}Ti_{0.2}CoSb_{0.8}Sn_{0.2}$ + 1.5 %wt HfO_2 samples. Indeed, the “standard” sample exhibits the same kind of microstructure as the one observed for the n-type materials previously observed in Chapters III and IV. That is to say, a micronic average grain size (3.5 to 5.4 µm, depending on the sintering temperature) with nanometer-sized Hf oxide-based precipitates located at the grain boundaries. On the opposite, the “oxidized” $Zr_{0.8}Ti_{0.2}CoSb_{0.8}Sn_{0.2}$ + 1.5 %wt HfO_2 sample exhibits an original microstructure, with large grains (3 µm) surrounded by a mixture of half-Heusler small grains, Ti enriched precipitates, Zr oxide-based precipitates (450 nm average size for the three kinds of compounds) and aggregates (3 µm) constituted of the HfO_2 powder incorporated before sintering.

When looking at the ZT values, they are relatively close for both materials on the 100 to 500 °C temperature range, with ZT maximum values of 0.8 and 0.7 at 500 °C for the “standard” and the oxidized” $Zr_{0.8}Ti_{0.2}CoSb_{0.8}Sn_{0.2}$ + 1.5 %wt HfO_2 samples, respectively.

The material stoichiometry modification used to elaborate the “oxidized” $Zr_{0.8}Ti_{0.2}CoSb_{0.8}Sn_{0.2}$ + 1.5 %wt HfO_2 sample leads to a 70 % reduction of the cost per kilogram of raw material, as shown in Figure V.15. Additionally, the global manufacturing process is simplified, without drastically changing the thermoelectric properties. To conclude, it could be much more favourable for practical applications to use such a cheaper but slightly less performant material.

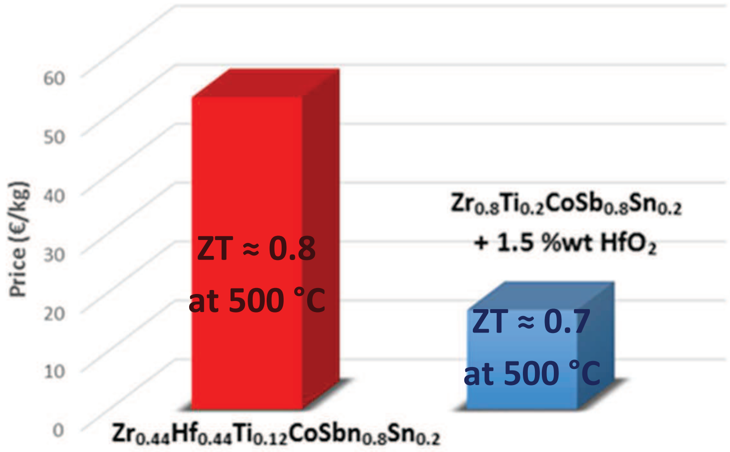

Figure V.15 : *Price comparison between the p-types $Zr_{0.8}Ti_{0.2}CoSb_{0.8}Sn_{0.2}$ + 1.5 %wt HfO_2 and $Zr_{0.44}Hf_{0.44}Ti_{0.12}CoSn_{0.2}Sb_{0.8}$ raw material compositions*

---

[1] Yan, X., Liu, W., Chen, S., Wang, H., Zhang, Q., Chen, G. and Ren, Z., Thermoelectric Property Study of Nanostructured p-Type Half-Heuslers (Hf, Zr, Ti)$CoSb_{0.8}Sn_{0.2}$, Adv. Energy Mater.,2013, 3: 1195–1200

[2] JCPDS file 00-043-1017

[3] Chen, S., Ren, Z., Recent progress of half-Heusler for moderate temperature thermoelectric applications, Maretials Today, 2013, 16, 10 387–395

[4] Y. Xia, V. Ponnambalam, S. Bhattacharya, A.L. Pope, S.J. Poon, T.M. Tritt, Electrical transport properties of TiCoSb half-Heusler phases that exhibit high resistivity, J. Phys. Condens. Matter, 2001, 13, 77-89

[5] https://www.metalprices.com.

[6] Joshi, G., He, R., Engber, M., Samsonidze, G., Pantha, T., Dahal, E., Dahal, K., Yang, J., Lan, Y., Kozinskyc, B. and Ren Z., NbFeSb-based p-type half-Heuslers for power generation applications, Energy Environ. Sci., 2014, 7, 4070

[7] Fang, T., Zheng, S., Chen, H., Cheng, H., Wang, L. and Zhang, P. Electronic structure and thermoelectric properties of p-type half-Heusler compound NbFeSb: a first-principles study, RSC Adv., 2016, 6, 10507-10512

[8] JCPDS file 04-004-7747

[9] JCPDS file 04-004-7747

[10] Rausch, E., Balke, B., Deschauer, T., Ouardi, S., Felser, C., Charge carrier concentration optimization of thermoelectric p-type half-Heusler compounds, APL Materials, 2015, 3, 041516

[11] Katsuyama, S., Kobayashi, T., Effect of mechanical milling on thermoelectric properties of half-Heusler $ZrNiSn_{0.98}Sb_{0.02}$ intermetallic compound, Materials Science and Engineering, 2010, 15, 99-103

[12] He, R., Seok Kim, H., Lan, Y., Wang, D., Chen, S., and Ren, Z., Investigating the thermoelectric properties of p-type half-Heusler $Hf_x(ZrTi)_{1\_x}CoSb_{0.8}Sn_{0.2}$ by reducing Hf concentration for power generation, RSC Adv., 2014, 4, 64711

[13] Rausch E., Balke B., Ouardi S., Felser C., Enhanced thermoelectric performance in the p-type half-Heusler (Ti/Zr/Hf)CoSb0.8Sn0.2 system via phase separation, Phys Chem., 2014, 16, 25258-62

Conclusion

During the present PhD work, the half-Heusler materials family has been chosen to address the development of thermoelectric materials, devoted to be incorporated in devices, for applications in the 300 to 500 °C temperature range. This work is focused on the development and understanding of the link between the microstructure and thermoelectric properties of n and p-types half-Heusler alloys having the generic compositions MNiSn (n-type) and MCoSb (p-type), with M being Ti, Zr and Hf. The review of current literature indicates that such compositions exhibit among the best figures of merit for half-Heusler alloys.

All the investigated compositions have been elaborated following the same process. First, raw materials were melted using a cold crucible levitation melting furnace. Subsequently, ball milling and sieving of the ingots were used to obtain a calibrated half-Heusler powder. Afterwards, spark plasma sintering (SPS) was used to manufacture dense polycrystalline pellets. Finally, the sintered materials were characterised in terms of their microstructure and thermoelectric properties, from room temperature to 500 °C.

Based on the literature review on half-Heusler compounds, a preferential stoichiometry to investigate was retained for both n and p-types materials. Accordingly, the n-type $Hf_{0.25}Zr_{0.25}Ti_{0.5}NiSb_{0.006}Sn_{0.994}$ and p-type $Hf_{0.44}Zr_{0.44}Ti_{0.12}CoSb_{0.8}Sn_{0.2}$ formulations were synthetized and sintered at different temperatures. For both kinds of materials, we shown that the sintered microstructure is constituted by a half-Heusler micron-sized grains (3 to 5 µm) matrix with in-situ precipitated nanosized Hf oxide-based particles, manly located at the grain boundaries. In parallel, thermoelectric properties have been measured and discussed in the temperature range of interest. The link with the microstructure (density, grain size, precipitate formation...) has been established. High relative density and grain size values have a positive impact on electrical conductivity, whereas precipitates are believed to scatterephonons, leading to a decrease in thermal conductivity. With a maximum ZT values of 0.9 and 0.8 at 500 °C for the n and p types compositions sintered at 1140 and 1300 °C, respectively, optimal sintering temperatures have been identified.

Cost is one of the primary issues for commercial applications of thermoelectric devices. As a result, in a second phase, the PhD work concentrated on cost reduction and simplification of the manufacturing process, without negatively impacting the materials' thermoelectric properties. To achieve these goals, two approaches have been retained, based on the role played by the oxide-based precipitates in the previously investigated materials. First, as Hf is known to be the most expensive constituent incorporated in the chosen generic compositions, sintered pellets of a composite material have been elaborated by mixing an Hf-free half-Heusler powder with HfO_2 nanoparticles. The second approach, was to carry out some critical steps in an ambient atmosphere (air) and not in inert glove boxes. While this promotes the formation of in-situ oxide-based precipitates that decrease thermal conductivity, it also greatly simplifies handling operations.

On the one hand, both approaches were tested separately for the n-type material. First, a $Zr_{0.5}Ti_{0.5}NiSb_{0.006}Sn_{0.994}$ powder was synthetized and mixed with HfO_2 nanoparticles. In that case, in situ formation of ZrO_2 precipitates occurs, in complement to the ex-situ HfO_2 particles incorporated. It leads to a 15 to 20 % thermal conductivity reduction and to an 11 to 23 % ZT improvement in the 200 to 500 °C temperature range. In the same time, a 50 to 60 % decrease in the cost per kilogram of the raw powder was calculated for a composite formulation incorporating 1.5 %wt of HfO_2, compared to the $Hf_{0.25}Zr_{0.25}Ti_{0.5}NiSb_{0.006}Sn_{0.994}$ composition. Secondly, the synthesis of the

$Hf_{0.25}Zr_{0.25}Ti_{0.5}NiSb_{0.006}Sn_{0.994}$ powder under air leads to the formation of more Hf-oxide based precipitates, which promotes, once again, low thermal conductivity values. For both solutions adopted, maximum ZT values around 1.0 were obtained at 500 °C.

On the other hand, both solutions to reduce the material cost and simplify the manufacturing process have been used simultaneously for the p-type composition. Therefore, a $Zr_{0.8}Ti_{0.2}CoSb_{0.8}Sn_{0.2}$ powder was synthetized under ambient air and mixed with 1.5 %wt of HfO_2 nanoparticles before sintering. In this case, the observed microstructure was considerably different that the one observed for all the other investigated samples. Indeed, an original microstructure with large half-Heusler grains (3 µm) surrounded by a mix of nanometer-sized half-Heusler grains, Ti enriched precipitates, Zr oxide-based precipitates and 3 µm aggregates constituted by relics of the HfO_2 nanoparticles incorporated before sintering is observed. Surprisingly, the thermal conductivity of this material is not lowered compared to the one of the $Hf_{0.44}Zr_{0.44}Ti_{0.12}CoSb_{0.8}Sn_{0.2}$ composition. However, the ZT parameter is relatively similar in the 100 to 400 °C temperature range. A 7 % decrease was observed at 500 °C, with a maximum ZT value around 0.7 at 500 °C obtained for the $Zr_{0.8}Ti_{0.2}CoSb_{0.8}Sn_{0.2}$ + 1.5 %wt of HfO_2 oxidized sample. Such a composite formulation enables a 70 % reduction of the cost per kilogram of raw material and a strong simplification of the manufacturing process. To conclude, it could be much more favourable for practical applications to use such a cheaper but slightly less performant material.

To put in a nutshell, cost reduction and the simplification of the manufacturing process has been achieved for both n and p types materials. Considering that, for the n-type material, an improvement in thermoelectric properties was observed for both approaches described above, it could be interesting to combine them. On the contrary, for the p-type material, the separation of both approaches could help to understand changes observed in the microstructure and therefore the slight decrease of the thermoelectric properties.

Furthermore, it has also to be outlined that we tried to evaluate the precipitates concentrations in the sintered materials investigated using SEM or TEM observations. Unfortunately, up to now no conclusive results have been obtained, because of the heterogeneous distribution of the different kind of precipitates. Therefore, it could be interesting to use the Rietveld analysis method on XRD diffractograms to evaluate the quantity of oxide-based precipitates in the sintered materials. Additionally, HRTEM observations at grain boundaries and at the different interfaces could also be a useful characterisations to complete this work.

In order to be suitable for commercial applications, further developments on the investigated n and p-types materials would be to evaluate their thermoelectric properties and microstructure evolutions regarding thermal ageing in a desired atmosphere. Additionally, a mandatory point is to scale up the material production volume per day, by manufacturing larger/more pellets of both types of materials without inducing any detrimental effect on the thermoelectric properties (whether by using SPS to synthesise 60 mm diameter pellets or by investigating another sintering process).

It should be noticed that this PhD work has been the first one to focus on half-Heusler materials in the lab. A European project (INTEGRAL) is currently running in collaboration with Isabellenhütte (Dillenburg, Gremany). It is focused on further developments of this materials family for commercial applications.

Résumé en français

Depuis les cinquante dernières années, les préoccupations d'ordre énergétique et le réchauffement climatique sont au cœur de l'actualité. En effet, l'énergie nucléaire étant grandement controversée en Europe et l'appauvrissement des matières fossiles engendrent un fort intérêt pour le développement de nouvelles sources d'énergie renouvelable. Il est intéressant de noter que de nos jours, une grande partie de l'énergie produite est rejetée et perdue sous forme de chaleur. Ainsi, dans cette quête de nouvelles sources d'énergie renouvelable, la récupération d'énergie par des générateurs thermoélectriques apparait comme une solution viable pour le mix énergétique de demain.

La thermoélectricité est la conversion directe et réciproque entre énergie thermique et électrique. Les générateurs thermoélectriques sont constitués d'un assemblage de plots de semi-conducteurs de type n et p, connectés électriquement en série et thermiquement en parallèle. Un gradient de température appliqué entre les deux faces du générateur entraine une migration des charges du matériau (flux d'électrons dans le cas du type n et de trous pour le type p) vers le coté froid. Un courant électrique est donc généré.

La performance d'un matériau thermoélectrique est exprimée par le facteur de mérite ZT, donné par l'expression : $ZT=S^2\sigma T/\kappa$. Un ZT élevé peut être obtenu en optimisant les propriétés de transport du matériau. Le coefficient de Seebeck, (S), et la conductivité électrique, (σ), doivent être le plus élevé possible, alors que la conductivité thermique (κ) doit rester faible. Une des stratégies pour maximiser le ZT est donc de limiter la conductivité thermique du semi-conducteur considéré sans affecter ses propriétés de transport électroniques. Cela peut être obtenu en multipliant les sources de diffusion des phonons dans le matériau, ce qui diminue ainsi leur temps de vie.

La thermoélectricité a commencé à susciter l'attention des scientifiques en 1950, quand Ioffe déclare que des semi-conducteurs dopés peuvent être utilisés pour générer du froid ou de l'électricité. A partir de ce moment, et ce malgré leur faible efficacité et leur coût relativement élevé, les systèmes thermoélectriques ont attiré l'attention du monde scientifique grâce à leurs avantages comparativement aux moyens de récupération d'énergie plus conventionnels. En effet, ce sont des dispositifs compacts, statiques, silencieux et fiables, qui possèdent une longue durée de vie sans nécessiter de maintenance et impactant peu l'environnement.

Vers la fin du 20$^{\text{ème}}$ siècle, les générateurs thermoélectriques sont couramment utilisés dans la production de froid par module a effet Peltier et pour des générateurs radio-isotopiques intégrés dans les sondes spatiales. L'augmentation croissante de la demande en énergie, combinée avec les actuels enjeux environnementaux, a suscité un regain d'intérêt pour la thermoélectricité, notamment pour son utilisation face à l'importante quantité d'énergie perdue sous forme de chaleur dans l'industrie ou dans le cadre domestique. De nos jours, l'utilisation des modules thermoélectriques est limitée par sa faible efficacité de conversion, environ 10 %, principalement liée aux propriétés des matériaux incorporés dans le système thermoélectrique. En effet, bien que ces faibles performances soient acceptables pour des applications de niches telles que celles citées plus haut, elles doivent encore être améliorées afin d'être rentables dans des applications « grand public ». Par exemple, actuellement, les études de modules thermoélectriques émergent pour leur utilité en tant que sources de récupération d'énergie perdue sous forme de chaleur dans des applications comme l'automobile ou les systèmes d'énergie solaire et géothermique.

Ainsi, en ce qui concerne la récupération d'énergie perdue sous forme de chaleur, le challenge actuel se situe dans la gamme de température allant de 300 à 500 °C. En effet, la perte d'énergie thermique des automobiles et des camions est une préoccupation grandissante car le transport est responsable d'environ 20 % du carbone rejeté dans l'atmosphère. De plus, la chaleur perdue générée dans les industries de la métallurgie ou du nucléaire, par exemple, est également non négligeable. Pour ces deux segments, la récupération d'énergie thermique pourrait donc être mise à profit grâce à l'utilisation de modules thermoélectriques ayant un rendement optimum dans la gamme de température 300-500 °C.

Un grand nombre de matériaux thermoélectriques ont été étudiés depuis les vingt dernières années. La plupart des familles de matériaux les plus connues ont été améliorées et de nouvelles familles de matériaux ont été développées, entrainant une nette amélioration du ZT quelle que soit la gamme de température des applications considérées. Afin d'être viable pour une production industrielle, un matériau thermoélectrique doit répondre à un certain nombre de critères. Premièrement, les composants du matériau thermoélectrique doivent être non toxiques, bas coût et abondants. Ensuite, la voie de fabrication doit être robuste et compatible avec une production en grand volume. Enfin, les matériaux élaborés doivent posséder des propriétés thermoélectriques satisfaisantes dans la gamme de température de l'application visée. Ils doivent également être stables selon les environnements liés à l'application et avoir une bonne tenue mécanique.

Les matériaux de type half-Heusler apparaissent comme prometteurs pour la génération de puissance thermoélectrique dans la gamme de température 300-500 °C. En effet, grâce à leur structure de bande de type semi-conducteur, ils possèdent un coefficient de Seebeck et une conductivité électrique élevés. Cependant, leur conductivité thermique est relativement haute, comparée aux autres matériaux thermoélectriques. C'est pour cela que la recherche liée à cette famille de matériaux se concentre principalement sur la réduction de la conductivité thermique, tout en essayant de maintenir un bon transport électrique.

Ce travail de thèse s'est donc focalisé sur l'étude des relations microstructure-propriétés thermoélectriques de matériaux half-Heusler de formule générique $Hf_{0.25}Zr_{0.25}Ti_{0.5}NiSb_{0.002}Sn_{0.998}$, pour le type n, et $Hf_{0.44}Zr_{0.44}Ti_{0.12}CoSb_{0.8}Sn_{0.2}$, pour le type p, et de leurs possibles variantes. Les compositions testées ont toutes été synthétisées de la même manière : une fusion par induction permet d'obtenir des lingots qui sont ensuite réduits en poudre par broyage, celle-ci est ensuite frittée par frittage SPS (spark plasma sintering) afin d'obtenir une pastille dense et polycristalline. Les propriétés thermoélectriques et la microstructure de ces échantillons sont ensuite caractérisées et discutées de manière interactive.

Un des objectifs de ce travail de thèse était également de réduire le coût au kilogramme de ces matériaux half-Heusler, sans impacter de manière négative leurs propriétés thermoélectriques.

Nous y sommes parvenus, d’une part, en réduisant la concentration en hafnium incorporé dans les formulations (l’hafnium est responsable de plus de 70 % du coût total des précurseurs d’apport), et d’autre part, en simplifiant le procédé global de fabrication. En effet, nous avons observé qu’une synthèse et une manipulation sous air des poudres half-Heusler permettaient la formation in-situ de précipités d’oxydes pendant le frittage, agissant comme source de diffusion des phonons et donc favorisant la diminution de la conductivité thermique des matériaux frittés d’intérêt.